The Dissertation Committee for Jessica Joy Hung Certifies that this is the approved version of the following Dissertation:

Design of Co-solute Formulations for Stable, Highly Concentrated Monoclonal Antibody Solutions with Low Viscosity

Committee:

Keith Johnston, Supervisor

Thomas Truskett, Co-Supervisor

Benjamin Keith Keitz

Jennifer Maynard

Jeanne Stachowiak

Design of Co-solute Formulations for Stable, Highly Concentrated Monoclonal Antibody Solutions with Low Viscosity

by

Jessica Joy Hung

Dissertation

Presented to the Faculty of the Graduate School of

The University of Texas at Austin

in Partial Fulfillment

of the Requirements

for the Degree of

Doctor of Philosophy

The University of Texas at Austin

May 2018

Acknowledgements

I would like to acknowledge the numerous collaborators who have helped to make this thesis possible, given the incredible breadth and richness of the research challenges addressed in this work. First, I would like to thank my advisor Dr. Keith Johnston and my co-advisor Dr. Thomas Truskett, who were invaluable in guiding me throughout my thesis. They introduced me to entire new fields of science as well as to collaborators from across industry and academia, all of whom and which has served to greatly enrich my research and enhance my understanding of the complexity of the fundamental challenges in drug delivery, protein stability and biophysical behavior, as well as the practical considerations and challenges of those same problems from the perspective of industrial pharmaceutical scientists. I would also like to acknowledge our collaborators Dr. Jennifer Maynard and Dr. Jeanne Stachowiak from UT Austin, who greatly enriched and expanded the scope of my work at the beginning and end of my thesis, respectively, with their respective expertise in immunology and fluorescence correlation spectroscopy of proteins. I would also especially like to thank my current and former lab mates Aileen Dinin, Ameya Borwankar, Joshua Laber, Brian Wilson, and especially Barton Dear and Amjad Chowdhury, who were always there to provide intellectual feedback, experimental or troubleshooting assistance, and general encouragement in my day-to-day research work. I also want to thank the numerous undergraduate students that I have had the privilege of mentoring and supervising, whose invaluable assistance in the lab have allowed me and my fellow lab mates to greatly accelerate the intellectual development of our work. In no particular order, I would like to acknowledge Carl Karouta, Maria Nieto, Kishan Ramachandran, Tony Shay, Logan Wilks, Ayush Sharma, Sumarth Mehta, Vamshi Poladi, Majid Abdel-Raziq, Arathi Kumar, Sanket Dahotre, Anuj Kudva and Dan Lubis. I would also like to thank the current and former members of the Johnston group, including Robert Stover, Andrew Worthen, William

Hardin, Amro Elhag, Shehab Alzobaidi, Caleb Alexander, Ehsan Moaseri, Behzad Changalvaie, Chola Dandamudi, Carson Chang Da, Muhammad Iqbal, Goliath Beniah, Joohyung Lee, Esteban Benavidez and Tyler Mefford for their encouragement and support, scientific discussions, and technical assistance.

Given the multidisciplinary nature of this research topic, I also had the privilege to collaborate with numerous researchers from across industry and academia to enhance the scope of our work and understanding, whom I would like to acknowledge at this time.

For my work on static light scattering (chapter 1), I would like to acknowledge Dr. Allen Minton (National Institute of Health, Bethesda, MA) for providing me with the Matlab script used to analyze the scattering data by a self-association model, as well as providing intellectual discussions that contributed to the development of the chapter. I would also like to acknowledge P. Douglas Godfrin (MIT, Cambridge, MA) and Jonathan Bollinger (Sandia National Labs, Albuquerque, NM; formerly UT Austin) for their intellectual contributions and provision of Matlab code to analyze the scattering data by a Yukawa interaction potential model.

For my work on fluorescence correlation spectroscopy (chapter 2), I would like to acknowledge Dr. Jeanne Stachowiak (UT Austin) and her group members Carl Hayden (Sandia National Labs), Wade Zeno, Wilton Snead, and Justin Houser for providing training, technical and troubleshooting assistance with the FCS technique and associated experimental methods.

Finally, I would like to thank my family for their tireless support and encouragement throughout my PhD, as well as my funding sources, including the Welch Foundation (F-1319), the National Science Foundation (DGE-1110007), AbbVie Inc., Pfizer Inc., and Merck & Company, Inc., of which the latter three additionally provided monoclonal antibodies and intellectual feedback for the studies presented in this thesis.

Abstract

Design of Co-solute Formulations for Stable, Highly Concentrated Monoclonal Antibody Solutions with Low Viscosity

Jessica Joy Hung, Ph.D.

The University of Texas at Austin, 2018

Supervisor: Keith Johnston, Thomas Truskett

Highly concentrated (> 200 mg/mL) monoclonal antibody (mAb) formulations with low viscosities are strongly desired for subcutaneous drug delivery for the treatment of diseases such as cancer, as well as for improved process performance and yield in the manufacture of biologic drug products using techniques such as tangential flow ultrafiltration (TFF). High solution viscosities and protein aggregation at high concentration lead to significant challenges in delivery and manufacture due to large injection forces, product loss to aggregation, and significant filter membrane fouling and flux decay. Small-molecule co-solutes such as arginine and various electrolytes have in some cases been shown to greatly reduce the viscosity of concentrated mAbs. However, the mechanism by which co-solutes modify mAb viscosity is not well understood. Herein, we investigate the effects of several amino acids and inorganic ionic co-solutes on the viscosity of mAbs up to 250 mg/mL. We relate the viscosities to measurable changes in the protein-protein interactions (PPI), mAb structure and self-association behavior as assessed through small-volume techniques such as dynamic light scattering (DLS), static light scattering (SLS) and fluorescence correlation spectroscopy (FCS) in order to develop a hierarchical understanding of the co-solute effects on the mAb behavior. We demonstrate that the

viscosity reduction is correlated with the disruption of mAb self-association and attractive PPI, as directly probed by SLS, DLS, FCS and rheology. We also relate these changes in the PPI and viscosity to the physical properties of the co-solute, including the co-solute charge, size and shape. Finally, we demonstrate that the ability to mitigate aggregation and membrane fouling by the combined addition of viscosity-reducing co-solutes and selection of hollow fiber filter geometries resulted in a high-concentration transmembrane flux three-fold higher than that of conventional low co-solute buffer formulations. The reduced viscosities also led to more uniform axial transmembrane pressure and shear stress profiles, which led to reduce irreversible aggregation and solution turbidity during ultrafiltration.

Table of Contents

List of Tables

List of Figures

Figure 3.15. Normalized autocorrelation function (ACF) replicates of mAb2 for all co-solute systems at 60, 125, 150, 200, ~225 and ~250 mg/mL. The ACFs were normalized by the G(0) values of the raw ACFs (Table 3.6). ACFs are shown for 5 mM $ZnSO_4$ at **(a)** 60 mg/mL, **(b)** 125 mg/mL, **(c)** 150 mg/mL, **(d)** 200 mg/mL; 50 mM NaCl at **(e)** 60 mg/mL, **(f)** 150 mg/mL, **(g)** 200 mg/mL, **(h)** 250 mg/mL; 150 mM NaCl at **(i)** 60 mg/mL, **(j)** 150 mg/mL, **(k)** 200 mg/mL, **(l)** 250 mg/mL; 250 mM NaCl at **(m)** 60 mg/mL, **(n)** 125 mg/mL, **(o)** 150 mg/mL, **(p)** 200 mg/mL, **(q)** 219 mg/mL; 50 mM Arg.HCl at **(r)** 60 mg/mL, **(s)** 125 mg/mL, **(t)** 200 mg/mL; 150 mM Arg.HCl at **(u)** 60 mg/mL, **(v)** 125 mg/mL, **(w)** 200 mg/mL, **(x)** 250 mg/mL; 250 mM Arg.HCl at **(y)** 60 mg/mL, **(z)** 125 mg/mL, **(aa)** 150 mg/mL, **(ab)** 200 mg/mL, **(ac)** 225 mg/mL, **(ad)** 250 mg/mL; 1 M Imid(HCl) **(ae)** 60 mg/mL, **(af)** 125 mg/mL, **(ag)** 150 mg/mL, **(ah)** 200 mg/mL, and **(ai)** 241 mg/mL.

Figure 3.15 cont. Normalized autocorrelation function (ACF) replicates of mAb2 for all co-solute systems at 60, 125, 150, 200, ~225 and ~250 mg/mL. The ACFs were normalized by the G(0) values of the raw ACFs (Table 3.6). ACFs are shown for 5 mM $ZnSO_4$ at **(a)** 60 mg/mL, **(b)** 125 mg/mL, **(c)** 150 mg/mL, **(d)** 200 mg/mL; 50 mM NaCl at **(e)** 60 mg/mL, **(f)** 150 mg/mL, **(g)** 200 mg/mL, **(h)** 250 mg/mL; 150 mM NaCl at **(i)** 60 mg/mL, **(j)** 150 mg/mL, **(k)** 200 mg/mL, **(l)** 250 mg/mL; 250 mM NaCl at **(m)** 60 mg/mL, **(n)** 125 mg/mL, **(o)** 150 mg/mL, **(p)** 200 mg/mL, **(q)** 219 mg/mL; 50 mM Arg.HCl at **(r)** 60 mg/mL, **(s)** 125 mg/mL, **(t)** 200 mg/mL; 150 mM Arg.HCl at **(u)** 60 mg/mL, **(v)** 125 mg/mL, **(w)** 200 mg/mL, **(x)** 250 mg/mL; 250 mM Arg.HCl at **(y)** 60 mg/mL, **(z)** 125 mg/mL, **(aa)** 150 mg/mL, **(ab)** 200 mg/mL, **(ac)** 225 mg/mL, **(ad)** 250 mg/mL; 1 M Imid(HCl) **(ae)** 60 mg/mL, **(af)** 125 mg/mL, **(ag)** 150 mg/mL, **(ah)** 200 mg/mL, and **(ai)** 241 mg/mL.

Figure 3.15 cont. Normalized autocorrelation function (ACF) replicates of mAb2 for all co-solute systems at 60, 125, 150, 200, ~225 and ~250 mg/mL. The ACFs were normalized by the G(0) values of the raw ACFs (Table 3.6). ACFs are shown for 5 mM $ZnSO_4$ at **(a)** 60 mg/mL, **(b)** 125 mg/mL, **(c)** 150 mg/mL, **(d)** 200 mg/mL; 50 mM NaCl at **(e)** 60 mg/mL, **(f)** 150 mg/mL, **(g)** 200 mg/mL, **(h)** 250 mg/mL; 150 mM NaCl at **(i)** 60 mg/mL, **(j)** 150 mg/mL, **(k)** 200 mg/mL, **(l)** 250 mg/mL; 250 mM NaCl at **(m)** 60 mg/mL, **(n)** 125 mg/mL, **(o)** 150 mg/mL, **(p)** 200 mg/mL, **(q)** 219 mg/mL; 50 mM Arg.HCl at **(r)** 60 mg/mL, **(s)** 125 mg/mL, **(t)** 200 mg/mL; 150 mM Arg.HCl at **(u)** 60 mg/mL, **(v)** 125 mg/mL, **(w)** 200 mg/mL, **(x)** 250 mg/mL; 250 mM Arg.HCl at **(y)** 60 mg/mL, **(z)** 125 mg/mL, **(aa)** 150 mg/mL, **(ab)** 200 mg/mL, **(ac)** 225 mg/mL, **(ad)** 250 mg/mL; 1 M Imid(HCl) **(ae)** 60 mg/mL, **(af)** 125 mg/mL, **(ag)** 150 mg/mL, **(ah)** 200 mg/mL, and **(ai)** 241 mg/mL.

Chapter 1: Introduction

1.1 CHALLENGES OF HIGH CONCENTRATION PROTEIN THERAPEUTICS

The biophysical behavior of protein molecules in crowded environments is of great interest for advanced drug therapies, especially for the subcutaneous delivery of therapeutic proteins such as antibodies. Therapeutic proteins such as antibodies are of great interest for the treatment of chronic diseases and conditions such as cancer, arthritis and allergies, as well as acute life-threatening illnesses such as Ebola. The high selectivity of antibodies for recognizing pathogens and diseased cells are crucial to their role in the immune system. Due to their greater efficacy and milder side effects compared to more conventional small-molecule drugs, antibodies represent an already large and rapidly growing sector of the biopharmaceutical market, and addressing the challenges that limit their manufacture and delivery is of urgent interest. However, dosages on the order of several hundred milligrams are typically needed to achieve the desired therapeutic effect (1).

Antibodies are typically administered by IV infusion as dilute solutions, which require large injection volumes (1 L), resulting in long injection times and need for specialized equipment. Instead, it would be preferable to deliver them via low-volume (~1.5 mL) subcutaneous injections. To administer the same dosage in such a small volume, however, the antibodies must be delivered at concentrations on the order of 100 – 200 mg/mL or higher (1). Such concentrated solutions present challenges for manufacturing and delivery due to high solution viscosities as well as protein instability against aggregation (1-4), leading to large injection forces (5, 6) as well as reduced fluxes and enhanced aggregation during filtration processes (3, 7, 8) that decrease product yield and process throughputs.

In order to minimize the required injection force during drug administration (6, 9), as well as to reduce the loads on pumps during manufacturing (1, 3), it is desirable to maintain the

solution viscosity below 20 cP (10). However, the viscosities of antibody solutions increase exponentially with protein concentration (2), causing this viscosity limit to be exceeded at relatively low concentrations. In addition, the concentrated solutions often exhibit poor colloidal and conformational stability during long-term storage, resulting in protein unfolding and/or aggregation (1). The protein aggregates are especially problematic, as antibodies not only lose their therapeutic effect in the aggregated state, but can also provoke negative immunogenic responses (11). The challenges of high viscosities and protein instability must therefore be addressed to advance the development of concentrated antibody solutions for subcutaneous delivery of protein drugs. Highly detailed backgrounds and descriptions of the theory and developed understanding of protein biophysical behavior at high concentration in relation to viscosity are provided in the introduction section of each individual chapter, and are presented in a more concise form below.

1.2 INFLUENCE OF SHORT-RANGED ATTRACTIVE PROTEIN INTERACTIONS AND SELF-ASSOCIATION ON VISCOSITY

Many studies have been undertaken to understand the cause of the large increases in viscosity and colloidal instability (aggregation) of highly concentrated protein solutions, as well as how formulation conditions such as pH, salt concentration and co-solutes affect those properties. Pioneering work on static and small-angle light scattering of concentrated (>200 mg/mL) antibody solutions by Shire, Scherer and coworkers at Genentech (12-17), as well as Godfrin (18-20) and Fukuda (21) have shown that the increase in solution viscosity corresponds with the formation of transient, loose protein networks or reversible aggregates. Rheological models also suggest that the large viscosity increase in protein solution relative to colloidal solutions is disproportionately caused by the presence of oligomers in solution (22, 23). The presence of these networks at high protein concentration is also evident in the non-Newtonian response of concentrated solutions to shear; high shear rheological studies (5, 24) have found

that concentrated antibody solutions show significant shear-thinning behavior, whereas dilute solutions do not. Similarly, coarse-grained molecular dynamics simulations at high concentration of mAbs represented by 12-bead models (where each Fab and Fc domain are represented by 4 beads) have demonstrated that viscous mAbs form larger, more loosely-expanded oligomers that may eventually span the system volume (25-27), consistent with the formation of larger oligomers and networks observed from rheological and light scattering studies of viscous mAbs.

Protein self-association and resulting network formation at high concentration is mediated by strong, attractive short-ranged PPI, which dominate over the long-range electrostatic and steric repulsion at short interparticle separation distances (18-20, 28, 29). These short-ranged PPI include electrostatic attraction between oppositely charged sites and charge dipoles as well as between hydrophobic surface residues on adjacent protein molecules, in addition to hydrogen bonds, Van der Waals forces and other non-electrostatic interactions. However, due to charge and hydrophobicity heterogeneity on the protein surface, the net protein-protein interactions (PPI) are highly complex and hard to delineate into individual contributions from electrostatic, hydrophobic, steric, and hydrodynamic forces. Furthermore, empirical models to predict viscosities of concentrated mAbs a priori from their sequence have seen limited success given the complexities of how charge and charge asymmetries in the various domains along with other short ranged attraction influence self-association (25-27, 30). The complex protein topology also leads to coupling of the different forces (31). Since these interactions influence the rheological, conformational and colloidal properties of the protein solutions, an understanding of these interactions at high concentration and their dependence on solution conditions would be greatly beneficial for the development of protein therapeutics with desirable solution properties.

1.3 REDUCTION OF PROTEIN SOLUTION VISCOSITIES AT HIGH CONCENTRATION BY MODIFICATION OF PROTEIN INTERACTIONS USING CO-SOLUTES

To mitigate the physical challenges associated with high concentration protein drug delivery and manufacturing, high solution viscosities and protein self-association may be reduced by engineering the sequence to remove hydrophobic patches or reduce charge anisotropy (28, 32-37). However, such approaches are time consuming and complicated. A simpler approach would be to mitigate the underlying attractive PPI that drive self-association and viscosity increases through formulation design (i.e. addition of co-solutes). In some cases, charge screening alone by addition of NaCl is sufficient to reduce viscosity (2, 38, 39), but in many cases organic acids and bases such as camphorsulfonic acid and arginine are more effective due to the additional screening of hydrophobic attraction (21, 28, 39-47). In our group's previous work, organic electrolytes such as arginine (Arg), histidine (His) and imidazole (Im) have been shown to reduce the viscosity to a greater extent than traditional inorganic electrolytes such as NaCl and Na2SO4 (42). However, the efficacy of many of these co-solutes is protein-dependent, in some cases causing opposite effects on different antibodies (2, 44, 48). Correlations and predictions of high concentration viscosities with low concentration measurements of PPI, such as the second osmotic virial coefficient B_{22} and diffusion interaction parameter k_D, have not always been consistent for a series of mAbs (28, 37, 49). The variability is likely due to the heterogeneous distribution of charged/hydrophobic surface residues and the balance of electrostatic, hydrophobic and steric forces, resulting in a net interaction profile unique to each protein as mentioned previously. In addition, the specific locations of the attractive sites with respect to the protein topology may also strongly influence the effective strength of the mAb interaction potential (31), potentially leading to large changes in self-association behavior for small changes in the overall (net) PPI strength.

Previous light and X-ray/neutron scattering studies have provided further insight into how co-solutes modify the PPI and corresponding microstructure in relation to their influence on

the solution viscosity. Small angle X-ray (SAXS) studies (16, 17, 20) revealed that the addition of the salt NaCl reduced the viscosity of a highly viscous mAb at high concentration by suppressing self-association, as seen from the reduction in the intermediate-range order (IRO) peak (occurring at the length scale of dimers) in the scattering profile of that mAb (20). The concurrent reduction in viscosity and suppression of the IRO peak by the addition of NaCl strongly suggests that screening of the attractive electrostatic PPI led to dissolution of the protein microstructure (dimer network), which in turn caused the viscosity reduction. In contrast, the addition of the salt Na2SO4 was seen to cause an increase in self-association for another mAb, based on the increase in the protein hydrodynamic radius seen by dynamic light scattering and neutron spin echo, concurrent with a large increase in the mAb viscosity (50). These contrasting effects of salt on the mAb microstructure and viscosity reveal the complexity of protein interactions and co-solute effects on PPI. In addition, these more sophisticated biophysical characterization studies have been primarily limited to the inorganic salts NaCl and Na2SO4. As a result, the mechanism by which the more potent organic co-solutes (such as arginine, histidine and imidazole) modify the PPI and mAb static and dynamic structures in relation to viscosity at high concentration is still not well understood.

1.4 OBJECTIVES

Highly concentrated (> 200 mg/mL) monoclonal antibody (mAb) formulations with low viscosities are strongly desired for subcutaneous drug delivery for the treatment of diseases such as cancer, as well as for improved process performance and yield in the manufacture of biologic drug products using techniques such as tangential flow ultrafiltration (TFF). Small-molecule co-solutes such as arginine and various electrolytes have in some cases been shown to greatly reduce the viscosity of concentrated mAbs, mitigating the physical challenges (large injection forces and low product yields from high viscosity, aggregation, etc.) encountered at high concentration. However, the mechanism by which co-solutes modify mAb viscosity is not well

understood. The goals of this dissertation are therefore to: (1) characterize the effects of viscosity-modifying co-solutes on the protein-protein interactions (PPI) and equilibrium microstructures in highly concentrated mAb solutions, (2) characterize the co-solute effects on the mAb dynamic (diffusion) behavior, and (3) relate the mAb solution rheology to the mAb biophysical behavior at high concentration in order to develop a fundamental understanding of how co-solutes modify mAb solution viscosity and stability to provide for more efficient, guided formulation design across a variety of mAbs. The improved viscosity and stability profiles will further be demonstrated to (4) improve the process performance of the tangential flow ultrafiltration process used in industry to manufacture highly concentrated mAb solutions.

In the course of the thesis, the objectives were generalized to understand the structure of protein solutions with static light scattering as a function of the strength of the shorted ranged attraction. In this approach, the co-solutes and ionic strength were used as tools to control the PPI over a wide range. The SLS studies provided important information to guide my collaborations with two other PhD students, Bart Dear and Amjad Chowdhury on SAXS of protein structure and dynamic light scattering studies in additional papers that will be completed after this dissertation.

For the first objective of this dissertation, the effects of a range of viscosity-modifying ionic co-solutes on the static structure and PPI of two mAbs, mAb2 and mAb3, as a function of concentration (2 – 225 mg/mL) will be investigated by static light scattering (SLS) (12-14, 51). The strength of the net PPI in each co-solute formulation will be quantified by the zero-q structure factor $S(q \rightarrow 0)$ and Kirkwood-Buff integral G22 determined from the scattering profile measured by SLS. S(0) will also be fit to a single-attractive Yukawa interaction potential to quantify the strength of the short-ranged attractive interactions (K) reflected in the scattering behavior. The concentration-dependent scattering intensities will also be interpreted with the interacting hard sphere (IHS) model (52) to investigate the co-solute effects on the apparent self-

association of both mAbs from low to high concentration, as quantified by an average apparent cluster size $<N_c>$ and corresponding oligomer mass ratio $m_{oligomer}/m_{mono+dimer}$.

For the second objective of this dissertation, the effects of a range of ionic co-solutes on the dynamic behavior (namely the self-diffusion) of mAb2 from low to high concentration will be probed by fluorescence correlation spectroscopy (FCS). The diffusion retardation D_0/D_s will be interpreted with the length-scale dependent viscosity (LDV) model to explain deviations from generalized Stokes-Einstein behavior and to obtain a quantitative measure of the PPI strength via the co-solute effects on D_0/D_s. The LDV model will also be used to attempt to decouple the influence of hydrodynamic effects, structural length scale effects and PPI on the mAb self-diffusion. In order to facilitate measurements of mAb self-diffusion at high concentration by FCS, for which there is very limited precedence in literature, the FCS methodology will also be optimized through a series of method development studies to enable high-quality, more reproducible measurements at high concentration and solution viscosities.

For the third objective of this dissertation, the net PPI strength and self-association behavior determined from both SLS (static structure) and FCS (dynamic structure) will be correlated with the solution viscosity at high concentration for mAb2 and mAb3 to attempt to derive a more universal relation between the solution viscosity and underlying protein interactions and microstructure. Furthermore, the co-solute effects on the diffusion probe size and PPI, as interpreted from D_0/D_s from FCS will be related to the measurements of PPI and self-association from SLS to construct a more complete and consistent understanding of the co-solutes' effects on the physical behavior and corresponding solution viscosity for highly concentrated mAbs. Co-solute effects on the mAb viscosity and stability will also be investigated for a systematic set of co-solutes ranging from inorganic and organic ionic co-solutes (NaCl, arginine, histidine, imidazole, lysine) to neutral osmolytes (proline, glycine, trehalose) for three mAbs (mAb1 – mAb3) to develop a more general fundamental understanding of the relation

between the co-solutes' physical properties (size, charge, shape) and their effects on PPI. The work supporting the development of this objective are closely interrelated with the work for the first two objectives.

For the fourth objective of this dissertation, the influence of the solution viscosity on the performance (process throughput and yield) of high concentration tangential flow filtration (TFF) for the antibody mAb1 will be investigated. The addition of 320 mM histidine will be used to reduce the viscosity of the concentrated (~250 mg/mL) mAb solution. The viscosity reduction will be related to changes in the axial local transmembrane pressure (TMP) and wall shear stress profiles. The extent of protein aggregation and membrane fouling will be related to the uniformity and magnitude of the applied local TMP and wall shear stresses in order to develop a mechanistic understanding of how formulation design for lower viscosities influence the TFF process yield and throughput. The rate of flux decay as well as maximum achievable protein concentration will also be related to the viscosity to understand what the controlling factors in the TFF performance are, and how they can be tuned through formulation design.

1.5 DISSERTATION OUTLINE

The work represented in Chapters 2 to 5 of the dissertation are not presented in the chronological order of when the work was done. The actual chronological order was Chapter 4 to 3 to 1 and finally to 2. To present a more strategic structure for explaining the logic behind the studies, the order of the chapters was chosen to evolve from more fundamental studies to more applied studies. The main experimental techniques in Chapters 2 and 3 were static light scattering (SLS) and fluorescence correlation spectroscopy (FCS) respectively. In contrast Chapters 4 used viscometry, size exclusion chromatography (SEC), and dynamic light scattering (DLS) to evaluate the effects of co-solutes on mAb stability and solution viscosity, while Chapter 5 used tangential flow filtration (TFF) in combination with the protein characterization

techniques from chapter 4 to understand the interrelation between TFF process parameters, mAb stability and viscosity, and TFF process performance.

In chapter 1, this dissertation introduces the concept of tuning protein-protein interactions using co-solutes in order to modify the mAb self-association behavior and viscosity at high concentration, as investigated through the co-solute effects on the mAb static structure measured by SLS. In chapter 2, the strength of protein-protein interactions (PPI) of two IgG1 monoclonal antibodies (mAbs) from low to high concentration were determined by static light scattering (SLS) and used to understand viscosity data. The PPI were tuned using NaCl and five organic ionic co-solutes. The PPI strength was quantified by the normalized structure factor $S(0)/S(0)_{HS}$ and Kirkwood-Buff integral $G_{22}/G_{22,HS}$ (HS = hard sphere) determined from the SLS data, and also by fits with (1) a spherical Yukawa potential and (2) an interacting hard sphere (IHS) model. The IHS model describes attraction in terms of hypothetical oligomers. For each descriptor of PPI, linear correlations were obtained between the viscosity at high concentration (200 mg/mL) and the interaction strengths evaluated both at low (20 mg/mL) and high concentration (200 mg/mL) for a given mAb. However the only parameter that provided a correlation across both mAbs was the oligomer mass ratio ($m_{oligomer}/m_{monomer+dimer}$) from the IHS model, indicating the importance of self-association (in addition to the direct influence of the attractive PPI) on the viscosity.

The investigation of the co-solute effects on the PPI and mAb self-association through measurement of the mAb static structure was complemented by evaluation of the co-solute effects on the mAb dynamic behavior (self-diffusion) obtained by fluorescence correlation spectroscopy. The data are interpreted using a length-scale dependent viscosity model. In chapter 3, the suitability of fluorescence correlation spectroscopy (FCS) technique for measuring the self-diffusion of mAb2 from low to high concentration (60 – 250 mg/mL) across a range of co-solute formulations with varying viscosities (ex. 10 cP to 100 cP at 200 mg/mL) was

demonstrated after initial method optimization. The self-diffusion D_0/D_s was found to deviate from the generalized Stokes-Einstein (GSE) relation with respect to the macroscopic viscosity. Given that the probe (labeled mAb) was the same size as the crowding agent (unlabeled mAb), D_0/D_s was fit to a length-scale dependent viscosity (LDV) model to partially decouple the effects of structure, hydrodynamic interactions and PPI on the diffusion. The lowest-viscosity formulations had the weakest attraction based on the interaction parameter b extracted from fits of D_0/D_s, in agreement with measurements of PPI by SLS and SAXS for the same mAb. In contrast, the polydispersity of the solution as measured by FCS appeared to be decoupled from the viscosity, despite known differences in the mAb's self-association behavior between formulations as assessed by SLS and SAXS. The apparent decoupling was hypothesized to be caused by the long time scale of the FCS measurements relative to the fast equilibrium exchange of the labeled mAb between monomer and oligomers.

The influence of the ionic co-solutes investigated in chapters 2 and 3 (NaCl, arginine, lysine, imidazole, etc. for mAb2 and mAb3) was contrasted with the effects of neutral osmolytes (proline, glycine, trehalose) on the viscosity and stability for a different mAb (mAb1). Although the use of different mAbs for the different co-solutes prevented direct comparison of general co-solute effects on PPI and stability, the comparison of the neutral osmolytes against histidine (an organic ionic co-solute similar to arginine and imidazole) in chapter 4 for the same mAb (mAb1) provided for a more developed fundamental understanding of the relation between the co-solute physical properties and the general co-solute effects on PPI seen from SLS and FCS. The choice of mAbs at various stages of the thesis was governed by availability of the mAbs from the three biopharmaceutical sponsors and this limited somewhat the flexibility in integrating the various thesis chapters, although important conclusions were obtained in all chapters.

In chapter 4, the viscosity of ~225 mg/mL mAb1 solutions was measured with proline, glycine and trehalose as a function of pH and co-solute concentration up to 1.3M. The stability

was assessed via turbidity as well as size exclusion chromatography after 4 weeks storage at 40°C. The PPI strength was assessed qualitatively via the high concentration diffusion rate by dynamic light scattering. Proline was found to significantly reduce the mAb viscosity and increase the colloidal stability at pH 6 with increasing proline concentration, but not at pH 5 further from the mAb pI. In contrast, glycine and trehalose were found not to improve the viscosity nor stability. The greater efficacy for improving mAb viscosity and stability demonstrated by proline in contrast to glycine and trehalose was hypothesized to be due to its amphipathic structure and partial charge on the pyrrolidine side chain, which likely allow proline to screen the attractive electrostatic and hydrophobic interactions that promote self-association and high viscosities.

To illustrate the importance of formulation development (based on the fundamental understanding of co-solute effects on protein biophysical behavior, as developed in chapters 2 – 4) for protein drug manufacturing, two low viscosity formulations identified for mAb1 during formulation development were integrated with process development for TFF to demonstrate improved process performances as a result of the lower viscosity. In chapter 5, the co-solutes histidine or imidazole were added at high concentrations from 250 to 320 mM to reduce the viscosity of mAb1 by up to ten-fold relative to conventional low co-solute formulations, to as low as 40 cP at 250 mg/mL. At high mAb concentrations of up to 280 mg/mL, the transmembrane flux was increased threefold by adding high concentrations of co-solutes that also lowered the viscosity. Furthermore, the co-solutes also increased the mAb gel point concentration c_g by up to 100 mg/mL mAb and thus enhanced concentration polarization-driven back-diffusion of the mAb at the membrane wall, which led to increased fluxes. The low viscosity and use of hollow fiber filter modules with straight flow paths enabled more uniform TMP and wall shear stress τ_w profiles, which mitigated the reversible flux decay that results from

an axial decline in the local TMP. The concentrated mAb was found to be stable by SEC before and after extended storage at 4°C and 37°C.

1.6 REFERENCES

1. Shire SJ, Shahrokh Z, Liu J. Challenges in the Development of High Protein Concentration Formulations. J Pharm Sci. 2004;93(6):1390-402.
2. Liu J, Nguyen MDH, Andya JD, Shire SJ. Reversible Self-Association Increases the Viscosity of a Concentrated Monoclonal Antibody in Aqueous Solution. J Pharm Sci. 2005;94(9):1928-40.
3. Rosenberg E, Hepbildikler S, Kuhne W, Winter G. Ultrafiltration concentration of monoclonal antibody solutions: Development of an optimized method minimizing aggregation. J Membr Sci. 2009;342(1-2):50-9.
4. Ahrer K, Buchacher A, Iberer G, Jungbauer A. Effects of ultra-/diafiltration conditions on present aggregates in human immunoglobulin G preparations. J Membr Sci. 2006;274(1-2):108-15.
5. Allmendinger A, Fischer S, Huwyler J, Mahler H-C, Schwarb E, Zarraga IE, et al. Rheological characterization and injection forces of concentrated protein formulations: An alternative predictive model for non-Newtonian solutions. Eur J Pharm Biopharm. 2014;87(2):318-28.
6. Burckbuchler V, Mekhloufi G, Giteau AP, Grossiord JL, Huille S, Agnely F. Rheological and syringeability properties of highly concentrated human polyclonal immunoglobulin solutions. Eur J Pharm Biopharm. 2010;76(3):351-6.
7. Binabaji E, Ma J, Rao S, Zydney AL. Theoretical analysis of the ultrafiltration behavior of highly concentrated protein solutions. J Membr Sci. 2015:JMS151044.
8. Baek Y, Singh N, Arunkumar A, Borys M, Li ZJ, Zydney AL. Ultrafiltration behavior of monoclonal antibodies and Fc-fusion proteins: Effects of physical properties. Biotechnol Bioeng. 2017;114(9):2057-65.
9. Jezek J, Rides M, Derham B, Moore J, Cerasoli E, Simler R, et al. Viscosity of concentrated therapeutic protein compositions. Adv Drug Deliv Rev. 2011;63(13):1107-17.
10. Srinivasan C, Weight AK, Bussemer T, Klibanov AM. Non-Aqueous Suspensions of Antibodies are Much Less Viscous Than Equally Concentrated Aqueous Solutions. Pharm Res. 2013.
11. Wang W, Singh SK, Li N, Toler MR, King KR, Nema S. Immunogenicity of protein aggregates-Concerns and realities. International journal of pharmaceutics. 2012;431(1-2):1-11.
12. Scherer TM. Cosolute Effects on the Chemical Potential and Interactions of an IgG1 Monoclonal Antibody at High Concentrations. J Phys Chem B. 2013;117(8):2254-66.
13. Scherer TM, Liu J, Shire SJ, Minton AI. Intermolecular Interactions of IgG1 Monoclonal Antibodies at High Concentrations Characterized by Light Scattering. J Phys Chem B. 2010;114(40):12948-57.
14. Scherer TM. Role of Cosolute–Protein Interactions in the Dissociation of Monoclonal Antibody Clusters. J Phys Chem B. 2015;119(41):13027-38.

15. Yearley EJ, Zarraga IE, Shire SJ, Scherer TM, Gokarn Y, Wagner NJ, et al. Small-Angle Neutron Scattering Characterization of Monoclonal Antibody Conformations and Interactions at High Concentrations. Biophys J. 2013;105(3):720-31.

16. Lilyestrom WG, Shire SJ, Scherer TM. Influence of the Cosolute Environment on IgG Solution Structure Analyzed by Small-Angle X-ray Scattering. J Phys Chem B. 2012;116(32):9611-8.

17. Lilyestrom WG, Yadav S, Shire SJ, Scherer TM. Monoclonal Antibody Self-Association, Cluster Formation, and Rheology at High Concentrations. J Phys Chem B. 2013;117(21):6373-84.

18. Godfrin PD, Zarzar J, Zarraga IE, Porcar L, Falus P, Wagner NJ, et al. The Effect of Hierarchical Cluster Formation on the Viscosity of Concentrated Monoclonal Antibody Formulations Studied by Neutron Scattering. J Phys Chem B. 2015.

19. Godfrin PD, Hudson SD, Hong K, Porcar L, Falus P, Wagner NJ, et al. Short-Time Glassy Dynamics in Viscous Protein Solutions with Competing Interactions. Phys Rev Lett. 2015;115(22):228302.

20. Yearley Eric J, Godfrin Paul D, Perevozchikova T, Zhang H, Falus P, Porcar L, et al. Observation of Small Cluster Formation in Concentrated Monoclonal Antibody Solutions and Its Implications to Solution Viscosity. Biophys J. 2014;106(8):1763-70.

21. Fukuda M, Moriyama C, Yamazaki T, Imaeda Y, Koga A. Quantitative Correlation between Viscosity of Concentrated MAb Solutions and Particle Size Parameters Obtained from Small-Angle X-ray Scattering. Pharm Res. 2015;32(12):3803-12.

22. Kastelic M, Dill KA, Kalyuzhnyi YV, Vlachy V. Controlling the viscosities of antibody solutions through control of their binding sites. Journal of Molecular Liquids. 2017.

23. Schmit JD, He F, Mishra S, Ketchem RR, Woods CE, Kerwin BA. Entanglement Model of Antibody Viscosity. J Phys Chem B. 2014;118(19):5044-9.

24. Zarraga IE, Taing R, Zarzar J, Luoma J, Hsiung J, Patel A, et al. High shear rheology and anisotropy in concentrated solutions of monoclonal antibodies. J Pharm Sci. 2013;102(8):2538-49.

25. Chaudhri A, Zarraga IE, Kamerzell TJ, Brandt JP, Patapoff TW, Shire SJ, et al. Coarse-Grained Modeling of the Self-Association of Therapeutic Monoclonal Antibodies. J Phys Chem B. 2012;116(28):8045-57.

26. Chaudhri A, Zarraga IE, Yadav S, Patapoff TW, Shire SJ, Voth GA. The Role of Amino Acid Sequence in the Self-Association of Therapeutic Monoclonal Antibodies: Insights from Coarse-Grained Modeling. J Phys Chem B. 2013;117(5):1269-79.

27. Buck PM, Chaudhri A, Kumar S, Singh SK. Highly Viscous Antibody Solutions Are a Consequence of Network Formation Caused by Domain-Domain Electrostatic Complementarities: Insights from Coarse-Grained Simulations. Mol Pharmaceutics. 2015;12(1):127-39.

28. Connolly Brian D, Petry C, Yadav S, Demeule B, Ciaccio N, Moore Jamie MR, et al. Weak Interactions Govern the Viscosity of Concentrated Antibody Solutions: High-Throughput Analysis Using the Diffusion Interaction Parameter. Biophys J. 2012;103(1):69-78.

29. Kumar V, Dixit N, Zhou L, Fraunhofer W. Impact of short range hydrophobic interactions and long range electrostatic forces on the aggregation kinetics of a monoclonal

antibody and a dual-variable domain immunoglobulin at low and high concentrations. International journal of pharmaceutics. 2011;421(1):82-93.

30. Corbett D, Hebditch M, Keeling R, Ke P, Ekizoglou S, Sarangapani P, et al. Coarse-Grained Modeling of Antibodies from Small-Angle Scattering Profiles. J Phys Chem B. 2017;121(35):8276-90.

31. Quang LJ, Sandler SI, Lenhoff AM. Anisotropic Contributions to Protein–Protein Interactions. J Chem Theory Comput. 2014;10(2):835-45.

32. Nichols P, Li L, Kumar S, Buck PM, Singh SK, Goswami S, et al. Rational design of viscosity reducing mutants of a monoclonal antibody: Hydrophobic versus electrostatic inter-molecular interactions. mAbs. 2015;7(1):212-30.

33. Chow C-K, Allan BW, Chai Q, Atwell S, Lu J. Therapeutic Antibody Engineering To Improve Viscosity and Phase Separation Guided by Crystal Structure. Mol Pharmaceutics. 2016;13(3):915-23.

34. Geoghegan JC, Fleming R, Damschroder M, Bishop SM, Sathish HA, Esfandiary R. Mitigation of reversible self-association and viscosity in a human IgG1 monoclonal antibody by rational, structure-guided Fv engineering. mAbs. 2016;8(5):941-50.

35. Kuhn AB, Kube S, Karow-Zwick AR, Seeliger D, Garidel P, Blech M, et al. Improved Solution-State Properties of Monoclonal Antibodies by Targeted Mutations. J Phys Chem B. 2017;121(48):10818-27.

36. Yadav S, Sreedhara A, Kanai S, Liu J, Lien S, Lowman H, et al. Establishing a Link Between Amino Acid Sequences and Self-Associating and Viscoelastic Behavior of Two Closely Related Monoclonal Antibodies. Pharm Res. 2011;28(7):1750-64.

37. Yadav S, Laue TM, Kalonia DS, Singh SN, Shire SJ. The Influence of Charge Distribution on Self-Association and Viscosity Behavior of Monoclonal Antibody Solutions. Mol Pharmaceutics. 2012;9(4):791-802.

38. Kanai S, Liu J, Patapoff TW, Shire SJ. Reversible Self-Association of a Concentrated Monoclonal Antibody Solution Mediated by Fab-Fab Interaction That Impacts Solution Viscosity. J Pharm Sci. 2008;97(10):4219-27.

39. Wang S, Zhang N, Hu T, Dai W, Feng X, Zhang X, et al. Viscosity-Lowering Effect of Amino Acids and Salts on Highly Concentrated Solutions of Two IgG1 Monoclonal Antibodies. Mol Pharmaceutics. 2015;12(12):4478-87.

40. Du W, Klibanov AM. Hydrophobic salts markedly diminish viscosity of concentrated protein solutions. Biotechnol Bioeng. 2011;108(3):632-6.

41. Guo Z, Chen A, Nassar R, Helk B, Mueller C, Tang Y, et al. Structure-Activity Relationship for Hydrophobic Salts as Viscosity-Lowering Excipients for Concentrated Solutions of Monoclonal Antibodies. Pharm Res. 2012;29(11):3102-9.

42. Dear BJ, Hung JJ, Truskett TM, Johnston KP. Contrasting the Influence of Cationic Amino Acids on the Viscosity and Stability of a Highly Concentrated Monoclonal Antibody. Pharm Res. 2017;34(1):193-207.

43. Borwankar AU, Dear BJ, Twu A, Hung JJ, Dinin AK, Wilson BK, et al. Viscosity Reduction of a Concentrated Monoclonal Antibody with Arginine·HCl and Arginine·Glutamate. Ind Eng Chem Res. 2016;55(43):11225-34.

44. Inoue N, Takai E, Arakawa T, Shiraki K. Specific Decrease in Solution Viscosity of Antibodies by Arginine for Therapeutic Formulations. Mol Pharmaceutics. 2014;11(6):1889-96.

45. Binabaji E, Ma J, Zydney A. Intermolecular Interactions and the Viscosity of Highly Concentrated Monoclonal Antibody Solutions. Pharm Res. 2015;32(9):3102-9.

46. Whitaker N, Xiong J, Pace SE, Kumar V, Middaugh CR, Joshi SB, et al. A Formulation Development Approach to Identify and Select Stable Ultra–High-Concentration Monoclonal Antibody Formulations With Reduced Viscosities. J Pharm Sci. 2017;106(11):3230-41.

47. Larson AM, Weight AK, Love K, Bonificio A, Wescott CR, Klibanov AM. Bulky Polar Additives That Greatly Reduce the Viscosity of Concentrated Solutions of Therapeutic Monoclonal Antibodies. J Pharm Sci. 2017;106(5):1211-7.

48. Wang S, Zhang N, Hu T, Dai WG, Feng X, Zhang X, et al. Viscosity-Lowering Effect of Amino Acids and Salts on Highly Concentrated Solutions of two IgG1 Monoclonal Antibodies. Mol Pharmaceutics. 2015.

49. Yadav S, Shire SJ, Kalonia DS. Factors Affecting the Viscosity in High Concentration Solutions of Different Monoclonal Antibodies. J Pharm Sci. 2010;99(12):4812-29.

50. Godfrin PD, Zarraga IE, Zarzar J, Porcar L, Falus P, Wagner NJ, et al. Effect of Hierarchical Cluster Formation on the Viscosity of Concentrated Monoclonal Antibody Formulations Studied by Neutron Scattering. J Phys Chem B. 2016;120(2):278-91.

51. Ghosh R, Calero-Rubio C, Saluja A, Roberts CJ. Relating protein-protein interactions and aggregation rates from low to high concentrations. J Pharm Sci. 2016;105(3):1086-96.

52. Minton AP. Static Light Scattering from Concentrated Protein Solutions, I: General Theory for Protein Mixtures and Application to Self-Associating Proteins. Biophys J. 2007;93(4):1321-8.

Chapter 2: Protein-Protein Interactions of Highly Concentrated Monoclonal Antibody Solutions via Static Light Scattering and Influence on the Viscosity[1]

Jessica J. Hung, Barton J. Dear, Carl A. Karouta, P. Douglas Godfrin, Jonathan A. Bollinger, Maria P. Nieto, Logan R. Wilks, Tony Y. Shay, Kishan Ramachandran, Ayush Sharma, Thomas M. Truskett, Keith P. Johnston

2.1 ABSTRACT

The ability to design and formulate mAbs for weak attractive interactions at high concentrations is important for protein processing, stability and administration, particularly in subcutaneous delivery, where high viscosities are often challenging. The strength of protein-protein interactions (PPI) of two IgG1 monoclonal antibodies (mAbs) from low to high concentration were determined by static light scattering (SLS) and used to understand viscosity data. The PPI were tuned using NaCl and five organic ionic co-solutes. The PPI strength was quantified by the normalized structure factor $S(0)/S(0)_{HS}$ and Kirkwood-Buff integral $G_{22}/G_{22,HS}$ (HS = hard sphere) determined from the SLS data, and also by fits with (1) a spherical Yukawa potential and (2) an interacting hard sphere (IHS) model. The IHS model describes attraction in terms of hypothetical oligomers. For each descriptor of PPI, linear correlations were obtained between the viscosity at high concentration (200 mg/mL) and the interaction strengths evaluated both at low (20 mg/mL) and high concentration (200 mg/mL) for a given mAb. However the only parameter that provided a correlation across both mAbs was the oligomer mass ratio ($m_{oligomer}/m_{monomer+dimer}$) from the IHS model, indicating the importance of self-association (in addition to the direct influence of the attractive PPI) on the viscosity.

[1] The first-author was responsible for method development for SLS measurements of viscous high concentration mAb solutions, the design of all experiments, ~70 % of the execution and data analysis (with direct supervision of the remaining ~30% conducted by Carl Karouta), and all of the data interpretation, intellectual development and writing of the manuscript, with theoretical support for the Yukawa model from Barton J. Dear, P. Douglas Godfrin and Jonathan A. Bollinger.

2.2 INTRODUCTION

Highly concentrated monoclonal antibody (mAb) solutions up to 300+ mg/mL often have a tendency to aggregate and become highly viscous, presenting challenges in protein processing, storage and subcutaneous delivery (1). These factors may influence safety and efficacy (1-4), and produce unacceptably large subcutaneous injection forces (5, 6) as well as reduced filtration fluxes and process yields (1, 7, 8). Strategies to mitigate these challenges may be based on reduction of the attractive short-ranged local anisotropic electrostatic (charge-charge; charge-dipole) (9-12) and hydrophobic (13, 14) protein-protein interactions (PPI) that promote self-association, as shown in simulations (15-17) and experimentally (18-23).While self-association may be reduced by engineering the sequence to remove hydrophobic patches or reduce charge anisotropy (9, 24-29), it may also be mitigated through formulation design. Empirical models to predict viscosities of concentrated mAbs a priori from their sequence have seen limited success given the complexities of how charge and charge asymmetries in the various domains along with other short ranged attraction influence self-association (16, 17, 30, 31). In some cases, charge screening alone by addition of NaCl is sufficient to reduce viscosity (21, 32, 33), but in many cases organic acids and bases such as camphorsulfonic acid and arginine are more effective (13, 14, 28, 33-40). To better guide formulation design for ionic strength, pH and the addition of co-solutes to lower viscosity and self-association, it would be beneficial to develop a deeper understanding of mAb higher-order structure and PPI from experimental measurements at high concentration.

Correlations and predictions of high concentration viscosities with low concentration measurements of PPI, such as the second osmotic virial coefficient B_{22} and diffusion interaction parameter k_D, have not always been consistent for a series of mAbs (9, 28, 41). These correlations are limited by the increasing influence of the anisotropic short-ranged PPI with decreasing interparticle spacings at high concentration. Thus, recent efforts have evaluated multibody interactions and resulting mAb orientations directly at high concentration. From well-

known studies on three Genentech mAbs and derivative mutants, distinct classes of mAbs in terms of salt effects on mAb PPI, structure and viscosity at high concentration may be identified. Two of the mAbs, referred to as GmAb1 (Genentech "mAb1" (9, 12, 21, 29, 32, 42, 43)) and GmAbG ("mAb1," (19, 44) "mAbG" (18)) were highly viscous, but with differing responses to salt addition. For GmAb1, strongly anisotropic attraction was observed from the structure factors from SANS (45) in agreement with formation of large clusters suggested by coarse-grained (CG) models (30). Dimer formation was seen even at dilute conditions by SAXS and DLS (20) and led to extensive self-association at high concentration as measured by SLS (22). Addition of NaCl suppressed self-association, seen by SLS (22) and by an increase in the self-diffusion (equivalent to a decrease in RH) from NSE (20), via charge screening and reduction of the significant charge anisotropy in the Fab region of the electrostatic potential surface (9). The reduced self-association was correlated with a large decrease in viscosity (21, 32, 46) as well as shear-thinning behavior (46). In contrast, GmAbG underwent self-association upon addition of Na2SO4, as seen by SAXS (18) and SLS (19), accompanied by a large increase in viscosity (18, 19). In contrast with these two mAbs, the third mAb GmAb2 ("mAb2" (9, 21, 29)) had a low base viscosity, which was unchanged by addition of NaCl (20). This behavior was attributed to low charge anisotropy in GmAb2's Fab region (9) resulting in weaker anisotropic electrostatic attraction, as seen from the smaller value of the structure factor S(q) that was well-described by a purely repulsive potential, in contrast with GmAb1 (45). Due to the weaker electrostatic PPI, GmAb2 did not self-associate, as seen from CG models (30) and DLS/NSE measurements of R_h (20). Mutation of the Fv region in GmAb1 to more closely resemble GmAb2 via charge swapping greatly reduced the viscosity (9, 29). Whereas these findings provide great insight into the effects of NaCl and Na_2SO_4 on PPI and viscosity as seen for other mAbs (23, 33, 34), much less is known about more potent organic co-solutes (13, 14, 34, 36, 40). To date, such studies of co-solute effects on high concentration PPI have been limited primarily to arginine, and only

provided qualitative correlations of viscosity with scattering intensities (proportional to S(q)) at high concentration from SAXS (39, 47).

Static light scattering (SLS) is commonly used to measure protein interactions at dilute conditions via B_{22} (48) and also at high concentration (up to 200 mg/mL) (22, 49-51) at low q values, typically ~0.0018 Å-1. The small volume requirements (~20 µL) and potential for high-throughput measurements using commercial instruments (52-55) are relevant for guiding mAb discovery and formulation. SLS provides a quantitative measure of the net interaction strength via the protein-protein Kirkwood-Buff integral G_{22} (49, 50, 56, 57) or zero-q static structure factor S(0) (56, 58). G_{22} is the multibody, high concentration analogue of B_{22} (Eqn. 2.1) (57)

$$G_{22} = 4\pi \int_r \left[\exp\left(-\frac{W_{22}(r)}{k_B T}\right) - 1\right] r^2 dr \tag{2.1}$$

where W_{22} is the concentration (c) dependent potential of mean force between two protein molecules as a function of the center-to-center separation distance r. In the low concentration limit (c → 0), G_{22} becomes $-2B_{22}$ (56). Analogous to the case for B_{22}, increasingly negative (positive) G_{22} values indicate growing net repulsion (attraction). G_{22} can also be related to the structure factor S(0) (Eqn. 2.2 (56)) in the zero-q limit (experimental q = 0.0018 $Å^{-1}$),

$$S(0) = 1 + c * G_{22} \tag{2.2}$$

which can also be compared with S(0) from SAXS/SANS analysis of protein structure and interactions (18, 31, 45, 59, 60).

The concentration-dependent S(0) and G_{22} may be fit to interaction potentials U(r) to quantify the strength and length scale of the short-range attraction and long-range repulsion. Initial efforts focused on fitting S(0)) across the entire tested concentration range with a single Baxter adhesion potential for a spherical model (22, 61-63), while more sophisticated models include mAb shape anisotropy with CG models (31, 56). For example, 12-bead models with bead charges determined from the mAb sequence have been used to accurately predict high

concentration scattering (R/K_0) values from Yukawa-screened Coulombic (Eqn. 2.3a) and Lennard-Jones interaction potentials parameterized only from the low concentration scattering (50, 57, 64),

$$\frac{U(r_{ij})}{k_B T} = \zeta \psi_i \psi_j q_i q_j * \frac{\exp(-\kappa*(r_{ij} - \sigma_{ij})}{r_{ij}\left[1+\frac{1}{2}(\kappa\sigma_{ij})\right]^2} \tag{2.3a}$$

However, these approaches are successful primarily for repulsive or weakly attractive systems (22, 57) with limited charge anisotropy throughout the various Fab and Fc domains (9), where the net short-ranged attraction strength is not very sensitive to mAb concentration. For strongly attractive systems, such as GmAb1, the scattering cannot be predicted over a wide concentration range up to 200 mg/mL from a single potential (22, 57). The implication is that the net attraction strength changes with concentration, which is indeed seen for SAXS fits of S(q) for a mAb (31) as well as the model protein α-chymotrypsinogen (65).

To describe the more complex scattering behavior of strongly attractive/anisotropic systems, Minton (66) treated the scattering solution as a three-component equivalent hard sphere mixture. In this approach, termed the "interacting hard sphere" (IHS) model by Scherer (22, 51, 61), no knowledge of the mAb shape, sequence, or form of the interaction potential is needed. Instead, the behavior is represented by the relative concentrations of larger scattering species (formed by the reversible self-association of equivalent hard sphere 'monomers'), where the attractive interactions are implicit in forming these multimers. Using this approach, Scherer was able to demonstrate that high concentrations of arginine completely suppress apparent oligomerization of GmAb1 through preferential binding of arginine to the mAb surface, in contrast to NaCl, which had a smaller binding affinity (51). More recently, this approach was also combined with rheological measurements to attempt to quantitatively describe the morphology of the oligomers formed across different mAbs and solution conditions, in order to relate the solution viscosity to the protein solution microstructure (67). Given the quantitative

insight gained with the Yukawa/Lennard-Jones (22, 50, 57) and interacting hard sphere models (19, 22, 51, 61) for low-q light scattering of mAbs at high concentration with simple salts (NaCl, Na_2SO_4, NaSCN) and arginine (67), it would be desirable to investigate additional co-solutes.

Our objective were: (1) to tune short-ranged attraction over a wide range of concentration for two mAbs with co-solutes, and to quantify the PPI from fits of SLS data to two colloidal models; and (2) to measure and correlate viscosities in terms of SLS experimental data and interaction parameters obtained from those models. We investigate the effect of NaCl and five ionic organic co-solutes on S(0) (from SLS) and viscosity for two mAbs up to 230 mg/mL. We model the short-range attraction with a Yukawa model and the effective self-association behavior with the interacting hard sphere model. The co-solutes (lysine, arginine, guanidine, imidazole, and phenylalanine methyl ester) were chosen to selectively tune the electrostatic, hydrophobic and steric interactions based on systematic differences in the co-solute size and structure. Arginine, phenylalanine, guanidine and imidazole were chosen as they possess π-electron systems and have been shown in simulations (68-73) or from SAXS (74) to preferentially interact with aromatic residues on the mAb surface. S(0) was fit to a spherical Yukawa potential (Eqn. 2.3b)

$$\frac{U(r)}{k_B T} = -\frac{K}{r}\exp\left(-Z(r-1)\right) \tag{2.3b}$$

where r is the center-to-center interparticle distance normalized by the particle diameter, K is the depth of the attractive well, and the characteristic length scale Z^{-1} of the short-ranged attraction. The scattering data were also fit to a three-component interacting hard sphere self-association model to shed further insight into the influence of the attractive interactions on the resulting average effective cluster size $\langle N_c \rangle$ and the mass ratio of oligomers to the amount of monomer and dimer ("oligomer mass ratio"). The viscosities were correlated with the measured net attraction strength (based on S(0), G_{22}, K), $\langle N_c \rangle$ and the oligomer mass ratio in order to develop a

better understanding of the interrelation between viscosity, PPI strength, and oligomer formation and corresponding solution microstructure.

2.3 MATERIALS AND METHODS

2.3.1 Materials

Stock solutions of the IgG1 monoclonal antibodies used in this study, mAb2 and mAb3, were provided by Merck at 25 mg/mL (pH 5.5) and 35 mg/mL (pH 5), respectively. L-arginine hydrochloride (Arg.HCl), guanidine hydrochloride (Gdn.HCl as a high-purity 8M solution), hydrochloric acid, imidazole, L-lysine hydrochloride (Lys.HCl), and sodium chloride were purchased from Thermo-Fisher Scientific (Waltham, MA). L-phenylalanine methyl ester hydrochloride was obtained from Bachem (Torrance, CA). The arginine hydrochloride, imidazole, and lysine hydrochloride were all BioReagent grade (> 98.5% purity). All co-solutes were dissolved in de-ionized water (Barnstead Nanopure Diamond, Thermo Fisher Scientific, Waltham, MA).

2.3.2 Dialysis and sample preparation

Ultra-concentrated (~280 mg/mL), unformulated mAb stocks were prepared in 21:30 mM Na:OAc (pH 5) buffer by dialysis followed by centrifugal ultrafiltration. The initial 25 – 35 mg/mL mAb solutions as provided by Merck were dialyzed into 21:30 mM Na:OAc pH 5 buffer using 8-10 kDa Tube-A-Lyzer dynamic dialysis modules (Part #137046; Spectrum Labs, Rancho Dominguez, CA) as described in the Supporting Info. The dialyzed mAb was recovered and sterile filtered with 0.22 μm PES filters (CellTreat Scientific Products, Pepperell, MA) before being concentrated to ~280 mg/mL by centrifugal ultrafiltration at 4500 RCF using a 30 kDa MWCO Amicon Ultra-15 centrifugal filter unit (MilliporeSigma, Burlington, MA). The ultrafiltration was stopped at the target mAb concentration based on the retentate mass, as described previously (35). The final mAb stock concentrations were measured by UV-Vis

spectroscopy as described previously (7, 34, 35) with an extinction coefficient of 1.42 $mL*mg^{-1*}cm^{-1}$ (mAb2) and 1.44 $mL*mg^{-1}*cm^{-1}$ (mAb3).

The initial high-concentration (225 mg/mL) mAb solutions for static light scattering measurements were prepared by gravimetric dilution of the unformulated, ultra-concentrated mAb stock described above with concentrated co-solute and buffer stock solutions (prepared as described in Supporting Info) to generate ~1.5 mL of solution with the desired final formulation (50, 250 or 1000 mM co-solute in 21:30 mM Na:OAc pH 5 buffer). Intermediate concentration samples were prepared for scattering measurements by gravimetric dilution of the formulated mAb solution to 17 intermediate concentrations (between 1 and 200 mg/mL; ~120 uL each) in 1.5 mL microcentrifuge tubes with solvent prepared at the same co-solute composition, such that the co-solute and buffer compositions remained unchanged. The gravimetric dilution process is described in the Supporting Info. Based on an error propagation analysis using the systematic instrument errors and average standard error in the concentration measurements of the ~225 mg/mL formulated stock samples, the error in the concentration of the intermediate dilutions is expected to be less than 1.4% (~2.8 mg/mL) at high concentration (~200 mg/mL) and less than 11% (0.22 mg/mL) at the lowest concentrations (~2 mg/mL). The error propagation calculations are described in detail in the Supporting Info.

Dilutions below 150 mg/mL were mixed by a pipet (Research Plus, Eppendorf, Hamburg, Germany) set to 60 uL and pipetted until homogenous (~30 seconds) while dilutions above 150 mg/mL were mixed by stirring with a needle due to the high viscosity preventing even mixing from pipetting alone. The samples were allowed to equilibrate overnight at 4°C prior to SLS measurements the following day. The dilution series for each co-solute was prepared in duplicate from the same concentrated formulated mAb stock.

2.3.3 Viscosity

The viscosity of the initial, concentrated formulated mAb was measured using a custom syringe viscometer as described previously (7, 34, 35). Briefly, the flow rate of the mAb solution through a 25G needle attached to a 1 mL syringe under a constant pressure differential was converted to a viscosity following the Hagen-Poiseuille equation. The applied shear rate was ~1000 s^{-1}.

The viscosity was fit to the Ross-Minton equation (19, 21)

$$\frac{\eta}{\eta_0} = \exp\left(\frac{[\eta]c}{1-\frac{k}{\nu}[\eta]c}\right) \tag{2.4}$$

where c is the mAb mass concentration, η_0 is the solvent viscosity, [η] is the intrinsic viscosity, and k/ν is the combined packing/Simha shape parameter. The viscosity was also fit to a polymer entanglement/binding viscosity model (23), hereafter referred to as the reptation model, in order to obtain a measure of the attractive interaction strength from the viscosity behavior:

$$\eta = Ac^{3/(3\nu-1)}\left(\frac{2kc}{\sqrt{1+4kc}-1}\right)^3 \tag{2.5}$$

Here, ν ~ 3/5 is the Flory exponent, k is the partition function over all potential intermolecular binding states, and A is a proportionality constant that was determined to be $5.38*10^{-8}$ cP by fitting the viscosity data across all co-solutes and mAb concentrations simultaneously. In this model the mAb is considered to form linear chains through Fab-Fab interactions only.

2.3.4 Static light scattering (SLS)

Static light scattering measurements of both mAbs as a function of concentration from 2 – 225 mg/mL in each co-solute formulation were performed at 25°C with a laser wavelength λ of 658 nm (q = 0.0018 Å-1) and a scattering angle of 90° using the miniDAWN TREOS from

Wyatt Technology (Santa Barbara, CA) run in batch mode with the microcuvette accessory at ambient temperature. The samples were centrifuged at 10,000g for 15 minutes to dissipate any bubbles and sediment any trace particulates that might be present in the sample prior to the SLS measurements. The excess scattering at each concentration was measured with duplicate or triplicate sample insertions in the SLS instrument. The scattering intensity was allowed to stabilize at the equilibrium value (typically requiring ~1 – 2 minutes), and the stable scattering intensity was recorded over a period of 1 minute per insertion. In all cases, the scattering between replicate insertions were in very good agreement, and the scattering intensity was therefore averaged over all 3 insertions. Each co-solute mAb concentration series (2 – 225 mg/mL) was prepared and measured by SLS in duplicate. The co-solute refractive index increment $dn/dc_{co\text{-}solute}$ was measured using the Wyatt Technology Optilab T-rEX refractometer with a laser wavelength of 658 nm at room temperature. The co-solutes were treated as part of the solvent, following Scherer's treatment (51, 61), and the solvent refractive index n_0 was calculated from the co-solute refractive index increment as $n_0 = n_{water} + (dn/dc_{co\text{-}solute})*c_{co\text{-}solute}$. The light scattering data was collected and processed (baseline correction and conversion to Rayleigh ratios) using the Astra 6.1.2 software (Wyatt Technology, Santa Barbara, CA). Further analysis was conducted in Excel and with MATLAB scripts generously provided by Allen Minton and P. Douglas Godfrin, as will be described in later sections.

Measurements of the dilute protein-protein interactions via the second osmotic virial coefficient B_{22} can be determined from the low concentration scattering (75, 76):

$$\frac{Kc}{R_\theta} = \frac{1}{M_w} + 2B_{22}c \tag{2.6}$$

where R_θ is the excess Rayleigh ratio (35) calculated from the scattering intensity, M_w is the mAb molecular weight and K is an optical constant (77)

$$K = \frac{4\pi^2 n^2}{N_A \lambda^4}\left(\frac{dn}{dc}\right)^2 \quad (2.7)$$

Here n is the solution refractive index ($n = n_0 + (dn/dc)*c_{prot}$), λ is the incident laser wavelength (658 nm), and dn/dc is the protein refractive index increment, assumed to be 0.185 mL/g (66). The B_{22} in each co-solute formulation can be normalized against the hard sphere steric value ($B_{22,HS} = (2/3)\pi\sigma^3$) (64, 65) with $\sigma = 2R_h$ and

$$R_h = \left(\frac{3}{4\pi} * \frac{M_w}{N_A} * V_{eff}\right)^{1/3} \quad (2.8)$$

where V_{eff} is the partial specific volume. The best-fit average mAb V_{eff} was obtained from fits of the scattering data across all co-solute formulations for a given mAb to the interacting hard sphere (IHS) model (66) described in the following section and the Supporting Info. As will be shown later in the Results and Discussion section, the average V_{eff} was found to be 1.70 and 1.78 mL/g for mAb2 and mAb3 respectively, corresponding to $B_{22,HS}$ of 6.80 and 7.15 mL/g for mAb2 and mAb3 respectively.

The concentration-dependent net PPI can be quantified from the scattering by the zero-q limit structure factor S(0), which is calculated from the ratio of scattering intensities at a given concentration and at infinite dilution

$$S(0) = \left(\frac{R_\theta}{K_0 c}\right)/M_w \quad (2.9)$$

where K_0 is the optical constant (Eqn. 2.7) calculated with the solvent refractive index n_0 instead of the solution refractive index and $M_w = R_\theta/K_0 c$ as $c \rightarrow 0$. The derivation of Eqn. 2.9 is provided in the Supporting Info. This relation is applicable (49, 50, 57, 64) given that the angular dependence of the scattering intensity in the low-q region (SLS) has previously been shown to be negligible for two mAbs (22), due to the small size of the mAb molecule relative to the incident

laser wavelength (658 nm). The S(0) can be normalized against the spherical steric value $S(0)_{HS}$, which is calculated from the compressibility of a hard sphere following the Carnahan-Starling equation (78)

$$S(0)_{HS} = \frac{(1-\phi)^4}{(1+2\phi)^2+\phi^3(\phi-4)} \quad (2.10)$$

where the effective protein volume fraction ϕ is calculated from the best-fit mAb partial specific volume V_{eff} obtained by the IHS model fit ($\phi = c*V_{eff}$), rather than by the traditional protein 'dry-weight' specific volume of 0.73 mL/g (66) which does not account for protein hydration effects. The Kirkwood-Buff integral G_{22} was calculated from S(0) by Eqn. 2.2 and normalized against the steric $G_{22,HS}$ calculated from $S(0)_{HS}$ using Eqn. 2.2.

2.3.5 Solution non-ideality and self-association with the interacting hard sphere (IHS) model

The concentration-dependent light scattering of each mAb formulation could also be fit to a three-component interacting hard sphere model developed by Minton (66) in order to interpret the scattering in terms of apparent self-association and anisotropic distribution of site-specific attraction in the system. Previous applications of this model to describe the scattering of two mAbs are given elsewhere (19, 22, 51, 61). In this model, changes in the concentration-dependent scattering are attributed to the formation of reversible oligomers, such that the scattering intensity at a given concentration corresponds to a characteristic oligomer size and distribution of monomer, oligomer (typically dimer) and higher-order oligomer. The attractive protein interactions are implicit in the formation of these multimer entities. Changes in the interaction strength are captured via the activity coefficient, which in this model is related only to the size of the equivalent hard sphere scatterers (22, 66). Although this model fits the scattering to a mixture of monomer and two oligomeric species (typically dimers and a higher-order oligomer), the oligomers are hypothetical to represent association, but are not necessarily actual

physical aggregates that could for example be measured by SEC or SAXS/SANS (66). However, they have in some cases been interpreted as physical aggregates (19, 22, 51, 53, 79). This model may be used to fit both low and high concentration scattering for more strongly interacting systems, such as GmAb1 (22). Another advantage of this approach is that the self-association and the strong short-ranged attraction are not "masked" by the repulsive net PPI (very small S(0) (31, 49, 64)) from steric effects (19), but are instead clearly seen from the model fit across the entire concentration range. The model is fully described by Minton (66) and Scherer (22), and key intermediate equations are shown in the Supporting Info. Briefly, the concentration-dependent scattering is a function of fluctuations in the molar concentration of three equivalent hard sphere species with molar masses M_i corresponding to monomer (M_1), m-mer ($M_2 = m*M_1$) and n-mer ($M_3 = n*M_1$):

$$\frac{R_\theta}{K_0} = \left(\frac{n}{n_0}\right)^2 \left[M_1^2\langle\Delta\bar{c_1}^2\rangle + M_2^2\langle\Delta\bar{c_2}^2\rangle + M_3^2\langle\Delta\bar{c_3}^2\rangle + 2M_1M_2\langle\Delta\bar{c_1}\bar{c_2}\rangle + 2M_2M_3\langle\Delta\bar{c_2}\bar{c_3}\rangle + 2M_1M_3\langle\Delta\bar{c_1}\bar{c_3}\rangle\right] \quad (2.11)$$

The molar concentration fluctuations $\langle\Delta\bar{c_i}\rangle^2$ and $\Delta\bar{c_i}\Delta\bar{c_j}$ are driven by the chemical potential gradients of each scattering species (Eqn. 2.25). For equivalent hard spheres with only steric interactions, the chemical potential gradient is a function of the sphere size only. Three sphere sizes and corresponding sphere density (assumed fixed across all three species) are fit to the scattering intensity across the entire concentration range under a closed monomer-unit mole balance at each concentration, yielding two characteristic 'aggregate' sizes m (typically m = 2) and n, along with the corresponding self-association equilibrium constants K_{1m} and K_{1n} (based on concentrations and activity coefficients) such that

$$\overline{c_{tot}} = \frac{c}{M_w} = \bar{c_1} + m * K_{1m} * \bar{c_1}^m + n * K_{1n} * \bar{c_1}^n \quad (2.12)$$

where $\overline{c_{tot}}$ is the molar concentration of monomer-units, $\overline{c_1}$ is the molar concentration of free monomer, and the last two terms are the number of monomer-units incorporated into the two oligomer species. At high ionic strengths such that the electrostatic repulsion is fully screened (as is the case for all of the co-solute formulation conditions in this study), V_{ex} becomes the mAb partial specific volume V_{eff} (51). From the fitted m, n, K_{1m}, K_{1n}, and V_{eff}, the mass fraction x_i of each species at a given mAb concentration can be determined.

$$x_i = (M_i * \overline{c_i}) \,/\, \sum_i (M_i * \overline{c_i}) \tag{2.13}$$

Non-linear regression of the scattering data to the interacting hard sphere model was performed using scripts and functions written in MATLAB (R2016b, Mathworks, Natick, MA) generously provided by Allen Minton (National Institute of Health, Bethesda, MD) (66).

2.3.6 Solution non-ideality from fitting S(0) to the Yukawa interaction potential

At low q, the concentration-dependent structure factor S(q) determined from the scattering data (Eqn. 2.9) may be approximated with a spherical single-term Yukawa interaction potential U(r) (Eqn. 2.3) via integral equation theory (18, 36, 56, 88) in order to regress an effective length scale Z^{-1} and attraction strength K. A long-ranged Yukawa term (18, 20) was not needed for long ranged electrostatic interactions given the high ionic strengths (50, 57, 64, 81). Fits of S(0) to the U(r) interaction parameters K and Z were performed using a modified version of scripts written in MATLAB and generously provided by P. Douglas Godfrin (18).

The Yukawa interaction parameters K and Z were assumed to remain constant over the entire concentration range (2 – 225 mg/mL) for simplicity, given the limited information available for a single q-vector. The best-fit parameters were obtained by minimizing the average relative deviation (ARD) (50, 57) of the fitted S(0) curve for each mAb and co-solute formulation.

$$ARD\ (\%) = \frac{100}{n}\sum_{i=1}^{n}\left|\frac{S(0)_i^{experimental} - S(0)_i^{predicted}}{S(0)_i^{experimental}}\right| \quad (2.14)$$

In order to simplify and improve the uniqueness of the fit, Z was fixed at 3 to reduce the model to a single-parameter fit (K). Z is the inverse characteristic length scale of the attractive well scaled by the equivalent hard sphere particle diameter d (~9 nm for a typical mAb) (22, 45) such that for Z = 3 the characteristic attraction length scale is d/Z = 3 nm. This Z value was chosen by minimizing the total ARD across the entire co-solute data set for mAb2 with respect to Z, where the individual ARDs for each co-solute at a given Z were minimized with respect to K. In order to facilitate comparisons of the attraction strengths between co-solutes as well as between mAbs, the best-fit Z determined for mAb2 was also applied to mAb3. In the cases where Z = 3 yielded a poor fit (i.e. ARD > 5%), S(0) was additionally fit with other Z values.

2.4 RESULTS AND DISCUSSION

2.4.1 Co-solute effects on viscosity

Relatively few studies have examined the effects of concentrated co-solutes on viscosity at high protein concentrations (13, 14, 28, 32, 33, 36, 38, 40), especially at high co-solute concentrations. The effects of up to six ionic co-solutes (NaCl, Arg.HCl, Gdn.HCl, Lys.HCl, and Imid(HCl) and PheOMe(HCl) at pH 5.5) at 250 mM on the viscosity of concentrated mAb solutions up to 240 mg/mL were measured for mAb2 (Fig. 2.1a) and mAb3 (Fig. 2.1b), where Gdn.HCl and PheOMe(HCl) were only evaluated for mAb2. Here 50 mM NaCl was also evaluated as a low ionic strength control to provide modest electrostatic screening. Imid was studied up to 1 M as an upper extreme co-solute concentration, given the high solubility and low molecular weight. In general, the viscosities of mAb3 solutions are consistently ~2x higher than those of mAb2 for the same concentration and co-solute formulation. Furthermore, the rank order of co-solute effects on viscosity appears to be comparable for each mAb: NaCl and Lys have a negligible effect relative to the 50 mM NaCl control, while Arg, Gdn and Imid (250 mM)

cause a 2x – 3x viscosity reduction. For mAb2, PheOMe is even more effective, causing a 4x reduction, and highly concentrated Imid at 1 M causes the largest reduction of 6x from ~120 cP at 225 mg/mL (50 mM NaCl) to ~20 cP. For both mAbs, the cosolute-free viscosity (not shown) is nearly identical to that of both the 50 and 250 mM NaCl systems indicating a minor salt effect. Arg's greater effect compared to NaCl has been seen with other mAbs (14, 28, 33-38) and has been attributed to screening of the localized short ranged anisotropic attractive PPI (22, 34-37, 72, 82, 83).

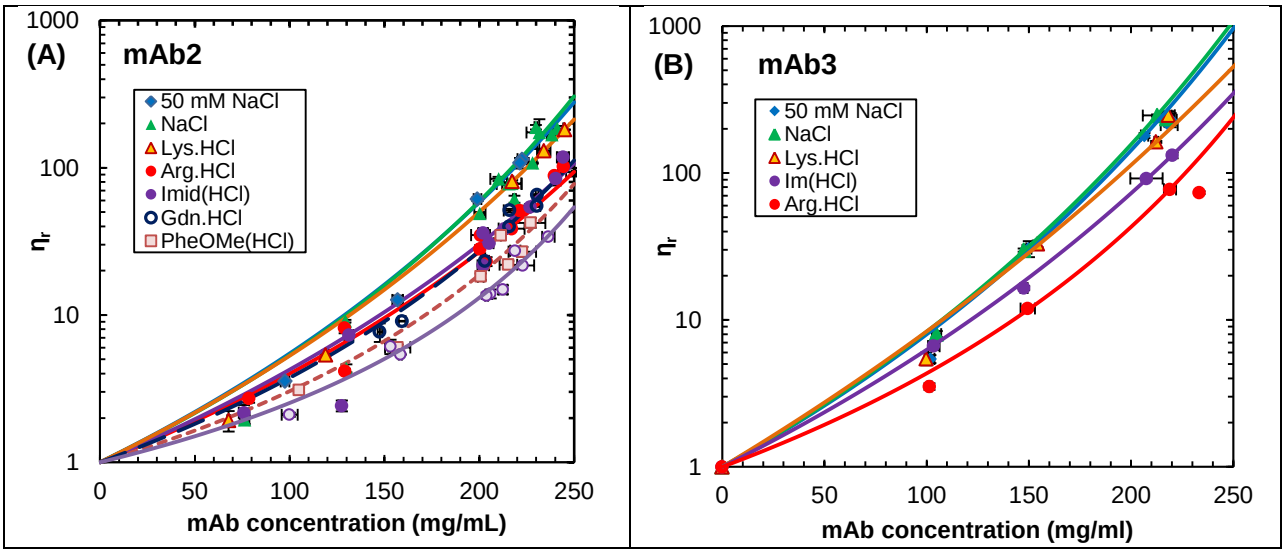

Figure 2.1. Viscosity of (A) mAb2 and (B) mAb3 with various co-solutes, fit to the Ross-Minton viscosity model. Symbols are measured values, and solid/dashed lines are fits of the viscosity data to the Ross-Minton equation. All co-solutes (with exception of NaCl) are titrated to, or already at pH ~5.5, and all samples are buffered with 30 mM (Na)OAc at pH 5. All co-solute concentrations are 250 mM unless specified otherwise. The model fit parameters are shown in Table 2.2. The corresponding fit of the viscosity to the reptation model is shown in Fig. 2.8.

The relative viscosity (η_{rel}) profiles were fit to the Ross-Minton (54) (Eqn. 2.4) and reptation (23) (Eqn. 2.5) viscosity models, shown by the solid curves on Fig. 2.1 and Fig. 2.8 respectively. As seen from the fit parameters for both mAbs (Table 2.2), Arg, Gdn, Imid and PheOMe reduce [η] and increase k/ν relative to the control. Thus, these co-solutes appear to

cause mAb2 to adopt more compact and/or more symmetric shapes. In contrast, the smaller k/ν and larger [η] for mAb3 may indicate greater shape asymmetry and possibly oligomer formation (18 - 20). Similarly, the four co-solutes reduce the interaction strength represented by the partition function parameter k and corresponding binding energy ΔG_{bind} fit from the reptation model (23) in Eqn. 2.5, which will be discussed in the context of protein interaction strengths below. Whereas these relative viscosities provide a crude estimate of the net PPI strength, the viscosity is also influenced by the cluster size and fractal dimension (16-19, 22, 23, 30, 67, 84), especially at high volume fractions, as discussed in greater detail below.

2.4.2 Co-solute effects on the static light scattering of mAb2 and mAb3

The concentration-dependent scattering Rθ/K0 of mAb2 and mAb3 as a function of the co-solute formulation is shown in Fig. 2.2a and 2.2b, respectively, whereas the reproducibility of the scattering profiles is shown in Figs. 2.9 and 2.10. Typical uncertainties in R_θ/K_0 were ~0.2 – 0.5% at low concentrations and 0.1% at high concentrations. The properties of the formulated stock solutions (initial concentration, viscosity, pH) used to generate the dilution series for the SLS measurements are listed in Table 2.3. Interestingly, the scattering intensities of mAb2 and mAb3 are comparable for a given co-solute, despite large differences in their viscosities. However, R_θ/K_0 for mAb3 increases more rapidly in the low concentration region. R_θ/K_0 is related to the osmotic compressibility dπ/dc by the relationship

$$\frac{R_\theta}{Kc} = M_w k_B T * \left(\frac{d\pi}{dc}\right)^{-1} \tag{2.15}$$

(see Eqn. 2.9) where S(0) is also an inverse compressibility ($d\pi/dc = k_BT/S(0)$) (85). The osmotic compressibility can be expressed as a virial expansion around the protein volume fraction ($\pi/c = (RT/M_w)*(B_1 + B_{22}\phi + B_3* \phi^2 + \ldots)$) (37, 50). Stronger attraction (more negative B_{22}) or a smaller dπ/dc corresponds to a faster increase in R_θ/K_0. The steeper low-concentration slopes of

R_θ/K_0 for mAb2 and for mAb3 with NaCl/Lys are therefore indicative of stronger attractive interactions than for the other co-solutes. However, at high concentration where steric repulsion (crowding) becomes dominant, R_θ/K_0 decreases despite the higher concentration of scattering species and presence of short-ranged attractive interactions.

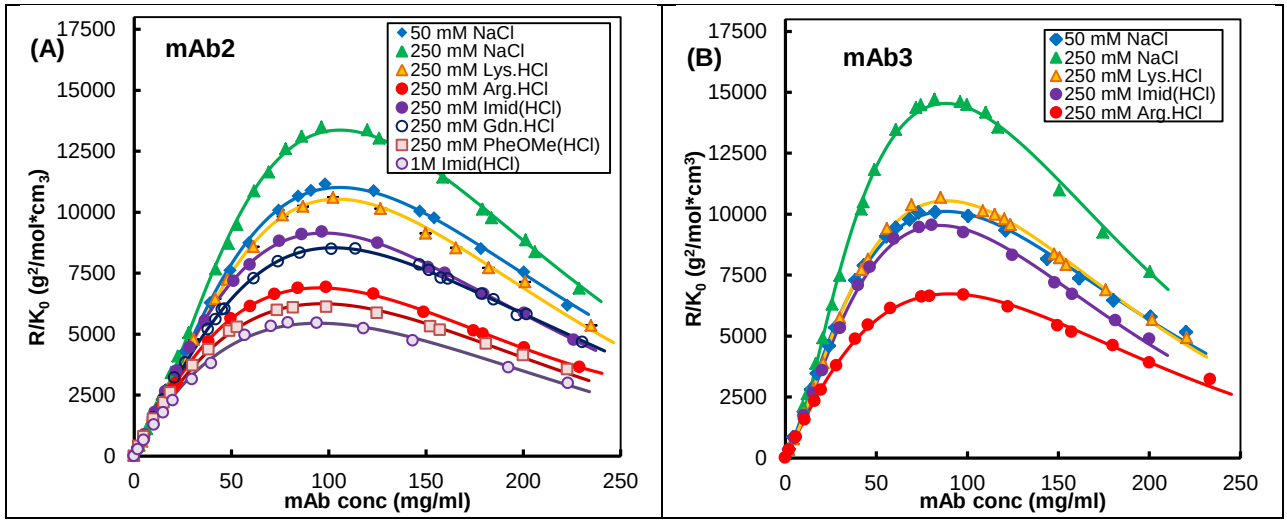

Figure 2.2. Measured light scattering intensity (symbols), represented by the Rayleigh ratio *R*, of **(A)** mAb 2 and **(B)** mAb 3 as a function of mAb concentration for multiple co-solutes. Solid lines indicate best fits of the scattering profile to the interacting hard sphere (IHS) model developed by Minton (57). The corresponding best-fit parameters are shown in Tables 2.7 and 2.8.

The co-solute effects on the concentration-dependent R_θ/K_0 are consistent between the two mAbs (Fig. 2.2) in the order: 1M Imid → PheOMe → Arg → Gdn → Imid → Lys → 50 mM NaCl → NaCl for mAb2; and Arg → Imid → 50 mM NaCl/Lys → NaCl for mAb3. In particular, 250 mM NaCl causes a larger increase in scattering intensity relative to the 50 mM NaCl control. In addition for mAb2, Gdn reduces the scattering intensity similarly to 250 mM Imid, while PheOMe and 1M Imid reduce R_θ/K_0 relative to even Arg. These trends largely correlate with those for viscosity (Fig. 2.1) (1M Imid → PheOMe → Arg/Gdn/Imid → Lys/50

mM NaCl/250 mM NaCl for mAb2; and Arg → Imid → Lys → 50 mM NaCl/250 mM NaCl for mAb3).

2.4.3 Low concentration interactions via the second osmotic virial coefficient

The second osmotic virial coefficients B_{22} fit from the dilute scattering (Eqn. 2.6, Fig. 2.11, 2.12) are reported in Table 2.4 for both mAbs in different formulations. $B_{22}/B_{22,HS}$ (Table 2.1) become less attractive with a decrease in the relative viscosity at 200 mg/mL for each mAb (Fig. 2.13), with the exception of the 50 mM NaCl system. The small B_{22} of 50 mM NaCl despite the high viscosity can instead be attributed to the more weakly screened long-ranged electrostatic repulsion (Debye length = 1.2 nm, compared to 0.6 nm for 250 mM monovalent co-solutes), which is more important at low mAb concentration. Overall, B_{22} values are more repulsive for mAb2 than mAb3, consistent with lower viscosities. Also Arg, PheOMe and 1M Imid greatly increase $B_{22}/B_{22,HS}$ relative to the 50 mM NaCl control for both mAbs (Table 2.1). Remarkably, $B_{22}/B_{22,HS}$ values of mAb2 with PheOMe and 1M Imid are very close to 1, indicating hard sphere-like interactions at low concentration, consistent with the smallest R_θ/K_0 and the lowest viscosities. However, the dependence of the relative viscosity on B_{22} is much steeper for mAb3 compared to mAb2. Furthermore, the effect of NaCl concentration on the net attraction is greater for mAb3. These observations will be discussed below with the Yukawa and interacting hard sphere models below.

2.4.4 Quantification of high concentration net PPI by S(0) and G_{22} from static light scattering

The co-solute effects on the net PPI of mAb2 and mAb3 were quantified by the structure factor S(0) determined from the ratios of concentration-normalized scattering intensities (Eqn. 2.24) as shown in Fig. 2.3a and 2.3b, which is essentially identical to the S(0) values calculated from the regressed M_w (Eqn. 2.9) as shown in Fig. 2.14. As discussed below, larger S(0) values may indicate greater solution microstructure interpreted as stronger attraction (18, 49) via a

smaller osmotic compressibility ($d\pi/dc = k_BT/S(0)$) (85). S(0) was also converted to the Kirkwood-Buff integral G_{22} by Eqn. 2.2 (Fig. 2.3c and 2.3d), which is more fundamentally related to the underlying PPI as it removes some of the effect of protein concentration (49, 50, 56, 57, 64). The net PPI becomes increasingly repulsive (decreasing S(0)) with concentration, as steric repulsion from protein crowding at high concentration becomes stronger relative to the weaker short-ranged attraction (19).

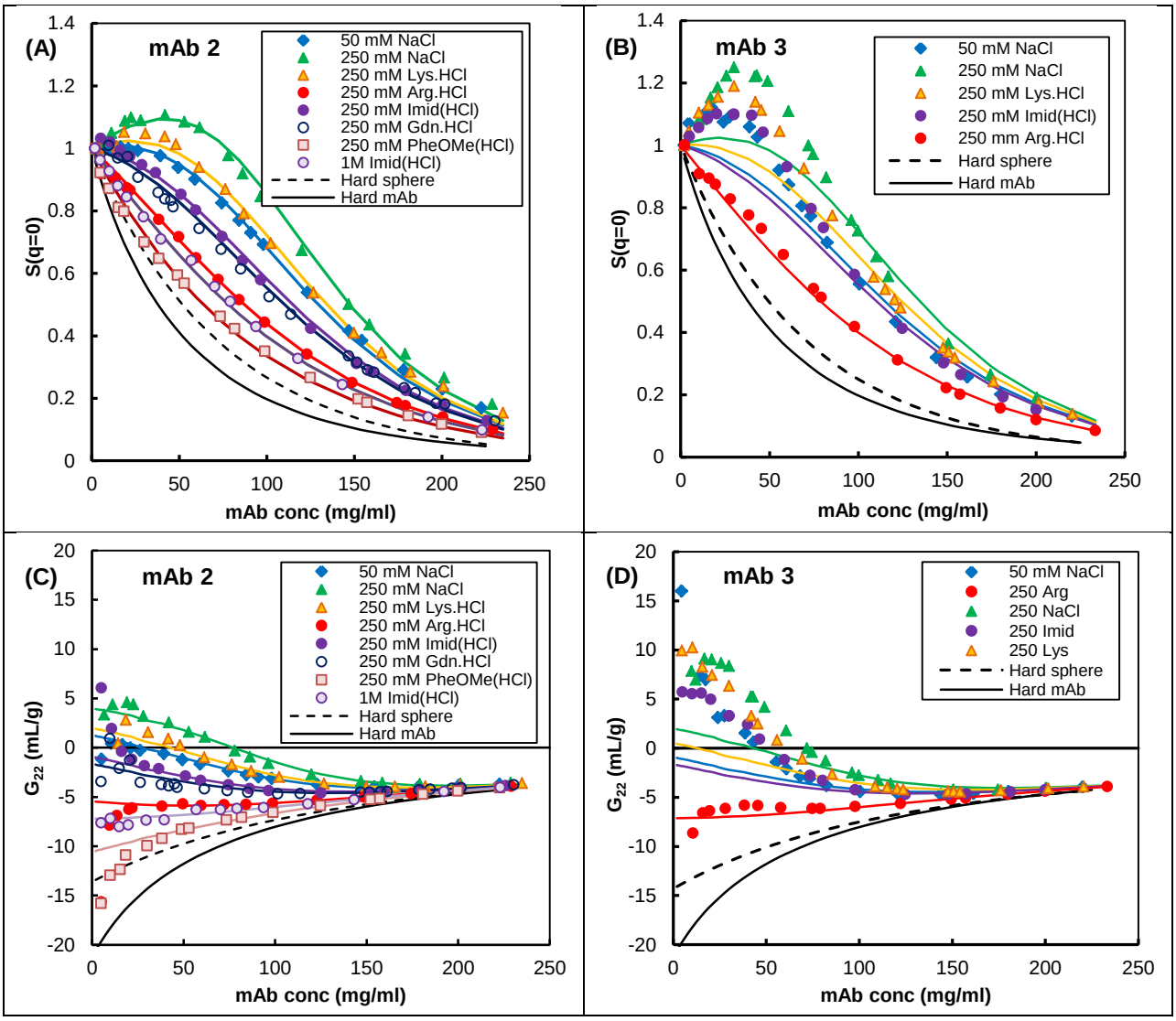

Figure 2.3. (A, B) Structure factors *S(0)* and **(C, D)** Kirkwood-Buff integral G_{22} from SLS of **(A, C)** mAb 2 and **(B, D)** mAb 3 as a function of mAb concentration for multiple co-solutes. Solid lines indicate best fits of *S(0)* (and corresponding G_{22}) to a single-Yukawa attractive pair potential, as described in the Materials and Methods section. The best-fit Yukawa parameter *K* (fixed Z = 3) is given in Table 2.1 and the corresponding error (ARD) is reported in Table 2.5. The hard mAb *S(0)* was obtained from Calero-Rubio et al.,(16) and is smaller than the hard sphere *S(0)* due to greater shape anisotropy resulting in less structured packing in solution. The mAb *S(0)* and G_{22} are compared against a hard sphere(35, 57) (---) and hard mAb(16) (—)model, where the mAb concentration was converted to ϕ using the average best-fit protein partial specific volume for each mAb.

However, despite the extremely repulsive net PPI at high concentration ($S(0) << 1$), differences in the short-range attraction strength can be seen as deviations from the hard sphere (HS) (Eqn. 2.10) and hard mAb (64) values (shown by the solid and dashed black lines, respectively). The order of the relative co-solute effects on $S(0)/S(0)_{HS}$ (Table21.1) match that of the scattering as expected from Eqn. 2.9, with the exception of PheOMe and 1M Imid for mAb2. The PheOMe system has a slightly smaller S(0) than 1M Imid due to small differences in the ~zero concentration scattering (i.e. form factor) (Fig. 2.3a). S(0) exhibits a peak at low concentration (~30 mg/mL) for both mAbs with 250 mM NaCl and Lys, and to a smaller extent for the 50 mM NaCl and 250 mM Imid systems for mAb3 (Fig. 2.3b). The S(0) peak is characteristic of strong attraction (22, 66) where the initial increase in S(0) at low concentration is caused by the strong short-ranged attraction, while the downturn at higher concentrations reflects the growing influence of steric repulsion on the net PPI. Peaks in S(0) have been seen for other mAbs at high ionic strengths in correlation with elevated aggregation rates (49). For both mAbs, the S(0) peak and magnitude (corresponding to stronger attraction) are increasingly suppressed by the co-solutes in the order NaCl/Lys → Imid / Gdn → Arg → PheOMe/1M Imid, such that S(0) becomes significantly more hard sphere-like.

The increasing suppression of the attractive PPI is also evident from the co-solute effects on G_{22} (Fig. 2.3c, 2.3d). For example, G_{22} of mAb2 falls on or near the HS curve with PheOMe and 1M Imid (mAb2) and 250 mM Arg (both mAbs). The effect of steric repulsion on the net PPI is more clearly seen from G_{22} relative to S(0), with G_{22} becoming negative (repulsive) at ~100 mg/mL for mAb2 (Fig. 2.3c) and ~70 mg/mL for mAb3 (Fig. 2.3d). However, the relative co-solute effects on the attractive PPI are still evident from the consistent differences in G_{22} between co-solutes across the entire concentration range, where the co-solute rankings for $G_{22}/G_{22,HS}$ match that of $S(0)/S(0)_{HS}$. The identical, strongly negative G_{22} values for mAb2 and mAb3 with Arg suggest that Arg greatly mitigates the short-ranged attractive PPI, consistent

with the relatively low viscosities. Interestingly, mAb3 exhibits much stronger net attraction than mAb2 at < 50 mg/mL, but also a much steeper increase in the net repulsion with increasing concentration. This difference in the concentration dependence of G_{22} (and to a lesser extent S(0)) may likely be attributed to differences in solution packing, as will be discussed in greater detail below.

	Data	Rept. Visc. model	SLS scattering data				Yukawa model[a]	SLS IHS (at 200 mg/mL)	
Formulation	**η_{rel} at 200 mg/mL**	**ΔG_{bind} (kJ/mol)**	**$B_{22}/B_{22,HS}$**	**$G_{22}/G_{22,HS}$ at 20 mg/mL**	**$G_{22}/G_{22,HS}$ at 200 mg/mL**	**$S(0)/S(0)_{HS}$ at 200 mg/mL**	**K (Z = 3)**	**Oligomass ratio**	**$\langle N_c \rangle$**
mAb2									
50 mM NaCl	58.3	-14.9	-0.02 ± 0.01	0.00 ± 0.03	0.83 ± 0.00	3.24 ± 0.03	0.763	6.6	2.8
250 mM NaCl	59.2	-15.7	-0.21 ± 0.02	-0.39 ± 0.02	0.79 ± 0.00	3.76 ± 0.02	0.900	5.9[b]	3.6
250 mM Lys.HCl	50.1	-15.4	-0.21 ± 0.13	-0.24 ± 0.02	0.82 ± 0.00	3.37 ± 0.01	0.800	7.8	2.8
250 mM Arg.HCl	26.9	-12.2	0.53 ± 0.01	0.53 ± 0.06	0.93 ± 0.00	1.98 ± 0.03	0.401	0.0	1.8
250 mM Imid(HCl)	30.2	-12.3	0.12 ± 0.01	0.10 ± 0.01	0.89 ± 0.00	2.51 ± 0.01	0.649	3.0	2.7
250 mM Gdn.HCl	27.2	-10.7	0.38 ± 0.02	0.11 ± 0.01	0.88 ± 0.00	2.55 ± 0.01	0.610	2.3	2.6
250 mM PheOMe(HCl)	18.7	-3.4	0.91 ± 0.03	0.92 ± 0.01	0.95 ± 0.00	1.66 ± 0.00	0.100	0.0	1.8
1000 mM Imid(HCl)	13.1	17.1	0.91 ± 0.02	0.66 ± 0.03	0.97 ± 0.00	1.97 ± 0.01	0.300	0.0	1.7
mAb3									
50 mM NaCl	142.7	-17.3	-0.13 ± 0.11	-0.57 ± 0.01	0.89 ± 0.00	2.64 ± 0.00	0.649	5.0	2.8
250 mM NaCl	156.3	-17.8	-0.43 ± 0.02	-0.73 ± 0.06	0.86 ± 0.00	3.1 ± 0.04	0.801	23.6[b]	3.9
250 mM Lys.HCl	113.3	-17.7	-0.31 ± 0.06	-0.60 ± 0.02	0.87 ± 0.00	2.83 ± 0.01	0.725	14.6	2.9
250 mM Imid(HCl)	72.8	-15.7	-0.33 ± 0.04	-0.40 ± 0.01	0.90 ± 0.00	2.46 ± 0.00	0.610	10.8	2.9
250 mM Arg.HCl	43.0	-13.6	-0.20 ± 0.03	0.52 ± 0.07	0.94 ± 0.00	1.95 ± 0.04	0.305	0.0	1.8

a. Fitted with Z held constant (Z = 3; see Materials and Methods section for how the Z value was chosen)

b. Best-fit oligomer species is tetrameric (n = 4)

Table 2.1. Relation between the viscosity of mAb 2 and mAb 3 with the PPI strengths measured by rheology and static light scattering. ΔG_{bind} was calculated from k (Table 2.2). B_{22}, G_{22}, $S(0)$ (normalized against the hard sphere value) were calculated directly from the scattering intensities. The corresponding Yukawa attractive well depth K is also shown, with the ARD listed in Table 2.5. The apparent average cluster size $\langle N_c \rangle$ fit from the IHS scattering model represents the attraction as self-association, where $\langle N_c \rangle$ is calculated from the oligomer distribution curves (Fig. 2.4, 2.5) calculated from the association constants $log(K_{1m})$ and $log(K_{1n})$ (Tables 2.7 and 2.8).

2.4.5 Describing S(0) with a single Yukawa potential model

The structure factor S(0) was fit to a single Yukawa potential U(r) (Eqn. 2.3b) to quantify the co-solute effects on the short-range attraction via the attraction strength K. The fit S(0) and corresponding G_{22} (calculated from Eqn. 2.2) are shown as solid curves in Fig. 2.3a – 2.3d, with the corresponding fitted K and ARD value reported in Table 2.1 and Table 2.5 respectively. Even though the Yukawa potential is an isotropic model, it is able to describe the scattering of mAb2 despite the inherently anisotropic mAb shape and interactions, as seen from the qualitatively good fits (Fig 2.3a, 2.3c) and the low ARDs of 5% and less (Table 2.5). In an SLS study with the protein α-chymotrypsinogen, an ARD of 5% and less for fits of R_θ/K_0 to a screened Coulomb and Lennard-Jones potential was used as the metric for a 'good' fit, and was found to correlate with systems that had small charge dipoles, shallow attractive wells, and/or large net charges, all of which lead to more repulsive, isotropic interactions (57). Since S(0) is proportional to R_θ/K_0 (Eqn. 2.9), the S(0) ARD is numerically equivalent to R_θ/K_0 ARD. The low ARDs of the mAb2 S(0) fits thus suggest more isotropic attractive interactions. The K values follow the same co-solute order as S(0) and G_{22}, with 50 mM NaCl, Lys, and NaCl having the largest (most attractive) K's, followed by Imid and Gdn. Finally, Arg, PheOMe and 1M Imid give extremely small K's approaching zero, suggesting the near-complete suppression of the short-range attraction.

In contrast, the single Yukawa potential is unable to describe the mAb3 scattering behavior for both S(0) and G_{22} at low concentrations (Fig. 2.3b, 2.3d) as evidenced by large ARD values (Table 2.5), especially for 250 mM NaCl and Lys. The fits were improved only modestly by using Z's that were too small to be physically meaningful ($Z \leq 0.1$), such as is shown for 250 mM NaCl in Fig. 2.15a and Table 2.6, instead of the best-fit Z of 3 determined for mAb2 as described in the Methods section. Alternatively, the fit of S(0) of mAb3 with 250 mM NaCl could also be improved slightly by using a double Yukawa potential (Fig. 2.15a, 2.15b) with both a shorter and longer-ranged attractive term (best-fit Z_1 and Z_2 are both ~1).

$$\frac{U(r)}{k_B T} = \frac{1}{r}\left[-K_1 \exp\left(-Z_1(r-1)\right) - K_2 \exp\left(-Z_2(r-1)\right)\right] \quad (2.16)$$

The longer attraction length scales implied by the mAb3 S(0) profiles have been suggested to indicate strong multipolar attraction (45). The under-prediction of the dilute S(0) for mAb3 by the Yukawa potential may also indicate non-specific attraction sites far from the mAb center of mass (45); mAbs have enough configurational freedom at low concentration to order themselves via anisotropic attractive pair contacts (in spite of reduced system entropy) that are not captured with a spherical potential, leading to more solution structure (larger S(0)) than expected. These attractive anisotropic interactions may drive formation of reversible linear or branched clusters at high concentration (84). At high concentration however the S(0) and G_{22} curves become well-described by the spherical potential, even for the most strongly attractive systems (ex. mAb3 with 250 mM NaCl). The apparently more isotropic behavior results from the confinement of the mAb molecules, causing the pair interactions to become dominated by interactions between regions closer to the mAb center of mass and smoothing out the effects of any anisotropically distributed attraction sites on the overall interaction potential.

2.4.6 Capturing solution non-idealities with the interacting hard sphere (IHS) model

The significant non-ideality present in the mAb3 scattering may be captured with a simple interacting hard sphere (IHS) light scattering model (57) to describe apparent self-association, via the formation of equivalent hard sphere 'pseudo-oligomers'. The fits of R_θ/K_0 to the IHS model are shown as solid curves in Figs. 2a and 2b. The corresponding fits of the 'oligomer' sizes m and n, the self-association equilibrium constants K_{1m} and K_{1n} and mAb partial specific volume V_{eff} are reported in Table 2.7 and 2.8. The equilibrium constants were used to generate oligomer distribution profiles as a function of mAb concentration with each co-solute, as shown in Figs. 4 and S10 (mAb2) and Figs. 5 and S11 (mAb3). A weighted average effective

cluster size $\langle N_c \rangle$ was also calculated from the oligomer distribution at 200 mg/mL (Table 2.1), $\langle N_c \rangle = \sum_{i=1,m,n}(x_i N_i)$, where x_i is the mass fraction of the equivalent oligomeric species with aggregation number N_i (which is either 1, m, or n).

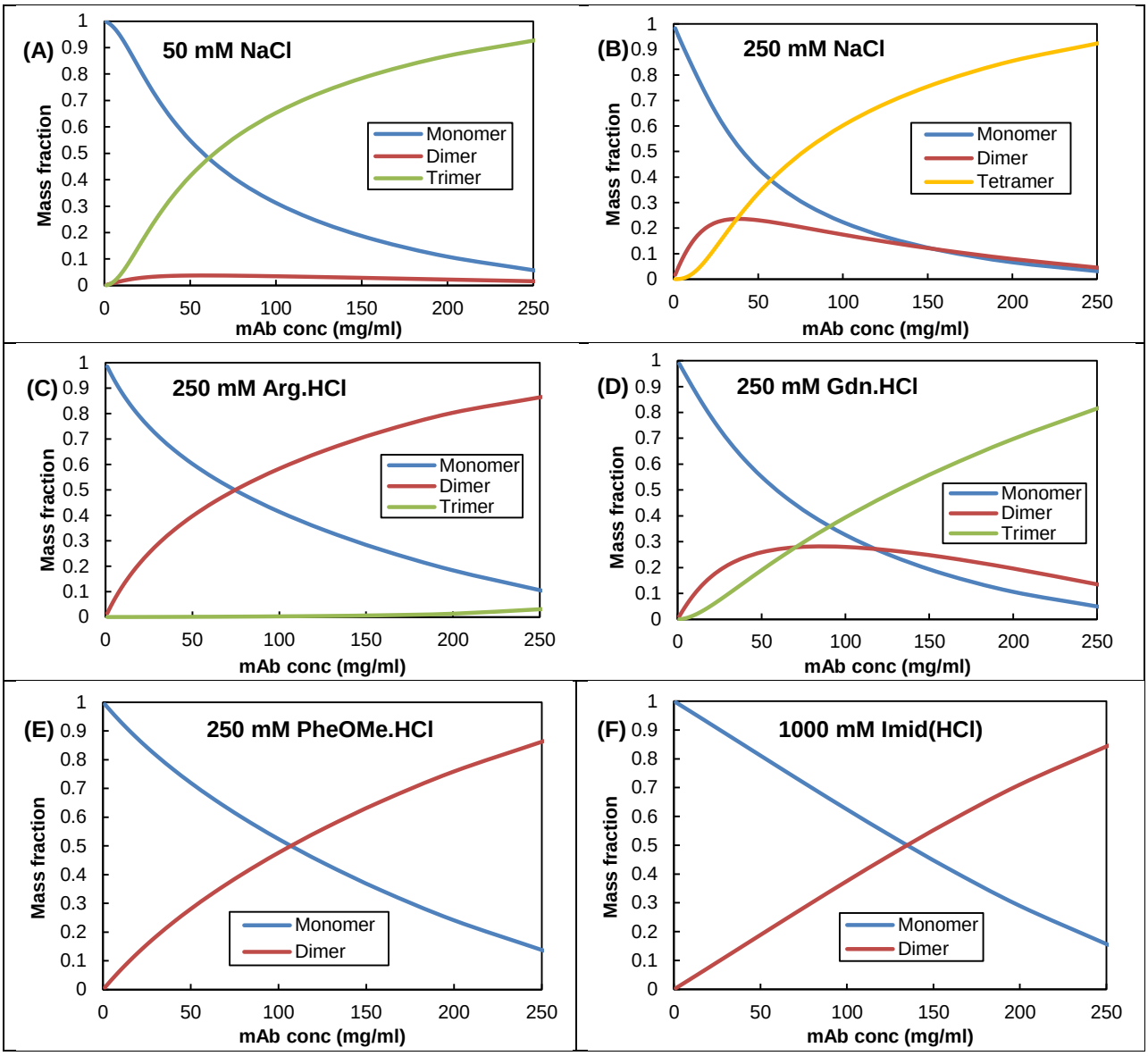

Figure 2.4. Mass fraction distribution of mAb 2 "oligomers" as a function of mAb concentration as calculated from the IHS best-fit association constants (Table 2.7) formulated with (A) 50 mM NaCl, (B) 250 mM NaCl, (C) 250 mm Arg.HCl, (D) 250 mM Gdn.HCl, (E) 250 mM PheOMe.HCl and (F) 1000 mM Imid(HCl). Additional distributions for 250 mM Lys.HCl and 250 mM Imid(HCl) are shown in Fig. 2.17.

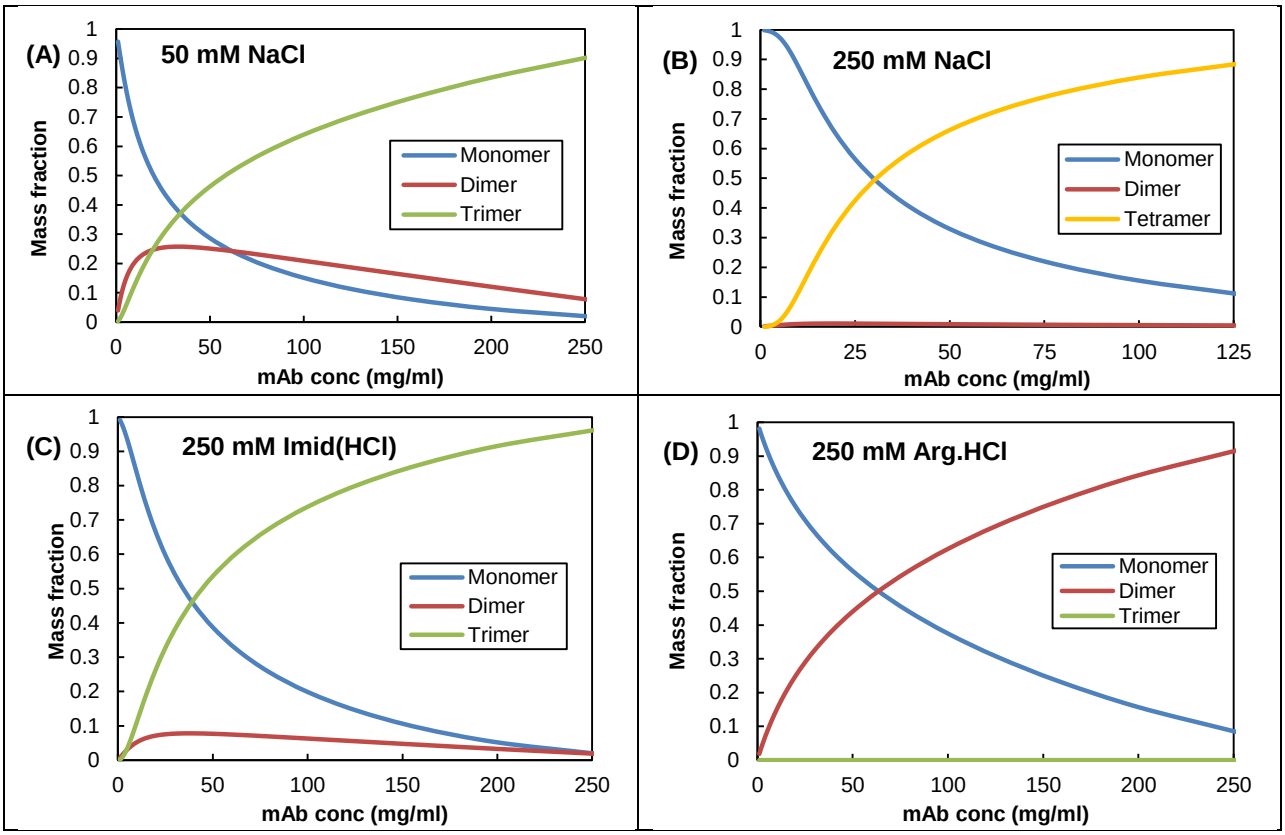

Figure 2.5. Mass fraction distribution of mAb 3 "oligomers" as a function of mAb concentration as calculated from the IHS best-fit association constants (Table 2.8) formulated with **(A)** 50 mM NaCl, **(B)** 250 mM NaCl, **(C)** 250 mm Imid(HCl) and **(D)** 250 mM Arg.HCl. The distribution for 250 mM Lys.HCl is shown in Fig. 2.18.

As can be seen from the IHS fits, mAb2 experiences strong local attraction in 250 mM NaCl, as seen from the extensive apparent tetramer formation (Fig. 2.4b, 2.17). 50 mM NaCl and 250 mM Gdn, Lys and Imid (Fig. 2.4a, 2.4d, 2.17a, 2.17b) cause moderate attraction, as seen from the formation of trimers at intermediate to high concentration, with 50 mM NaCl and 250 mM Lys exhibiting stronger attraction than Imid and Gdn based on the faster onset of trimer formation at low concentration (Fig. 2.17) Arg, PheOMe and 1M Imid greatly suppress the attractive PPI, seen from the complete suppression of higher-order oligomer formation (Fig. 2.4c, 2.4e and 2.4f). This progressive reduction in the attraction leads to a decrease in $\langle N_c \rangle$ as seen in Table 2.1. Similarly, mAb3 also experiences strong attraction in 250 mM NaCl (Fig. 2.5b),

which is weakened by changing the co-solute to Imid (Fig. 2.5c) or reducing the ionic strength to 50 nM NaCl (Fig. 2.5a). Similar to for mAb2, Arg significantly weakens the attractive PPI for mAb3, resulting in the complete suppression of higher-order oligomer formation (Fig. 2.5d).

Although the mAb2 and mAb3 oligomer distribution profiles look similar, a steeper onset of oligomer formation at low concentration was observed for mAb3 (compare 250 mM Imid in Fig. 2.17b (mAb2) and 2.5c (mAb3)). The differences between mAb2 and mAb3 are more evident in the oligomer mass ratio ($m_{oligo}/m_{(mono+dimer)}$) rather than the average cluster size $\langle N_c \rangle$ in Table 2.1, with mAb2 consistently having smaller oligomer mass ratios than mAb3 for the same co-solute system. Although the Yukawa and IHS models are quite different conceptually, the qualitative trends in K and $\langle N_c \rangle$ (Table 2.1) are somewhat similar with respect to the co-solute, whereby Arg, PheOMe and 1M Imid suppress the attractive PPI relative to NaCl and Lys. The oligomer ratio also increases with the attractive PPI strength as quantified by S(0), G_{22}, and K (Table 2.1). The apparent self-association from the IHS fits of the most attractive mAb3 systems (250 mM NaCl, Lys) provides an important alternative interpretation of the S(0) deviations from the isotropic potential at low concentration, since the Yukawa model does not account for self-association effects on scattering. Interestingly, while K and $\langle N_c \rangle$ did not change much between mAbs for a given co-solute, larger changes were observed in the oligomer mass ratio (Table 2.1).

2.4.7 Categorization of mAb2, mAb3 classes from their viscosity and scattering response to NaCl

Based on the viscosity and scattering response of mAb2 and mAb3 to the addition of NaCl from 50 to 250 mM, these two mAbs can be described in the context of the aforementioned mAb classes. Both mAbs appear to be similar to GmAb2 (20, 22): NaCl increases R_θ/K_0 and S(0) (Fig. 2.2a-2.2b, 2.3a-2.3b) (where S(0) is proportional to $M_{w,app}$ in Scherer et al., (22)) but has a negligible effect on viscosity (Fig. 2.1a, 2.1b). Interestingly, S(0) (i.e. $M_{w,app}$) of GmAb2 at 10 mM ionic strength resembles the hard mAb S(0) determined from coarse-grain modeling (64),

indicating that the base mAb interactions (in the absence of charge screening or co-solutes) are already very weak and approaching the steric limit. However, while the net PPI was already sufficiently weak enough that NaCl had no effect on the viscosity for this mAb class, our work shows that the viscosity (as well as R_θ/K_0 and S(0)) can still be further reduced with amphipathic co-solutes such as Arg and Imid, likely by additional screening of non-electrostatic interactions. Similarly, mAb4 in Scherer et al. (67) resembles mAb2 and mAb3 in scattering (R_θ/K_0) and viscosity, and may provide some context for the behavior of both mAbs in terms of co-solute effects on viscosity. The mAb in Calero-Rubio et al. (50) also appears to fall into this class, based on the very repulsive, hard mAb-like S(0) (64) at minimal ionic strength, as well as the increase in R_θ/K_0 and S(0) with NaCl addition. However, viscosities were not considered in that study.

2.4.8 Protein-dependent correlation between viscosity and net PPI strength at high concentration

To our knowledge, this is one of the first studies to demonstrate a quantitative correlation between viscosity and the net PPI strength (tuned with co-solutes) at high concentration as measured by light scattering. To begin, the system attraction energy fit from the mAb viscosity using the reptation model, ΔG_{bind}, qualitatively trends with the system net PPI strength quantified by G_{22}, S(0) and K determined from light scattering for a given mAb (Table 2.1).

While S(0) and G_{22} closely approach the hard sphere curve at high concentration due to the dominant steric repulsion, their relative deviation from the hard sphere curve becomes increasingly different between co-solute systems with increasing mAb concentration (Fig. 2.19a, 2.19b). This difference in PPI between systems (Table 2.1) explains the increasing relative deviation of the viscosity from the hard sphere viscosity (Fig. 2.19c, 2.19d). A linear correlation between $S(0)/S(0)_{HS}$ and the relative viscosity η_{rel} at 200 mg/mL was seen for each mAb (Fig. 2.6a). A similarly strong correlation was seen for η_{rel} with $G_{22}/G_{22,HS}$ at 200 mg/mL (Fig. 2.6b),

as well as with the short-range attraction strength K determined from fits of S(0) to the single-Yukawa U(r) (Eqn. 2.3) (Fig. 2.6c). It is interesting that the viscosity is still correlated with K for mAb3 despite the poor fits of S(0) at low concentration, but is not altogether surprising, given that the mAb3 Yukawa fits described S(0) above 100 mg/mL well. However, the viscosity of mAb3 was significantly larger than for mAb2 at the same net PPI strength (i.e. same value of $S(0)/S(0)_{HS}$ or $G_{22}/G_{22,HS}$). Similarly, η_{rel} at 200 mg/mL was correlated with both $S(0)/S(0)_{HS}$ and $G_{22}/G_{22,HS}$ at lower concentrations of 20 to 160 mg/mL (Fig. 2.20), although the correlation is significantly weaker for mAb3 (Fig. 2.20b, 2.20d) than mAb2 (2.20a, 2.20c). Both mAbs show increasing sensitivity of the high concentration ηrel to $S(0)/S(0)_{HS}$ and $G_{22}/G_{22,HS}$, as well as more divergent slopes for the correlation curves with increasing concentration, which may reflect stronger or more anisotropic interactions for mAb3.

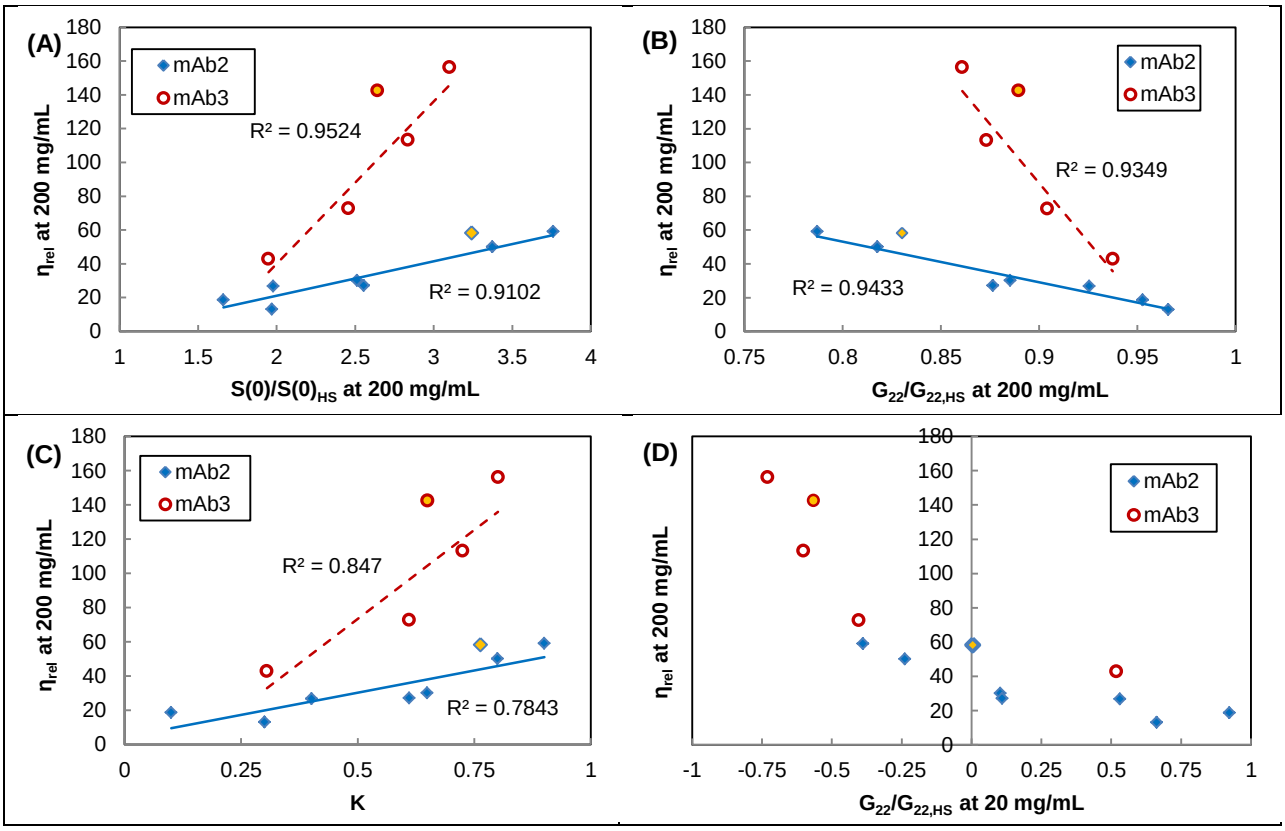

Figure 2.6. Correlation of the relative viscosity η_{rel} at 200 mg/mL with (A) the normalized *S(0)*, (B) normalized G_{22} at 200 mg/mL, (C) the attractive well depth *K* and (D) normalized G_{22} at 20 mg/mL for mAb2 and mAb3 across all co-solute systems. The HS values for *S(0)* were obtained from the Carnahan-Starling equation.(57) The filled orange symbols correspond to the 50 mM NaCl systems for both mAbs. These two points were excluded from the linear fits of the viscosity to *S(0)*, G_{22} and *K*, as explained in the Results and Discussion section.

The larger values of η_{rel} in Figs. 6a-6c for mAb3 versus mAb2 may indicate the influence of confounding factors such as mAb shape, flexibility and packing efficiencies on the rheological behavior. A study showed a power law dependence of ηrel on the cluster size (23), while others showed that high viscosities correlated with the formation of open, linear/branched clusters (19, 67, 84) that in extreme cases may lead to expanded percolating networks (17), due in part to the inefficient packing and larger effective solute volume fraction. As a confirmation of the significant influence of cluster formation on viscosity, a roughly linear correlation between η_{rel}

(on a log scale) and average apparent cluster size $\langle N_c \rangle$ (Fig. 2.7a, Table 2.1) was seen for both mAbs, as a consequence of the attractive PPI strength implicit in the size and amount of oligomer formed. Interestingly, the two mAbs exhibited similar dependencies (slopes) of η_{rel} relative to $\langle N_c \rangle$, as opposed to the divergent slopes seen for the ηrel correlations with K and the experimental descriptors S(0) and G_{22}. However, the viscosity of mAb3 is still consistently higher than mAb2 for comparable $\langle N_c \rangle$ (Fig. 2.7a).The failure of the ensemble properties S(0), G_{22} and $\langle N_c \rangle$ to differentiate between mAbs in terms of viscosity may potentially be caused by their inability to account for mAb shape and packing effects as well as cluster formation.

In contrast, the correlation for η_{rel} versus the oligomer mass ratio ($m_{oligomer}/m_{(mono+dimer)}$) (Fig. 2.7b) was linear over a wide range, and was consistent across both mAbs, with the exception of the 50 mM NaCl point for mAb3. This unusual point (the filled orange circle) may be influenced by the more weakly-screened electrostatic repulsion at lower ionic strength. This more universal correlation for this descriptor relative to the others (S(0), G_{22}, K), suggests that the formation of oligomers has a large influence on viscosity, as would be expected in a reptation model (23). A small difference in the mass fraction δ of oligomers formed will not perturb $\langle N_c \rangle$ significantly, but will cause a much larger change in the oligomer mass ratio (($m_{trimer,initial}$ $+\delta)/(m_{mono+di,initial} - \delta)$). The IHS model fits of the SLS data thus suggest that viscosity-reducing co-solutes work by improving the mAb packing efficiency by suppressing cluster formation. The amphipathic co-solutes Arg, Imid, Gdn and PheOMe are therefore likely more effective than NaCl and Lys because they may better shield the hydrophobic interaction sites via preferential interactions with aromatic residues through cation-π and π-π interactions (68, 71) in addition to screening the short ranged electrostatic attraction, as seen from the smaller (more repulsive) $S(0)/S(0)_{HS}$, $G_{22}/G_{22,HS}$, K, $\langle N_c \rangle$, and oligomer mass ratio (Table 2.1) for both mAbs.

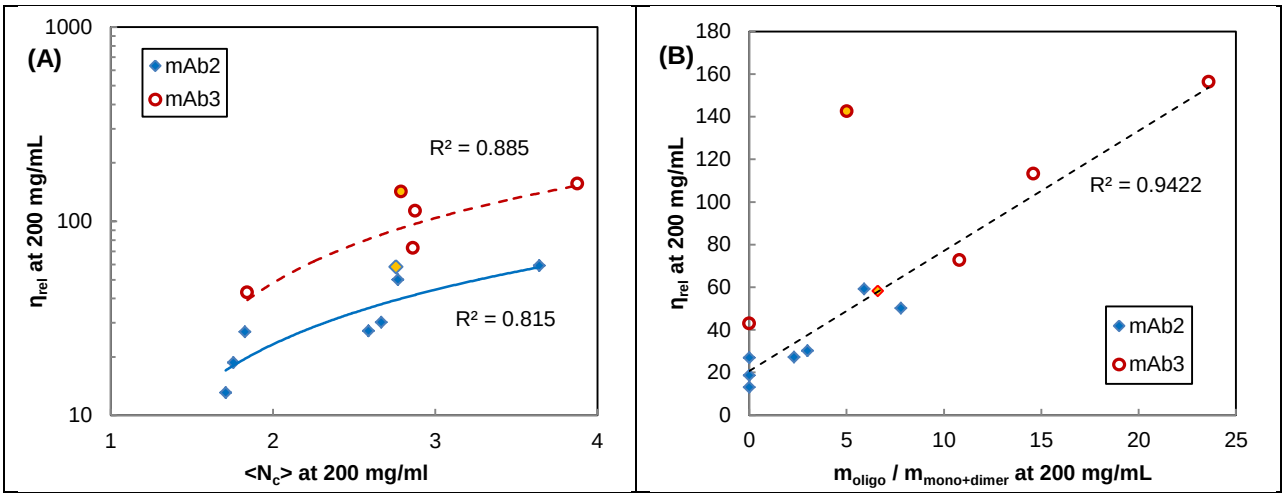

Figure 2.7. Correlation of the calculated relative viscosity at 200 mg/mL with (A) the average apparent cluster size $\langle N_c \rangle$ and (B) mass fraction ratio of oligomer to monomer and dimer, $\left(\frac{m_{oligomer}}{m_{mono}+m_{dimer}}\right)$, at 200 mg/mL calculated from the interacting hard sphere (IHS) model fits of the scattering R/K_0 to oligomerization profiles (Figs. 4, 5) for both mAb2 and mAb3 across all tested co-solute systems. The filled orange symbols correspond to 50 mM NaCl for both mAbs. The solid and dashed lines in (A) are linear fits of the viscosity to average apparent cluster size for mAb2 and mAb3 respectively. The dashed line in (B) is a single linear fit of the viscosity to the oligomer mass ratio across *both* mAbs, where the two 50 mM NaCl data points were excluded from the fit, as explained in the Results and Discussion section. The relative viscosities were calculated from the Ross-Minton equation (Eqn. 2.4) using the best-fit viscosity parameters (Table 2.2).

2.4.9 Explanation of the divergent mAb viscosity correlations in the context of protein microstructure from bead models

The underlying differences in the mAb cluster formation, packing efficiencies and corresponding solution microstructure implied by the divergence in PPI-dependent viscosities between mAb2 and mAb3 may be understood further in the context of coarse-grained bead models and q-dependent scattering (SAXS, SANS, etc.). The longer-ranged attraction implicit in the steep low-concentration S(0) peaks for mAb3 has also been used in the literature to describe the SANS S(q) of a mAb with known charge anisotropy and high viscosity (45). The relation between high solution viscosities and protein solution microstructures with open, fractal clusters

has also been suggested by numerous experimental (19, 67) and computational studies (15-17, 30). The formation of these fractal clusters has been suggested to be caused by non-specific attractive interactions between local sites on the mAb surface, as shown with coarse-grained bead model simulations (15-17, 30) or from q-dependent scattering techniques such as SAXS or SANS (20, 44, 45). 12-bead mAb models have been used to show that the anisotropy of the mAb shape alone leads to steeper increases in R_θ/K_0 and decreases in S(0) with concentration (64). Thus, the steeper concentration dependence of S(0) and G_{22} for mAb3 may also likely be attributed in part to shape anisotropy. The addition of domain-specific charges to each bead based on the mAb sequence, in combination with an interaction potential with short-range attraction and long-range repulsion, showed that increasing charge anisotropy relative to the net charge (dependent upon pH, ionic strength, etc.) is responsible for greater deviations in R_θ/K_0 relative to simple colloidal models (57), and eventually leads to phase separation. The greater deviation in the low concentration fits of S(0) to the single-Yukawa potential for mAb3 (Fig. 2.3b) and the greater oligomer mass ratio in combination with the higher viscosity may therefore likely also be attributed to greater charge anisotropy or stronger multipolar attractive interactions. Similarly, Buck et al. (17) incorporated domain-specific charges into a 12-bead mAb model to demonstrate that a more dipolar charge distribution led to more domain-domain contacts between mAbs, resulting in a higher network density and elevated viscosities. Kastelic et al. (84) also found that branched oligomer assemblies contributed to higher viscosities relative to linear chains of associated mAbs. The insight from these bead models strongly suggests that the higher viscosity of mAb3 in combination with its scattering behavior is likely indicative of greater anisotropy in mAb3's interaction sites, leading to more branched protein microstructures.

2.4.10 Low concentration predictions of high concentration viscosity

Interestingly, the net PPI quantified by G_{22} at low concentration (20 mg/mL) is still well correlated with the high concentration relative viscosity across both mAbs (Fig. 2.6d), and does

not exhibit the divergent viscosity behavior seen for correlations of viscosity with the net PPI at high concentration (Fig. 2.6a, 2.6b). This result may be understood in the context of minimal confinement at low concentration, such that any potential differences in the attraction site anisotropy between mAbs will not significantly influence the net PPI, allowing for a more accurate measurement of the mAb total attraction energy. SLS measurements of G_{22} at low concentration (ex. 20 mg/mL) thus provide a powerful tool for screening mAb candidates and formulations for low viscosities at high concentration, using as little as 0.4 mg of protein for a 20 uL measurement.

The low concentration SLS predictions of high concentration viscosity via G_{22} is a comparable approach to the small-scale SAXS screening experiments proposed by Fukuda et al. for a mAb formulated with NaCl or Arg (47), where a strong correlation was seen between the viscosity at high concentration (175 mg/mL) and the PPI strength measured at low concentration (15 mg/mL) through $S(q\rightarrow 0)$ from SAXS, using low temperatures to amplify the short-range attraction and make them more distinguishable at low concentration. However, the authors did not propose using S(0) to predict the viscosity due to the practical challenges of getting a good form factor P(q) by SAXS for calculating S(q) (47). In contrast, the dilute scattering R_θ/K_0 as $c \rightarrow 0$, which is proportional to the zero-q form factor, is easily measured by SLS, removing the practical limitation of measuring P(0) and hence S(0) or G_{22} at low concentration. The ease of measuring S(0) by SLS at low concentration with low material usage, combined with the ability to automate this process using existing equipment (Calypso; Wyatt Technology Corporation etc.) (52, 53), creates a robust approach for high throughput screening of mAbs and formulations for weak PPI and low viscosities. With regards to the SAXS screening approach proposed in Fukuda et al. (47), the challenges associated with measuring S(0) prompted the authors to develop a correlation between the viscosity and the mAb molecular size instead, where the characteristic sizes R_g (radius of gyration) and D_{max} (maximum particle diameter) were obtained from form

factor fits of the SAXS scattering at dilute conditions. Interestingly, the correlation of R_g and D_{max} with viscosity were tighter than with S(0). Additionally, the systems with larger D_{max} also exhibited broader peaks in their pair distribution function P(r) (47), suggesting a strong relation between self-association, shape anisotropy and the high concentration viscosity.

2.5 CONCLUSIONS

Static light scattering was used to quantitatively rank the strength of the short-ranged attractive PPI for six ionic co-solutes for each of two mAbs from low to high concentration (up to 230 mg/mL). The co-solute rankings by the SLS experimental descriptors ($S(0)/S(0)_{HS}$, $G_{22}/G_{22,HS}$) were consistent with those by the fit parameters from the spherical Yukawa model (K) and the interacting hard sphere model (oligomer mass ratio $m_{oligomer}/m_{monomer+dimer}$ and average cluster size $\langle N_c \rangle$). For the two mAbs, the relative order of the co-solute effects on the attractive PPI was the same: 250 mM Arg and PheOMe as well as 1M Imid greatly weakened the attractive PPI relative to the 50 mM NaCl control, resulting in a large decrease in $S(0)/S(0)_{HS}$, $G_{22}/G_{22,HS}$, K, $\langle N_c \rangle$ and oligomer mass ratio. 250 mM Gdn and Imid modestly weakened the attractive PPI, while 250 mM NaCl and Lys increased them. The attraction range of Z^{-1} of 3 nm for the fit of mAb3 by the spherical Yukawa model was unusually long, suggesting the influence of longer-ranged anisotropic attractive interactions (not included in the model) (88). These stronger interactions were described somewhat more explicitly in terms of the higher oligomer mass ratios from the interacting hard sphere model.

For a given mAb, strong correlations were seen between ηrel and the SLS descriptors of the overall and short-ranged PPI at high concentration ($S(0)/S(0)_{HS}$, $G_{22}/G_{22,HS}$, K, and $\langle N_c \rangle$), as well as with low concentration properties such as $B_{22}/B_{22,HS}$ and $G_{22}/G_{22,HS}$ at 20 mg/mL. Thus, the short-ranged attraction has a major influence on η_{rel} as was also seen previously with SLS (22) and SAXS/SANS (18, 20) for systems without co-solutes. η_{rel} was more sensitive to nearly all of these experimental and model fit descriptors for mAb3 than mAb2, reflecting potential

differences in the mAb packing (fractal dimension), possible formation of reversible oligomers, or dynamic factors (18, 19, 67) that were not considered. The η_{rel} correlations with $S(0)/S(0)_{HS}$ and $G_{22}/G_{22,HS}$ also showed increasing divergence between mAbs 2 and mAb3 with increasing concentration. The calculated average cluster sizes from the IHS fit, which accounts for oligomer formation, does a modestly better job of capturing the underlying physical behavior in that the slope of η_{rel} versus $\langle N_c \rangle$ was the same for both mAbs. However, the η_{rel} values were higher for mAb3. This failure of the ensemble properties ($S(0)$, G_{22}, $\langle N_c \rangle$) to differentiate between the viscosities of two mAbs may indicate the confounding influence of mAb packing efficiency and related microstructure (67). The only property that η_{rel} could be correlated with for both mAbs (excluding the less-screened 50 mM NaCl control systems) was the oligomer mass ratio. This ratio of oligomers to monomer and dimer emphasizes the larger oligomers much more than does $\langle N_c \rangle$, and also emphasizes the relative polydispersity, both of which will influence the mAb packing efficiency and relative viscosity in solution. The large effect of oligomerization on η_{rel} may be anticipated from theoretical self-association models for both Fab-Fab and/or Fab-Fc interactions (19, 23, 84).

2.6 ACKNOWLEDGMENTS

The authors gratefully acknowledge Dr. Allen P. Minton (National Institute of Health, Bethesda, MA) for providing the Matlab scripts used to fit the SLS data to the interaction hard sphere self-association model, as well for intellectual discussion on the general interpretation of the IHS model fits. The authors also thank Mahlet A. Woldeyes (University of Delaware, Newark, Delaware) for helpful advice on the experimental methodology for SLS measurements at high protein concentration. Finally, the authors also gratefully acknowledge Merck & Company, Inc. and the Welch Foundation (F-1319) for their financial support.

2.7 SUPPORTING INFORMATION

2.7.1 Dialysis for buffer exchange

30 mL of the 25 – 35 mg/mL starting mAb solutions as provided by Merck were dialyzed into 21:30 mM Na:OAc (pH 5) buffer by dynamic dialysis using 8 – 10 kDa MWCO Tube-A-Lyzer dynamic dialysis modules (30 mL capacity) from Spectrum Labs (Rancho Dominguez, CA). The buffer was recirculated through the dialysis module at 300 mL/min, which prevents accumulation of the dissolved species (removed by dialysis) at the dialysis membrane surface and ensures even mixing of the buffer and dissolved solids, reducing the amount of time needed for the dialysis process to reach equilibrium. To ensure a complete buffer exchange, the mAb solution was dialyzed against 500 mL of the pH 5 sodium acetate buffer using 3 12-hour buffer exchanges at 10°C in order to remove undesired solutes from the original mAb solution. The final concentration of the dialyzed mAb solution was typically 20 mg/mL.

2.7.2 Preparation of concentrated co-solute and buffer stocks

Concentrated imidazole was dissolved in and titrated to pH 5 with 12N HCl, and phenylalanine methyl ester hydrochloride was titrated to pH 5.5 with 1N NaOH. Concentrated solutions of all other protonated basic excipients (Arg.HCl, Lys.HCl and Gdn.HCl) were used as is without further titration, corresponding to solution pH values of ~5.3 – 5.4. Concentrated (500 mM) pH 5 sodium acetate buffer stock was prepared by mixing 500 mM Na.OAc and 500 mM acetic acid in a 7:3 volume ratio. All co-solute and buffer stock solutions were filtered with 0.22 um filters (CellTreat Scientific Products, Pepperell, MA) prior to use.

2.7.3 Gravimetric dilution for preparation of mAb samples

Due to the challenges and inaccuracies of working with viscous solutions on a volumetric basis, the concentrated, formulated mAb solutions were prepared by gravimetric dilution instead. An approximate volume (~1.2 mL) of the concentrated, unformulated 280 mg/mL mAb stock

solution was transferred to an empty, tared microcentrifuge tube. The mass of the added mAb stock (weighed using a Mettler Toledo (Columbus, OH) NewClassic MS analytical balance) was converted to a volume using the mAb stock solution density calculated from the measured protein concentration and the known buffer composition:

$$\rho_{solution} = (\sum(c_i V_{soln}) + \rho_{water} * V_{water})/V_{soln} \quad (2.17a)$$

where V_{soln} is a volume basis (which cancels out), c_i is the mass concentration of each solute/co-solute (protein, buffer components, etc.), ρ_{water} is the density of water, and V_{water} is the volume (out of the volume basis) occupied by water. V_{water} is given by

$$V_{water} = V_{soln} - \sum (c_i V_{soln}/\rho_i) \quad (2.17b)$$

where ρ_i is the anhydrous density of each solute/co-solute species, and the protein density was taken to be ~1350 mg/mL calculated from the dry-weight partial specific volume of 0.73 – 0.74 mL/g (66). The remaining buffer and co-solute stock solutions were mixed with the concentrated, unformulated mAb stock at the appropriate volume ratios to achieve the desired solution composition (225 mg/mL mAb with 30 mM pH 5 sodium acetate buffer and 50, 250 or 1000 mM co-solute). The co-solute/buffer stock solutions were added volumetrically given their low viscosities. Due to the small volumes of each co-solute stock solutions needed for each sample, the co-solute and buffer stocks were first mixed together (separately from the mAb stock) at the same volume ratio needed, but scaled to a larger volume in order to increase the accuracy of the volumetric addition (ex. 30:70 µL of buffer:co-solute would be scaled to 150:350 µL, etc.). An aliquot of this pre-mixed buffer would then be added to the mAb stock at the correct mAb:buffer volume ratio to achieve the desired final solution composition. The final mAb concentration was then checked by UV-visible spectroscopy with 5 – 6 replicate measurements to ensure accuracy.

2.7.4 Error propagation analysis for concentration from gravimetric dilutions

To determine the expected error in the calculated concentrations of the intermediate concentration SLS samples prepared by gravimetric dilution of the formulated ~225 mg/mL mAb stocks (with measured concentrations and standard errors), error propagation analysis was done on the dilution equation

$$C_2 = \frac{C_1 V_1}{V_2} = \frac{C_1 * \left(\frac{m_p}{\rho_{ps}}\right)}{\left(\frac{m_p}{\rho_{ps}}\right) + V_{buffer}} \tag{2.18}$$

with the systematic instrument errors reported by the instrument manufacturers. Here, C_2 is the target mAb concentration for the gravimetrically-diluted sample, C_1 is the initial concentration of the formulated mAb stock (~225 mg/mL), m_p is the mass of the mAb stock used for the dilution, ρ_{ps} is the density of the formulated mAb stock, and V_{buffer} is the volume of same-composition solvent added to dilute the mAb stock to the desired concentration C_2. The density of the formulated mAb stock is determined from C_1, the background solvent density ρ_{buffer} calculated from Eqn. 2.17a and 2.17b (no protein, only co-solute and acetate buffer), and the protein dry-weight density of 1350 mg/mL (66).

$$\rho_{ps} = C_1 + \rho_{buffer} * \left(1 - \frac{C_1}{\rho_{protein,dry}}\right) \tag{2.19}$$

Applying error propagation analysis to Eqn. 2.18 gives the expected variance in the dilution concentration C_2 as a function of the measurement error in C_1 (σ_{C1}) as well as the systematic error of the mass balance used to measure m_p (σ_{mp}) and of the pipette used to add the dilution solvent with volume V_{buffer} (σ_{V_buffer}).

$$\sigma_{C_2}^2 = \left\{ \frac{\left(\frac{m_p}{\rho_{ps}}\right)}{\left(\frac{m_p}{\rho_{ps}}\right)+V_{buffer}} * \sigma_{C_1} \right\}^2 + \left\{ \frac{\left(\frac{C_1 V_{buffer}}{\rho_{ps}}\right)}{\left(\left(\frac{m_p}{\rho_{ps}}\right)+V_{buffer}\right)^2} * \sigma_{m_p} \right\}^2 + \left\{ \frac{-C_1 V_{buffer} m_p}{\rho_{ps}^2 * \left(\left(\frac{m_p}{\rho_{ps}}\right)+V_{buffer}\right)^2} * \sigma_{\rho_{ps}} \right\}^2 + \left\{ \frac{-C_1 m_p}{\rho_{ps} * \left(\left(\frac{m_p}{\rho_{ps}}\right)+V_{buffer}\right)^2} * \sigma_{V_{buffer}} \right\}^2 \quad (2.20a)$$

The variance in the calculated mAb stock density $\sigma_{\rho_{ps}}^2$ is also calculated by error propagation analysis.

$$\sigma_{\rho_{ps}}^2 = \sigma_{C_1}^2 * \left(1 - \frac{\rho_{buffer}}{\rho_{protein,dry}}\right)^2 \quad (2.20b)$$

The known parameter values and uncertainties used to calculate the variance in C_2 are reported in Table 2.9. Note that an average ρ_{buffer} of 1010 mg/mL (representative of the 250 mM co-solute formulations) and ρ_{ps} of 1070 mg/mL (corresponding to 225 mg/mL mAb in buffer with 250 mM Arg or Lys; density will be slightly smaller for NaCl, Gdn and Imid due to lower co-solute MW) were used, and that the systematic error for the pipette volume is a function of the pipette used (2 – 20 µL vs 20 – 200 µL Research Plus adjustable volume pipetters from Eppendorf (Hamburg, Germany)), as reported by Eppendorf. The error/reproducibility of the mass measurements (σ_{mp}) was reported by the manufacturer (Mettler Toledo, Columbus, OH) to be within 0.1 mg. The known parameters m_p and V_{buffer} are listed for the two extreme cases (i) ultra-dilute dilution (2 mg/mL) and (ii) highest-concentration dilution (200 mg/mL) to evaluate the expected error at the lowest and highest concentrations in the dilution series. The resulting standard error in C_2 (σ_{C2}) is 0.22 mg/mL at a target concentration of 2 mg/mL (11% error) and 2.8 mg/mL at a target concentration of 200 mg/mL (1.4% error).

2.7.5 Calculation of the static structure factor S(q→0) from static light scattering

At low values of q, the generalized scattering intensity I(q) of non-spherically symmetric particles such as mAbs (18, 45) is given by

$$I(q) = c * V_{eff} * (\Delta\rho)^2 * \langle P(q)\rangle S(q) \quad (2.21a)$$

where ϕ is the protein volume fraction ($\phi = c*V_{eff}$), q is the scattering vector ($q=4\pi/\lambda*\sin(\theta/2)$), $\Delta\rho$ is the scattering length density difference between the protein and the solvent, θ is the scattering angle, P(q) is the normalized particle form factor, and S(q) is the interparticle structure factor. The static light scattering measurements in this study were performed at a λ of 658 nm nm and a single θ of 90°, corresponding to q = 0.0018 $Å^{-1}$, or a Bragg scattering length $2\pi/q$ (86) of 350 nm. In the limit $q \rightarrow 0$, the decoupling function (18, 45) $\beta(q)$ goes to 1 (not shown in Eqn. 2.21a) (18, 45) and $S_{eff}(q) = S(0)$. For dilute concentrations (c < 5 mg/mL (18, 45)), the scattering becomes a function of the protein shape only, such that S(0) = 1. Eqn. 2.21a therefore becomes

$$I(q) = (c \rightarrow 0) * V_{eff} * (\Delta\rho)^2 * \langle P(q)\rangle \quad (2.21b)$$

The protein-solvent scattering length difference $\Delta\rho$ is assumed to be independent of the protein concentration.

The value of S(0) for q = 0.0018 $Å^{-1}$ can be obtained by dividing Eqn. 2.21a by Eqn. 2.21b. SLS can therefore be used to directly measure S(0) by comparing the concentration-normalized scattering intensity at low and high concentration (13) (Eqn. 2.22b).

$$\frac{I(q\rightarrow 0,c)}{I(q\rightarrow 0,c_{dilute})} = \frac{c*S(q\rightarrow 0)}{c_{dilute}} \quad (2.22a)$$

$$S(q \rightarrow 0) = \frac{I(q\rightarrow 0,c)/c}{I(q\rightarrow 0,c_{dilute})/c_{dilute}} \quad (2.22b)$$

In this study, the form factor was measured at ~2 mg/mL (c_{dilute}). The scattering intensity $I(q\rightarrow 0)$ is directly proportional to the Rayleigh ratio R_θ (Eqn. 2.23) (87), where the incident laser intensity I_0, illuminated scattering volume V and distance from the scattering volume to light detector r are constants specific to the SLS instrument configuration.

$$I = (R_\theta * I_0 * V)/r^2 \tag{2.23}$$

Using Eqn. 2.23, Eqn. 2.22b can be rewritten in terms of the Rayleigh ratio

$$S(q \to 0) = \frac{(R_\theta/c)_{high\ conc}}{(R_\theta/c)_{dilute}} \tag{2.24}$$

Multiplying the numerator and denominator by the optical constant K_0 (Eqn. 2.7 using the solvent refractive index n_0), and recognizing that in the dilute limit $R_\theta/K_0c = M_w$, Eqn. 2.24 becomes Eqn. 2.9 in the main text.

2.7.6 Interacting hard sphere model of light scattering

In the interacting hard sphere (IHS) model of light scattering developed by Minton (66) and summarized here, the light scattering of a concentrated protein solution can be described by a three-component equivalent hard sphere mixture as described in the main text. The Rayleigh ratio, calculated from the scattering intensity, is regressed to mole/mass fraction distribution of monomer and two oligomeric species of aggregation number m (typically m = 2) and n, as shown in Eqn. 2.11 in the main text.

The concentration fluctuation of each species $\langle \Delta \bar{c}_i \rangle$ depends on the gradients ζ_{ij} of their chemical potential, represented here by their thermodynamic activity coefficients γ_i (Eqn. 2.25a – 2.25d):

$$\left\langle \Delta \bar{c}_i^{\,2} \right\rangle = \bar{c}_i \frac{(1+\zeta_{jj})(1+\zeta_{kk}) - \zeta_{kj}\zeta_{jk}}{D} \tag{2.25a}$$

$$\left\langle \Delta \bar{c}_i \Delta \bar{c}_j \right\rangle = \frac{\bar{c}_k \zeta_{ki}\zeta_{kj} - \bar{c}_i \zeta_{ij}(1+\zeta_{kk})}{D} \tag{2.25b}$$

$$D = (1+\zeta_{11})(1+\zeta_{22})(1+\zeta_{33}) + 2\zeta_{12}\zeta_{21}\zeta_{31} - (1+\zeta_{11})\zeta_{32}\zeta_{23} - (1+\zeta_{22})\zeta_{31}\zeta_{13} - (1+\zeta_{33})\zeta_{21}\zeta_{12} \tag{2.25c}$$

$$\zeta_{ij} = \bar{c_j}\frac{\partial \ln(\gamma_i)}{\partial \bar{c_j}} = \rho_j \frac{\partial\, ln(\gamma_i)}{\partial \rho_j} \tag{2.25d}$$

In the limit of steric-only interactions, such as in this scattering model, the activity coefficient of each spherical species is a function of the sphere size only (Eqn. 2.26a), where Q is defined in Eqn. 2.26b, ρ_i is the number density of each species (Eqn. 2.26c), and N_A is Avogadro's number.

$$\frac{\partial \ln(\gamma_i)}{\partial \rho_j} = \frac{4\pi r_i^3}{3Q} + \left[\frac{4\pi r_i^2}{Q} + \frac{16\pi^2 r_i^3}{3Q^2}\sum_i \rho_i r_i^2\right] r_j + \left[4\pi\left(\frac{r_i}{Q} + \frac{4\pi r_i^2 \sum_i \rho_i r_i^2 + \frac{4\pi r_i^3}{3}\sum_i \rho_i r_i}{Q^2} + \frac{\frac{32\pi^2 r_i^3}{3}\left(\sum_i \rho_i r_i^2\right)^2}{3Q^2}\right) + \frac{\frac{64\pi^3 r_i^3}{3}\left(\sum_i \rho_i r_i^2\right)^2}{3Q^3}\right] r_j^2 + \frac{4\pi}{3}\left[\frac{1}{Q} + \frac{4\pi r_i \sum_i \rho_i r_i^2 + 4\pi r_i^2 \sum_i \rho_i r_i + \frac{4\pi r_i^3}{3}\sum_i \rho_i}{Q^2} + \frac{16\pi^2 r_i^2\left(\sum_i \rho_i r_i^2\right)^2 + \frac{32\pi^2 r_i^3}{3}\sum_i \rho_i r_i \sum_i \rho_i r_i^2}{Q^3} + \frac{\frac{64\pi^3 r_i^3}{3}\left(\sum_i \rho_i r_i^2\right)^3}{Q^4}\right] r_j^3 \tag{2.26a}$$

$$Q = 1 - \frac{4\pi}{3}\sum_i \rho_i r_i^3 \tag{2.26b}$$

$$\rho_i = \bar{c_i} * N_A \tag{2.26c}$$

The effective sphere radius r_i is calculated from the molar mass of the spherical species (M_i = i*M_1) and the protein specific exclusion volume V_{ex} (Eqn. 2.27). As mentioned in the main text, in the limit of screened charge repulsion (as is the case for all of the co-solute formulations investigated in this study), V_{ex} becomes the effective protein partial specific volume V_{eff}.

$$r_i = \left(\frac{3V_{eff}M_i}{4\pi N_A}\right)^{\frac{1}{3}} \tag{2.27}$$

The thermodynamic self-association equilibrium constants K_i^0 for each oligomer species is calculated from the activity a_i of each species, as shown in Eqn. 2.28a, where a_1, γ_i and $\bar{c_1}$ are the activity, activity coefficient and molar concentration of the free monomer, respectively. The

thermodynamic equilibrium association constant is in turn related to the apparent equilibrium association constant $K_i = \frac{\bar{c_i}}{\bar{c_1}^i}$ by Eqn. 2.28b and 2.28c.

$$K_i^0 \equiv \frac{a_i}{a_1^i} = \frac{\gamma_i \bar{c_i}}{\gamma_1^i \bar{c_1}^i} \tag{2.28a}$$

$$K_i^0 = K_i \frac{\gamma_i}{\gamma_1^i} \tag{2.28b}$$

$$\ln(K_i) = \ln\left(\frac{\bar{c_i}}{\bar{c_1}^i}\right) = \ln(K_i^0) + i * \ln(\gamma_1) - \ln(\gamma_i) \tag{2.28c}$$

The scattering intensities (via the Rayleigh ratio R_θ) were fit across the entire concentration range simultaneously to Eqn. 2.11 for a single value of the fit parameters m, n, K_{1m}, K_{1n}, and V_{eff} using Eqn. 2.25a through 1.28c, while also observing the closed mole/mass balance for the monomer-units (Eqn. 2.12). Due to the iterative process needed to simultaneously regress the five fit parameters across the entire mAb concentration range, the fits of the scattering data to this model were conducted using scripts and functions written in MATLAB (Mathworks, Natick, MA) and generously provided by Allen Minton (National Institute of Health, Bethesda, MA).

2.7.7 Viscosity of hard sphere solutions

The mAb viscosity can be normalized by the viscosity of a reference hard sphere solution at the same volume fraction ϕ. The hard sphere solution viscosity was determined from the Ross-Minton equation ($\frac{\eta}{\eta_0} = \exp\left(\frac{2.5\phi}{1-1.56\phi}\right)$) (41, 88) assuming random close packing of the spheres (ϕ_{max} = 0.64) (89), where the equivalent ϕ at a given mAb concentration c was calculated from the average best-fit mAb density as determined from the interacting hard sphere (IHS) model fit of the mAb scattering across all co-solute formulations ($\phi = c*V_{eff}$).

2.7.8 Comparison of single (short-range attraction only) and two-term (short-range attraction + long-range repulsion or attraction) interaction potential fits of the mAb light scattering

While the scattering of mAbs is typically fit with interaction potentials that describe both the short-range attraction and long-range repulsion (18, 45, 49, 50, 56, 57, 64, 65), this work demonstrates that in the limit of moderate to high ionic strengths (≥ 50 nM), a single short-range attraction term (ex. Yukawa) is sufficient to describe the mAb scattering from low to high concentration. Two-parameter models such as the screened Coulomb + Lennard-Jones U(r) have been used with coarse-grained mAb bead models to increase the accuracy of model predictions of the high concentration scattering by better capturing the effects of shape and charge anisotropy on S(0) and consequently the scattering. However, these models carry the cost of greater complexity in data fitting, requiring at least two fit parameters in addition to knowledge of the mAb domain-specific charges (obtained from the mAb sequence) (50, 57, 64). In addition, these models still required the inclusion of a short-range attraction term, even for more ideal systems with more uniform and net repulsive PPI, such as the model protein α-chymotrypsinogen in buffer conditions promoting minimal charge dipoles and high net charge (57). The single attractive Yukawa potential therefore has the advantage of being able to describe S(0) across the entire concentration range for mAb2 and to a smaller extent mAb3 without the added analytical complexity of the two-term models, Thus in the interest of simplicity for screening co-solutes and understanding their effect on PPI, operating at higher ionic strengths may be sufficient for quantification of the short-range attraction from light scattering using a single-parameter (K) model without prior knowledge of the mAb sequence or domain-specific charges.

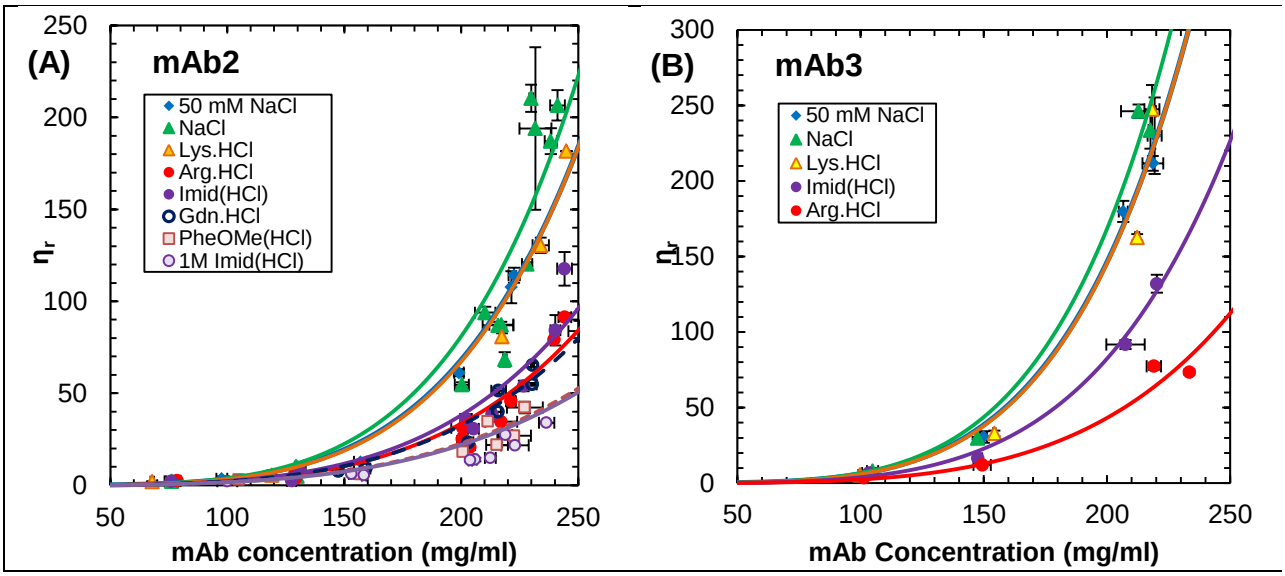

Figure 2.8. Viscosity of **(A)** mAb2 and **(B)** mAb3 with various co-solutes at 250 mM (unless otherwise specified), fit to the reptation model. Symbols are measured values, and solid/dashed lines are fits of the viscosity to the reptation model. All co-solutes (with exception of NaCl) are titrated to, or already at pH ~5.5, and all samples are buffered with 30 mM (Na)OAc at pH 5. Model fit parameters are shown in Table 2.2.

Co-solute formulation	η_0 (cP)	Ross-Minton		Reptation
		$[\eta]$ (mL/g)	k/v	k
mAb2				
50 mM NaCl	0.91	14.63	0.0957	410.0
250 mM NaCl	0.94	14.23	0.1064	555.1
250 mM Lys.HCl	1.05	14.50	0.0893	500.1
250 mM Arg.HCl	1.05	11.97	0.1141	134.7
250 mM Imid(HCl) pH 5.5	0.95	12.60	0.1033	143.3
250 mM Gdn.HCl	0.91	11.01	0.1514	75.5
250 mM PheOMe(HCl) pH 5.5	1.02	8.96	0.2167	3.9
1000 mM Imid(HCl) pH 5.5	1.04	7.25	0.3008	0.001*
mAb3				
50 mM NaCl	0.91	17.86	0.0783	1071.0
250 mM NaCl	0.94	18.24	0.0761	1297.6
250 mM Lys.HCl	1.05	19.27	0.0481	1248.8
250 mM Imid(HCl) pH 5.5	0.95	16.05	0.0783	570.4
250 mM Arg.HCl	1.05	12.01	0.1505	242.4

* Reptation model cannot accurately capture the low viscosity in the 1000 mM Imid(HCl) formulation. Best fit k approaches zero (infinite repulsion).

Table 2.2. Regressed parameters for fits of the mAb2 and mAb3 viscosities with different co-solutes to the Ross-Minton and reptation viscosity models. The parameter A in the reptation model was fitted across multiple data sets and held fixed at $5.38*10^{-8}$ cP.

Protein	Formulation	mAb conc (mg/ml)	η (cP)	η_0 (cP)	η_{inh} (mL/g)	pH	Solvent RI	q ($Å^{-1}$)
mAb 2	50 mM NaCl	222.5 ± 2.3	103.3 ± 3.6	0.91	21.3	5.4	1.334	0.00180
mAb 2	250 mM NaCl	228.1 ± 2.1	113.4 ± 1	0.94	21.0	5.4	1.336	0.00180
mAb 2	250 mM Lys.HCl	233.9 ± 3.5	137.3 ± 4.3	1.05	20.8	5.4	1.339	0.00181
mAb 2	250 mM Arg.HCl	228.9 ± 1.8	76.8 ± 3.7	1.05	18.7	5.3	1.344	0.00181
mAb 2	250 mM Imid(HCl)	226.7 ± 0.2	51.1 ± 2.6	0.95	17.6	5.9	1.337	0.00181
mAb 2	250 mM Gdn.HCl	230.3 ± 1.8	50.1 ± 0.7	0.91	17.4	5.6	1.338	0.00181
mAb 2	250 mM PheOMe.HCl	222.6 ± 7.2	27.5 ± 2.1	1.02	14.8	5.4	1.343	0.00181
mAb 2	1000 mM Imid(HCl)	222.9 ± 5.8	22.6 ± 0	1.04	13.8	6.3	1.351	0.00182
mAb 3	50 mM NaCl	218.6 ± 4.1	191.6 ± 4.3	0.91	24.5	5.3	1.334	0.00180
mAb 3	250 mM NaCl	217.6 ± 0.7	220.5 ± 11.6	0.94	25.1	5.4	1.336	0.00180
mAb 3	250 mM Lys.HCl	218.2 ± 3	260.5 ± 17	1.05	25.2	5.6	1.339	0.00181
mAb 3	250 mM Imid(HCl)	220.2 ± 0.4	125.1 ± 5.5	0.95	22.2	6.1	1.337	0.00181
mAb 3	250 mM Arg.HCl	233.4 ± 0.3	77.4 ± 1.7	1.05	18.4	5.4	1.344	0.00181

Table 2.3. Physical properties of original high-concentration mAb 2 and 3 solutions with different co-solutes used for SLS dilution series.

Protein	Co-solute formulation	M_w (Da)	B_{22} (mL/g)
mAb 2	50 mM NaCl	162059 ± 789	-0.14 ± 0.07
mAb 2	250 mM NaCl	166804 ± 1987	-1.43 ± 0.11
mAb 2	250 mM Lys.HCl	161324 ± 3312	-1.46 ± 0.85
mAb 2	250 mM Arg.HCl	156900 ± 87	3.59 ± 0.05
mAb 2	250 mM Imid(HCl) pH 5.5	172265 ± 210	0.80 ± 0.07
mAb 2	250 mM Gdn.HCl	164629 ± 1476	2.58 ± 0.11
mAb 2	250 mM PheOMe.HCl(NaOH) pH 5.5	181161 ± 5497	6.20 ± 0.17
mAb 2	1000 mM Imid(HCl) pH 5.5	139667 ± 800	6.20 ± 0.16
mAb 3	50 mM NaCl	169180 ± 5926	-0.94 ± 0.77
mAb 3	250 mM NaCl	194176 ± 587	-3.10 ± 0.13
mAb 3	250 mM Lys.HCl	163802 ± 3699	-2.22 ± 0.44
mAb 3	250 mM Imid(HCl) pH 5.5	160850 ± 549	-2.37 ± 0.26
mAb 3	250 mM Arg.HCl	155051 ± 2770	-1.41 ± 0.22

Table 2.4. M_w and B_{22} values for mAb2 and mAb3 in different co-solute formulations measured by static light scattering. The linear fits of the scattering profiles used to determine M_w and B_{22} are shown in the Supporting Info (Fig. 2.11, 2.12).

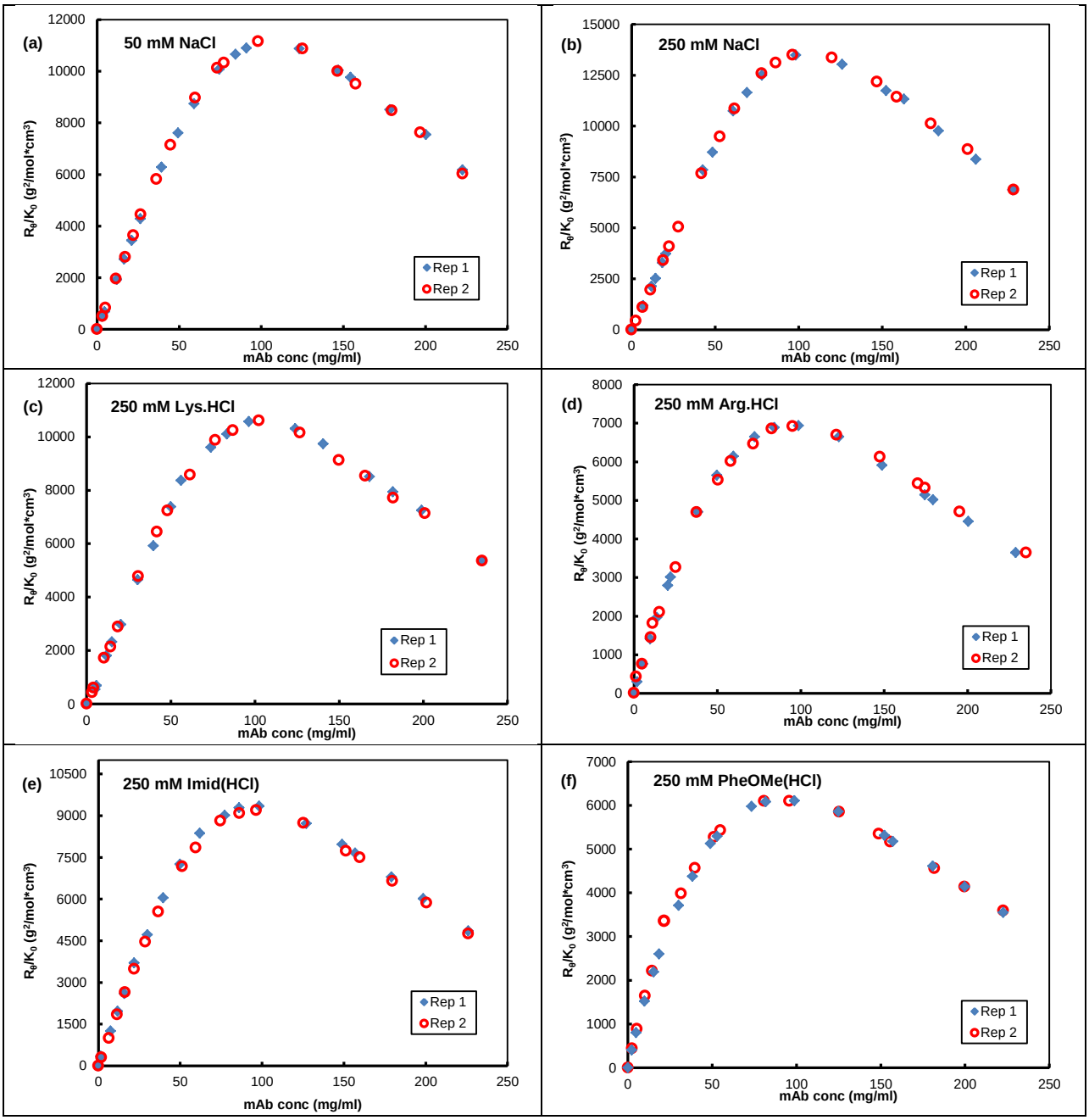

Figure 2.9. Reproducibility of SLS measurements for mAb2 with (a) 50 mM NaCl, (d) 250 mM Arg.HCl, (b) 250 mM NaCl, (d) 250 mM Imid(HCl) pH 5.5, (c) 250 mM Lys.HCl, (f) 250 mM PheOMe(HCl) pH 5.5, (g) 250 mM Gdn.HCl and (h) 1M Imid(HCl) pH 5.5; all buffered with 30 mM (Na)OAc at pH 5. The second replicate of 1M Imid was only measured up to 50 mg/mL mAb2. Both replicates of each co-solute formulation were prepared by parallel gravimetric dilution of the same concentrated, formulated original sample (Table 2.3).

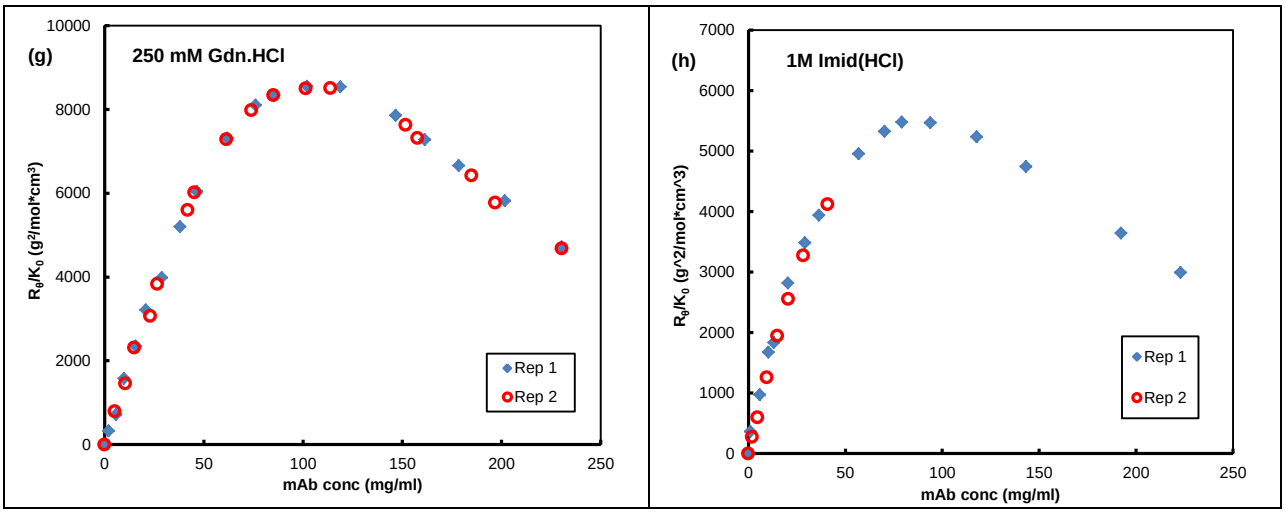

Figure 2.9, cont. Reproducibility of SLS measurements for mAb2 with (a) 50 mM NaCl, (d) 250 mM Arg.HCl, (b) 250 mM NaCl, (d) 250 mM Imid(HCl) pH 5.5, (c) 250 mM Lys.HCl, (f) 250 mM PheOMe(HCl) pH 5.5, (g) 250 mM Gdn.HCl and (h) 1M Imid(HCl) pH 5.5; all buffered with 30 mM (Na)OAc at pH 5. The second replicate of 1M Imid was only measured up to 50 mg/mL mAb2. Both replicates of each co-solute formulation were prepared by parallel gravimetric dilution of the same concentrated, formulated original sample (Table 2.3).

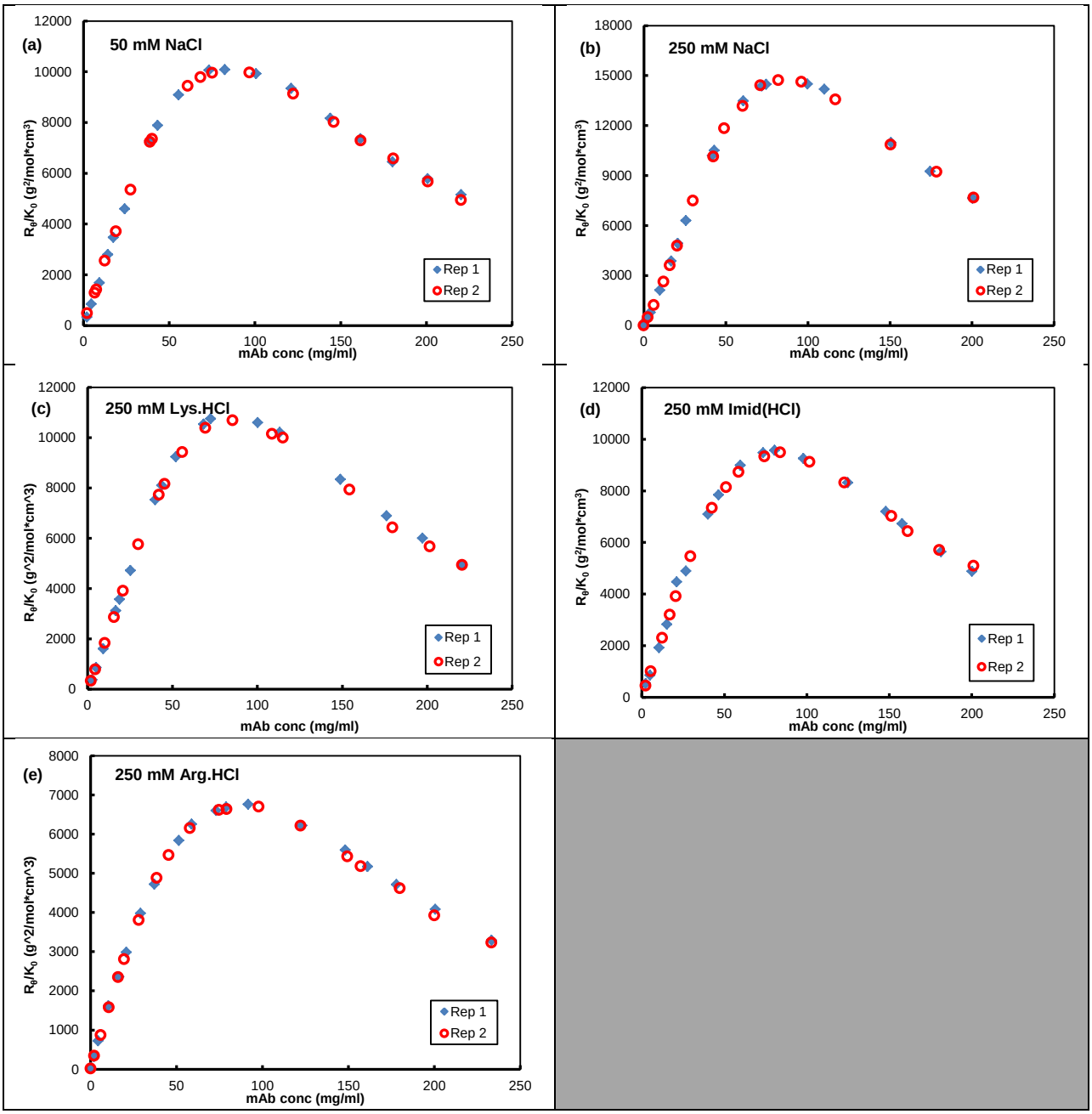

Figure 2.10. Reproducibility of SLS measurements for mAb3 with (a) 50 mM NaCl, (b) 250 mM NaCl, (c) 250 mM Lys.HCl, (d) 250 mM Imid(HCl) pH 5.5 and (e) 250 mM Arg.HCl; all buffered with 30 mM (Na)OAc at pH 5. Both replicates of each co-solute formulation were prepared by parallel gravimetric dilution of the same concentrated, formulated original sample (Table 2.3).

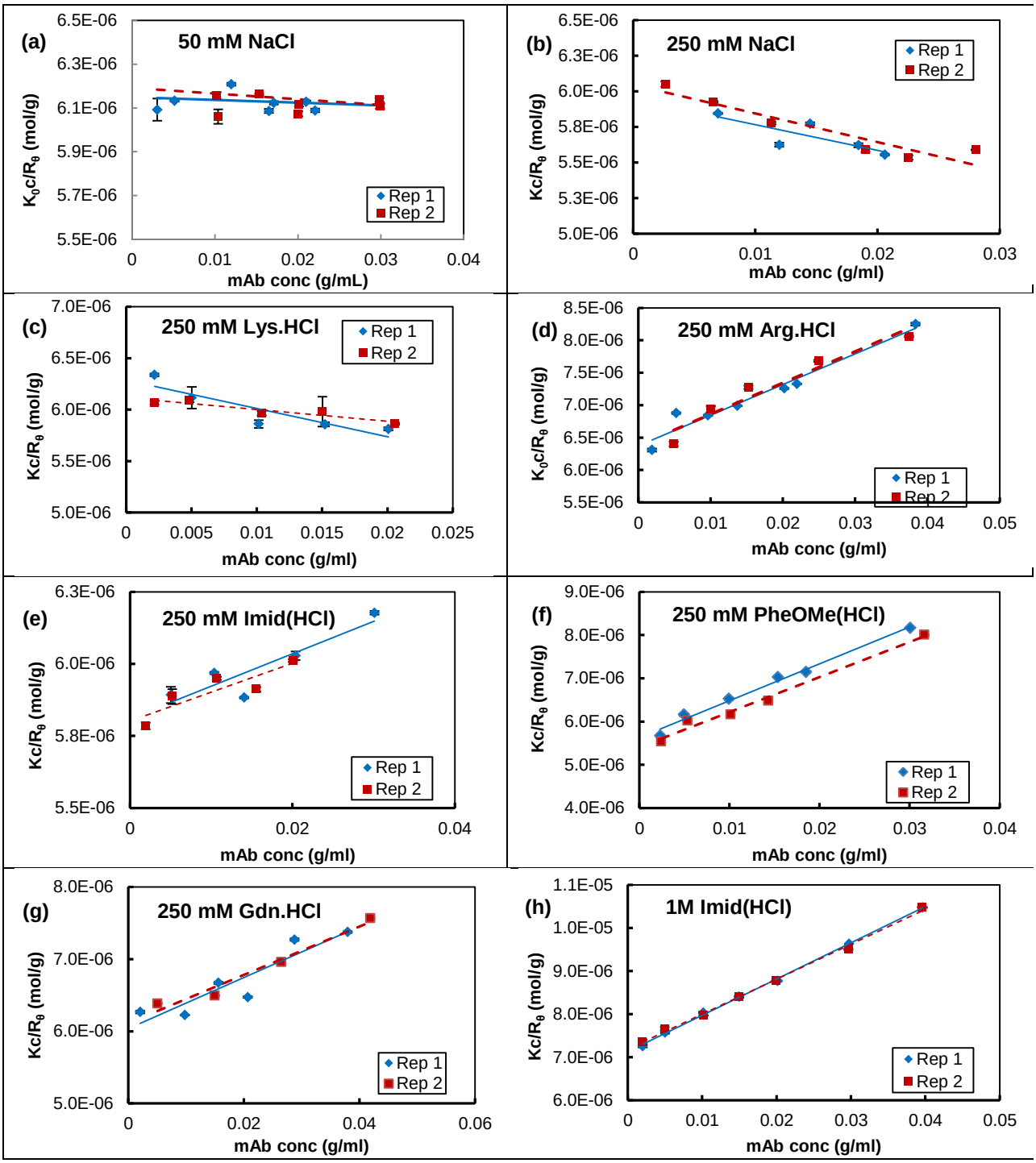

Figure 2.11. Best-fit lines of the scattering profiles to Eqn. 2.6 for determining M_w and B_{22} for mAb2 in different co-solute formulations (see individual labels, same formulations/samples as in Fig. 2.9).

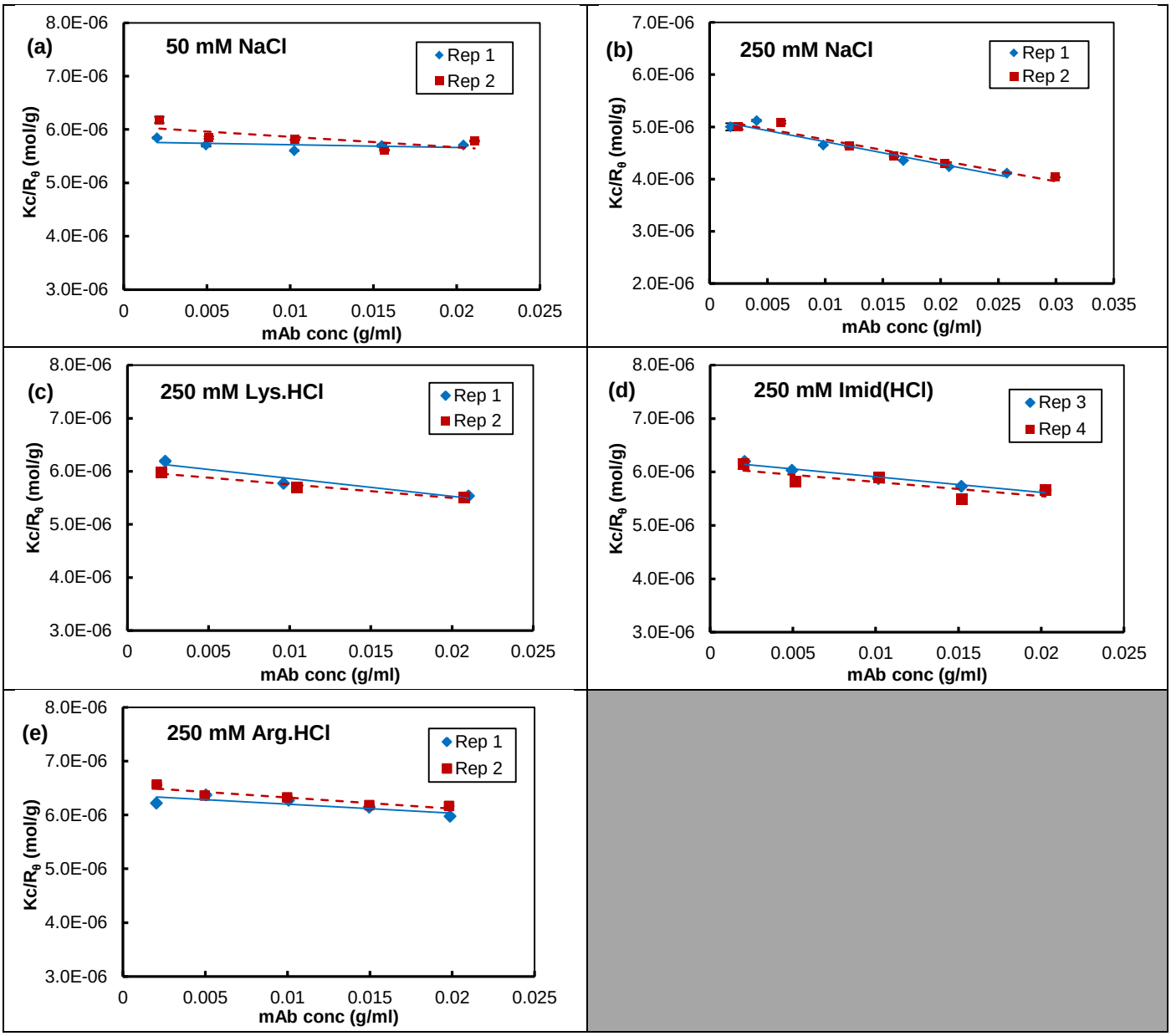

Figure 2.12. Best-fit lines of the scattering profiles to Eqn. 2.6 for determining M_w and B_{22} for mAb3 in different co-solute formulations (see individual labels, same formulations/samples as in Fig. 2.10).

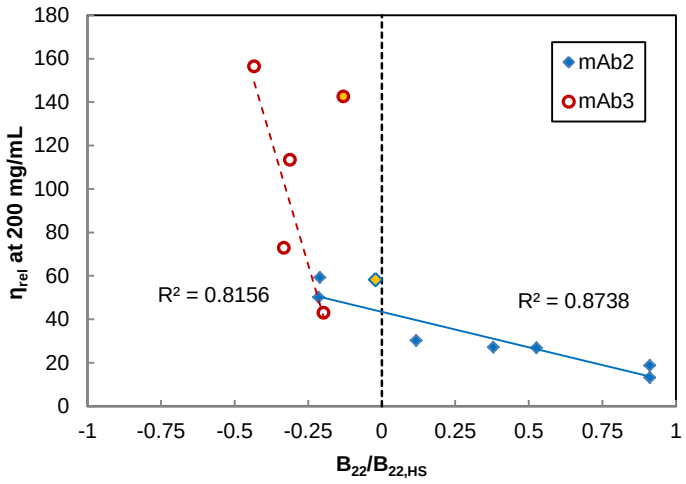

Figure 2.13. Correlation between the normalized B_{22} calculated from the low concentration scattering (Fig. 2.11, 2.12) and viscosity at 200 mg/mL for mAb2 and mAb3 across all co-solutes. The normalizing hard sphere term $B_{22,HS}$ was calculated(11, 37) to be 6.8 mL/g (mAb2) and 7.1 mL/g (mAb3) using the average R_h of ~4.7 nm, which was determined from the average best-fit density across all co-solutes by the interacting hard sphere model fits for each mAb (Table 2.7, 2.8). The filled orange symbols correspond to 50 mM NaCl, which has a Debye length of 1.2 nm, compared to 0.6 nm for the 250 mM co-solute systems and 0.3 nm for the 1M Imid system; the 30 mm (Na)OAc buffer in all formulations contributes 16 mM ionic strength. The best-fit lines (solid and dashed curves) do not include the 50 mM NaCl data points in the fit, given the less-screened, longer-ranged electrostatic repulsion.

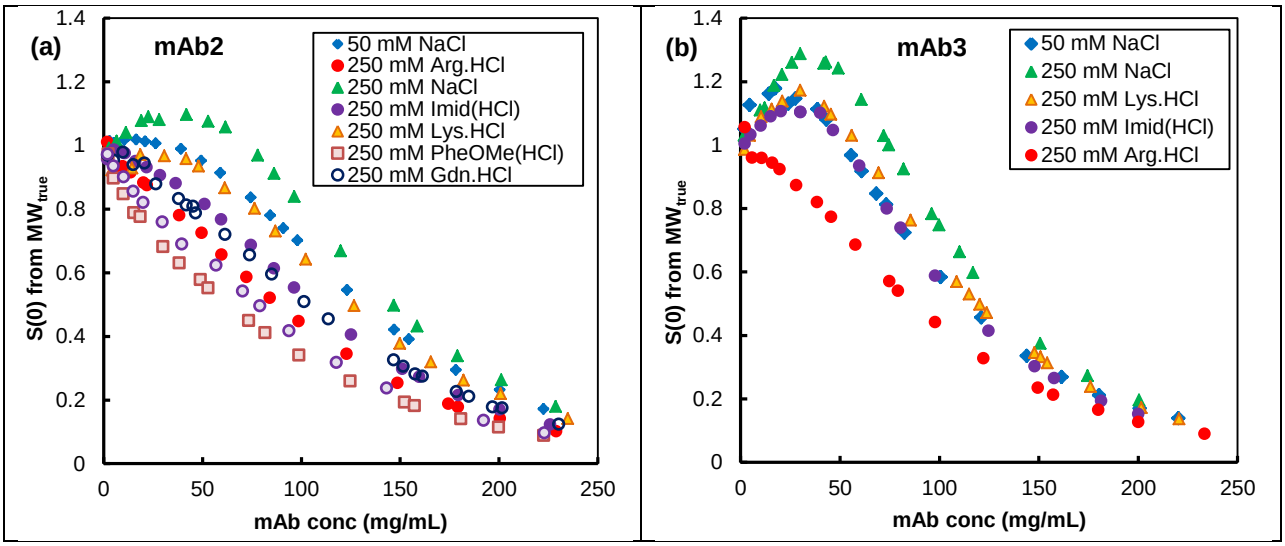

Figure 2.14. Structure factor *S(0)* calculated from the best-fit M_w (Table 2.4) instead of the lowest-concentration data point.

Protein	Co-solute formulation	ARD (%)
mAb 2	50 mM NaCl	3.4
mAb 2	250 mM NaCl	3.7
mAb 2	250 mM Lys.HCl	4.4
mAb 2	250 mM Arg.HCl	1.4
mAb 2	250 mM Imid(HCl) pH 5.5	2.5
mAb 2	250 mM Gdn.HCl	5.0
mAb 2	250 mM PheOMe.HCl(NaOH) pH 5.5	3.5
mAb 2	1000 mM Imid(HCl) pH 5.5	1.5
mAb 3	50 mM NaCl	8.0
mAb 3	250 mM NaCl	9.9
mAb 3	250 mM Lys.HCl	8.7
mAb 3	250 mM Imid(HCl) pH 5.5	10.1
mAb 3	250 mM Arg.HCl	3.1

Table 2.5. Average relative deviation (ARD) of S(0) fits to the single-Yukawa potential for fixed Z = 3 and variable K.

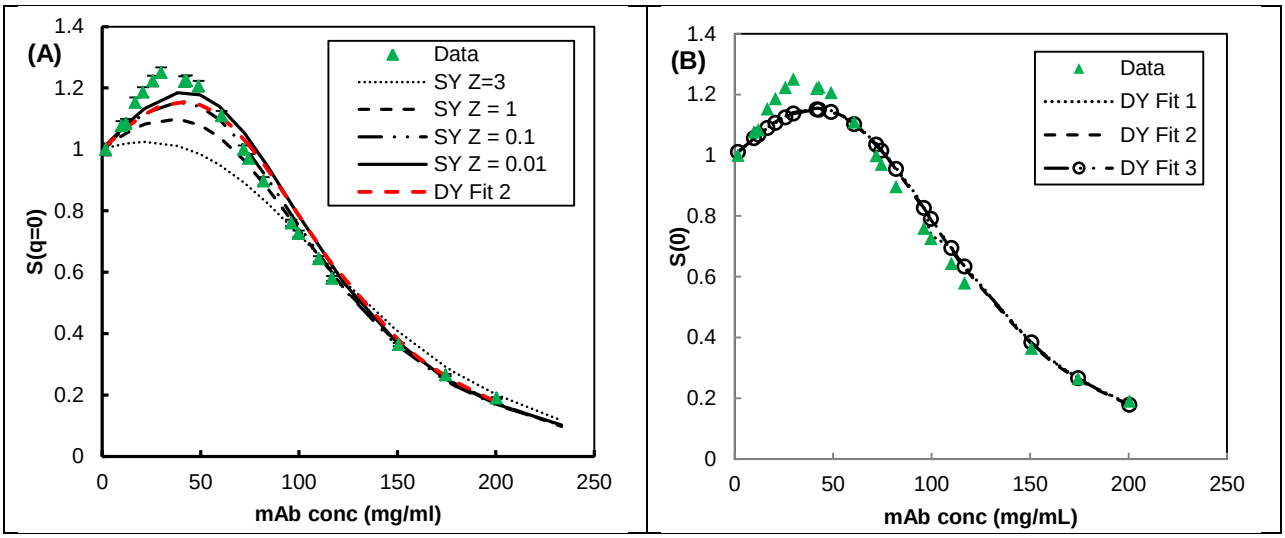

Figure 2.15. (A) Single-Yukawa ("SY") best fits of *S(0)* of mAb3 with 250 mM NaCl using different *Z*'s, compared against the double-attractive Yukawa ("DY") fit. (B) Convergent behavior of the best-fit double-Yukawa (DY) fits of *S(0)* of mAb3 with 250 mM NaCl for different fit parameter combinations (values shown along with ARDs in Table 2.6). The corresponding best-fit *K*'s are shown in the legend. A *Z* of 3 was used for mAb2 in Fig. 2.3a, and also for mAb3 in Fig. 2.3b for comparison against mAb2.

Fit	Model	K_1	Z_1	L_1 (nm)	K_2	Z_2	L_2 (nm)	ARD (%)
SY Z = 3	Single	0.801	3.00	3	---	---	---	9.9
SY Z = 1	Single	0.236	1.00	9	---	---	---	5.6
SY Z = 0.1	Single	0.022	0.10	90	---	---	---	4.6
SY Z = 0.01	Single	0.014	0.01	900	---	---	---	5.0
DY fit 1	Double	0.028	1.06	8.5	0.14	0.71	12.7	5.0
DY fit 2	Double	0.070	0.72	12.5	0.08	0.67	13.4	5.1
DY fit 3	Double	0.102	0.83	10.8	0.08	0.79	11.4	5.3

Table 2.6. Best-fit parameters and error (ARD) for mAb3 with 250 mM NaCl fit to the single-term Yukawa (SY) or the double-attractive term Yukawa (DY). The corresponding fits of *S(0)* are shown in Fig. 2.15. The best-fit values for the DY model are confounded, as shown in Fig. 2.16.

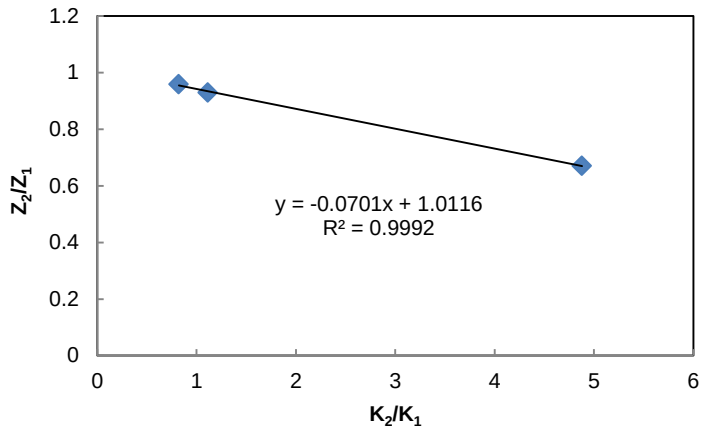

Figure 2.16. Confounded fits of K_1, K_2, Z_1 and Z_2 for the double Yukawa fits of *S(0)* for mAb3 with 250 mM NaCl (Table 2.6).

	"Oligomer" size		log(K_{1m})		log(K_{1n})		V_{ex} (mL/g)	
Formulation	**m**	**n**	**Avg**	**Std Error**	**Avg**	**Std Error**	**Avg**	**Std Error**
50 mM NaCl	2	3	2.12	+0.61 / ---	6.56	+0.1 / -0.09	1.59	+0.02 / -0.02
250 mM NaCl	2	4	3.11	+0.22 / -0.25	10.31	+0.21 / -0.18	1.68	+0.02 / -0.01
250 mM Lys.HCl	---	3	NA	NA	6.43	+0.08 / -0.07	1.65	+0.02 / -0.02
250 mM Arg.HCl	2	3	3.05	+0.04 / -0.04	3.67	+0.34 / -1.06	1.67	+0.02 / -0.02
250 mM Imid(HCl)	2	3	3.08	+0.12 / -0.13	6.55	+0.07 / -0.06	1.76	+0.01 / -0.01
250 mM Gdn.HCl	2	3	2.94	+0.11 / -0.14	6.17	+0.06 / -0.06	1.76	+0.01 / -0.01
250 mM PheOMe.HCl	2	---	2.74	+0.09 / -0.10	NA	NA	1.70	+0.02 / -0.02
1000 mM Imid(HCl)	2	---	2.44	+0.13 / -0.13	NA	NA	1.79	+0.04 / -0.04

Table 2.7. Best-fit parameters for mAb 2 light scattering data (1 – 225 mg/mL) fit to the IHS model with different co-solutes. The upper and lower standard errors of estimate for the fit parameters were evaluated for a P value of 0.5. A finite lower standard error could not be obtained for 50 mM NaCl and 250 mM Lys.HCl. The 1000 mM Imid(HCl) data was best fit by a monomer-dimer equilibrium (no third species).

	"Oligomer" size		$\log(K_{1m})$		$\log(K_{1n})$		V_{ex} (mL/g)	
Formulation	**m**	**n**	**Avg**	**Std Error**	**Avg**	**Std Error**	**Avg**	**Std Error**
50 mM NaCl	2	3	3.51	+0.39 / -0.51	7.44	+0.31 / -0.24	1.77	+0.03 / -0.03
250 mM NaCl	---	4	NA	NA	11.10	+0.12 / -0.12	1.77	+0.02 / -0.02
250 mM Lys	2	3	2.00	+1.1 / ---	7.18	+0.17 / -0.1	1.77	+0.03 / -0.02
250 mM Imid	2	3	2.71	+0.49 / ---	7.08	+0.17 / -0.13	1.89	+0.03 / -0.02
250 mM Arg	2	---	3.15	+0.09 / -0.08	NA	NA	1.73	+0.02 / -0.02

Table 2.8. Best-fit parameters for mAb 3 light scattering data (1 – 225 mg/mL) fit to the IHS model with different co-solutes. The upper and lower standard errors of estimate for the fit parameters were evaluated for a P value of 0.5. A finite lower standard error could not be obtained for 250 mM Lys.HCl and 250 mM Imid(HCl). The 250 mM NaCl data was best fit by a monomer-tetramer equilibrium, and the 250 mM Arg.HCl data by a monomer-dimer equilibrium (no third species).

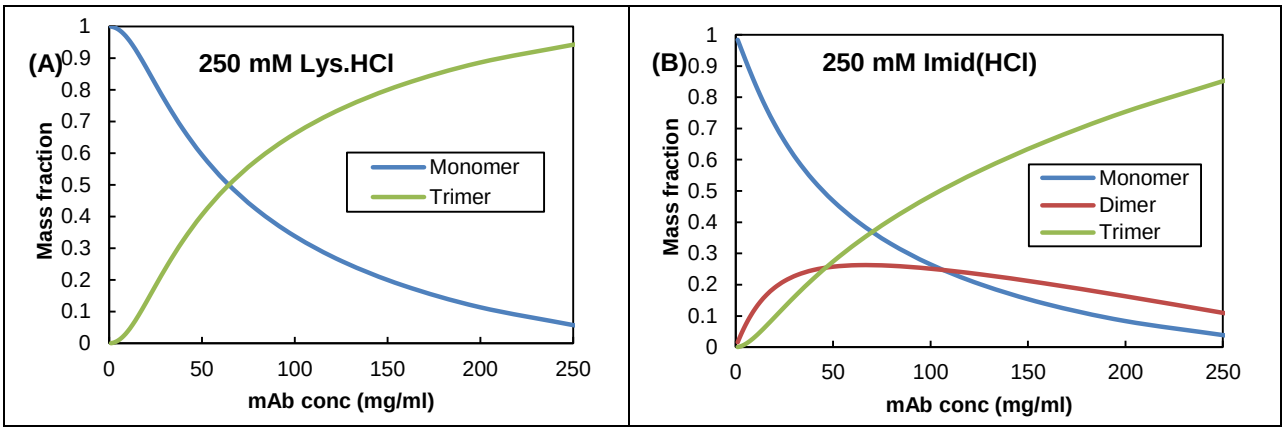

Figure 2.17. Mass fraction distribution of mAb 2 "oligomers" as a function of mAb concentration as calculated from the IHS best-fit association constants (Table 2.7) formulated with (A) 250 mM Lys.HCl and (B) 250 mM Imid(HCl).

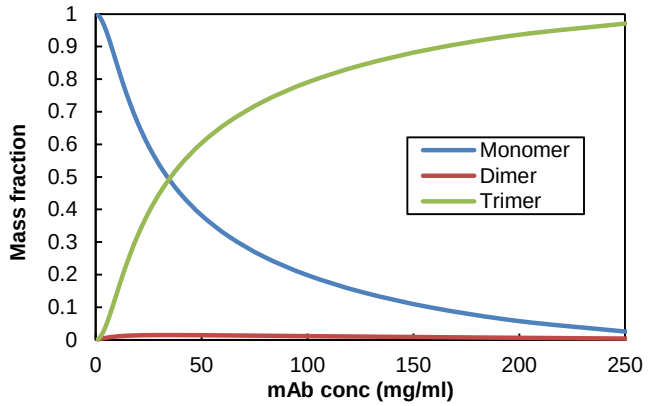

Figure 2.18. Mass fraction distribution of mAb 3 "oligomers" as a function of mAb concentration as calculated from the IHS best-fit association constants (Table 2.8) formulated with 250 mM Lys.HCl.

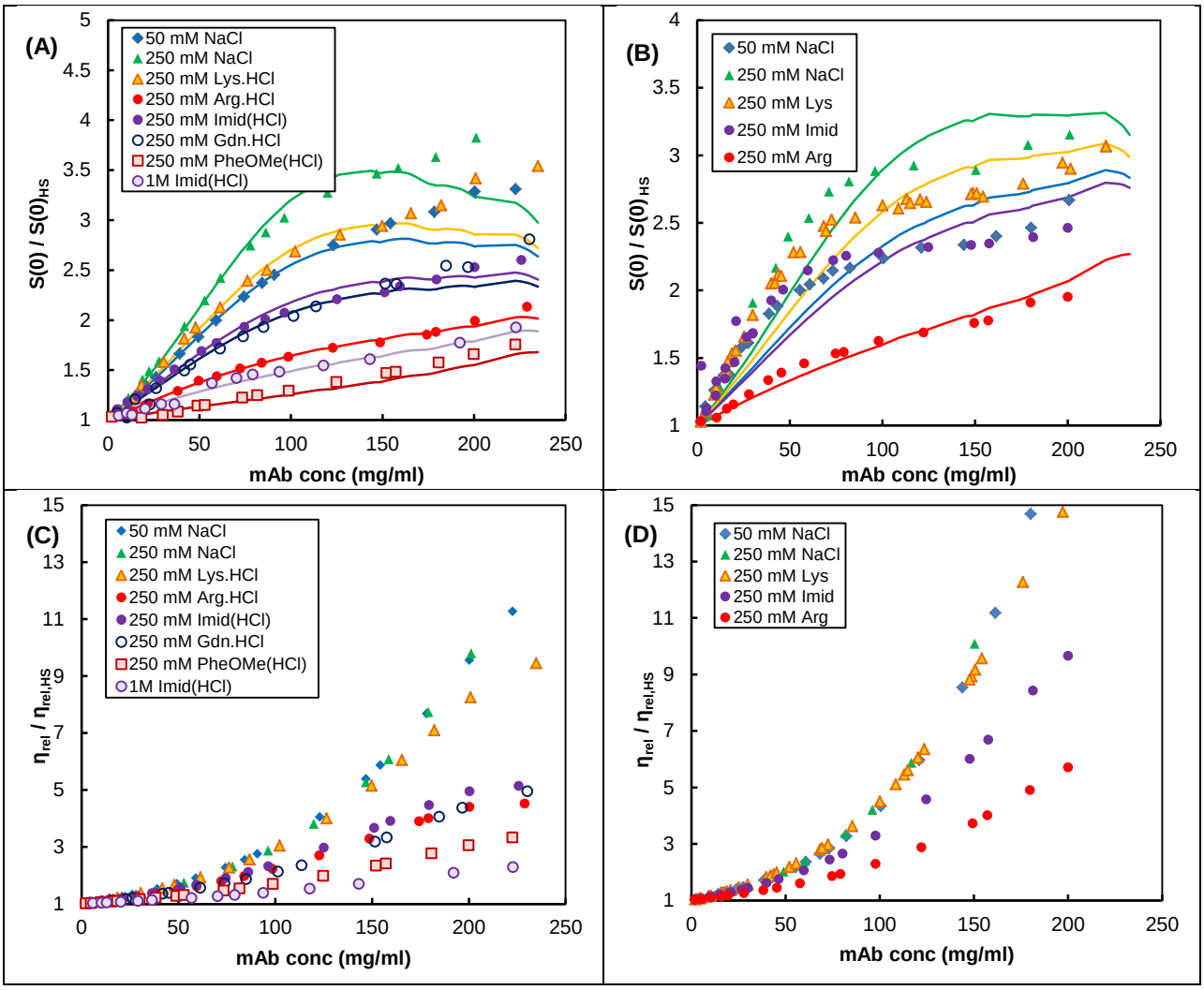

Figure 2.19. Concentration dependence of the (A, B) structure factor *S(0)* and (C, D) relative viscosity η_{rel} normalized against the hard sphere (HS) value for mAb2 (A, C) and mAb3 (B, D). Solid curves indicate fits of *S(0)* to the single-Yukawa interaction potential (Eqn. 2.3b) with a fixed Z = 3.

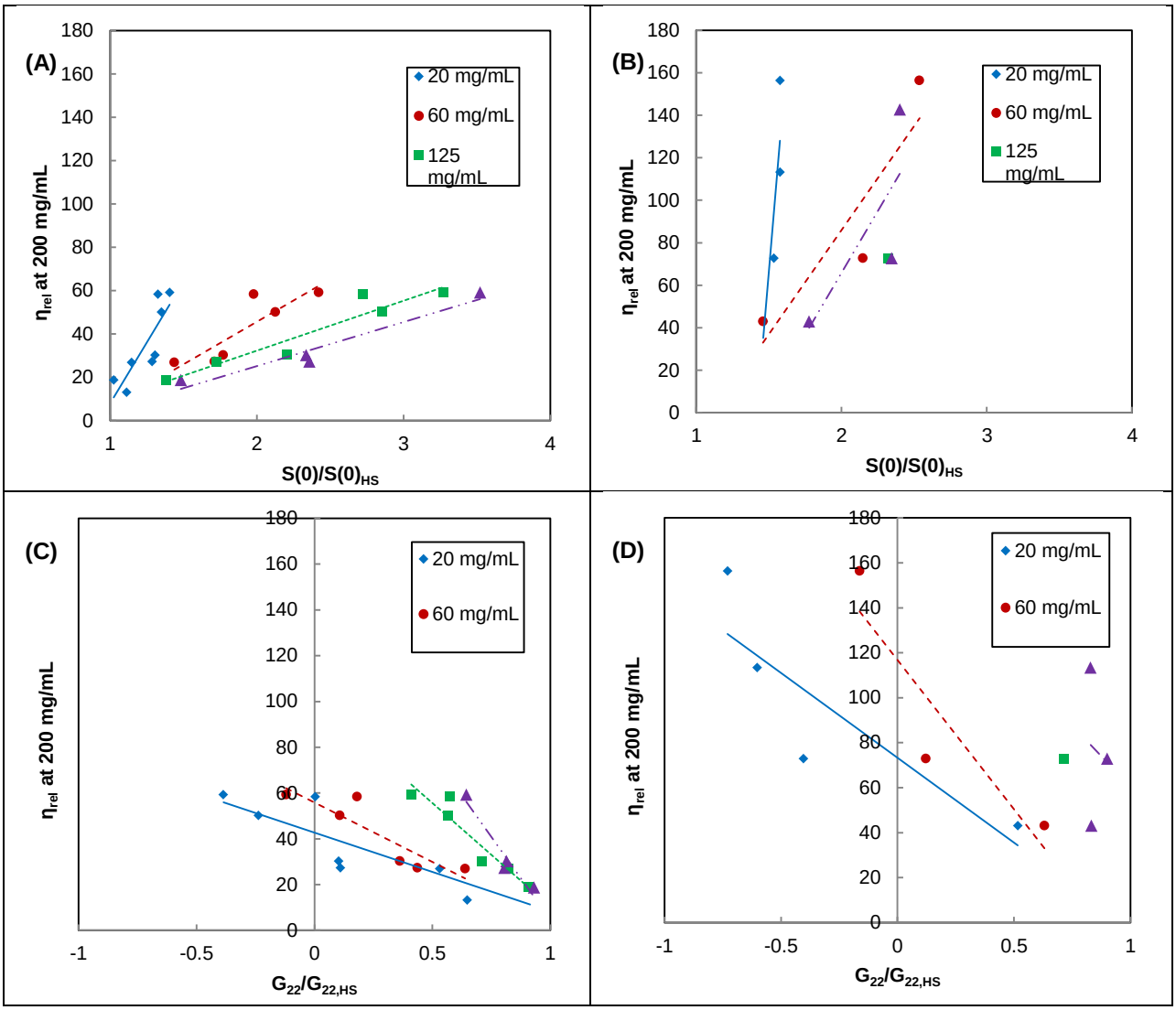

Figure 2.20. Concentration-dependent correlation of the viscosity at 200 mg/mL with $S(0)/S(0)_{HS}$ for (A) mAb2 and (B) mAb3, as well as with $G_{22}/G_{22,HS}$ for (C) mAb2 and (D) mAb3 evaluated at 20, 60, 125 and 160 mg/mL. The 50 mM NaCl data points for mAb3 were omitted from the correlation, as explained in the Results and Discussion section and following the analysis used for Fig. 2.6. The graphs are scaled identically between mAbs in order to aid visual comparison.

Fixed parameters/uncertainties		
Parameter	**Value**	**Source**
C_1	225 mg/mL	Methods
ρ_{buffer}	1010 mg/mL	Eqn. 2.17a + 2.17b
ρ_{ps}	1070 mg/mL	Eqn. 2.17a + 2.17b evaluated at 225 mg/mL with 250 mM Arg/Lys
σ_{C1}	3 mg/mL	~Mode of stdev of conc. measurements in Table 2.3
σ_{mp}	0.1 mg	Mettler Toledo NewClassic MS – Technical Specifications
Concentration-dependent values and uncertainties		
$\sigma_{Vbuffer}$	1.3 μL (low concentration; 20 – 200 μL pipet) 0.26 μL (high concentration; 2 – 20 μL pipet)	Eppendorf Research Plus adjustable volume – Technical Specifications
m_p	0.5 mg (low concentration) 90 mg (high concentration)	Methods
V_{buffer}	96 μL (low concentration) 10 μL (high concentration)	Methods (assuming basis of 100 μL samples in SLS dilution series)

Table 2.9. Known parameters values and uncertainties for calculating the propagated error in the calculated mAb concentration C_2 after gravimetric dilution.

2.8 REFERENCES

1. Shire SJ, Shahrokh Z, Liu J. Challenges in the Development of High Protein Concentration Formulations. J Pharm Sci. 2004;93(6):1390-402.
2. Amin S, Barnett GV, Pathak JA, Roberts CJ, Sarangapani PS. Protein aggregation, particle formation, characterization & rheology. Current Opinion in Colloid & Interface Science. 2014;19(5):438-49.
3. Roberts CJ. Therapeutic protein aggregation: mechanisms, design, and control. Trends in Biotechnology. 2014;32(7):372-80.
4. Roberts CJ. Protein aggregation and its impact on product quality. Current Opinion in Biotechnology. 2014;30:211-7.
5. Burckbuchler V, Mekhloufi G, Giteau AP, Grossiord JL, Huille S, Agnely F. Rheological and syringeability properties of highly concentrated human polyclonal immunoglobulin solutions. Eur J Pharm Biopharm. 2010;76(3):351-6.
6. Allmendinger A, Fischer S, Huwyler J, Mahler H-C, Schwarb E, Zarraga IE, et al. Rheological characterization and injection forces of concentrated protein formulations: An alternative predictive model for non-Newtonian solutions. Eur J Pharm Biopharm. 2014;87(2):318-28.

7. Hung JJ, Borwankar AU, Dear BJ, Truskett TM, Johnston KP. High concentration tangential flow ultrafiltration of stable monoclonal antibody solutions with low viscosities. J Membr Sci. 2016;508:113-26.
8. Baek Y, Singh N, Arunkumar A, Borys M, Li ZJ, Zydney AL. Ultrafiltration behavior of monoclonal antibodies and Fc-fusion proteins: Effects of physical properties. Biotechnol Bioeng. 2017;114(9):2057-65.
9. Yadav S, Laue TM, Kalonia DS, Singh SN, Shire SJ. The Influence of Charge Distribution on Self-Association and Viscosity Behavior of Monoclonal Antibody Solutions. Mol Pharmaceutics. 2012;9(4):791-802.
10. Roberts CJ, Blanco MA. Role of Anisotropic Interactions for Proteins and Patchy Nanoparticles. J Phys Chem B. 2014;118(44):12599-611.
11. Chari R, Jerath K, Badkar AV, Kalonia DS. Long- and Short-Range Electrostatic Interactions Affect the Rheology of Highly Concentrated Antibody Solutions. Pharm Res. 2009;26(12):2607-18.
12. Yadav S, Liu J, Shire SJ, Kalonia DS. Specific Interactions in High Concentration Antibody Solutions Resulting in High Viscosity. J Pharm Sci. 2010;99(3):1152-68.
13. Du W, Klibanov AM. Hydrophobic salts markedly diminish viscosity of concentrated protein solutions. Biotechnol Bioeng. 2011;108(3):632-6.
14. Guo Z, Chen A, Nassar R, Helk B, Mueller C, Tang Y, et al. Structure-Activity Relationship for Hydrophobic Salts as Viscosity-Lowering Excipients for Concentrated Solutions of Monoclonal Antibodies. Pharm Res. 2012;29(11):3102-9.
15. Li L, Kumar S, Buck P, Burns C, Lavoie J, Singh S, et al. Concentration Dependent Viscosity of Monoclonal Antibody Solutions: Explaining Experimental Behavior in Terms of Molecular Properties. Pharm Res. 2014;31(11):3161-78.
16. Chaudhri A, Zarraga IE, Yadav S, Patapoff TW, Shire SJ, Voth GA. The Role of Amino Acid Sequence in the Self-Association of Therapeutic Monoclonal Antibodies: Insights from Coarse-Grained Modeling. J Phys Chem B. 2013;117(5):1269-79.
17. Buck PM, Chaudhri A, Kumar S, Singh SK. Highly Viscous Antibody Solutions Are a Consequence of Network Formation Caused by Domain-Domain Electrostatic Complementarities: Insights from Coarse-Grained Simulations. Mol Pharmaceutics. 2015;12(1):127-39.
18. Godfrin PD, Zarraga IE, Zarzar J, Porcar L, Falus P, Wagner NJ, et al. Effect of Hierarchical Cluster Formation on the Viscosity of Concentrated Monoclonal Antibody Formulations Studied by Neutron Scattering. J Phys Chem B. 2016;120(2):278-91.
19. Lilyestrom WG, Yadav S, Shire SJ, Scherer TM. Monoclonal Antibody Self-Association, Cluster Formation, and Rheology at High Concentrations. J Phys Chem B. 2013;117(21):6373-84.
20. Yearley Eric J, Godfrin Paul D, Perevozchikova T, Zhang H, Falus P, Porcar L, et al. Observation of Small Cluster Formation in Concentrated Monoclonal Antibody Solutions and Its Implications to Solution Viscosity. Biophys J. 2014;106(8):1763-70.
21. Liu J, Nguyen MDH, Andya JD, Shire SJ. Reversible Self-Association Increases the Viscosity of a Concentrated Monoclonal Antibody in Aqueous Solution. J Pharm Sci. 2005;94(9):1928-40.

22. Scherer TM, Liu J, Shire SJ, Minton AI. Intermolecular Interactions of IgG1 Monoclonal Antibodies at High Concentrations Characterized by Light Scattering. J Phys Chem B. 2010;114(40):12948-57.

23. Schmit JD, He F, Mishra S, Ketchem RR, Woods CE, Kerwin BA. Entanglement Model of Antibody Viscosity. J Phys Chem B. 2014;118(19):5044-9.

24. Nichols P, Li L, Kumar S, Buck PM, Singh SK, Goswami S, et al. Rational design of viscosity reducing mutants of a monoclonal antibody: Hydrophobic versus electrostatic inter-molecular interactions. mAbs. 2015;7(1):212-30.

25. Chow C-K, Allan BW, Chai Q, Atwell S, Lu J. Therapeutic Antibody Engineering To Improve Viscosity and Phase Separation Guided by Crystal Structure. Mol Pharmaceutics. 2016;13(3):915-23.

26. Geoghegan JC, Fleming R, Damschroder M, Bishop SM, Sathish HA, Esfandiary R. Mitigation of reversible self-association and viscosity in a human IgG1 monoclonal antibody by rational, structure-guided Fv engineering. mAbs. 2016;8(5):941-50.

27. Kuhn AB, Kube S, Karow-Zwick AR, Seeliger D, Garidel P, Blech M, et al. Improved Solution-State Properties of Monoclonal Antibodies by Targeted Mutations. J Phys Chem B. 2017;121(48):10818-27.

28. Connolly Brian D, Petry C, Yadav S, Demeule B, Ciaccio N, Moore Jamie MR, et al. Weak Interactions Govern the Viscosity of Concentrated Antibody Solutions: High-Throughput Analysis Using the Diffusion Interaction Parameter. Biophys J. 2012;103(1):69-78.

29. Yadav S, Sreedhara A, Kanai S, Liu J, Lien S, Lowman H, et al. Establishing a Link Between Amino Acid Sequences and Self-Associating and Viscoelastic Behavior of Two Closely Related Monoclonal Antibodies. Pharm Res. 2011;28(7):1750-64.

30. Chaudhri A, Zarraga IE, Kamerzell TJ, Brandt JP, Patapoff TW, Shire SJ, et al. Coarse-Grained Modeling of the Self-Association of Therapeutic Monoclonal Antibodies. J Phys Chem B. 2012;116(28):8045-57.

31. Corbett D, Hebditch M, Keeling R, Ke P, Ekizoglou S, Sarangapani P, et al. Coarse-Grained Modeling of Antibodies from Small-Angle Scattering Profiles. J Phys Chem B. 2017;121(35):8276-90.

32. Kanai S, Liu J, Patapoff TW, Shire SJ. Reversible Self-Association of a Concentrated Monoclonal Antibody Solution Mediated by Fab-Fab Interaction That Impacts Solution Viscosity. J Pharm Sci. 2008;97(10):4219-27.

33. Wang S, Zhang N, Hu T, Dai W, Feng X, Zhang X, et al. Viscosity-Lowering Effect of Amino Acids and Salts on Highly Concentrated Solutions of Two IgG1 Monoclonal Antibodies. Mol Pharmaceutics. 2015;12(12):4478-87.

34. Dear BJ, Hung JJ, Truskett TM, Johnston KP. Contrasting the Influence of Cationic Amino Acids on the Viscosity and Stability of a Highly Concentrated Monoclonal Antibody. Pharm Res. 2017;34(1):193-207.

35. Borwankar AU, Dear BJ, Twu A, Hung JJ, Dinin AK, Wilson BK, et al. Viscosity Reduction of a Concentrated Monoclonal Antibody with Arginine·HCl and Arginine·Glutamate. Ind Eng Chem Res. 2016;55(43):11225-34.

36. Inoue N, Takai E, Arakawa T, Shiraki K. Specific Decrease in Solution Viscosity of Antibodies by Arginine for Therapeutic Formulations. Mol Pharmaceutics. 2014;11(6):1889-96.

37. Binabaji E, Ma J, Zydney A. Intermolecular Interactions and the Viscosity of Highly Concentrated Monoclonal Antibody Solutions. Pharm Res. 2015;32(9):3102-9.

38. Whitaker N, Xiong J, Pace SE, Kumar V, Middaugh CR, Joshi SB, et al. A Formulation Development Approach to Identify and Select Stable Ultra–High-Concentration Monoclonal Antibody Formulations With Reduced Viscosities. J Pharm Sci. 2017;106(11):3230-41.

39. Fukuda M, Moriyama C, Yamazaki T, Imaeda Y, Koga A. Quantitative Correlation between Viscosity of Concentrated MAb Solutions and Particle Size Parameters Obtained from Small-Angle X-ray Scattering. Pharm Res. 2015;32(12):3803-12.

40. Larson AM, Weight AK, Love K, Bonificio A, Wescott CR, Klibanov AM. Bulky Polar Additives That Greatly Reduce the Viscosity of Concentrated Solutions of Therapeutic Monoclonal Antibodies. J Pharm Sci. 2017;106(5):1211-7.

41. Yadav S, Shire SJ, Kalonia DS. Factors Affecting the Viscosity in High Concentration Solutions of Different Monoclonal Antibodies. J Pharm Sci. 2010;99(12):4812-29.

42. Yadav S, Shire SJ, Kalonia DS. Viscosity behavior of high-concentration monoclonal antibody solutions: Correlation with interaction parameter and electroviscous effects. J Pharm Sci. 2012;101(3):998-1011.

43. Yadav S, Scherer TM, Shire SJ, Kalonia DS. Use of dynamic light scattering to determine second virial coefficient in a semidilute concentration regime. Analytical biochemistry. 2011;411(2):292-6.

44. Lilyestrom WG, Shire SJ, Scherer TM. Influence of the Cosolute Environment on IgG Solution Structure Analyzed by Small-Angle X-ray Scattering. J Phys Chem B. 2012;116(32):9611-8.

45. Yearley EJ, Zarraga IE, Shire SJ, Scherer TM, Gokarn Y, Wagner NJ, et al. Small-Angle Neutron Scattering Characterization of Monoclonal Antibody Conformations and Interactions at High Concentrations. Biophys J. 2013;105(3):720-31.

46. Zarraga IE, Taing R, Zarzar J, Luoma J, Hsiung J, Patel A, et al. High shear rheology and anisotropy in concentrated solutions of monoclonal antibodies. J Pharm Sci. 2013;102(8):2538-49.

47. Fukuda M, Watanabe A, Hayasaka A, Muraoka M, Hori Y, Yamazaki T, et al. Small-scale screening method for low-viscosity antibody solutions using small-angle X-ray scattering. Eur J Pharm Biopharm. 2017;112:132-7.

48. Minton AP. Recent applications of light scattering measurement in the biological and biopharmaceutical sciences. Analytical biochemistry. 2016;501:4-22.

49. Ghosh R, Calero-Rubio C, Saluja A, Roberts CJ. Relating protein-protein interactions and aggregation rates from low to high concentrations. J Pharm Sci. 2016;105(3):1086-96.

50. Calero-Rubio C, Ghosh R, Saluja A, Roberts CJ. Predicting protein-protein interactions of concentrated antibody solutions using dilute solution data and coarse-grained molecular models. J Pharm Sci. 2017.

51. Scherer TM. Role of Cosolute–Protein Interactions in the Dissociation of Monoclonal Antibody Clusters. J Phys Chem B. 2015;119(41):13027-38.

52. Fernandez C, Minton AP. Automated measurement of the static light scattering of macromolecular solutions over a broad range of concentrations. Analytical biochemistry. 2008;381(2):254-7.
53. Esfandiary R, Parupudi A, Casas-Finet J, Gadre D, Sathish H. Mechanism of Reversible Self-Association of a Monoclonal Antibody: Role of Electrostatic and Hydrophobic Interactions. J Pharm Sci. 2015;104(2):577-86.
54. Arora J, Hu Y, Esfandiary R, Sathish HA, Bishop SM, Joshi SB, et al. Charge-mediated Fab-Fc interactions in an IgG1 antibody induce reversible self-association, cluster formation, and elevated viscosity. mAbs. 2016;8(8):1561-74.
55. Some D, Pollastrini J, Cao S. Characterizing Reversible Protein Association at Moderately High Concentration Via Composition-Gradient Static Light Scattering. J Pharm Sci. 2016;105(8):2310-8.
56. Blanco MA, Sahin E, Li Y, Roberts CJ. Reexamining protein–protein and protein–solvent interactions from Kirkwood-Buff analysis of light scattering in multi-component solutions. The Journal of Chemical Physics. 2011;134(22):225103.
57. Woldeyes MA, Calero-Rubio C, Furst EM, Roberts CJ. Predicting Protein Interactions of Concentrated Globular Protein Solutions Using Colloidal Models. J Phys Chem B. 2017;121(18):4756-67.
58. Bucciarelli S, Casal-Dujat L, De Michele C, Sciortino F, Dhont J, Bergenholtz J, et al. Unusual Dynamics of Concentration Fluctuations in Solutions of Weakly Attractive Globular Proteins. J Phys Chem Lett. 2015;6(22):4470-4.
59. Inouye H, Houde D, Temel DB, Makowski L. Utility of Solution X-ray Scattering for the Development of Antibody Biopharmaceuticals. J Pharm Sci. 2016.
60. Mosbaek CR, Konarev PV, Svergun DI, Rischel C, Vestergaard B. High Concentration Formulation Studies of an IgG2 Antibody Using Small Angle X-ray Scattering. Pharm Res. 2012;29(8):2225-35.
61. Scherer TM. Cosolute Effects on the Chemical Potential and Interactions of an IgG1 Monoclonal Antibody at High Concentrations. J Phys Chem B. 2013;117(8):2254-66.
62. Hoppe T, Minton AP. Incorporation of hard and soft protein-protein interactions into models for crowding effects in binary and ternary protein mixtures: Comparison of approximate analytical solutions with numerical simulation. J Phys Chem B. 2016;120(46):11866-72.
63. Fine BM, Lomakin A, Ogun OO, Benedek GB. Static structure factor and collective diffusion of globular proteins in concentrated aqueous solution. The Journal of Chemical Physics. 1996;104(1):326-35.
64. Calero-Rubio C, Saluja A, Roberts CJ. Coarse-Grained Antibody Models for "Weak" Protein-Protein Interactions from Low to High Concentrations. J Phys Chem B. 2016;120(27):6592-605.
65. Blanco MA, Perevozchikova T, Martorana V, Manno M, Roberts CJ. Protein–Protein Interactions in Dilute to Concentrated Solutions: α-Chymotrypsinogen in Acidic Conditions. J Phys Chem B. 2014;118(22):5817-31.
66. Minton AP. Static Light Scattering from Concentrated Protein Solutions, I: General Theory for Protein Mixtures and Application to Self-Associating Proteins. Biophys J. 2007;93(4):1321-8.

67. Wang W, Lilyestrom WG, Hu ZY, Scherer TM. Cluster Size and Quinary Structure Determine the Rheological Effects of Antibody Self-Association at High Concentrations. J Phys Chem B. 2018;122(7):2138-54.

68. Heyda J, Mason PE, Jungwirth P. Attractive Interactions between Side Chains of Histidine-Histidine and Histidine-Arginine-Based Cationic Dipeptides in Water. J Phys Chem B. 2010;114(26):8744-9.

69. Vondrášek J, Mason PE, Heyda J, Collins KD, Jungwirth P. The Molecular Origin of Like-Charge Arginine−Arginine Pairing in Water. J Phys Chem B. 2009;113(27):9041-5.

70. Du Q-S, Meng J-Z, Liao S-M, Huang R-B. Energies and physicochemical properties of cation–π interactions in biological structures. J Mol Graphics Modell. 2012;34:38-45.

71. Liao SM, Du QS, Meng JZ, Pang ZW, Huang RB. The multiple roles of histidine in protein interactions. Chem Cent J. 2013;7.

72. Shukla D, Trout BL. Interaction of Arginine with Proteins and the Mechanism by Which It Inhibits Aggregation. J Phys Chem B. 2010;114(42):13426-38.

73. Shukla D, Schneider CP, Trout BL. Molecular level insight into intra-solvent interaction effects on protein stability and aggregation. Adv Drug Deliv Rev. 2011;63(13):1074-85.

74. Ito L, Shiraki K, Matsuura T, Okumura M, Hasegawa K, Baba S, et al. High-resolution X-ray analysis reveals binding of arginine to aromatic residues of lysozyme surface: implication of suppression of protein aggregation by arginine. Protein Engineering Design and Selection. 2011;24(3):269-74.

75. Heimenz PC, Rajagopalan R. Principles of Colloid and Surface Chemistry. 3rd ed. New York: Marcel Dekker, Inc.; 1997.

76. McQuarrie D. Statistical Mechanics: University Science Books; 2000.

77. Tanford C. The physical chemistry of macromolecules. New York: John Wiley & Sons; 1961.

78. Banchio AJ, Nägele G. Short-time transport properties in dense suspensions: From neutral to charge-stabilized colloidal spheres. The Journal of Chemical Physics. 2008;128(10):104903.

79. Esfandiary R, Hayes DB, Parupudi A, Casas-finet J, Bai S, Samra HS, et al. A Systematic Multitechnique Approach for Detection and Characterization of Reversible Self-Association during Formulation Development of Therapeutic Antibodies. J Pharm Sci. 2013;102(1):62-72.

80. Castellanos MM, Clark NJ, Watson MC, Krueger S, McAuley A, Curtis JE. Role of Molecular Flexibility and Colloidal Descriptions of Proteins in Crowded Environments from Small-Angle Scattering. J Phys Chem B. 2016;120(49):12511-8.

81. Blanco MA, Sahin E, Robinson AS, Roberts CJ. Coarse-Grained Model for Colloidal Protein Interactions, B-22, and Protein Cluster Formation. J Phys Chem B. 2013;117(50):16013-28.

82. Inoue N, Takai E, Arakawa T, Shiraki K. Arginine and lysine reduce the high viscosity of serum albumin solutions for pharmaceutical injection. J Biosci Bioeng. 2014;117(5):539-43.

83. Arakawa T, Ejima D, Tsumoto K, Obeyama N, Tanaka Y, Kita Y, et al. Suppression of protein interactions by arginine: A proposed mechanism of the arginine effects. Biophys Chem. 2007;127(1–2):1-8.

84. Kastelic M, Dill KA, Kalyuzhnyi YV, Vlachy V. Controlling the viscosities of antibody solutions through control of their binding sites. Journal of Molecular Liquids. 2017.

85. Pecora R. Dynamic Light Scattering: Applications of Photon Correlation Spectroscopy. New York: Springer 1985.

86. Myers HP. Introductory solid state physics. 2 ed. Boca Raton, FL: CRC Press; 1997.

87. ASTRA 6 User's Guide. Santa Barbara, CA: Wyatt Technology Corporation; 2015.

88. Sun Y, Li X, Düzgüneşv N, Takaoka Y, Ohi S, Hirota S. The Shape Parameter of Liposomes and DNA-Lipid Complexes Determined by Viscometry Utilizing Small Sample Volumes. Biophys J. 2003;85(2):1223-32.

89. Torquato S, Truskett TM, Debenedetti PG. Is Random Close Packing of Spheres Well Defined? Phys Rev Lett. 2000;84(10):2064-7.

90. Grünberger A, Lai P-K, Blanco MA, Roberts CJ. Coarse-Grained Modeling of Protein Second Osmotic Virial Coefficients: Sterics and Short-Ranged Attractions. J Phys Chem B. 2013;117(3):763-70.

Chapter 3: Protein-protein interactions and length-scale dependent viscosities assessed by the self-diffusion of highly concentrated monoclonal antibodies via fluorescence correlation spectroscopy[2]

Jessica J. Hung, Amjad Chowdhury, Barton J. Dear, Wade F. Zeno, Kishan Ramachandran, Maria P. Nieto, Tony Y. Shay, Carl Karouta, Thomas M. Truskett, Jeanne C. Stachowiak, Keith P. Johnston

3.1 ABSTRACT

The dynamic behavior of mAbs at high concentration plays a crucial role in protein processing and delivery, and provides insight into the length scales of protein microstructure and protein interactions (PPI) that influence the overall solution viscosity and protein stability. Measurements of the collective-diffusion coefficient D_c at high concentration by DLS are routine, but interpretation is complicated due to the dependence on steric effects, hydrodynamic interactions, and the osmotic compressibility. Self-diffusion is simpler to understand but more difficult to measure given the need to quantify the dynamics of a single molecule in a crowded solution. High concentration studies of mAb self-diffusion are currently limited to challenging techniques such as neutron spin echo or pulsed-field gradient NMR. Herein, we demonstrate the suitability of the simpler fluorescence correlation spectroscopy (FCS) technique, after method optimization, for measuring the self-diffusion of mAb2, which has previously been studied by SLS and SAXS, from low to high concentration (60 – 250 mg/mL) across a range of co-solute formulations with varying viscosities (ex. 10 cP to 100 cP at 200 mg/mL). The self-diffusion D_0/D_s was found to deviate from the generalized Stokes-Einstein (GSE) relation with respect to the macroscopic viscosity. Given that the probe (labeled mAb) was the same size as the

[2] The first-author was responsible for the design and execution of all of the FCS experiments and the preparation of ~50% of the mAb samples, but was assisted in the preparation of the dry-passivated slides and the other ~50% of the mAb samples by the co-authors. The first-author directly supervised the preparation of samples that were made by the co-authors. The first-author was also responsible for all method development activities, the majority of data analysis, and all of the data interpretation, intellectual development and writing of the manuscript. The first-author received assistance from the co-authors to write and execute code to facilitate the fitting of large quantities of raw data, and also had intellectual discussion with the co-authors that contributed to the GDM portion of this work.

crowding agent (unlabeled mAb), D_0/D_s was fit to a length-scale dependent viscosity (LDV) model to partially decouple the effects of structure, hydrodynamic interactions and PPI on the diffusion. The lowest-viscosity formulations had the weakest attraction based on the interaction parameter b extracted from fits of D_0/D_s, in agreement with measurements of PPI by SLS and SAXS for the same mAb. In contrast, the polydispersity of the solution as measured by FCS appeared to be decoupled from the viscosity, despite known differences in the mAb's self-association behavior between formulations as assessed by SLS and SAXS. The apparent decoupling was hypothesized to be caused by the long time scale of the FCS measurements relative to the fast equilibrium exchange of the labeled mAb between monomer and oligomers.

3.2 INTRODUCTION

The dynamic behavior of proteins in highly concentrated solutions have significant implications for the stability and viscosity of protein drug products, especially for monoclonal antibody (mAb) solutions that are increasingly frequently formulated at high concentrations (100 – 300+ mg/mL) for subcutaneous delivery. At such high concentrations, reversible self-association of proteins may lead to irreversible and/or non-native aggregation (1, 2) that may raise concerns of safety and efficacy (3), as well as high solution viscosities that pose challenges for manufacturing (4-6) and drug delivery (7-9). There is extensive growing evidence for the strong correlation between reversible self-association and high viscosities, as seen from simulations (10-14), light scattering (15-18) and rheological models (19). Self-association is in turn driven by short-ranged attractive protein-protein interactions (PPI) (2, 17, 18, 20-25), which include anisotropic electrostatic attraction (26-28), hydrophobic attraction (29-31), Van der Waals dispersion forces and hydrogen bonds (32, 33). These attractive PPI can be tuned using co-solutes in order to modify the viscosity (18, 34-38) and stability (16, 17, 34, 39-44), for which hydrophobic and/or organic acids and bases such as arginine, histidine and camphorsulfonic acid

have received increasing attention for their greater efficacy relative to more conventional salts such as NaCl (23, 29, 30, 41, 44-49).

There is a growing understanding of how these diverse co-solutes influence the viscosity of highly concentrated mAbs through their effects on the mAb microstructure and PPI, using techniques that probe the static protein structure such as small-angle X-ray scattering (SAXS), small-angle neutron scattering (SANS) and static light scattering (SLS). Through a combination of simulations with measurements of protein structure, high viscosities were linked to the formation of extended or rigid dimers and oligomers that occupy large volumes (14-18, 50). The formation of viscosity-raising oligomeric microstructures were correlated with strong attractive PPI as quantified by the static structure factors S(q) and S(0) from SAXS/SANS and SLS respectively (24, 25, 41, 47, 48, 51).

While the influence of the protein static structure on the solution viscosity has been extensively studied using SAXS/SANS and SLS, there is less understanding of how the PPI affects the solution viscosity and protein stability through its influence on the protein dynamic behavior. Protein transport through the solution medium, as quantified by the diffusion rate, plays a critical role in determining the performance of common manufacturing processes such as membrane filtration via mechanisms such as back-diffusion and concentration polarization (4-6, 52). The diffusion coefficient also reports on the effective viscosity experienced by the diffusing probe, as seen by the generalized Stokes-Einstein equation ($D_s = k_BT/(6\pi\eta R)$) (53), and has also been correlated in one study with the critical shear rate of a shear-thinning concentrated lysozyme solution (54). Thus the diffusion rate may provide insight into the relevant length scales of PPI and structure that influence the mAb solution viscosity.

The diffusion coefficients of mAbs from low to high concentration are routinely measured by dynamic light scattering (DLS) in order to quantify the dilute PPI using the diffusion interaction parameter k_D (22, 27, 28, 34, 36, 44, 55, 56), as well as to attempt to

quantify the PPI and protein stability and structure at high concentration (37, 54, 57-59). Given that DLS measures the concentration gradient fluctuations of the ensemble average of the protein molecules rather than of intensity fluctuations from individual particles, the diffusion coefficient measured by this technique at higher concentrations is the collective diffusion coefficient Dc. Interpretation of D_c is challenging, as D_c is influenced both by the osmotic compressibility of the protein in a given formulation condition (58, 60, 61), as well as by concentration gradient fluctuations of both the protein and dissolved co-solutes/counterions (56). In contrast, the mechanism of self-diffusion (coefficient = D_s) is much simpler to understand, as it depends mainly on steric interactions (crowding/occupied volume) and to a lesser extent hydrodynamic interactions (62-66). As such, one of the long-term objectives of this study is to use the mAb self-diffusion behavior to better understand the collective diffusion behavior, especially at high concentration.

A common application for measuring particle diffusion rates in protein solutions is microrheology, where the effective solution viscosity is measured indirectly through application of the generalized Stokes-Einstein (GSE) relation to the measured diffusion of a probe molecule in the protein solution. In conventional microrheology done using DLS, the probes of interest are typically large polymer beads such as polystyrene on the order of 0.1 – 1 μm (59, 67-69), which are much larger than both the solvent and protein, and therefore sample (and report on) the macroscopic solution viscosity (53). However, there is considerable evidence in the literature for the apparent breakdown of the GSE relation for nanoprobes (dyes, proteins, etc. on the order of 1 – 10 nm) diffusing in polymer solutions or complex media (53, 59, 70, 71). This breakdown was attributed to the nanoprobe experiencing a length-scale dependent local microviscosity rather than the macroscopic viscosity, due to the small size of the probe relative to the polymer matrix and/or colloidal crowder molecules that constitute the fluid the probe diffuses through (53, 71-74). In this framework, dubbed the “length-scale dependent viscosity (LDV) model” by Holyst

and co-workers (53, 73), the GSE relation is seen to hold for the diffusion of probes of all length scales, but with respect to the length-scale dependent microviscosity rather than the macroviscosity. The GSE relation then becomes

$$\frac{D_0}{D_s} = \frac{\eta_{eff}}{\eta_0} \tag{3.1a}$$

where D_0 is the self-diffusion coefficient of the probe at infinite dilution, D_s is the measured self-diffusion coefficient at finite concentration, η_0 is the solvent viscosity and η_{eff} is the effective local microviscosity, which is a function of both the probe and crowder/solvent matrix sizes. Therefore, for measurements of mAb self-diffusion in concentrated mAb solutions, several questions must be answered to obtain a meaningful interpretation of the diffusion behavior, especially in systems with known or suspected self-association: (i) what is the probe that is being measured? Is it monomeric or oligomeric? Does the probe size change over time due to equilibrium exchange between monomer and oligomer? (ii) What is the probe diffusing through? Does it experience the solvent viscosity, the macroscopic viscosity, or an intermediate viscosity? Both the probe size and effective local microviscosity will affect the diffusion retardation D_0/D_s independent of other effects (crowding, PPI, etc.), so care must be taken to account for the length-scale effects on D_s in the interpretation of the mAb diffusion behavior.

The local microviscosity and diffusion D_0/D_s are also both further perturbed by the PPI, as seen from significant differences in the GSE scaling (coupling/decoupling of the macroscopic viscosity and self-diffusion) observed with FCS and NMR using nanoprobes for proteins that range in PPI profiles from hard sphere-like (α-crystallin) to strongly anisotropic and attractive (lysozyme, mAbs) (43, 72, 75). The effective viscosity was found to follow an Arrhenius-like scaling law (76), such that the effective viscosity retardation factor η_{eff}/η_0 (and by extension, the diffusion retardation factor D_0/D_s) is related to an 'activation energy' E_a for viscous flow (72, 73) or alternatively for diffusion (76).

$$\frac{D_0}{D_s} = \frac{\eta_{eff}}{\eta} = \exp\left(\frac{E_a}{RT}\right) \tag{3.1b}$$

The activation energy for flow is a function of the interparticle interactions and structural/ hydrodynamic screening effects (72, 73, 76),

$$\frac{E_a}{RT} = b * \left(\frac{R_{eff}}{\xi}\right)^a = \frac{\gamma}{RT} * \left(\frac{R_{eff}}{\xi}\right)^a \tag{3.2}$$

where R_{eff} is an effective hydrodynamic radius that accounts for the relative sizes of the diffusion probe r_p to the particles/polymer chains that constitute the diffusion medium R_h (R_{eff}=((r_p^2 *R_h^2)/((r_p^2+R_h^2)))^0.5) (73), and ξ is the screening length for hydrodynamic interactions and is related to the solution network structure (71).

$$\xi = R_g \left(\frac{\psi}{\psi_{rcp}}\right)^{-1} \tag{3.3a}$$

$$\psi = \frac{\Phi}{1-\Phi} \quad and \; \psi_{rcp} = \frac{\Phi_{rcp}}{1-\Phi_{rcp}} \tag{3.3b}$$

ξ is also considered the characteristic length scale of flow and is a function of the protein radius of gyration R_g, the protein volume fraction φ, the maximum volume fraction in random close packing (φ_{rcp} = 0.638) (72). The physical meaning of a is still not well-understood (72, 76, 77), but was found to be < 1 for entangled polymer systems and ~1.29 for hard sphere-like systems (71, 72). The parameter b (b = γ/RT) is related to the interparticle interaction strength (72, 76). Thus the influence of the PPI on D_0/D_s can be partially decoupled from the effects of hydrodynamic effects and structural confinement (the length-scale effects) via the LDV model. This influence of the PPI on D_0/D_s was also observed directly by NSE, where the relative diffusion of a protein with known patchy attraction (γ_B-crystallin) exhibited a drastic slowdown compared to its hard sphere-like complement (α-crystallin) (78). Similarly, noticeable differences in the PPI parameter b based on fits of D_0/D_s from FCS were seen for different model

proteins with known differences in the magnitude and anisotropy of their attractive PPI (72). Beyond local microviscosity and PPI effects, the mAb diffusion may also be influenced by shape or steric effects (79) as well as hydrodynamic interactions (65, 80). However, all four of these factors are confounded to some degree, and work is ongoing to better separate and understand their individual influences on self-diffusion.

Investigation of the effects of the length-scale dependent viscosity on the self-diffusion of proteins in relation to PPI at high concentration has until recently been mostly limited to globular proteins such as bovine serum albumin (BSA) (75, 81-83), lysozyme (75, 81, 84), and α (78, 81) and γ-crystallin (78). Furthermore, among the limited studies available for mAbs using techniques such as neutron spin echo (NSE) and neutron back scatter (NBS) (85, 86), pulsed-field gradient nuclear magnetic resonance spectroscopy (PFG-NMR) (43), and fluorescence correlation spectroscopy (FCS) (79), only one study attempted to address the influence of co-solutes (arginine glutamate) on the PPI, viscosity and stability of highly concentrated mAbs through their effects on the mAb translational and rotational self-diffusion (43). It would therefore be of great interest to investigate how viscosity-reducing co-solutes modify the mAb self-diffusion and length-scale dependent microviscosities to complement the growing understanding of co-solute effects on the bulk mAb solution properties from a static structure perspective.

Among the techniques available for measuring protein self-diffusion, FCS offers great ease of access and reduced complexity compared to NSE/NBS and NMR. FCS is a single-molecule technique that tracks the fluctuations in fluorescence intensity originating from fluorescently labeled mAb molecules (present at ultradilute concentrations of ~1 nM) diffusing in a concentrated solution of unlabeled mAb molecules, allowing for direct measurement of mAb self-diffusion even at high concentration (87, 88). This technique is commonly used to measure protein diffusion in crowded medium such as cell cytoplasm (89, 90) as well as on cell

membranes (91-93) to investigate the driving forces for many biological processes. FCS is more experimentally accessible than NSE and NBS, but measures diffusion on much longer time scales (> 100 μs for FCS, compared to < 600 ps for NSE/NBS) (78, 81, 82), and so provides information on structure and PPI on longer length scales than NSE/NBS. PFG-NMR is more comparable to FCS in that it also measures long-time diffusion (81), but interpretation of NMR traces is difficult for mAbs given the complexities of the relaxational processes for high MW proteins (43). As such, FCS was chosen for the high concentration measurements of mAb self-diffusion in this study. To our knowledge, only one other study has used FCS to probe the high concentration dynamics of mAbs (79), but did not attempt to investigate the influence of co-solutes or relate the diffusion to viscosity. One of the objectives of this study was therefore to extend FCS to systematically investigate the dynamic behavior of mAbs at high concentration in the presence of PPI modifying co-solutes.

To facilitate high concentration measurements of mAb diffusion by FCS, several experimental and analytical challenges associated with highly concentrated and viscous protein solutions must be addressed to ensure accurate, reproducible measurements. To prevent protein adsorption on the imaging surface (cover slip, etc.), which leads to inaccurate measurements of the correlation function decay time (and therefore incorrect measurements of D_s), the imaging surface is typically passivated to resist protein adsorption. A common passivation technique is the adsorption of a thin vesicle layer on the glass cover slip (93, 94). The resulting thin liquid film in the imaging well creates some difficulties, as the concentrated, viscous mAb sample has to be mixed with the liquid film to ensure a homogenous sample inside the imaging well for reproducible measurements. However, mixing two liquids with greatly differing viscosities inside a confined space is difficult, and a poorly mixed sample will result in non-ergodicity and irreproducible measurements. As an alternative to this liquid-based passivation technique, the imaging surface can also be passivated with a dry protein-resistant film (95-97), bypassing the

need to mix the mAb sample during loading. Furthermore, due to the non-negligible change in the solution refractive index across the range of co-solutes and mAb concentrations investigated (60 – 250 mg/mL), possible artifacts in the data resulting from potential distortion of the confocal molecular detection function (MDF) or confocal volume (98-102) have to be addressed. Finally an appropriate form of the autocorrelation function (ACF) must be chosen for interpreting the FCS data. Given the likely presence of oligomers and polydispersity, two 3D diffusion models were chosen to account for the polydispersity of the probe diffusion coefficient: (i) the anomalous diffusion model (73, 103), which captures the polydispersity with an anomaly coefficient α, and (ii) the Gaussian distribution model (GDM) (104, 105), which directly fits a polydispersity index from the variance of the fitted Gaussian distribution.

The objectives of this study were (1) to develop FCS methodologies further to address the technical challenges mentioned earlier in order to extend FCS to mAbs at high concentration and viscosity; (2) advance our understanding of what information is obtained from FCS with respect to the identity of the probe (given the reversible self-association) as well as the length scale of the structure and viscosity experienced by the probe; and (3) relate the long time self-diffusion retardation factor D_0/D_s and polydispersity measured by FCS to the macroscopic viscosity of a given mAb, mAb2 (24, 25), in order to quantify the co-solute effects on the self-association behavior and the PPI via the b parameter from the LDV model for mAb2. The available knowledge on mAb2's macroscopic viscosity, PPI (quantified by the structure factor S(0) and short-range attraction strength K) and self-association behavior (quantified by the cluster size distribution and oligomerization profile) from previous SLS (24) and SAXS (25) studies with the same co-solute formulations will also be used to guide understanding of the self-diffusion behavior and length-scale dependent viscosity measured by FCS. This study will also attempt to contribute to the ongoing developing understanding of how length-scale dependent structure, viscosity and PPI influence protein self-diffusion at high concentration.

3.3 MATERIALS AND METHODS

3.3.1 Materials

The IgG1 monoclonal antibody used in this study, mAb2, was provided by Merck at 25 mg/mL (pH 5.5) and is the same mAb described previously (24, 25). Glacial acetic acid, L-arginine hydrochloride (Arg.HCl), hydrochloric acid, imidazole, and sodium chloride were purchased from Thermo-Fisher Scientific (Waltham, MA). Anhydrous (99.8%, extra dry) isopropanol was obtained from Acros Organics (Morris Plains, NJ). Hellmanex III cleaning detergent concentrate was purchased from Thermo Fisher Scientific (Waltham, MA). The arginine hydrochloride and imidazole were BioReagent grade (> 98.5% purity). DOPC (1,2-dioleoyl-sn-glycero-3-phosphocholine) was purchased from Avanti Polar Lipids, Inc (Alabaster, AL). mPEG-silane-5000 (item # MPEG-SIL-5000-1g) was purchased from Laysan Bio (Arab, AL). Atto-488 NHS ester (λ_{abs} = 500 nm; λ_{em} = 520 nm) from Sigma-Aldrich (St. Louis, MO) was used to fluorescently label the mAb. Glass microscope cover slips (No. 1.5; 0.17 mm) were obtained from VWR International (Radnor, PA), and 0.8 mm thick silicone gaskets were obtained from Grace Bio-Labs (Bend, OR). Centri-Spin 20 miniature SEC columns were purchased from Princeton Separations (Adelphia, NJ). All co-solutes were dissolved in de-ionized water (Barnstead Nanopure Diamond, Thermo Fisher Scientific, Waltham, MA).

3.3.2 mAb sample preparation

Concentrated (~250 mg/mL) solutions of mAb2 were formulated in the desired co-solute composition (50 – 250 mM NaCl, 50 – 250 mM Arg.HCl and 1 M Im(HCl) titrated to pH 5.5) via gravimetric dilution of ~280 mg/mL unformulated mAb stock solutions with concentrated co-solute stock solutions, as described previously (24). Briefly, the mAb2 stock as provided was buffer exchanged into 21:30 mM Na:OAc (pH 5) buffer by centrifugal diafiltration at 4500 RCF using a 30 kDa MWCO Amicon Ultra-15 centrifugal filter unit (MilliporeSigma, Burlington, MA), and then sterile filtered using 0.22 μm PES filters (CellTreat Scientific Products, Pepperell,

MA). The stock was then further concentrated to ~280 mg/mL by centrifugal ultrafiltration. The final mAb stock concentration was measured by UV-Vis spectroscopy (4, 44, 45) with an extinction coefficient of 1.42 $mL*mg^{-1}cm^{-1}$. Aliquots (~300 uL) of the ~280 mg/mL mAb stock was diluted with appropriate amounts of concentrated co-solute stock solutions to achieve the final desired co-solute composition at ~250 mg/mL mAb. Intermediate concentration samples were prepared for diffusion measurements by dilution of the formulated ~250 mg/mL samples with solvents prepared at the same co-solute composition. The concentration and viscosity of all samples (both original and intermediate concentration) were checked with UV-Vis spectroscopy and custom syringe viscometers, as described previously (24). The concentration-dependent viscosity was also fit to the Ross-Minton equation (16, 38)

$$\frac{\eta}{\eta_0} = \exp\left(\frac{[\eta]c}{1-\frac{k}{\nu}[\eta]c}\right) \tag{3.4}$$

where c is the mAb mass concentration, η_0 is the solvent viscosity, $[\eta]$ is the intrinsic viscosity, and k/ν is the combined packing/Simha shape parameter.

3.3.3 Dynamic light scattering (DLS)

The diffusion coefficient of the mAb at infinite dilution, D_0, in each co-solute formulation was measured by DLS using a ZetaPALS zeta potential analyzer (Brookhaven Instruments, Holtsville, NY; λ = 660 nm, θ = 90°). mAb samples at 2, 5, 10, 15 and 20 mg/mL were sterile-filtered with 0.22 μm PES filters prior to DLS measurements (to remove dust and particulates) and measured in triplicate, where each run consisted of 4 15-second scans that were averaged together. The DLS autocorrelation functions (ACFs) were fit using Brookhaven Instruments' Dynamic Light Scattering software using the quadratic cumulant algorithm (106) to obtain the collective diffusion coefficient D_c as a function of mAb concentration. D_c was fit to Eqn. 3.5 (20, 28, 36) to obtain D_0, where k_D is the diffusion interaction parameter.

$$D_c(c) = D_0(1 + k_D c) \tag{3.5}$$

3.3.4 Fluorescent labeling of the high concentration mAb solutions

~25 μM stock solutions of mAb2 labeled with Atto-488 were prepared as described in the Supporting Information and frozen at -20°C for longer-term storage. Prior to FCS measurements, a 20 μL aliquot of the thawed labeled mAb was ultracentrifuged (Sorvall MX 120+ floor micro-ultracentrifuge; Thermo Fisher Scientific, Waltham, MA) at 400,000g for 10 minutes to sediment any aggregated mAb probes. The top 90% of the solution was recovered, and the labeled mAb stock was then diluted to 50 nM and added at the appropriate volume to unlabeled, concentrated mAb FCS samples in small-volume low-binding tubes (USA Scientific, Ocala, FL) to achieve a final label concentration of 1 nM, resulting in a 2% dilution of the unlabeled mAb. The unlabeled mAb samples were therefore prepared at 102% of the desired mAb concentration, such that the final concentration after addition of the labeled mAb was the desired level (i.e. 60, 125, 150, 200 and 250 mg/mL). Due to the high viscosity of the concentrated mAb solutions preventing even mixing using pipettes, the labeled mAb was mixed into the unlabeled sample by stirring with 25G needles (Becton & Dickinson, Franklin Lakes, NJ) for ~1 – 2 minutes until homogenous. The labeled samples were then measured in sets of 8 samples by FCS over a ~3 hour time period per set, with the first sample measured within 10 – 15 minutes after addition of the labeled mAb.

3.3.5 Sample assembly and loading for fluorescence correlation spectroscopy

The glass microscope cover slips used for creating the FCS imaging wells were first cleaned and passivated using either a dry passivation technique (RCA (Radio Corporation of America) clean, followed by silane-PEGylation) or wet passivation (cleaned with Hellmanex, followed by adsorption of a DOPC vesicle film) as described in the Supporting Information. The imaging wells were created by gently pressing cleaned 0.8 mm thick 1 cm x 1 cm silicone

gaskets (with a hole diameter of ~0.5 cm) onto the cleaned, passivated cover slips to create a temporary water-tight seal. In the case of wet passivation, the slides were passivated after assembling the gaskets on the cleaned cover slip, as described in the Supporting Information. The gaskets were soaked in a hot (lightly steaming) solution of 2% v/v Hellmanex III detergent for 10 minutes to remove residual protein and other adsorbed organic matter, individually rinsed under running ultrapure water to remove all residual detergent and dried under a N2 stream prior to use.

For the dry passivation technique, which produced the best results and was used for the majority of the experiments in this work, 40 μL of labeled mAb sample was added to the imaging well using an adjustable volume pipet (ResearchPlus, Eppendorf, Hauppauge, NY). To minimize changes to the sample due to evaporation, the samples were loaded into the imaging wells and measured in triplicate within 10 – 15 minutes of loading. For the highest concentration samples (≥ 200 mg/mL), the imaging well was also sealed with a second dry-passivated cover slip (with the passivated side facing down towards the imaging well) to further prevent sample evaporation. For the wet passivation technique, the labeled mAb sample was added to the imaging well using a serial addition scheme to bring the final (unlabeled) mAb concentration in the well to 95.83% of the original mAb sample concentration, as described in the Supporting Information.

3.3.6 Fluorescence correlation spectroscopy (FCS)

The self-diffusion of mAb2 was measured by FCS using a home-built system based on a modified Zeiss Axio Observer.A1 inverted fluorescence microscope equipped with a Zeiss Plan Apochromat 100x 1.4 NA oil immersion lens and a time-correlated single-photon counting (TCSPC) correlator card from Becker and Hickle GmbH (Berlin, Germany), as described previously (92-94). The sample was illuminated with a 486 nm diode laser (Becker and Hickl), and the laser was focused through a Di02-R488 dichroic mirror (Semrock, Lake Forest, IL) into

the solution 3 – 20 μm above the sample cover slip. The distance between the lens focal point and the cover slip was controlled by adjusting the height of the sample stage with a precision 3-axis piezoelectric stage from Mad City Labs (Madison, WI) using home-built control software. Sample fluorescence collected with the microscope objective was split into separate Hamamatsu GaAsP photomultiplier tubes (Hamamatsu, Japan) equipped with different emission filters (510 nm with a 42 nm width; 511 nm with a 20 nm width) for cross-correlation using the Becker and Hickl software. FCS autocorrelation function (ACF) traces were collected in triplicate per sample for a minimum of 120 seconds per replicate. For the high concentration (≥ 200 mg/mL) samples, the individual FCS traces were collected over 180 – 300 seconds improve the signal-to-noise ratio and smoothness of the FCS traces. The individual ACF traces were then fitted to the anomalous diffusion model and Gaussian distribution models described below.

3.3.7 Anomalous diffusion model

Anomalous diffusion behavior was seen from the stretched nature of the exponential decay in the autocorrelation function (ACF), potentially arising in part from the refractive index mismatch between the aqueous sample and immersion oil, but also likely from the greater extent of crowding and self-association commonly seen in concentrated mAb solutions (10, 15-18). The ACF was therefore fit to the 3D anomalous diffusion equation (72, 73, 89, 90, 103, 107, 108)

$$G(\tau) = 1 + \frac{1}{N} * \left(1 + \frac{T}{1-T} * \exp\left(-\frac{\tau}{\tau_T}\right)\right) * \frac{1}{\left(1+\left(\frac{\tau}{\tau_D}\right)^{\alpha}\right)\left(1+\frac{1}{S^2}*\left(\frac{\tau}{\tau_D}\right)^{\alpha}\right)^{0.5}} \quad (3.6)$$

where G(τ) is the autocorrelation value, α is an anomaly coefficient, N is the number of fluorescent probes detected in the confocal volume at a given time, T is the fraction of probes in the triplet (dark) state, τ_T is the triplet lifetime (fixed at 5 μs (109)), S is the aspect ratio of the confocal volume and was fixed at 5/3 ($S = \omega_z/\omega_{xy}$, where ω_z is the length of the axial waist and ω_{xy} is the length of the radial waist of the confocal volume) and τ_D is the diffusion crossover

time. Due to instrument noise at short delay times, and given that the characteristic τ_D was on the order of 1000 – 10,000 μs, the ACFs were fit for τ from 100 to 1,000,000 μs. The autocorrelation value G(τ) was determined from the fluctuations of the fluorescence intensity (87, 88) ($G(\tau)=\langle \delta F(t)*\delta F(t+\tau)\rangle/\langle F(t)\rangle^2$). The self-diffusion coefficient D_s is determined from the diffusion crossover time (79, 87, 88, 107, 110)

$$D_s = \frac{\omega_{xy}^2}{4\tau_D} \tag{3.7}$$

and can further be converted into an apparent hydrodynamic radius R_h via the Stokes-Einstein equation

$$R_h = \frac{k_B T}{6\pi\eta D_s} = \frac{4k_B T\tau_D}{6\pi\eta\omega_{xy}^2} \tag{3.8}$$

where η is the solution viscosity.

3.3.8 Gaussian distribution model

The stretched ACF decay can also be described via a Gaussian distribution model (GDM) to explain the anomalous diffusion behavior in terms of solution polydispersity. In this model, the ACF is essentially fit to an infinitely multi-component model, where the probability (weighting factor) of each possible diffusion crossover time $\tau_{D,i}$ follows a Gaussian distribution. The ACF then becomes (104, 105)

$$G(\tau) = \sum_{i=1}^{m} a_i(\tau_{D,i}) \left(1 + \frac{\tau}{\tau_{Di}}\right)^{-1} \left[1 + \left(\frac{\omega_{xy}}{\omega_z}\right)^2 \left(\frac{\tau}{\tau_{Di}}\right)\right]^{-\frac{1}{2}} \tag{3.9}$$

where the normalized distribution probability $a_i(\tau_{D,i})$ is a Gaussian distribution in terms of $\ln(\tau_D)$,

$$a_i(\tau_{Di}) = A * \exp\left[-\left(\frac{(ln(\tau_{Di}) - ln(\tau_p))}{\sqrt{2}\ln(\sigma)}\right)^2\right] \tag{3.10}$$

centered around an average characteristic value $\ln(\tau_p)$ with standard deviation ln(σ). A is a normalization constant such that the sum of the probability distribution $a_i(\tau_{D,i})$ is 1. The ACFs

were fit to the GDM equation through χ^2 minimization, where the variance was determined from the mean value of $G(\tau_{D,i})$ at each $\tau_{D,i}$ smoothed over an interval of 10 $\tau_{D,i}$ values for multiple intervals around $\tau_{D,i}$.

The width of the probability distribution in terms of $\ln(\tau_D)$ was converted to a full-width at the half-maximum (fwhm) of the probability distribution peak for the corresponding R_h to better quantify the solution polydispersity from the fitted σ. The derivation of Eqn. 3.11 is shown in the Supporting Information.

$$fwhm = \overline{R_h} * \left(\exp\left(\sqrt{2\ln(2)}\ln(\sigma)\right) - \exp\left(-\sqrt{2\ln(2)}\ln(\sigma)\right)\right) \tag{3.11}$$

3.3.9 Deviation from hard sphere diffusion and viscosity

The mAb self-diffusion and viscosity can be normalized against the hard sphere behavior at the same volume fraction ($\varphi = c^*\bar{v}$ where $\bar{v}$ is the mAb partial specific volume determined from fits of mAb2's static light scattering behavior to the interacting hard sphere model (24)), where the hard sphere system represents the behavior in the absence of protein-protein interactions.

The long-time self-diffusion retardation of hard sphere solutions as a function of volume fraction is given by Eqn. 3.12 (65, 81).

$$\frac{D_0}{D_{HS}} = \frac{1+1.5\varphi+2\varphi^2+3\varphi^3}{(1-\varphi)^3} \tag{3.12}$$

The corresponding viscosity is given by the Ross-Minton viscosity equation (Eqn. 3.4), where for hard sphere solutions [η] is 2.5 (in terms of φ) and k/ν was determined assuming random close packing of the spheres ($\varphi_{max} = 0.64$) (111).

3.3.10 Length-scale dependent viscosity model

The diffusion retardation factor D_0/D_s was related to the local microviscosity to explain deviations from generalized Stokes-Einstein behavior in terms of length-scale dependent effects,

as described with the length-scale dependent viscosity (LDV) model developed by Holyst (53, 70-73) and detailed in the Introduction section. For the application of the LDV model (Eqn. 3.1a – 2.3b) to protein diffusing in protein solutions (the non-entangled colloidal case described in Kalwarczyk (72)), the value of R_{eff} is taken to be the $r_p \rightarrow \infty$ limit (i.e. R_h) (72). In the current study, R_h = 4.5 nm and R_g = 3.5 nm. (25)

Combining Eqn. 3.1a – 3.3b results in the following expression for relating diffusion retardation D_0/D_s to an interaction parameter (b, γ) and a hydrodynamic/structure parameter (a) for non-entangled systems.

$$\ln\left(\frac{D_0}{D_s}\right) = \frac{\Delta E_a}{RT} = b * \left(\frac{R_h}{R_g} * \frac{\psi}{\psi_{Rcp}}\right)^a \tag{3.13}$$

Eqn. 3.13 can also be plotted in a linearized form to facilitate linear regression of a and b, while also somewhat separating the influences of the hydrodynamic/structure effects and PPI effects on the self-diffusion retardation behavior.

$$\ln\left(\frac{E_a}{RT}\right) = \ln(b) + a * \ln\left(\frac{R_h}{R_g} * \frac{\psi}{\psi_{rcp}}\right) \tag{3.14}$$

3.4 RESULTS

3.4.1 Method development – fluorescence correlation spectroscopy at high concentration for mAbs

The FCS experimental technique was modified from the methodology previously used (92-94) for measuring protein diffusion on membrane surfaces, and was further optimized for mAbs diffusing in solution at high concentration. To minimize any complicating effects of the high viscosities that arise from the high mAb concentration, method development experiments were done with mAb2 (described previously by SLS (24) and SAXS (25)) formulated with 1 M Im(HCl) and 250 mM PheOMe(HCl) at pH 5.5, as these systems have relatively low viscosities (24) (~10 – 15 cP at 200 mg/mL). The key challenges that had to be addressed for the high

concentration FCS measurements were (i) possible changes in the confocal volume waist radius ωxy from the change in refractive index from low to high concentration and between different co-solute systems, (ii) complexity due to polydispersity from the presence of reversible oligomers, (iii) low G(0) values resulting in poorer signal-to-noise ratios given the high N (Eqn. 3.6), and (iv) uniform sample loading for viscous solutions in the FCS imaging well while minimizing or eliminating sample dilution and/or sample heterogeneity from uneven mixing.

To examine the influence of the refractive index (RI) on the confocal waist radius, ω_{xy} was determined from calibration measurements using 3 nM holo-transferrin (Tf) labeled with Atto-488 in solutions of either 50 mM $NaHCO_3$ (RI = 1.33) or 50 wt% glycerol in 50 mM $NaHCO_3$ (RI = 1.41) (loaded on dry-passivated slides). These two values cover the RI range from the lowest mAb concentration (10 mg/mL) in pure buffer (21:30 mM Na:OAc) to the highest concentration (250 mg/mL) in the most optically-dense co-solute solution (1 M Im(HCl)). The solution RI was determined from the mAb and co-solute concentrations with previously-measured co-solute dn/dc values (24) and an assumed protein dn/dc of 0.185 mL/g (112) as described previously (24). The change in RI caused a shift in the Tf τ_D (Fig. 3.11, Table 3.4). The corresponding expected diffusion coefficients D_s were calculated from the literature value (113) of $D_0 = 6.7*10^{-7}$ cm^2/s for Tf in water at 25°C and corrected for the measured solvent viscosities (Table 3.4) using the generalized Stokes-Einstein (GSE) equation (Eqn. 3.8). The ACFs were measured in triplicate for each solution condition, and the waist radius was then determined from the measured τ_D and known D_s using Eqn. 3.7, resulting in ω_{xy} values of 432 ± 8.8 nm for RI = 1.33 and 421 ± 8.3 nm for RI = 1.41. Based on the very small change, ω_{xy} was assumed to remain constant across the RI range relevant to the mAb diffusion measurements, and the average of the two ω_{xy} values (427 ± 6.1 nm) was used for all future calculations of D_s.

To ensure measurement of the diffusion of representative equilibrated mAb structures (monomer and possible oligomers) at high concentration, the labeled monomeric mAb was

added to the mAb solution either at low concentration before ultrafiltration to ~200 mg/mL ("pre-spiked") or after ultrafiltration ("post-spiked"). The two approaches were used to determine if there were any time-dependent effects relating to mixing of labeled and unlabeled mAb between monomer and oligomer. In the "pre-spiked" case, the probe mAb undergoes possible self-association and exchange with oligomers in solution as it is concentrated from ~25 mg/mL to 200+ mg/mL. In the "post-spiked" case, it was not known if the monomeric probe had sufficient time to exchange into the unlabeled oligomers in the viscous solution over a time scale of 10 – 15 minutes. However, an examination of the results for the two cases shows that there is no significant difference in terms of the ACF (Fig. 3.1) or the fit parameters G(0), τ_D (D_s) or α (Table 3.1), suggesting that the exchange of the labeled mAb between monomer and oligomer reaches equilibrium in the time frame between the probe addition and the FCS measurements (~10 minutes). This result is consistent with the short lifetimes of dynamic protein clusters, which have been suggested to be on the order of 25 ns (114). Another possibility is that the fraction of reversible oliogomers is too low to be measurable by FCS, as discussed below in the section on polydispersity. Thus for the remaining experiments, the labeled mAb was added to the formulated samples at high concentration ("post-spiked" case) for simplicity, as well as to minimize the amount of time the labeled mAb spends in the liquid state to minimize the risk of dye hydrolysis.

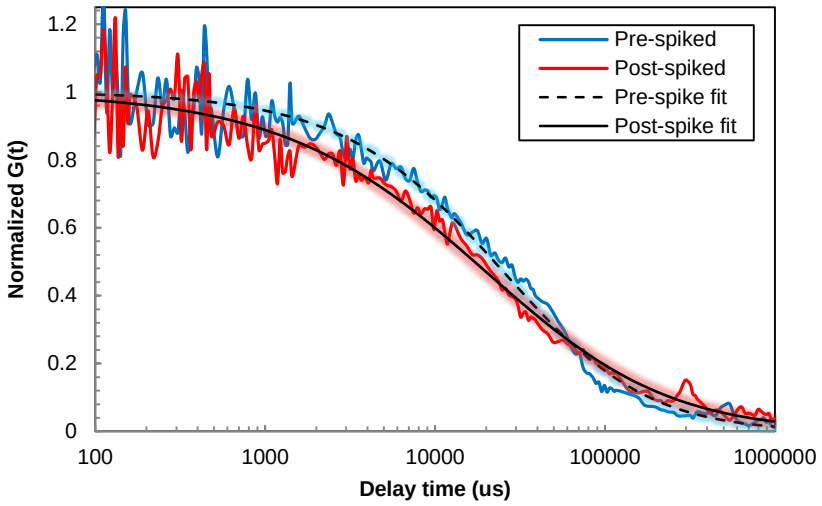

Figure 3.1. Measured normalized ACF of mAb2 at 200 mg/mL in buffer (21:30 mM Na:OAc pH 5) where the fluorescently-labeled mAb was added at low concentration before diafiltration ("pre-spiked") or at high concentration after ultrafiltration ("post-spiked"). The solid and dashed lines are fits of the ACF to the 3D anomalous diffusion equation, and the corresponding fit parameters are reported in Table 3.1. The samples were loaded on wet-passivated slides.

Label addition	Final mAb conc (mg/mL)	G(0)	τ_D (µs)	D_s/D_0	α
Before diafiltration ("pre-spiked")	195	1.22	22000 ± 3638	0.028 ± 0.005	0.64 ± 0.07
After ultrafiltration ("post-spiked")	200	1.19	21780 ± 5543	0.028 ± 0.007	0.69 ± 0.13

Table 3.1. ACF fit parameters (3D anomalous diffusion) for mAb2 at ~200 mg/mL in buffer (21:30 mM Na:OAc pH 5), where the Atto488-labeled mAb2 was added either at low concentration before diafiltration ("pre-spiked") or at high concentration after ultrafiltration ("post-spiked"). The corresponding ACFs are shown in Fig. 3.1.

The G(0) value has been shown to decrease with increasing crowder (protein, polymer, vesicles, etc.) concentration (99) to very small values (un-normalized << 2 or normalized << 1) (107, 115), which may potentially lead to poor signal-to-noise ratios. Based on Eqn. 3.6, the low G(0) may be caused by the detection of large number of fluorophores N in the confocal volume. Interestingly, G(0) decreased with increasing mAb concentration for the 250 mM PheOMe

system, as seen in Fig. 3.13 and Table 3.5, despite the fact that the labeled mAb concentration was held fixed at 1 nM. This unexpected increase in apparent N has been attributed in part to an enlargement in the effective confocal volume (molecular detection function, "MDF") due to multiple scattering effects by the surrounding unlabeled protein (99), but is still not fully understood. The distortion effects are minimized by working close to the cover slip, where the multiple scattering effect was shown in simulations to be eliminated at focal depths less than 50 μm from the cover slip (99). Similarly, while RI mismatch effects are known to distort the MDF under certain conditions (98, 102), they were also shown from simulations to be minimized at < 20 μm from the cover slip (98, 102). To optimize G(0) and minimize the MDF distortion effects, the ACFs and corresponding G(0) of mAb2 at 200 mg/mL in 1 M Im(HCl) were measured as a function of focal depth from the cover slip between 3 and 20 μm (precisely controlled using the piezoelectric stage). As can be seen in Fig. 3.2, G(0) increased with decreasing focal depth, with negligible effects on the corresponding τ_D and α within measurement error. Given that both G(0) is maximized and MDF distortion effects are minimized closest to the cover slip, the focal depth was fixed at 3 μm from the cover slip for subsequent measurements. The ACFs G(τ) were fit in the un-normalized form (Eqn. 3.6 and Eqn. 3.9). However, to facilitate easier visual comparison of ACFs between mAb concentrations and co-solute systems given the wide range of G(0)'s, they are shown in the Supporting Information as normalized G(τ)'s where the normalized G(0) = 1. Similarly, the normalized G(τ) → 0 as τ → ∞, since the un-normalized G(τ) → 1 as τ → ∞.

$$Normalized\ G(\tau) = \frac{G(\tau)-1}{G(0)-1} \tag{3.15}$$

In Eqn. 3.15, G(0) is the initial value of the un-normalized G(τ), and is reported (un-normalized) for all mAb concentrations and co-solute systems in Table 3.6.

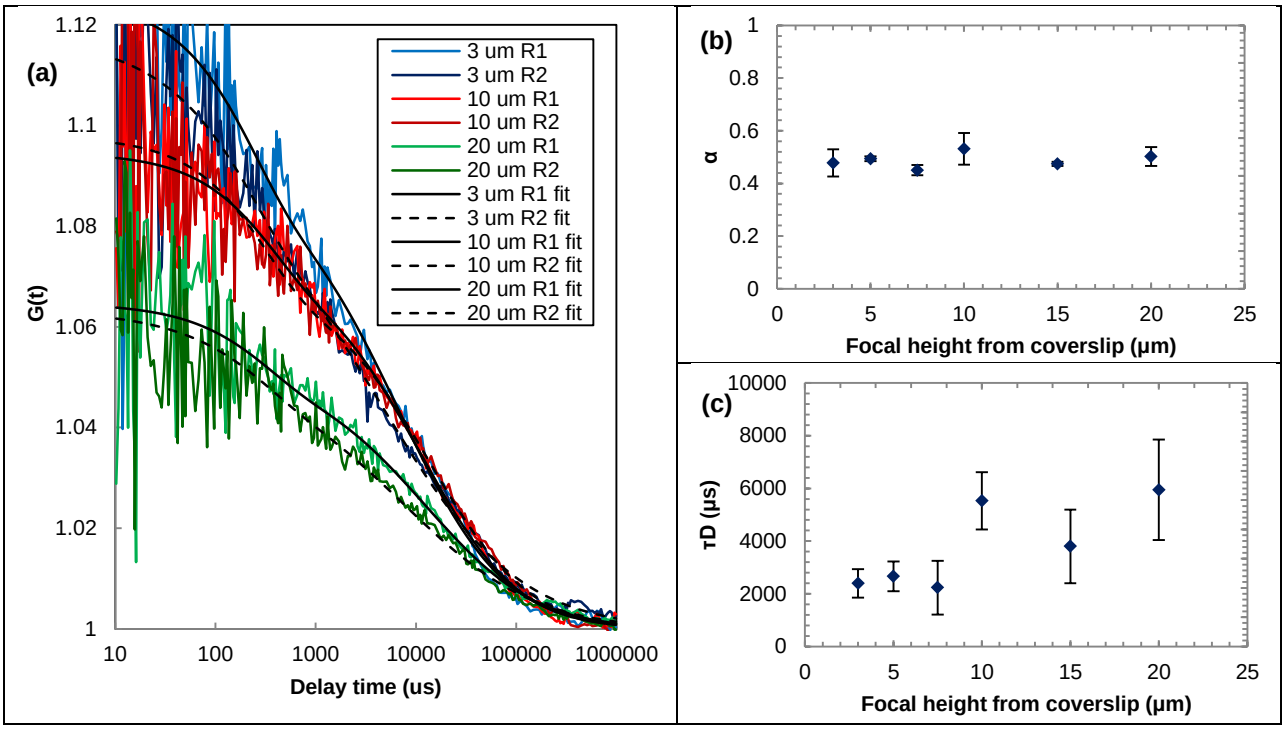

Figure 3.2.(a) Dependence of G(0) of the ACF for mAb2 at 207 mg/mL in 1M Im(HCl) pH 5.5 on the focal depth (distance of focal point from coverslip) from 3 to 20 µm. Also, relative independence of the **(b)** fitted anomaly coefficient α and **(c)** diffusion cross-over time τ_D on the focal depth. These measurements were made using wet-passivated slides. For clarity, the ACFs at 5 and 7 µm focal depth have been omitted from part **(a)**. Solid and dashed black lines in part **(a)** show fits of the ACFs to the anomalous 3D diffusion model.

To ensure reproducible, meaningful measurements of the mAb diffusion at high concentration and viscosity, the sample loading technique was refined in conjunction with the slide passivation strategy to eliminate sample heterogeneity introduced by the loading technique. In the wet passivation technique (92-94) as well as for the method development experiments described in previous sections, the mAb sample was added to the imaging well which already contains a thin layer of fluid. A serial addition/mixing scheme was utilized to bring the final mAb concentration in the well back to ~96% of the initial sample concentration. For relatively non-viscous samples such as 250 mM Arg.HCl (~20 cP at 200 mg/mL), the sample is easy to

mix evenly, resulting in good reproducibility of the ACF between replicate measurements (Fig. 3.3b). However, for viscous samples such as 250 mM NaCl (60 – 70 cP at 200 mg/mL), the confined geometry of the sample well and the high viscosity resulted in uneven mixing of the sample and poorer reproducibility between replicate ACF measurements (Fig. 3.3b). In contrast, the dry passivation technique demonstrated superior reproducibility even for viscous samples (Fig. 3.3a), since the mAb sample is loaded directly onto the dry, passivated slide without any mixing or sample dilution needed, resulting in consistent mAb concentrations and homogenous samples in the imaging well. The dry-passivated slides were therefore used for the remaining samples examined in this study.

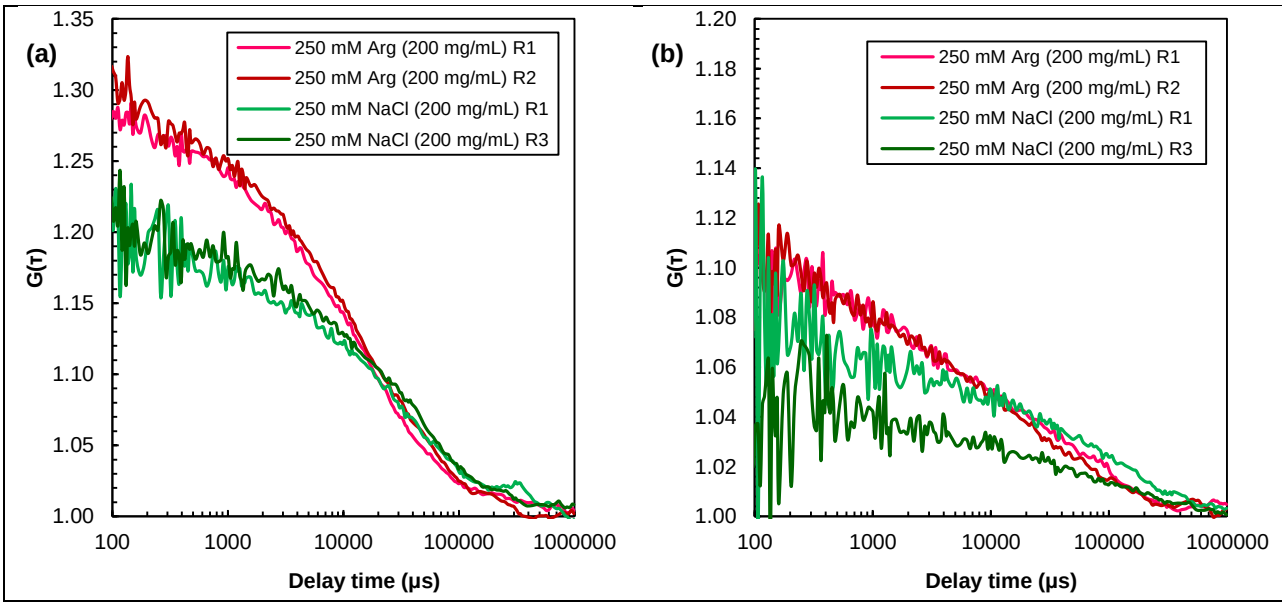

Figure 3.3. Reproducibility of the autocorrelation function for high concentration (~200 mg/mL) FCS measurements of mAb2 at pH 5.5 using glass slides passivated with a (a) dry passivation technique (silane-PEGylation) or (b) a wet passivation technique (adsorbed DOPC vesicles). The concentrated mAb sample was loaded as-is on the dry-passivated slide, and was added to the wet-passivated slide via serial addition and mixing with the wet passivating film.

3.4.2 Co-solute effects on the viscosity of mAb2

The survey of co-solute effects on the viscosity of mAb2(24) was expanded to include 150 mM NaCl, 50 mM Arg.HCl and 150 mM Arg.HCl in this study to systematically tune the PPI, including physiologically relevant co-solute concentrations (150 mM) as well as a more extreme attraction-suppressing (1 M Im(HCl)) system. As seen in Fig. 3.4a, increasing ionic strength from 50 to 250 mM with NaCl has no effect on viscosity, while Arg causes a progressive reduction in viscosity from 50 to 150 to 250 mM. The Arg solution viscosities were also consistently lower than NaCl at the same co-solute concentration, although the difference was small at 50 and 150 mM co-solute. The viscosity was also normalized by the hard sphere (HS) value at the same concentration (Eqn. 3.4). The mAb viscosity in 1 M Im was nearly HS-like (Fig. 3.4b). These viscosities will later be related to the mAb diffusion behavior in the context of the GSE relation in order to gain more insight on the local PPI, as described below and in the Discussion section.

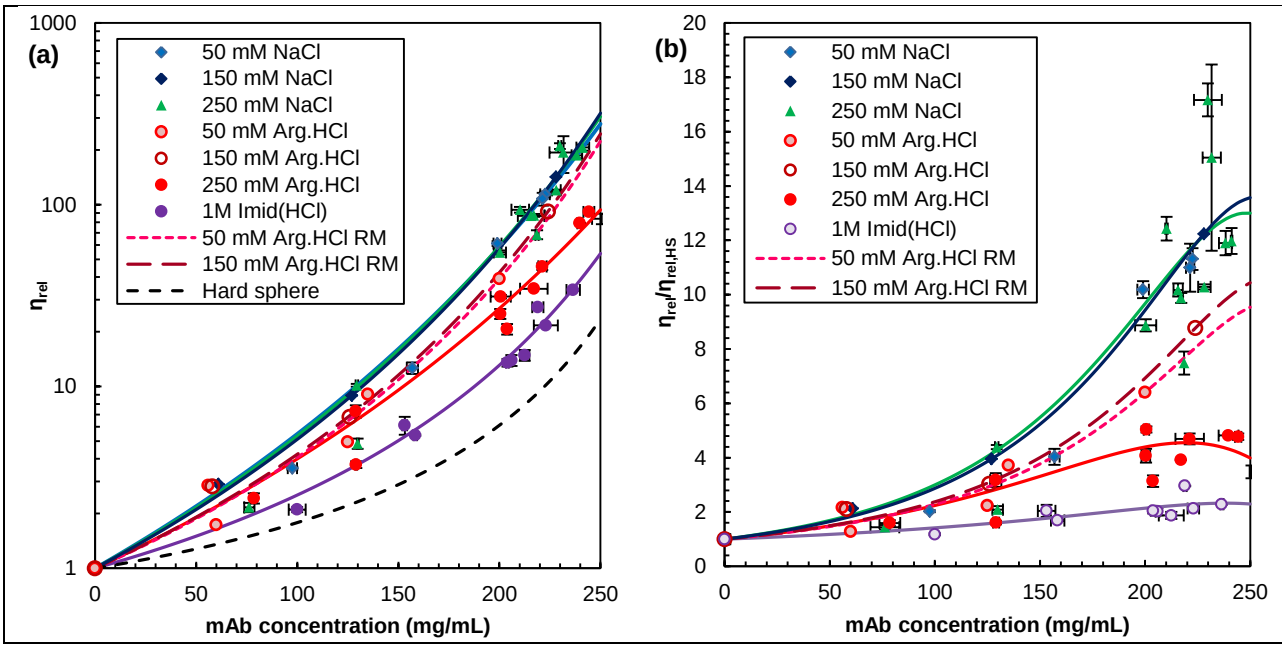

Figure 3.4. (a) Relative viscosity of mAb2 as a function of mAb concentration and co-solute formulation, and (b) relative viscosity of mAb2 normalized by the hard sphere relative viscosity at the same concentration (calculated with the Ross-Minton equation[1-2] with the hard sphere values $[\eta] = 2.5$ and $\varphi_{max} = 0.64$[3]), where the equivalent hard sphere volume fraction was calculated from the mAb concentration and mAb2's partial specific volume determined from SLS.[4] The solid and dashed curves are fits of the viscosity to the Ross-Minton equation.[5-6] The viscosity data and fits for 50 mM NaCl, 250 mM NaCl, 250 mM Arg and 1M Im are reproduced from Hung et al.[4]

3.4.3 Co-solute effects on the self-diffusion and diffusion retardation of mAb2

The diffusion coefficient of mAb2 at infinite dilution (D_0) and the corresponding hydrodynamic radius $R_{h,0}$ at infinite dilution in the different co-solute formulations were measured by DLS (Table 3.2) to normalize the long-time self-diffusion coefficients D_s measured at high concentration by FCS. The evolution of the long-time diffusion retardation factor D_0/D_s is shown as a function of mAb concentration in Fig. 3.5a and solution relative viscosity η_{rel} in Fig. 3.5b and 3.5c). For all co-solute systems, the retardation factor increases exponentially with concentration. Furthermore, a clear separation is seen between groups of co-solutes in terms of concentration (Fig. 3.5a), with the greatest D_s retardation for NaCl (50 – 250 mM) (nearly

identical) systems, and less retardation for Arg (similar retardation factors between 50 and 250 mM). Remarkably, 1 M Im reduced the diffusion retardation all the way to the hard sphere value (where the hard sphere D_0/D_s was calculated at the volume fraction φ corresponding to the same mAb concentration, as described in the Methods section). As a function of the relative macroscopic viscosity (Fig. 3.5b), the retardation factors become more convergent between all co-solute systems, but fall below the generalized Stokes-Einstein (GSE) line (i.e. $D_0/D_s = \eta/\eta_0$; Eqn. 3.8) at the higher concentrations. Here, the hard sphere D_0/D_s is still calculated at the same φ as for Fig. 3.5a, but is plotted against the corresponding HS viscosity calculated at that φ (Eqn. 3.4; Supporting Info). The deviations from the GSE relation are more apparent on a linear plot (Fig. 3.5c).

Formulation	**D_0 (cm^2/s)**	**$R_{h,0}$ from D_0 (nm)**	**η_0 (cP)**	**[η] (ml/mg)**	**k/v**
50 mM NaCl	5.03E-07	4.8	0.91	0.0146	0.0957
150 mM NaCl	4.80E-07	4.9	0.93	0.0137	0.1191
250 mM NaCl	4.68E-07	5.0	0.94	0.0142	0.1064
50 mM Arg.HCl	4.88E-07	4.6	0.98	0.0115	0.1907
150 mM Arg.HCl	4.57E-07	4.6	1.03	0.0117	0.1588
250 mM Arg.HCl	4.39E-07	4.7	1.05	0.0120	0.1141
1 M Im(HCl)	3.88E-07	5.4	1.04	0.0073	0.3008

Table 3.2. *D_0* from DLS and Ross-Minton viscosity fit parameters of mAb2 with different co-solutes. The Ross-Minton parameters (with the exception of 5 mM $ZnSO_4$) are reproduced from Hung et al.[4] All formulations are at pH 5.5. The linear fits of D_c vs mAb concentration from DLS to Eqn. 3.5 to obtain D_0 are shown in Fig. 3.14.

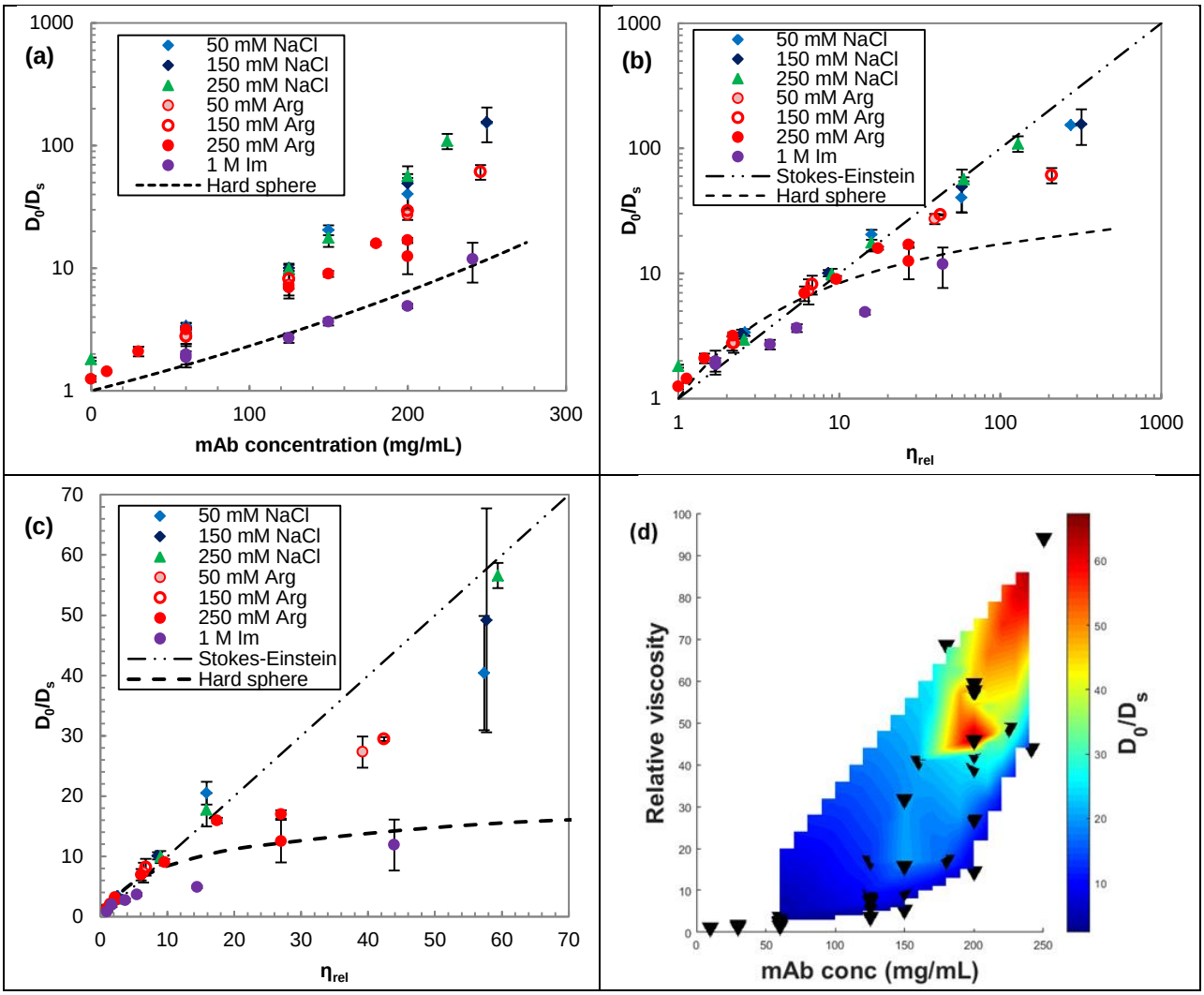

Figure 3.5. Dependence of D_0/D_s for mAb2 in different co-solute formulations on (a) the mAb concentration and (b) the solution viscosity. (c) Zoomed-in version of (b) plotted on a linear time scale. D_s was fit from the τ_D obtained from the Gaussian distribution model[7-8] (GDM) 3D diffusion fit of the ACFs measured using dry-passivated slides at 3 μm focal depth. D_0 was obtained from DLS (Table 3.2). (d) Heat map of D_0/D_s as a function of both mAb concentration and solution viscosity. An alternative version of part (b), where D_0/D_s is grouped by mAb concentration instead of by co-solute formulation, is shown in Fig. 3.17. The raw, normalized autocorrelation functions (ACFs) corresponding to the D_s measurements are shown in Fig. 3.15, and fits of the 200 mg/mL ACFs to both the 3D anomalous diffusion model and the Gaussian distribution model are shown with residuals in Fig. 3.16.

The diffusion retardation factor D_0/D_s is a function of both concentration and solution viscosity, as can be seen experimentally in Fig. 3.5d. It is known that even in the absence of interparticle interactions, the long-time self-diffusion of colloids slows down with increasing concentration (increasing D_0/D_s) simply due to crowding effects (65, 81), as seen from the hard sphere curve in Fig. 3.5a calculated from Eqn. 3.12. At the same time, the self-diffusion also slows down with increasing solution viscosity, as seen from the GSE equation (Eqn. 3.8). Since the viscosity is influenced both by the concentration (Eqn. 3.4) as well as PPI and solution structure (10, 15-18, 20, 24), the mAb diffusion retardation factor was normalized by the HS retardation factor at the same concentration in an attempt to decouple the effects of crowding and PPI/structure on mAb diffusion. As seen from HS-normalized retardation factor $D_{s,HS}/D_s$)which normalizes out the steric effects on D_s) in Fig. 3.6a, the mAb solutions show increasing deviation from HS behavior with mAb concentration, likely due to attractive PPI and self-association. However, Arg (50 – 250 mM) reduces the deviation relative to NaCl, while 1 M Im appears to completely remove all deviation and causes the mAb to diffuse like hard spheres (seen from the ratio of 1 across the entire concentration range). This behavior qualitatively agrees with previous studies of mAb2 by SLS and SAXS, where it was seen that 250 mM Arg and 1 M Im weakened the PPI and suppressed self-association relative to 250 mM NaCl (24, 25). The deviation from HS diffusion however appears to directly follow the viscosity deviation from the HS viscosity with the exception of 1 M Im, as seen in Fig. 3.6b.

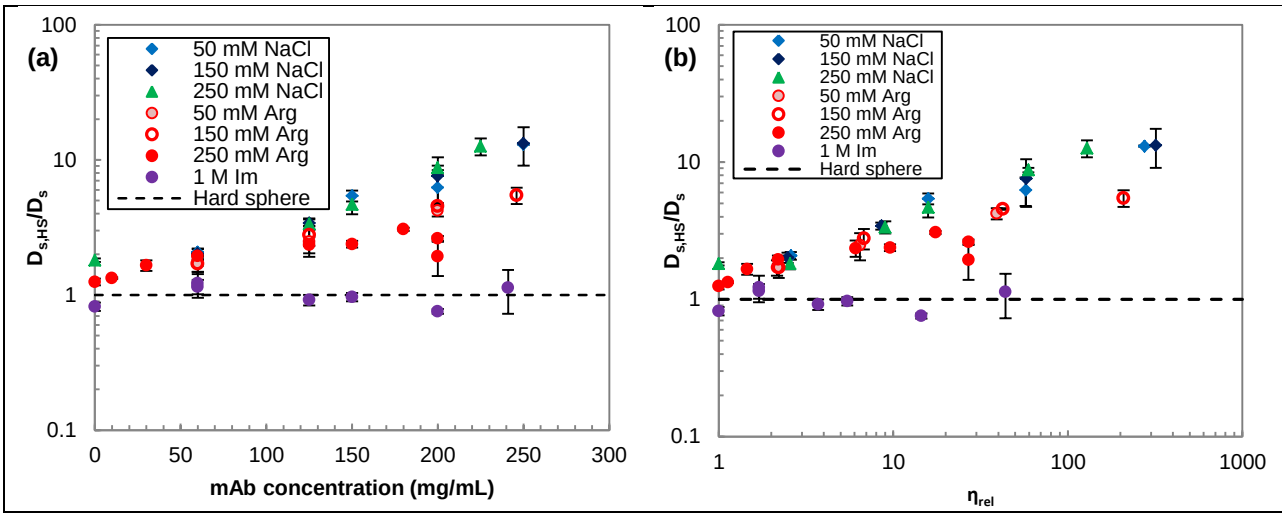

Figure 3.6. Dependence of the hard-sphere normalized self-diffusion coefficient $D_{s,HS}/D_s$ of mAb2 on the (a) mAb concentration and (b) solution relative viscosity (normalized by the hard sphere viscosity at the same concentration) in different co-solute formulations. $D_{s,HS}/D_0$ and $\eta_{rel,HS}$ were calculated following Roos et al. (81) and the Ross-Minton equation (Eqn. 3.4) respectively for each point at the same corresponding mAb concentration (i.e. volume fraction φ), where the concentration was converted to φ using the average partial specific volume of mAb2 determined from fits of the mAb static light scattering (24) to the IHS model (112). The mAb concentration groups and the corresponding normalizing HS values $D_0/D_{,HS}$ are shown in Fig. 3.17.

3.4.4 Deviation from generalized Stokes-Einstein behavior

The apparent deviation of the mAb diffusion from the GSE relationship seen in Fig. 3.5b may further be expressed in the form of a normalized hydrodynamic radius ($R_h/R_{h,0} = (D_0/D_s)/(\eta/\eta_0)$) (Fig. 3.7). The mAb samples follow the shape of the HS curve, showing a systematic positive deviation from GSE ($R_h/R_{h,0} > 1$) at low η_{rel} and increasing negative deviation ($R_h/R_{h,0} < 1$) at large $\eta_{rel} > \sim 10$. However, the NaCl (i.e. higher viscosity) systems showed less deviation from the GSE line compared to the other systems, while 1 M Im (lowest viscosity) showed the greatest deviation from GSE behavior. The differing degrees of deviation from the GSE relation between co-solute systems will be discussed in the context of self-association and PPI through viscosity scaling theories later in the Discussion section. The

unusual negative deviation of the 1 M Im system relative to even the hard sphere system is caused by the differences in concentration between the two systems at a given viscosity. As seen previously in Fig. 3.6a, the 1 M Im system shows the same diffusion retardation behavior as hard spheres as a function of concentration. However, at the same concentration the 1 M Im mAb solution is more viscous than the HS solution (Fig. 3.4b), such that at the same viscosity, the HS system is more concentrated than the 1 M Im mAb solution. Since D_0/D_s increases with concentration (Eqn. 3.12), the HS system is expected to have a higher D_0/D_s than the 1 M Im mAb solution at the same viscosity solely on the basis of the larger φ.

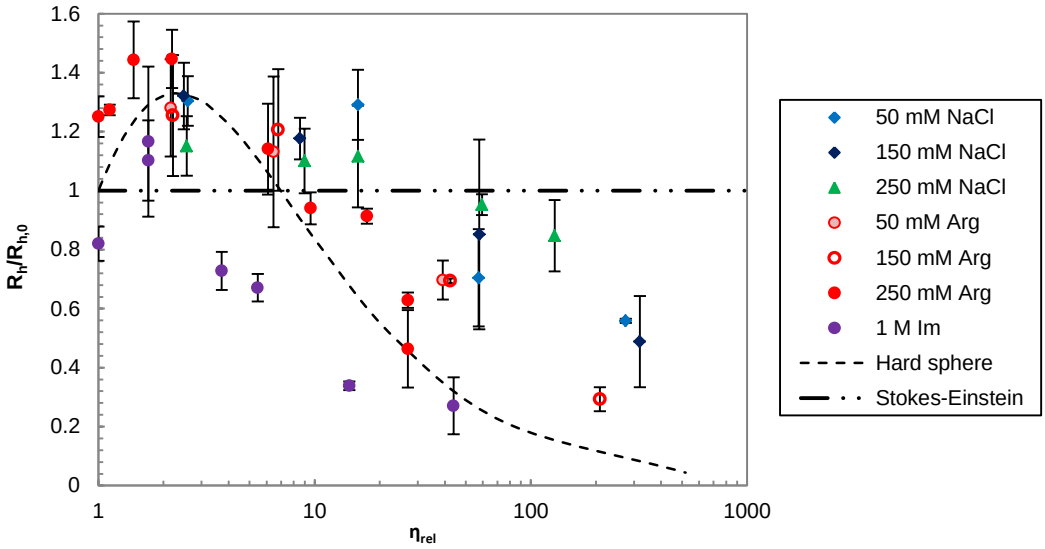

Figure 3.7. Viscosity dependence of the normalized apparent hydrodynamic radius $R_h/R_{h,0}$ of mAb2 in different co-solute formulations. $R_{h,0}$ is the apparent radius at infinite dilution, and R_h is calculated from the solution viscosity and τ_D obtained from fits of the FCS ACFs to the Gaussian distribution model for 3D diffusion. Measurements were done in triplicate on dry-passivated glass slides at a focal depth of 3 μm.

3.4.5 Measurement of the mAb solution polydispersity by FCS

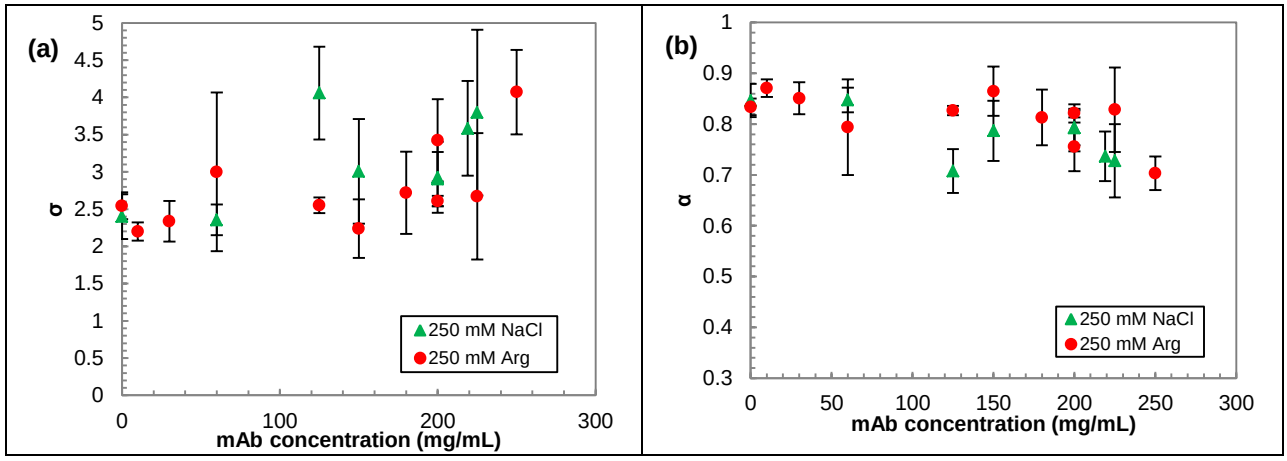

Figure 3.8. (a) Variance σ from the GDM model and (b) anomaly coefficient α from the 3D anomalous diffusion model fits of the mAb2 FCS ACFs as a function of mAb concentration for 250 mM Arg.HCl and 250 mM NaCl. The remaining co-solute formulations are shown in Fig. 3.18. All samples were measured in triplicate using dry-passivated slides at a focal depth of 3 μm.

The polydispersity of the mAb probe (which ostensibly represents the polydispersity of the mAb solution) was quantified by the anomaly coefficient α and variance σ obtained from fits of the ACF to the 3D anomalous diffusion and Gaussian distribution models respectively. The fitted σ and α of mAb2 are shown in Fig. 3.8a and 3.8b respectively as a function of concentration for 250 mM Arg and 250 mM NaCl only (for clarity), with the fitted values for the remaining co-solute systems show in Fig. 3.18a and 3.18b. The corresponding polydispersity quantifiers (σ and α) as well as the τ_D values from both fits correlate one-to-one (Fig. 3.19a, b). Similar, both fits give comparable residuals (Fig. 3.16), indicating that both the anomalous diffusion and Gaussian distribution model are equally suitable mathematical models for describing the polydispersity of the solution as seen from the ACFs. Further information about solution composition, such as from SAXS or SLS, would be needed to determine which model is the more physically relevant description of the solution.

As seen from Fig. 3.18a and 3.18b, there is a weak upward trend in σ and downward trend in α (both indicate increasing polydispersity or heterogeneity) with increasing concentration for all co-solute formulations. Additionally, for 250 mM Arg, the consistently smaller σ and larger α indicate lower polydispersity relative to 250 mM NaCl at the higher concentrations of 100 – 250 mg/mL (Fig. 3.8a, 3.8b), in correlation with the lower viscosities (Fig. 3.4a). However, there does not appear to be a significant correlation between either σ or α and the solution viscosity across the broader set of co-solute systems (Fig. 3.18c, 3.18d). Similarly, the polydispersity as quantified by the probability distribution of the diffusion crossover time $a(\tau_D)$ (shown only for 200 mg/mL in Fig. 3.20) calculated from σ (Eqn. 3.10) and the corresponding full-width at half-maximum (fwhm) for the probability distribution of the corresponding hydrodynamic radii R_h (Eqn. 3.11, Fig. 3.20) do not appear to differ significantly between co-solute systems whether in terms of the mAb concentration (Fig. 3.22a) or the solution viscosity (Fig. 3.22b).

3.5 DISCUSSION

3.5.1 Breakdown of the generalized Stokes-Einstein relation: PPI and the length-scale dependent viscosity

The apparent deviation of mAb2's long-time translational self-diffusion D_0/D_s from the generalized Stokes-Einstein (GSE) relation ($D_0/D_s \neq \eta_{rel}$) is in contrast with the behavior seen for the model proteins αB-crystallin, bovine serum albumin (BSA) and lysozyme in previous studies using FCS (81) and NMR (75, 81). In measurements of the three model proteins using the same protein as both the probe and crowder, the long-time self-diffusion followed the GSE relation with respect to the macroscopic viscosity (81). However, when a much smaller protein (CI2, MW = 7.4 kDa) was used as the probe, both BSA and lysozyme exhibited mild to significant positive deviation of D_0/D_s from GSE (75). mAb2 (which served as both the probe and the crowder) differed from both of these cases in that it exhibited a negative deviation from the GSE

relation across all tested co-solute formulations. This disparate behavior may be partially understood in the context of the local microviscosity from the length-scale dependent viscosity model developed by Holyst (53, 71-73).

As described earlier in the Introduction section, the apparent breakdown of the GSE relation is commonly seen for nanoprobes diffusing in complex media such as concentrated polymer or colloidal fluids (53, 70, 71) and polymer meshes (117). The decoupling of the diffusion and macroscopic viscosity was attributed to the nanoprobe experiencing a length-scale dependent local viscosity rather than the macroscopic viscosity (53, 71-73). Here the GSE relation may be modified, but with respect to the effective (length-scale dependent) microviscosity η_{eff} rather than the macroscopic viscosity η (71-73). In this empirical approach, η_{eff} is defined through the diffusion retardation factor ($D_0/D_s = \eta_{eff}/\eta_0$), and is a function of the size of the probe molecule relative to that of the particles that make up the fluid (polymer, protein, etc.). It also depends on the solution structure length scale ξ and interactions between the fluid particles, quantified by the parameter *b* in Eqn. 3.2 (72, 76). In the FCS measurements in this work, the probe is the same size as the mAb if the probe remains monomeric, but may become larger than the mAb if the probe self-associates (either labeled or unlabeled). The size ratio r_p/R_h is therefore equal to or slightly greater than 1. In this size ratio range, the probe still experiences the microviscosity rather than the macroviscosity (73, 76), leading to the negative deviation from GSE behavior. However, the microviscosity approaches the macroviscosity with increasing probe size. In this size regime, D_0/D_s also reports on the short length-scale PPI via b fit from this model, rather than simply following the macroscopic viscosity.

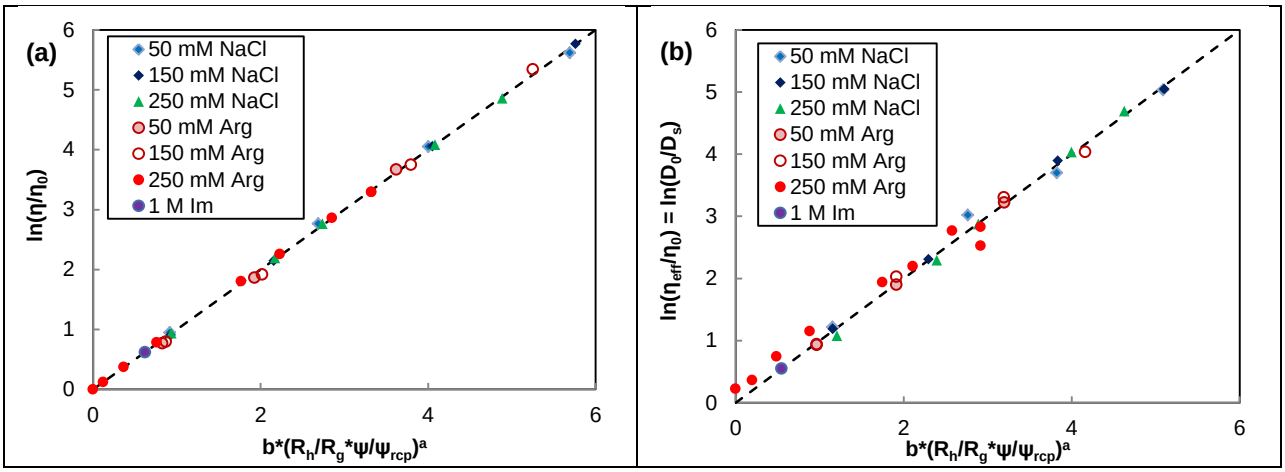

Figure 3.9. Scaling of the **(a)** micro (effective) relative viscosity and diffusion retardation factor and **(b)** macroscopic relative viscosity with the length-scale dependent model fits using an average *a* value (0.80 for the microscopic viscosity and 0.99 for the macroscopic viscosity) (Table 3.7) and formulation dependent fits of *b* (Table 3.3).

	Fit to microviscosity (D_0/D_s)			Fit to macroviscosity			Micro/macro b ratio	n_{rel} at 200 mg/ml
Formulation	**b**	**γ (kJ/mol)**	**R^2 of fit**	**b**	**γ (kJ/mol)**	**R^2 of fit**		
50 mM NaCl	10.35	25.64	0.988	13.63	33.76	0.999	0.76	57.4
150 mM NaCl	10.38	25.71	0.999	13.79	34.17	1.000	0.75	57.7
250 mM NaCl	10.82	26.81	0.970	13.90	34.43	1.000	0.78	59.4
50 mM Arg.HCl	8.66	21.44	0.999	12.33	30.54	0.998	0.70	39.2
150 mM Arg.HCl	8.65	21.43	0.993	12.92	32.01	0.998	0.67	42.4
250 mM Arg.HCl	7.90	19.57	0.948	11.31	28.01	1.000	0.70	27.0
1 M Imid(HCl)	4.91	12.16	0.966	9.21	22.82	0.993	0.53	14.5

Table 3.3. Co-solute effects on the interaction parameter *b* and corresponding interaction energy *γ* of mAb2 fit from the diffusion retardation factor D_0/D_s and macroscopic viscosity with the length-scale dependent viscosity model. The hydrodynamic parameter *a* was held fixed at 0.80 and 0.99 for the microviscosity and macroviscosity fits, respectively, based on the average value of *a* obtained from fits of the linearized length-scale dependent viscosity model (Eqn. 3.13) across all the co-solute formulations (Table 3.7)

The effects of both the mAb concentration and formulation on the deviation of η_{eff} from η can be seen from the ratio η_{eff}/η in Fig. 3.23. η_{eff} became increasingly smaller relative to η with increasing mAb concentration for all formulations, as well as with decreasing viscosity (i.e. co-solute formulation from most (NaCl) to least viscous (1 M Im)) for a given mAb concentration. The increasing degree of decoupling between η_{eff} and η reflects a combination of (i) the growing influence of the short-ranged PPI on the mAb dynamics with concentration and (ii) the probe size ratio r_0/R_h under the influence of self-association. To decouple the relative contributions of these two factors to the retardation of Ds, additional characterization of the concentrated mAb solutions from orthogonal techniques is needed, in combination with fits of the macroscopic and microviscosities to the LDV model.

The LDV model (Eqn. 3.13) was first applied to the macroscopic viscosity to determine the scaling parameter a for the hydrodynamic and structural contributions to the viscosity. No significant differences were seen for a between systems (Table 3.7, Fig. 3.24a), so a was averaged across all co-solute systems (excluding 1 M Im and 250 mM Arg, given the unusual diffusion behavior of 1 M Im, as well as the uncertainty and bias in the 250 mM Arg fit caused by the ultralow concentration (10, 30 mg/mL) data points) and held fixed at 0.99 for refitting the macroscopic viscosity to the LDV model to better isolate the influence of the PPI via the b parameter. Similarly, the a's fit from the microscopic viscosity (D0/Ds) were comparable across all formulations (Table 3.7, Fig. 3.24b) and a was therefore held fixed at the average value of 0.80 for subsequent refits. All of the co-solute systems were well-described by the model, as seen from the universal slope of 1 for the viscosity scaling plot for the micro and macro viscosities in Fig. 3.9a and 3.9b, respectively, as well as from the good fits of the calculated microscopic and macroscopic relative viscosities to the data seen in Fig. 3.25a and 3.25b. To determine whether the macroscopic a might still suitably describe the microviscosity, the microviscosity was also fit to the LDV model using the macroscopic a value of 0.99. However, it is clear from Fig. 3.25c

that the macroscopic scaling is unsuitable, given the large errors in the calculated microviscosity relative to the experimental values. Separate a values of 0.99 and 0.80 were therefore used for the comparisons of the LDV fits of the macro and microviscosities, respectively, in the remainder of this Discussion. The best-fit value of a close to 1 is consistent with macroscopic behavior, while fitted a of 0.80 for the microviscosity is comparable to the values obtained for entangled polymer systems (71, 72). Given that proteins behave more like colloids than polymers, it is likely that the cause of the stretched exponential ($a < 1$) is weak attractive interactions that perturb the diffusion behavior, rather than physical entanglements which slow diffusion.

Assuming that the probe remains monomeric (r_p is constant), a clear separation between co-solutes consistent with the macroscopic viscosity was seen in terms of the interaction parameter b (Table 3.3) for both the macro (ηrel) and micro-viscosity ($= D_0/D_s$) fits, reflecting the differences in PPI that contribute to the viscosity increase. The three NaCl formulations gave the largest b (strongest attraction), followed by the Arg formulations, and finally 1 M Imid with an attraction strength nearly 1/2 that of NaCl. The b parameter was larger for the macroscopic viscosity fits in general, which is consistent with the probe experiencing a macroscopic viscosity larger than the microviscosity. As this model is able to partially separate the combined structure and hydrodynamic effects (the $(R_{eff}/\xi)^a$ term) on D_0/D_s from those of the PPI effects (the b term) (72, 73, 76), the nearly identical values of a (Table 3.7) and corresponding hydrodynamic / structure term (Reff = Rh and ξ is the same between all co-solute systems for a given mAb concentration) therefore strongly suggest that the differences in the measured D_0/D_s between co-solute systems were caused by differences in the PPI rather than simply by steric or hydrodynamic effects.

This hypothesis is supported by the correlation between the HS-normalized D_s and the HS-normalized PPI quantified by the static structure factor S(0) measured previously for this

mAb (24) for 50 mM NaCl, 250 mM NaCl, 250 mM Arg (Fig. 3.26a). 1 M Im proved to be an exception with anomalously fast diffusion. It is important to note that S(0) is a thermodynamic quantity measured independently of dynamic behavior or hydrodynamic effects. At the same time, $S(0)/S(0)_{HS}$ is also correlated with the high concentration viscosity (Fig. 3.26b), similar to the correlation between the interaction energy γ (=b/RT) and the solution viscosity (Fig. 3.10a). Furthermore, the PPI strength (using a single parameter to describe the low-to-high concentration dynamic and structural behavior) quantified by b is monotonically correlated with the short-range attraction strength K obtained from fits of the concentration-dependent S(0) to the Yukawa interaction potential (Fig. 3.10b) for the mAb2 co-solute systems for which SLS S(0) data was available (24). Since FCS and SLS measure fundamentally different properties (dynamics vs static structure), the relation between b and K, as well as the similar dependence of ηrel on S(0)/S(0)HS strongly suggests that the correlation between D_0/D_s and macroscopic η_{rel} (Fig. 3.5b) is likely causal (i.e. D_0/D_s is influenced by PPI, which also influences viscosity) rather than incidental or self-referential. Again, it is important to note that D_0/D_s is not only reporting on the macroscopic viscosity, given the growing decoupling of η_{eff} and η with increasing concentration (Fig. 3.23).

Interestingly, the ratio of the microscopic to macroscopic b increased approaching 1 with increasing viscosity (Table 3.3), where a smaller ratio (< 1) corresponds to greater deviation of the microviscosity from the macroscopic viscosity. Since the microviscosity deviates from the macroviscosity due to length-scale effects (72), the increase in the b ratio (corresponding to the diffusing probe approaching macroscopic behavior) may indicate an increase in the probe size (73, 76) from self-association, as an alternative or complementary explanation for the varying degrees of deviation from GSE behavior between the different co-solute formulations. If the probe (labeled) mAb is incorporated into an oligomer, the probe size r_p increases. In contrast, the crowding agents (unlabeled mAb) will consist of a mix of monomer and oligomer, such that $r_p >$

$R_{h,avg}$. According to the LDV model, at $r_p/R_{h,avg} > 1$, the probe will experience a larger solution viscosity, closer to the macroscopic viscosity, than for a probe where $r_p/R_{h,avg} = 1$. The more GSE-like scaling of the mAb2 diffusion D_0/D_s with respect to the macroscopic viscosity for the more viscous systems (50 and 250 mM NaCl) would therefore be consistent with an increase in probe size, which may in turn be attributed to the greater degree of self-association seen for mAb2 previously in those formulation conditions, based on the larger effective average cluster sizes $<N_c>$ and larger oligomer mass ratios determined from SLS and SAXS (24, 25). This relation between self-association and more Stokes-Einstein like diffusion behavior can be seen in Table 3.4, where the larger η_{eff}/η (less deviation from GSE) for 50 and 250 mM NaCl correspond with larger $<N_c>$ and oligomer mass ratios from SLS (24). In contrast, the near complete suppression of the attractive PPI and corresponding self-association by 1 M Imid results in the probe mAb remaining monomeric ($r_p/R_{h,avg} < 1$) and experiencing the smallest possible microviscosity. Thus the smaller D_0/D_s and greater deviation from GSE behavior of the least viscous formulations (1 M Im, 250 mM Arg) may be attributed to a combination of weaker PPI (smaller b) and less self-association (smaller $r_p/R_{h,avg}$). However, the current level of information available is insufficient to decouple the contributions of these two factors to D_0/D_s further. Future studies with non-associating probes (such as eGFP and molecular dyes) in combination with this work may better provide insight into the independent influences of self-association vs PPI on D_0/D_s.

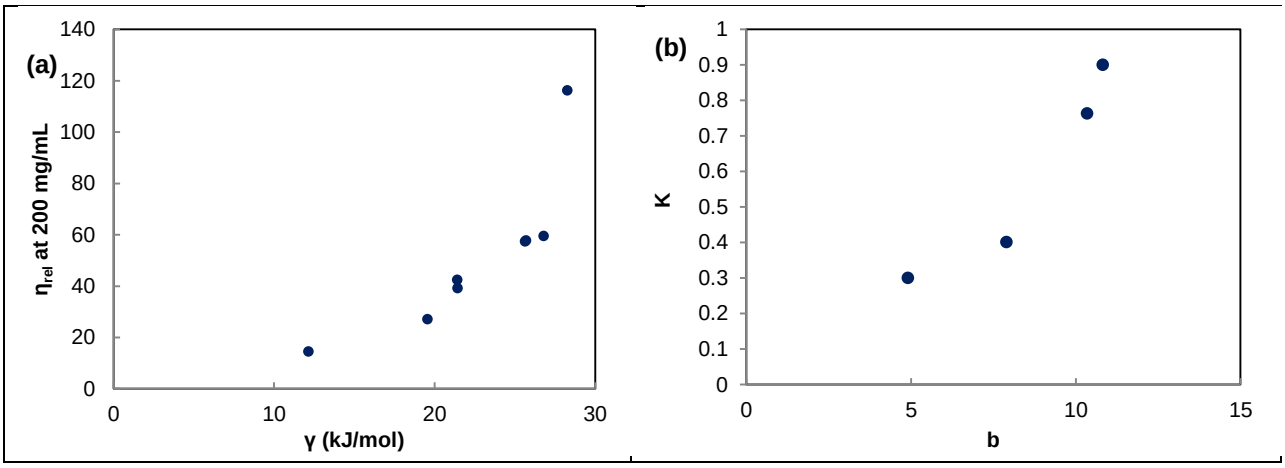

Figure 3.10. Correlation between **(a)** the relative macroscopic viscosity of mAb2 at 200 mg/mL and the interaction energy γ calculated from fits of D_0/D_s to the length-scale dependent viscosity model (72) across all tested co-solute formulations, and (b) the short-range attraction strength K from fits of the structure factor $S(0)$ from SLS (24) to the interaction parameter b ($b = \gamma/RT$) from the length-scale dependent viscosity model fit of D_0/D_s. SLS data was only available for mAb2 with 50 mM NaCl, 250 mM Nacl, 250 mM Arg.HCl and 1 M Im(HCl) at pH 5.5.

Formulation	η_{eff}/η_{macro}	$<N_c>$	Oligomer mass ratio
50 mM NaCl	0.70	2.8	6.6
250 mM NaCl	0.95	3.6	5.9*
250 mM Arg.HCl	0.46	1.8	0.0
1 M Im(HCl)	0.34	1.7	0.0

Table 3.4. Correlation of the deviation of the microviscosity from the macroscopic viscosity (η_{eff}/η_{macro}) from FCS (Fig. 3.23) with the average effective cluster size $<N_c>$ and oligomer mass ratio (relative to monomer and dimer) determined previously from SLS (24). All properties are evaluated at 200 mg/mL. All oligomer species are trimer, except for 250 mM NaCl, which is tetramer (24). SLS data was only available for selected co-solute formulations. The average cluster size for 250 mM Arg.HCl from SLS is comparable to the average aggregation number obtained under the same conditions (2.3 at 200 mg/mL) by SAXS (S(q) fit to the ALL4 association model for K = 0.7) (25).

The astute reader may notice that this analysis is very similar to conventional microrheology, where the diffusion coefficient of a large, inert probe such as polystyrene is measured by DLS or nanoparticle tracking in order to obtain the viscosity of concentrated protein

solutions (67, 68) via the GSE relation. Due to the large size ratio (the polymer bead probes used are typically an order of magnitude or more larger than the protein of interest), these probes experience the macroscopic viscosity (76). In contrast, the advantage of the FCS approach is that small probes on the same length scale as the crowder mAb can be used (i.e. the mAb is also the probe), allowing for access to the PPI on much smaller length scales. Furthermore, the differences in PPI between systems is magnified and more easily seen at the short length scales accessed by using small probes (size ratio << 1) (76), allowing for a deeper investigation and understanding of co-solute effects on the protein structure, dynamics and PPI on the time scales relevant to self-association and bulk viscosity.

3.5.2 Apparent decoupling of the viscosity from polydispersity measured by FCS

The seeming insensitivity of the mAb solution viscosity to the solution polydispersity, as measured by FCS, is surprising given the strong correlation between oligomer formation and high viscosities (10, 12, 13, 15, 16, 18). Specifically, the viscosity of mAb2 was found to correlate with the degree of self-association, as quantified by the oligomer mass ratios and average cluster sizes measured previously by SLS (24) as well as the cluster size distributions obtained previously from SAXS (25) as a function of co-solute formulation. Although it might be tempting to argue that perhaps there is no significant polydispersity in the solution, given the very small change in both α and σ with concentration from 60 – 250 mg/mL, it is also very likely that FCS is simply unable to detect polydispersity due to the combination of the transient nature of the reversible protein oligomers (60, 114, 118-121) and the long time scale of the FCS measurements. Reversible protein oligomers have been shown by neutron scattering experiments to be extremely short-lived, with lifetimes on the order of ns (18, 114). Given that the typical diffusion crossover time for a single probe is on the order of 1000 – 10,000 μs, a single mAb probe may exchange into multiple oligomer species and sample a wide range of configurations (monomer, dimer, oligomer) in the time it takes to cross through the confocal volume. However,

each mAb probe only reports a single, average crossover time τ_D. As such, while the solution itself may be highly polydisperse, the polydispersity may not be evident from the overall τ_D if the solution is uniformly polydisperse. Each probe may sample a similar distribution of monomer, dimer and oligomer as the other probes and report a similar (consistent) overall average τ_D, leading to an apparently monodisperse distribution of τ_D's. The relative solution composition (fraction monomer vs dimer vs oligomer) will influence the overall τ_D (solutions with more aggregates will have a larger τ_D), but may not significantly influence the polydispersity of the overall τ_D due to the fast equilibrium exchange process relative to the FCS measurement time scale. Furthermore, FCS has been shown to be relatively insensitive to small amounts of polydispersity, as seen from the large α's near 1 for polymer probes with known polydispersity (confirmed by GPC) (103) as well as for BSA and IgG (79), where anomalous diffusion was detected on the time scale of 1 μs from Brownian dynamics simulations, but not experimentally by FCS.

To interrogate the dynamics of individual oligomers and better quantify the solution polydispersity, ultrafast measurements of short-time self-diffusion using techniques such as neutron spin echo (NSE) and neutron back scattering (NBS) may be more conducive than measurements of long-time self-diffusion using FCS. The time scale of NBS/NSE measurements is on the order of 0.03 to 600 ns (78, 82), which is faster than the lifetime of the transient reversible oligomers (ranging from ~20 ns for small proteins such as α- and γ-crystallin (78) to ~50 ns for mAbs (18)) and therefore allows for direct observation of the caged dynamics of the oligomers. Although the availability of quasi-elastic neutron spin echo measurements is rare (18, 78, 82, 85, 86, 114, 119), this approach is of great value for probing small length scales $d \sim 2\pi/q$ where the scattering vector $q = (4\pi/\lambda)\sin(\theta/2)$ varied from 0.1 to 2.3 nm-1 (78). For α-crystallin, which behaved as a hard sphere, cage effects slowed down the short-time diffusion. A marked effect was observed for the influence of attractive patches on short-time diffusion (< 600 ns) at

these small length scales for γ_B-crystalline at high concentration. However, in some cases, the influence of direct interactions (tuned with the ionic strength) on the short-time self-diffusion was found to be negligible (80, 82). The lower limit of short-time diffusion is the time scale for hydrodynamic interactions, whereas the upper limit is the structural relaxation time, or R^2/D_o where R is the particle radius and D_o is the diffusion coefficient (78, 82). This upper limit was 5 μs, far below the time scale for FCS (> 100 μs), such that the diffusion measured by FCS is much longer ranged where the cage effect in the first coordination sphere is no longer important. Thus, FCS lacks the short-time resolution needed to probe the local protein microstructure inside the nearest-neighbor cage, but is instead more sensitive to the influence of interparticle interactions on the protein dynamics and local viscosity on the intermediate or long length scales relevant to the bulk solution behavior.

3.6 CONCLUSIONS

Reproducible measurements of mAb diffusion at high concentration (up to 250 mg/mL) and high viscosities (up to ~200 cP) in a range of co-solute formulations were successfully achieved by FCS after optimization of experimental methods to overcome the challenges associated with these conditions. Use of a dry slide passivation technique (silane-PEGylation) over wet passivation with lipid vesicles eliminated the challenges of sample heterogeneity from uneven mixing of highly viscous mAb solutions into the imaging well. Maintaining the focal depth close to the cover slip (3 μm) was sufficient to minimize optical distortion effects arising from the change in refractive index between samples (concentration and/or co-solute change) while also maximizing G(0) (which drastically decreases at high concentration) to improve the signal-to-noise ratio. The measured diffusion times was also shown to be insensitive to whether the labeled mAb probe was added to the mAb solution at low or high concentration (i.e. before or after large oligomers form), suggesting that the equilibrium monomer-oligomer exchange occurs on a fast-enough time scale that the probe is able to become incorporated into oligomers

and report on their diffusion in the time frame between probe addition and FCS measurements, even when the probe is added as a monomer to the concentrated mAb solution.

FCS was used to measure the retardation of the long-time self-diffusion D_0/D_s of mAb2 (24, 25) from low to high concentration (60 - 250 mg/mL) in the presence of NaCl or Arg (50, 150 or 250 mM), as well as 1 M Im(HCl) as a low viscosity extreme. The generalized Stokes-Einstein (GSE) relation was seen to break down for mAb2 with respect to the macroscopic viscosity, with the least viscous co-solute systems (1 M Im and 250 mM Arg) showing the greatest negative deviation from the GSE relation. The breakdown was attributed to length-scale dependent viscosity effects, given that the probe (labeled mAb) was the same size as the crowder (unlabeled mAb) (72, 74), causing the probe to experience a local microviscosity less than the macroscopic viscosity. The greater deviation of the solution microviscosity from the macroscopic viscosity for the lowest viscosity systems was attributed to a combination of weaker PPI (seen from the smaller interaction parameter b from fits of D_0/D_s to the length-scale dependent viscosity (LDV) model) and reduced self-association (based on previous SLS measurements of oligomer mass ratios and average cluster sizes for the same mAb and co-solute formulations) (24) leading to smaller $r_p/R_{h,avg}$ probe size ratios. The more GSE-like scaling between D_0/D_s and the macroscopic viscosity for the viscous formulations (50 – 250 mM NaCl) was consistent with the LDV model, given the larger probe size as a consequence of the greater degree of self-association seen previously by SLS and SAXS (24, 25) for those systems. However, while D_0/D_s was found to correlate with both the viscosity and PPI (as measured by orthogonal techniques such as SLS), the polydispersity obtained from fits of the FCS ACFs to both the anomalous diffusion and Gaussian distribution models appeared to be decoupled from the viscosity, despite evidence of greatly contrasting degrees of oligomer formations in the different formulations as seen by SLS (24) and SAXS (25) for the same mAb. The apparent inability of FCS to detect significant differences in the solution polydispersity is likely because

the dynamic behavior of the oligomers is averaged out, given the fast equilibrium monomer-oligomer exchange process relative to the time scale of the FCS measurements.

3.7 ACKNOWLEDGMENTS

The authors would like to acknowledge Carl Hayden (Sandia National Laboratories) as well as Wilton Snead and Justin Houser from the Stachowiak group at the University of Texas at Austin for helpful recommendations and technical assistance with the dry-passivation technique and troubleshooting of the fluorescence correlation spectroscopy instrument and setup. The authors also gratefully acknowledge financial support from the Welch Foundation (F-1319) and Merck and Company, Inc.

3.8 SUPPORTING INFORMATION

3.8.1 Preparation of labeled mAb stock solution

Stock solutions of fluorescently labeled mAb2 were prepared by conjugation of Atto-488 NHS ester to primary amines on the mAb surface. Briefly, a 5 mg/mL stock solution of mAb2 was buffer-exchanged into 150:150 mM $NaHCO_3$:NaCl (pH 8.3) solution using Centri-Spin 20 SEC columns (Princeton Separations, Adelphia, NJ) that had been hydrated in advance in the pH 8.3 $NaHCO_3$:NaCl buffer for 30 minutes. The mAb concentration was measured after buffer exchange using a NanoDrop 2000 UV-Vis spectrophotometer (Thermo Fisher Scientific, Waltham, MA). Atto-488 was dissolved in DMSO at 10 mM and stored at -80°C prior to use. The thawed dye was added to the pH 8.3 buffer-exchanged mAb solution at a 1:1 dye:mAb molar ratio for the labeling reaction. The amount of DMSO in the labeling reaction mixture (from the dye stock) did not exceed 1% v/v. The dye-mAb mix was kept in a dark environment (to avoid photobleaching) and allowed to react for 30 minutes at room temperature. Unreacted dye was then removed by buffer exchanging the labeled mAb solution (containing the unbound dye) back into the 21:30 mM Na:OAc (pH 5.5) solution with Centri-Spin 20 SEC columns.

The dye and mAb concentrations after buffer exchange were checked with the NanoDrop spectrophotometer. The dye absorbance was measured at 501 nm with an extinction coefficient of 90000 $M^{-1}cm^{-1}$, and the mAb absorbance was measured at 280 nm with an extinction coefficient of 213,000 $M^{-1}cm^{-1}$ (1.42 $mL*mg^{-1}cm^{-1}$ converted to molar concentration units). The absorbance at 280 nm was also corrected for contributions from the dye fluorescence ($A_{280,mAb} = A_{280,total} - 0.1*A_{501}$) prior to calculating the mAb concentration. The typical labeled mAb concentration after buffer exchange was ~25 μM, and the typical dye to mAb molar ratio was 0.7:1.

The labeled mAb solution was split into 20 μL aliquots in PCR tubes, frozen in liquid nitrogen, and kept frozen at -20°C prior to use. Aliquots were individually thawed up to 3 – 4 hours prior to their addition to unlabeled, concentrated mAb samples for fluorescence correlation spectroscopy (FCS) measurements.

3.8.2 Slide cleaning and passivation – wet passivation

Due to the high sensitivity of FCS measurements to optical artifacts introduced by dust and protein adsorption to the imaging surface, the glass cover slips used to hold the mAb samples were cleaned and passivated to resist protein adsorption. In the wet passivation technique (93, 94) (used only for the initial method development experiments), a thin liquid film of adsorbed DOPC (1,2-dioleoyl-sn-glycero-3-phosphocholine) vesicles was used to prevent protein adsorption on the glass surface. A stock solution of DOPC vesicles was prepared by first drying the DOPC solution as received from the vendor (dissolved in chloroform at 0.0127 M) under a N_2 stream and subsequently under vacuum for two hours. The dried DOPC was then reconstituted at 500 μM in the same buffer as the mAb samples (21:30 mM Na:OAc, pH 5) and probe sonicated in an ice bath to form small unilamellar vesicles. The DOPC solution was then centrifuged at 17,000g for 6 minutes to sediment metal particulates shed by the sonicator probe,

and the supernatant was filtered using 0.22 μm filters into low-adhesion microcentrifuge tubes. The DOPC stock solution was stored at 4°C for up to 1 week prior to use.

The glass cover slips were cleaned by soaking in a hot (lightly steaming) solution of 2% v/v Hellmanex III cleaning detergent for 30 minutes in glass carafes. The cover slips were then flushed with an excess of ultrapure water (drain/refill the carafe 10 times with water) to remove the detergent. The cover slips were then individually washed under running ultrapure water and dried under a N_2 stream. The cleaned silicone gaskets (as described in the Methods section) were gently pressed onto the top of the cleaned cover slips to create a temporary water-tight seal to form the imaging well. 20 μL of the 500 μM DOPC stock solution was added to the well and allowed to sit for 5 minutes to generate a thin layer of adsorbed DOPC vesicles. Excess DOPC vesicles were removed by by serially rinsing the liquid in the imaging well with excess mAb buffer (21:30 mM Na:OAc), resulting in a dilution of ~16,000-fold.

3.8.3 Slide cleaning and passivation – dry passivation

An alternative dry passivation technique was used in later experiments due to its superior performance for high concentration measurements relative to the wet passivation used in earlier method development experiments.

In the dry passivation technique, the glass cover slips were cleaned using a modified RCA protocol (95, 122) and passivated with a coupled silane-PEG layer to prevent protein adsorption (95, 97). Briefly, the cover slips were first soaked in ethanol for 10 minutes and simultaneously sonicated to dislodge organic contaminants. The cover slips were then flushed with an excess of ultrapure water to remove all organic solvents. The cover slips were then soaked in a hot (70 - 80°C) solution of 30% hydrogen peroxide in 1.5 M KOH for 10 minutes in glass carafes to etch the glass surface. IT IS CRITICAL that all trace organic solvent (ethanol) be removed prior to addition of the peroxide/KOH mixture, as peroxide will react with the ethanol and cause explosive boiling. Similarly, the KOH/peroxide mixture should be prepared by slowly

adding the peroxide to the KOH solution in order to prevent rapid, uncontrolled boiling of the mixture. The KOH/peroxide solution was then drained, and the cover slips were flushed with an excess of ultrapure water. The cover slips were then soaked in a hot (70 - 80°C) bath of 30% hydrogen peroxide in 2.4 M HCl for 10 minutes as a second, polishing etching step. The HCl/peroxide mixture was similarly prepared by slow addition of the peroxide to avoid rapid boiling of the solution. The HCl/peroxide solution was then drained, and the cover slips were flushed with an excess of ultrapure water. The slides were then dried under a N_2 stream.

The dried RCA-cleaned cover slips were passivated by coupling of a PEG-silane layer to the glass surface. Briefly, a 5 mg/mL solution of mPEG-silane-5000 was prepared in anhydrous isopropanol, where both the isopropanol and mPEG-silane (which is oxygen-reactive) were handled under a pure N2 atmosphere (using a Spilfyter "Hands-in-bag" artificial atmospheric chamber purchased from VWR International (Radnor, PA) to prevent contact with air). 1% v/v glacial acetic acid was added to catalyze the coupling reaction between the silane group and the OH- groups on the etched glass surface. 50 μL drops of the PEG-silane solution were placed on one cover slip, and a second cover slip was placed over the first one to sandwich the PEG-silane liquid film between the two cover slips, spreading out the PEG-silane solution evenly over the entire slide surface. The back (un-passivated) sides of the slides were marked for easier identification of the passivated surface. The cover slip/PEG-silane 'sandwiches' were then dried at 70°C for ~30 minutes to remove the isopropanol. The slides were then separated from each other by immersing the slide 'sandwiches' in ultrapure water and gently prying them apart underwater with tweezers. The passivated slides were then individually rinsed 2 – 3 times with ultrapure water and dried under a N_2 stream, before being stored in glass carafes under air prior to use. The passivated slides were used within 1 week of preparation.

3.8.4 Serial addition scheme for loading mAb samples onto wet-passivated slides

Due to the presence of 20 μL buffer present from DOPC passivation, it was necessary to add the labeled mAb sample to the imaging well using a serial addition scheme to minimize dilution. The mAb sample was added in a 4-step addition scheme to bring the final mAb concentration in the well to 95.83% of the original sample concentration. In this scheme, 20 μL of mAb sample was mixed into the imaging well by pipetting, and 20 μL of the mixed solution (out of the total 40 μL now in the well) was withdrawn. This step was repeated two more times, and in a final (4th) addition, 40 μL of the original labeled sample was added. This scheme can alternatively be seen as serial dilution of the original buffer in the imaging well to 4.17% v/v of the final solution in the imaging well, with the remaining 95.83% of the solution volume corresponding to the original (undiluted) mAb sample. Due to the high viscosity of the mAb solutions, the viscous mAb solution had to be gently mixed with the non-viscous buffer by pipetting over several minutes until the solution in the well was homogenous.

3.8.5 Converting the probability distribution of τ_D to the fwhm of the Rh probability distribution

The width of the probability distribution in terms of $\ln(\tau_D)$ can be converted to a full-width at the half-maximum (fwhm) of the probability distribution peak for the corresponding R_h. Briefly, the normalized probability for a given $\tau_{D,i}$ must be numerically equal to the normalized probability for the corresponding $R_{h,i}$. Thus $a_i(\tau_{Di}) = a_i(R_{h,i})$ and

$$A * \exp\left[-\left(\frac{(ln(\tau_{Di})-ln(\tau_p))}{\sqrt{2}\ln(\sigma)}\right)^2\right] = A' * \exp\left[-\left(\frac{(ln(R_{h,i})-ln(\overline{R_h}))}{\sqrt{2}\ln(\sigma')}\right)^2\right] \quad (3.16)$$

Combining with Eqn. 3.7 and 3.8 gives

$$A * \exp\left[-\left(\frac{(ln(\tau_{Di})-ln(\tau_p))}{\sqrt{2}\ln(\sigma)}\right)^2\right] = A' * \exp\left[-\left(\frac{(ln(\tau_{Di})-ln(\tau_p))}{\sqrt{2}\ln(\sigma')}\right)^2\right] \quad (3.17)$$

which can only hold if A = A' and σ = σ'. The fwhm in terms of ln(R_h) can then be calculated directly from σ as $\sqrt{2\ln(2)}\ln(\sigma)$. However, the fwhm in terms of R_h must be determined from the difference ($R_{h,2} - R_{h,1}$), where the two R_h's are the upper and lower endpoints respectively of the distribution curve at half maximum height, centered around the average value $\overline{R_h} = \frac{4k_BT\tau_p}{6\pi\eta\omega_{xy}^2}$ calculated from τ_p. The two endpoints can be determined as

$$\ln(R_{h,2}) = \ln(\overline{R_h}) + \sqrt{2\ln(2)}\ln(\sigma) \quad (3.18)$$

$$\ln(R_{h,1}) = \ln(\overline{R_h}) - \sqrt{2\ln(2)}\ln(\sigma) \quad (3.19)$$

leading to the fwhm in terms of R_h (Eqn. 3.11).

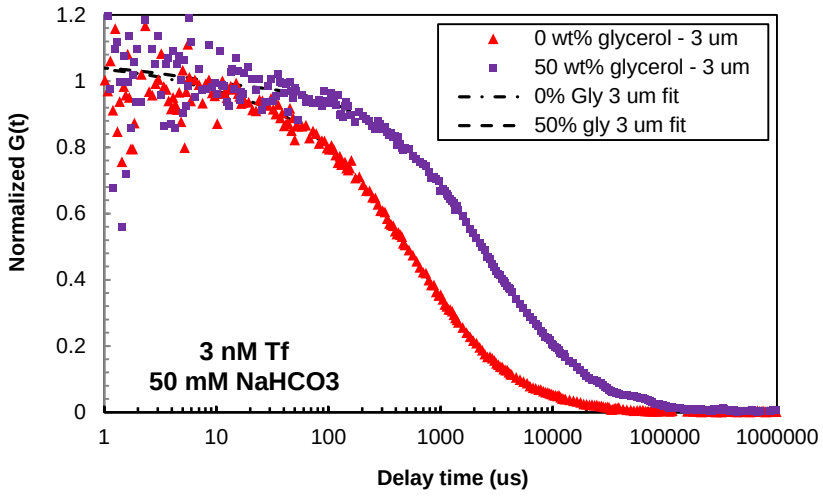

Figure 3.11. Effect of the solution refractive index (RI) on the normalized ACF of Atto488-labeled holo-transferrin in 50 mM NaHCO3 (pH 8.3). The RI were chosen to replicate the solution refractive index at the lowest (~1 mg/mL) and highest (~250 mg/mL) mAb concentrations. The transferrin ACFs were used to calibrate the confocal volume waist radius (Table 3.4) and determine if there were RI effects on the waist radius across the range of RI values relevant to the high concentration mAb FCS measurements. The samples were loaded on dry-passivated slides.

Focal depth (µm)	Glycerol conc (wt %)	Solution RI	η_0 (cP)	τ_D (µs)	α	Calc ω_{xy} from lit value of Tf D_0 (nm)
3	0	1.33	0.89	696 ± 28	0.81 ± 0.01	432 ± 8.8
3	50	1.41	4.97	3284 ± 130	0.84 ± 0.01	421 ± 8.3

Table 3.4. Dependence of the calibrated confocal volume waist radius on the solution refractive index (RI). The waist radius ω_{xy} was calculated from τ_D obtained from the 3D anomalous diffusion fits of the ACF of Atto488-labeled holo-transferrin in 0 and 50 wt% glycerol (Fig. 3.11) using the known value[6] of D_0 of 6.7*10^{-7} cm^2/s for holo-transferrin at 25°C in water, corrected for the solvent viscosity η_0. The samples were loaded on dry-passivated slides. ω_{xy} was taken as the average value 427 ± 6.1 nm.

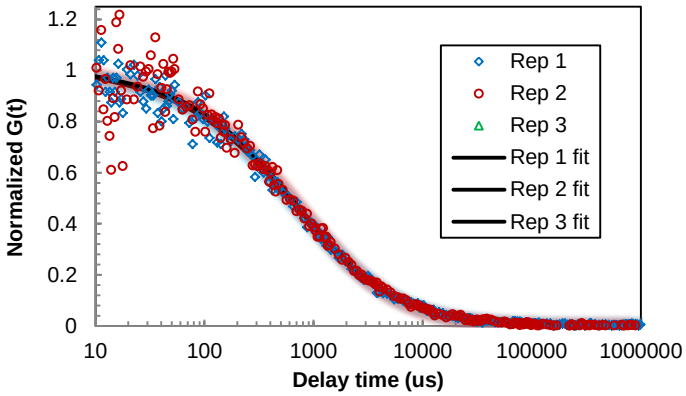

Figure 3.12. Normalized ACF of 1 nM Atto488-labeled mAb2 in buffer (21:30 mM Na:OAc, pH 5) measured in triplicate using wet-passivated slides. The ACF was fit to the 3D anomalous diffusion model (α = 0.81 ± 0.03), and the fitted τ_D of 846 ± 25 µs was used as the monomer diffusion time for calculating D_s/D_0 of mAb2 at high concentration in 250 mM PheOMe(HCl) (Fig. 3.13)

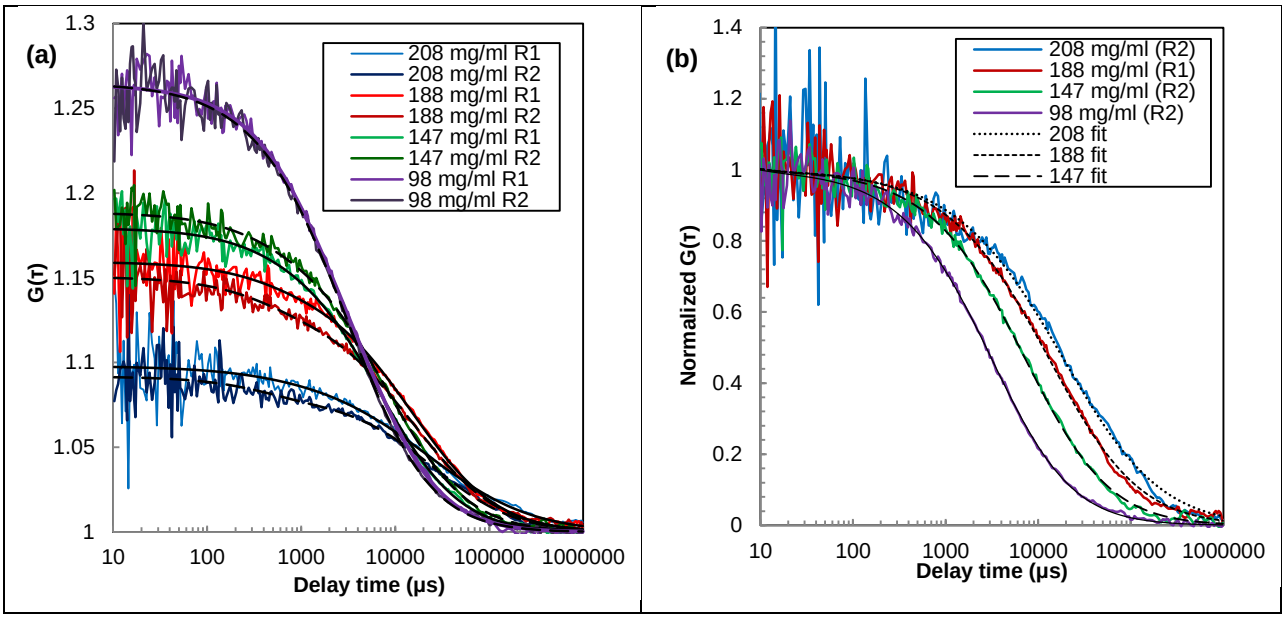

Figure 3.13. Concentration dependence of the (a) non-normalized and (b) normalized FCS ACFs of mAb2 in 250 mM PheOMe(HCl) at pH 5.5. Samples were loaded on wet-passivated slides. The corresponding τ_D, α and D_s/D_0 fit from the ACFs are reported in Table 3.5. Smoothed solid/dashed black curves show fits of the ACFs to the anomalous 3D diffusion model.

mAb conc (mg/mL)	G(0) (Not normalized)	τ_D (μs)	D_s/D_0	α
98	1.26	3872 ± 195	0.22 ± 0.01	0.85 ± 0.01
147	1.18	8211 ± 666	0.10 ± 0.01	0.83 ± 0.03
188	1.15	15262 ± 918	0.06 ± 0.00	0.74 ± 0.04
208	1.09	23640 ± 875	0.04 ± 0.00	0.71 ± 0.00

Table 3.5. Concentration dependence of the diffusivity D_s/D_0 and corresponding anomaly coefficient α of mAb2 in 250 mM PheOMe(HCl) at pH 5.5 fit from the ACFs in Fig. 3.13 to the anomalous 3D diffusion model. D_s/D_0 was calculated from the ratio of the monomer $\tau_{D,0}$ of 846 μm (Fig. 3.12) to τ_D.

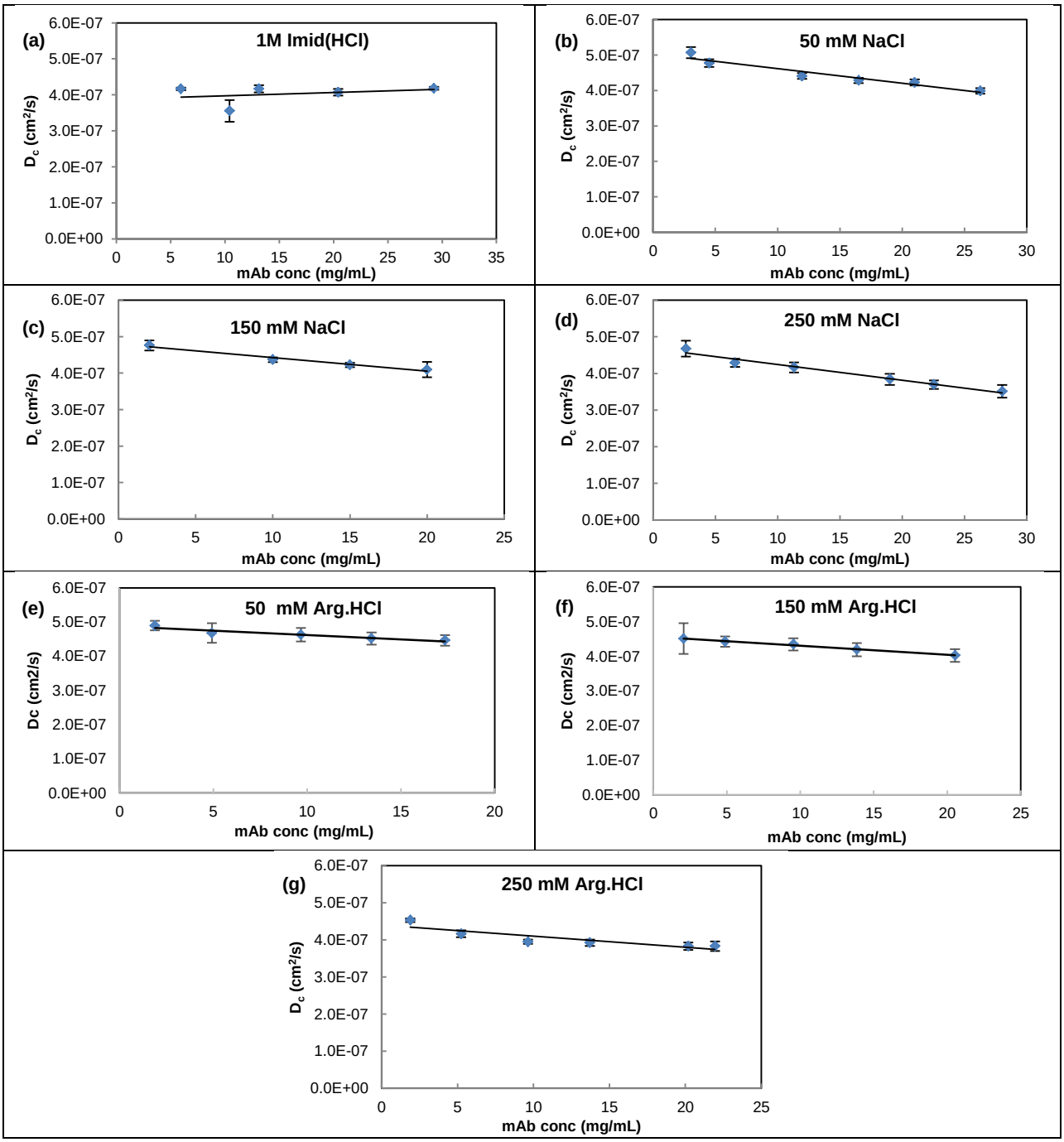

Figure 3.14. Dependence of D_c (~D_z) of mAb2 from 2 – 20 mg/mL in different co-solute formulations as measured by DLS. D_0 was obtained from linear fits of D_c vs concentration to Eqn. 3.5. The formulations are **(a)** 1 M Im(HCl) titrated to pH 5.5, **(b)** 50 mM NaCl, **(c)** 150 mM NaCl, **(d)** 250 mM NaCl, **(e)** 50 mM Arg.HCl, **(f)** 150 mM Arg.HCl, **(g)** 250 mM Arg.HCl.

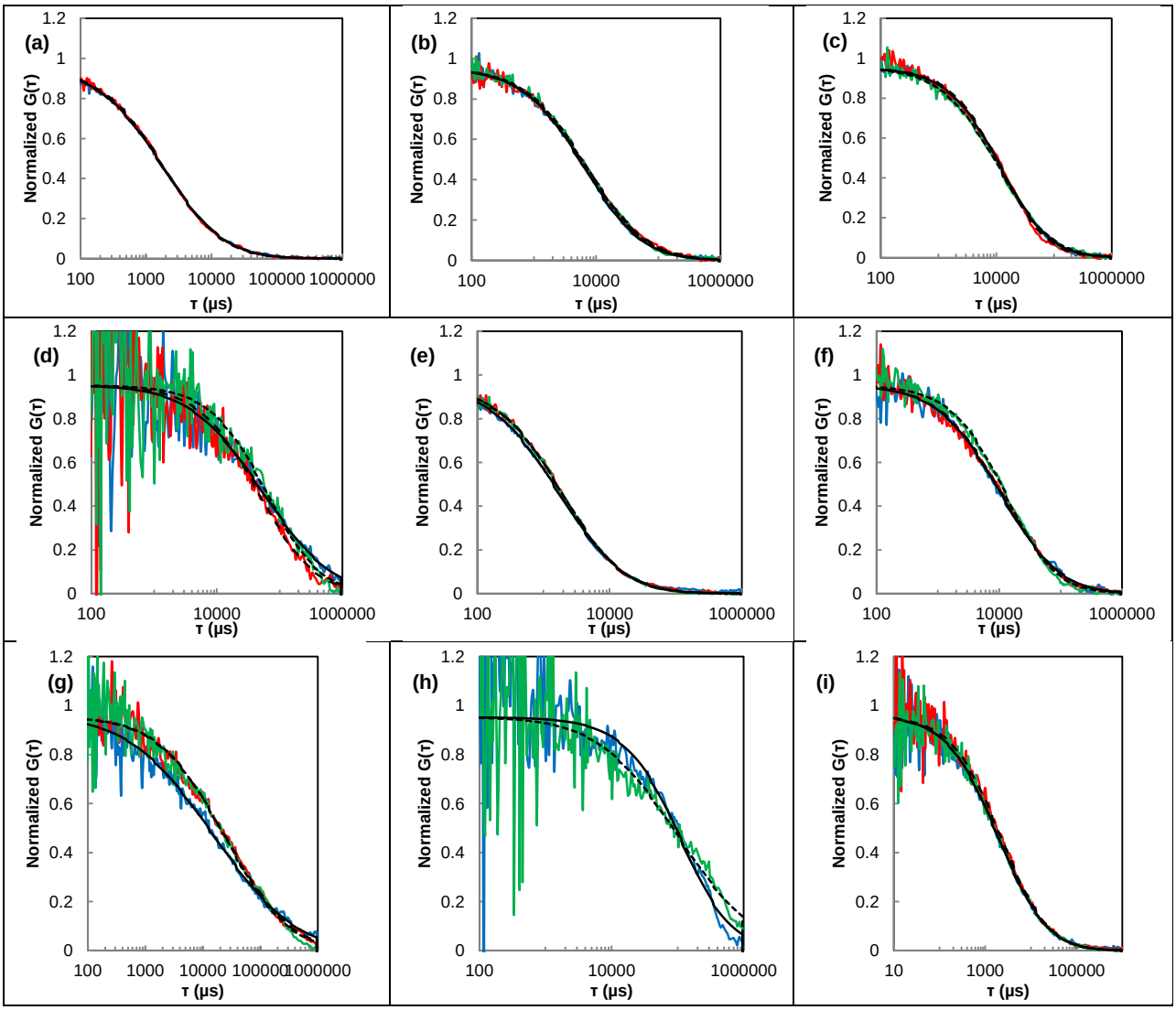

Figure 3.15. Normalized autocorrelation function (ACF) replicates of mAb2 for all co-solute systems at 60, 125, 150, 200, ~225 and ~250 mg/mL. The ACFs were normalized by the G(0) values of the raw ACFs (Table 3.6). ACFs are shown for 5 mM $ZnSO_4$ at **(a)** 60 mg/mL, **(b)** 125 mg/mL, **(c)** 150 mg/mL, **(d)** 200 mg/mL; 50 mM NaCl at **(e)** 60 mg/mL, **(f)** 150 mg/mL, **(g)** 200 mg/mL, **(h)** 250 mg/mL; 150 mM NaCl at **(i)** 60 mg/mL, **(j)** 150 mg/mL, **(k)** 200 mg/mL, **(l)** 250 mg/mL; 250 mM NaCl at **(m)** 60 mg/mL, **(n)** 125 mg/mL, **(o)** 150 mg/mL, **(p)** 200 mg/mL, **(q)** 219 mg/mL; 50 mM Arg.HCl at **(r)** 60 mg/mL, **(s)** 125 mg/mL, **(t)** 200 mg/mL; 150 mM Arg.HCl at **(u)** 60 mg/mL, **(v)** 125 mg/mL, **(w)** 200 mg/mL, **(x)** 250 mg/mL; 250 mM Arg.HCl at **(y)** 60 mg/mL, **(z)** 125 mg/mL, **(aa)** 150 mg/mL, **(ab)** 200 mg/mL, **(ac)** 225 mg/mL, **(ad)** 250 mg/mL; 1 M Imid(HCl) **(ae)** 60 mg/mL, **(af)** 125 mg/mL, **(ag)** 150 mg/mL, **(ah)** 200 mg/mL, and **(ai)** 241 mg/mL.

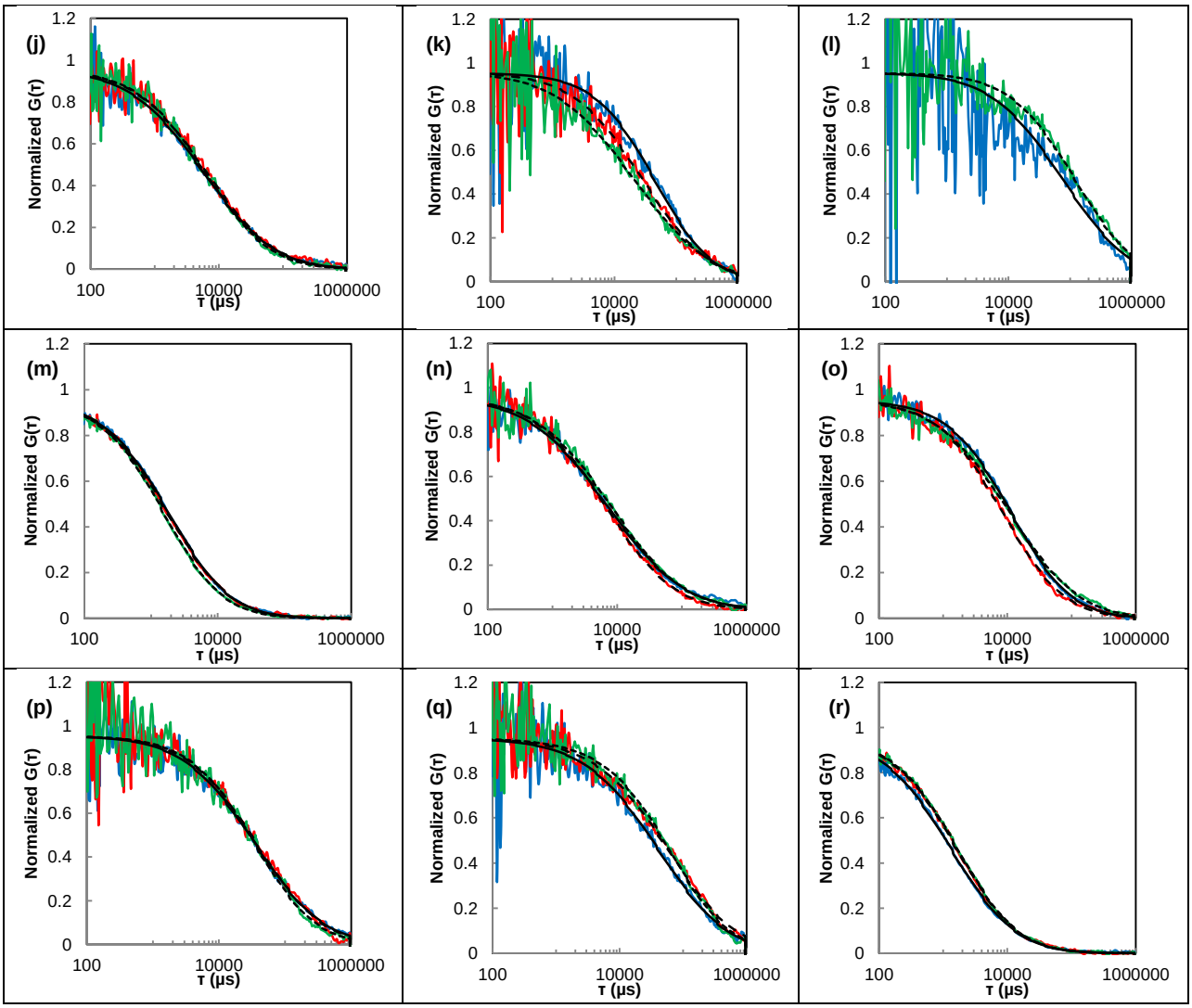

Figure 3.15 cont. Normalized autocorrelation function (ACF) replicates of mAb2 for all co-solute systems at 60, 125, 150, 200, ~225 and ~250 mg/mL. The ACFs were normalized by the G(0) values of the raw ACFs (Table 3.6). ACFs are shown for 5 mM $ZnSO_4$ at **(a)** 60 mg/mL, **(b)** 125 mg/mL, **(c)** 150 mg/mL, **(d)** 200 mg/mL; 50 mM NaCl at **(e)** 60 mg/mL, **(f)** 150 mg/mL, **(g)** 200 mg/mL, **(h)** 250 mg/mL; 150 mM NaCl at **(i)** 60 mg/mL, **(j)** 150 mg/mL, **(k)** 200 mg/mL, **(l)** 250 mg/mL; 250 mM NaCl at **(m)** 60 mg/mL, **(n)** 125 mg/mL, **(o)** 150 mg/mL, **(p)** 200 mg/mL, **(q)** 219 mg/mL; 50 mM Arg.HCl at **(r)** 60 mg/mL, **(s)** 125 mg/mL, **(t)** 200 mg/mL; 150 mM Arg.HCl at **(u)** 60 mg/mL, **(v)** 125 mg/mL, **(w)** 200 mg/mL, **(x)** 250 mg/mL; 250 mM Arg.HCl at **(y)** 60 mg/mL, **(z)** 125 mg/mL, **(aa)** 150 mg/mL, **(ab)** 200 mg/mL, **(ac)** 225 mg/mL, **(ad)** 250 mg/mL; 1 M Imid(HCl) **(ae)** 60 mg/mL, **(af)** 125 mg/mL, **(ag)** 150 mg/mL, **(ah)** 200 mg/mL, and **(ai)** 241 mg/mL.

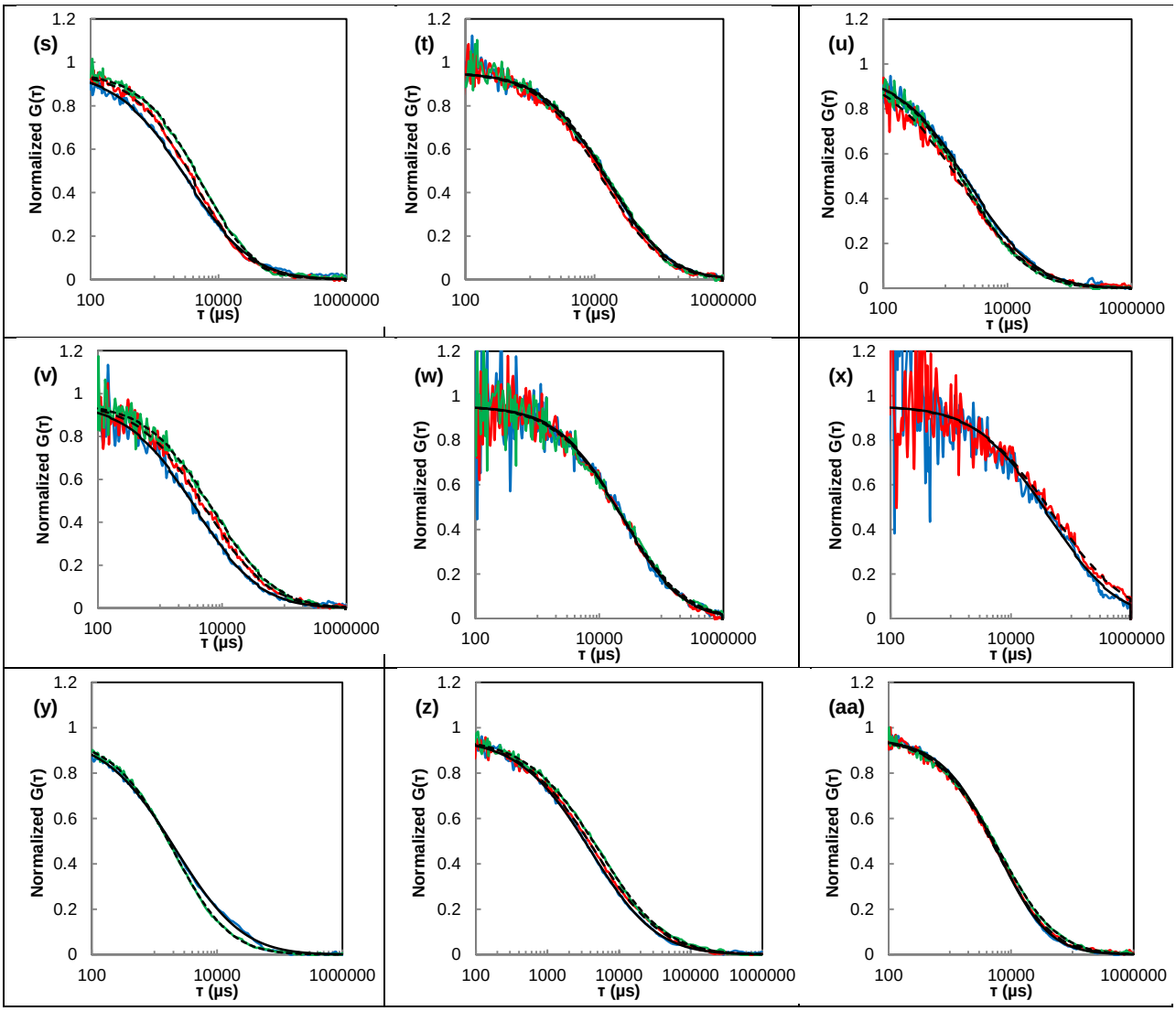

Figure 3.15 cont. Normalized autocorrelation function (ACF) replicates of mAb2 for all co-solute systems at 60, 125, 150, 200, ~225 and ~250 mg/mL. The ACFs were normalized by the G(0) values of the raw ACFs (Table 3.6). ACFs are shown for 5 mM $ZnSO_4$ at **(a)** 60 mg/mL, **(b)** 125 mg/mL, **(c)** 150 mg/mL, **(d)** 200 mg/mL; 50 mM NaCl at **(e)** 60 mg/mL, **(f)** 150 mg/mL, **(g)** 200 mg/mL, **(h)** 250 mg/mL; 150 mM NaCl at **(i)** 60 mg/mL, **(j)** 150 mg/mL, **(k)** 200 mg/mL, **(l)** 250 mg/mL; 250 mM NaCl at **(m)** 60 mg/mL, **(n)** 125 mg/mL, **(o)** 150 mg/mL, **(p)** 200 mg/mL, **(q)** 219 mg/mL; 50 mM Arg.HCl at **(r)** 60 mg/mL, **(s)** 125 mg/mL, **(t)** 200 mg/mL; 150 mM Arg.HCl at **(u)** 60 mg/mL, **(v)** 125 mg/mL, **(w)** 200 mg/mL, **(x)** 250 mg/mL; 250 mM Arg.HCl at **(y)** 60 mg/mL, **(z)** 125 mg/mL, **(aa)** 150 mg/mL, **(ab)** 200 mg/mL, **(ac)** 225 mg/mL, **(ad)** 250 mg/mL; 1 M Imid(HCl) **(ae)** 60 mg/mL, **(af)** 125 mg/mL, **(ag)** 150 mg/mL, **(ah)** 200 mg/mL, and **(ai)** 241 mg/mL.

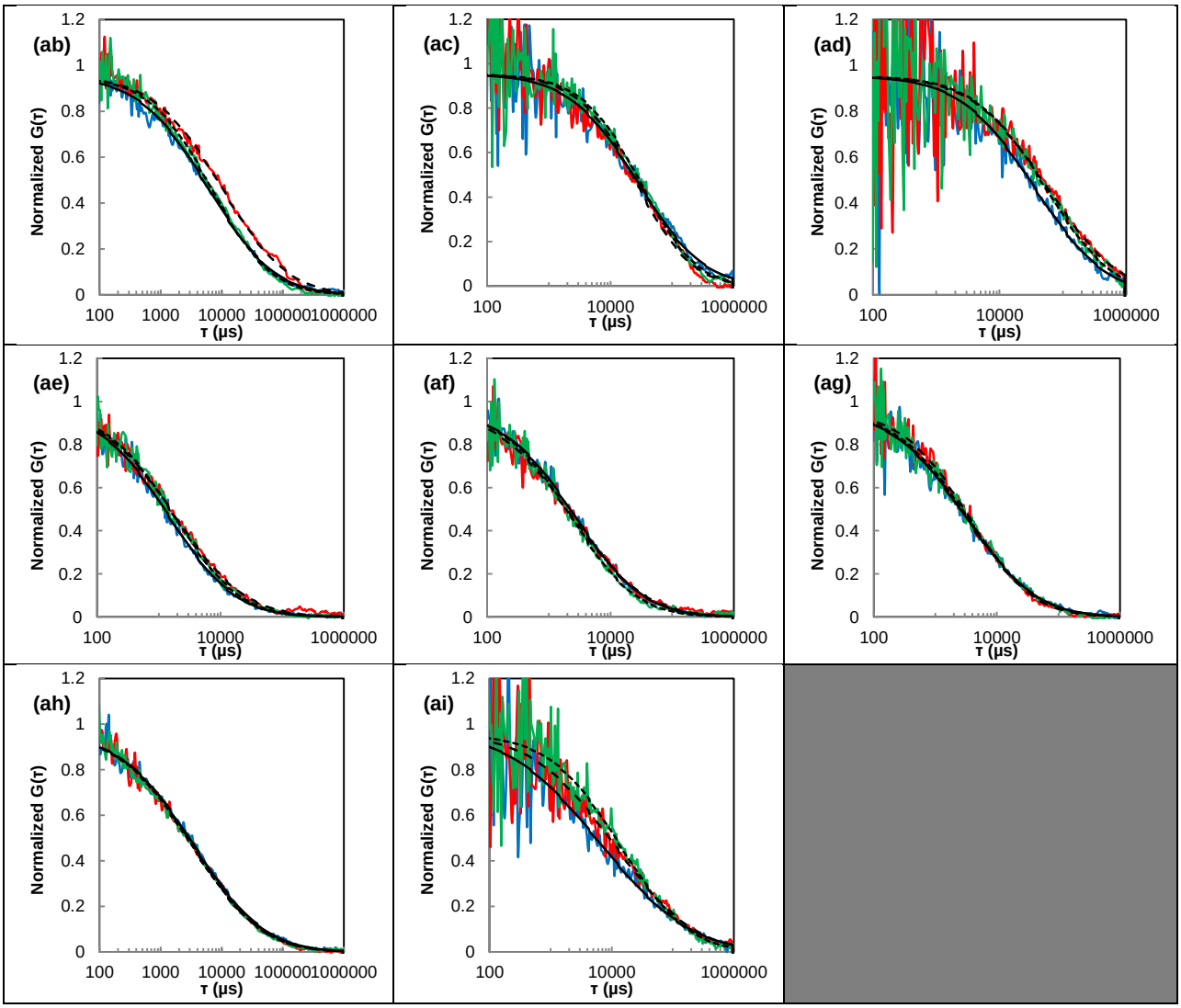

Figure 3.15 cont. Normalized autocorrelation function (ACF) replicates of mAb2 for all co-solute systems at 60, 125, 150, 200, ~225 and ~250 mg/mL. The ACFs were normalized by the G(0) values of the raw ACFs (Table 3.6). ACFs are shown for 5 mM $ZnSO_4$ at **(a)** 60 mg/mL, **(b)** 125 mg/mL, **(c)** 150 mg/mL, **(d)** 200 mg/mL; 50 mM NaCl at **(e)** 60 mg/mL, **(f)** 150 mg/mL, **(g)** 200 mg/mL, **(h)** 250 mg/mL; 150 mM NaCl at **(i)** 60 mg/mL, **(j)** 150 mg/mL, **(k)** 200 mg/mL, **(l)** 250 mg/mL; 250 mM NaCl at **(m)** 60 mg/mL, **(n)** 125 mg/mL, **(o)** 150 mg/mL, **(p)** 200 mg/mL, **(q)** 219 mg/mL; 50 mM Arg.HCl at **(r)** 60 mg/mL, **(s)** 125 mg/mL, **(t)** 200 mg/mL; 150 mM Arg.HCl at **(u)** 60 mg/mL, **(v)** 125 mg/mL, **(w)** 200 mg/mL, **(x)** 250 mg/mL; 250 mM Arg.HCl at **(y)** 60 mg/mL, **(z)** 125 mg/mL, **(aa)** 150 mg/mL, **(ab)** 200 mg/mL, **(ac)** 225 mg/mL, **(ad)** 250 mg/mL; 1 M Imid(HCl) **(ae)** 60 mg/mL, **(af)** 125 mg/mL, **(ag)** 150 mg/mL, **(ah)** 200 mg/mL, and **(ai)** 241 mg/mL.

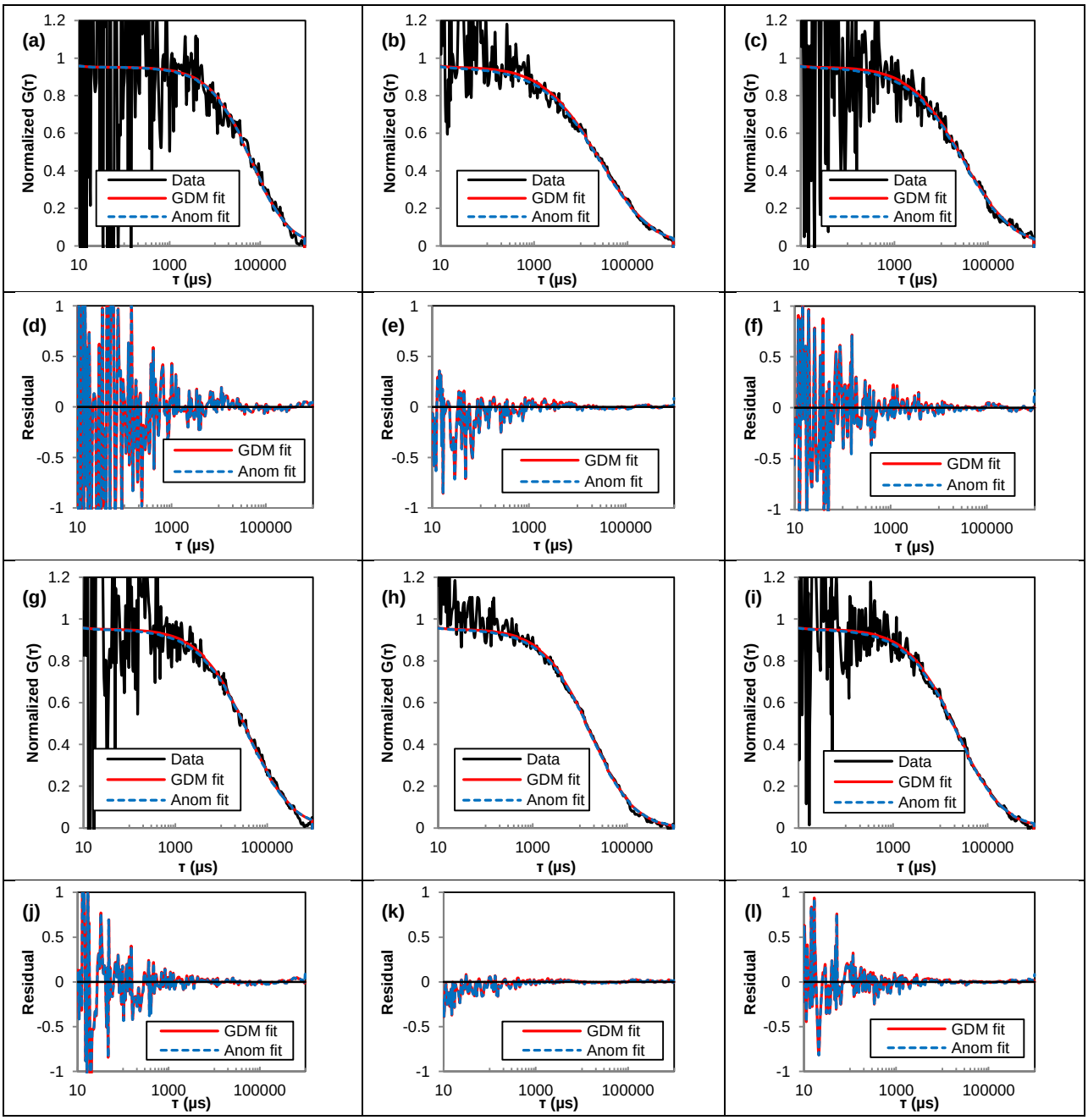

Figure 3.16. Comparison of fits (with residuals) of the 200 mg/mL mAb2 ACFs to the Gaussian distribution model (GDM) and anomalous 3D diffusion model (Anom). The fits and residuals are shown respectively for **(a, d)** 5 mM $ZnSO_4$, **(b, e)** 50 mM NaCl, **(c, f)** 150 mM NaCl, **(g, j)** 250 mM NaCl, **(h, k)** 50 mM Arg.HCl, **(i, l)** 150 mM Arg.HCl, **(m, o)** 250 mM Arg.HCl and **(n, p)** 1M Imid(HCl) at pH 5.5.

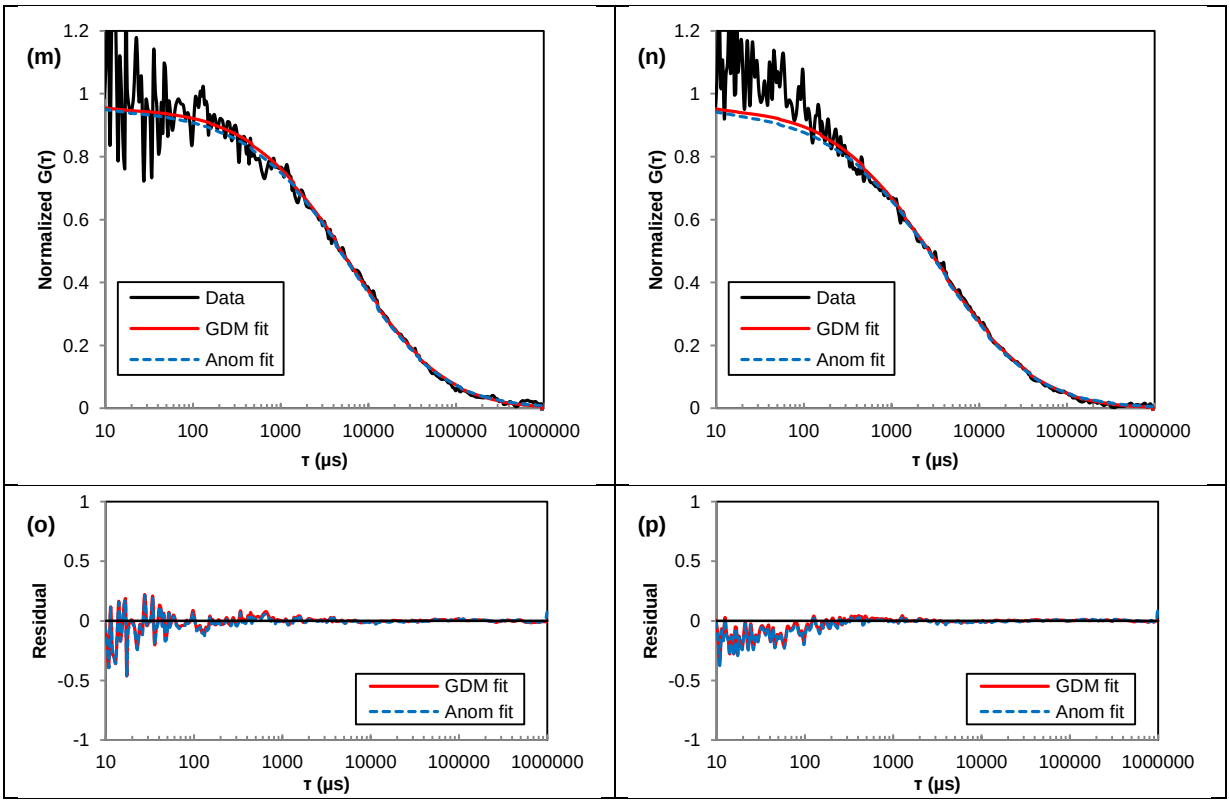

Figure 3.16 cont. Comparison of fits (with residuals) of the 200 mg/mL mAb2 ACFs to the Gaussian distribution model (GDM) and anomalous 3D diffusion model (Anom). The fits and residuals are shown respectively for (a, d) 5 mM $ZnSO_4$, (b, e) 50 mM NaCl, (c, f) 150 mM NaCl, (g, j) 250 mM NaCl, (h, k) 50 mM Arg.HCl, (i, l) 150 mM Arg.HCl, (m, o) 250 mM Arg.HCl and (n, p) 1M Imid(HCl) at pH 5.5.

	Un-normalized G(0)					
Formulation	**60**	**125**	**150**	**200**	**225**	**250**
50 mM NaCl	1.93 ± 0.12		1.3 ± 0.03	1.15 ± 0.02		1.05 ± 0.01
150 mM NaCl	1.39 ± 0.02		1.14 ± 0.03	1.10 ± 0.00		1.05 ± 0.04
250 mM NaCl	2.56 ± 0.38	1.17 ± 0.04	1.36 ± 0.06	1.11 ± 0.02	1.09 ± 0.01	
50 mM Arg.HCl	1.87 ± 0.10	1.82 ± 0.21		1.32 ± 0.02		
150 mM Arg.HCl	1.27 ± 0.02	1.21 ± 0.07		1.11 ± 0.01		1.06 ± 0.01
250 mM Arg.HCl	1.88 ± 0.15	1.31 ± 0.04	1.36 ± 0.04	1.20 ± 0.03	1.08 ± 0	1.04 ± 0.00
1 M Im(HCl)	1.12 ± 0.01	1.14 ± 0.03	1.09 ± 0	1.14 ± 0.00		1.02 ± 0.00

Table 3.6. Average G(0) of the un-normalized ACFs in Fig. 3.15. The G(0) values were calculated from the average *N* obtained from fits of the un-normalized ACFs (measured in triplicate) to the 3D anomalous diffusion model (Eqn. 3.6).

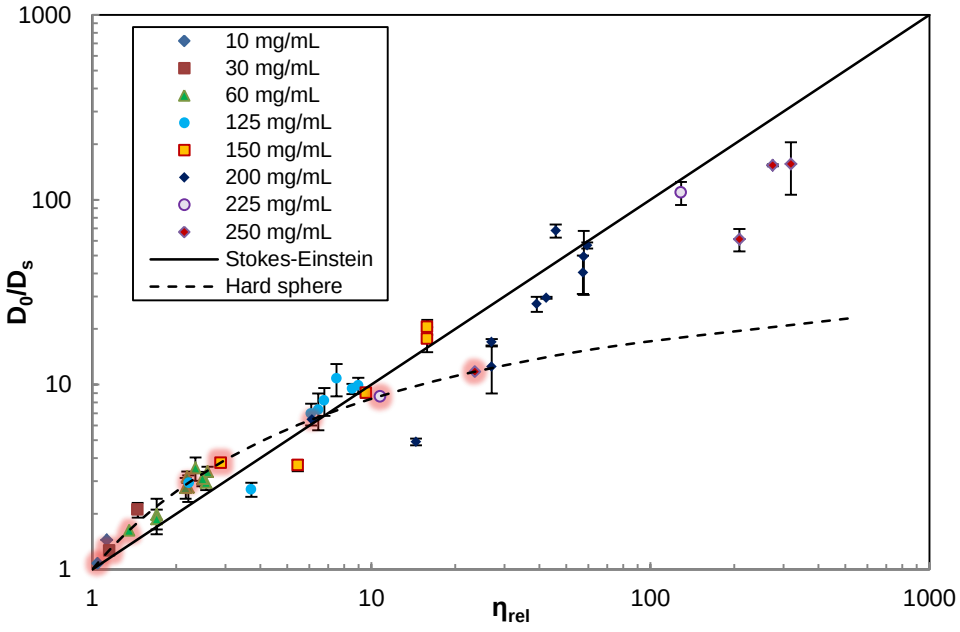

Figure 3.17. Dependence of the self-diffusion retardation factor D_0/D_s on the solution relative viscosity η_{rel}, grouped by the mAb concentration. Each concentration group was normalized by the corresponding hard sphere diffusion retardation factor $D_0/D_{s,HS}$ (glowing symbols) at the same concentration to generate Fig. 3.6a and 3.6b.

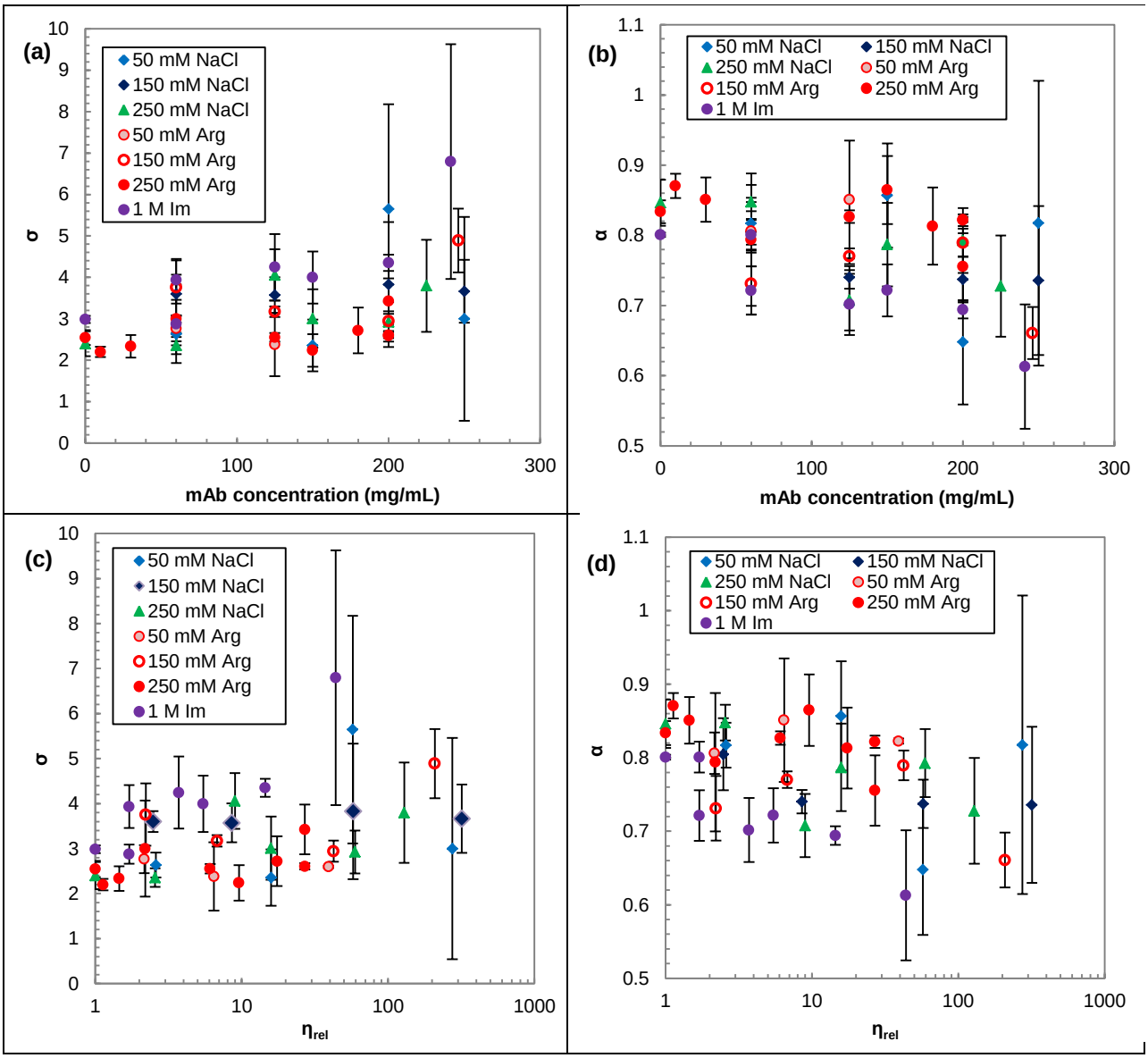

Figure 3.18. (a, c) Standard error σ from the GDM model and (b, d) anomaly coefficient α from the 3D anomalous diffusion model fits of the mAb2 FCS ACFs as a function of (a, b) mAb concentration and (c, d) solution viscosity for all tested co-solute formulations. All samples were measured in triplicate using dry-passivated slides at a focal depth of 3 μm.

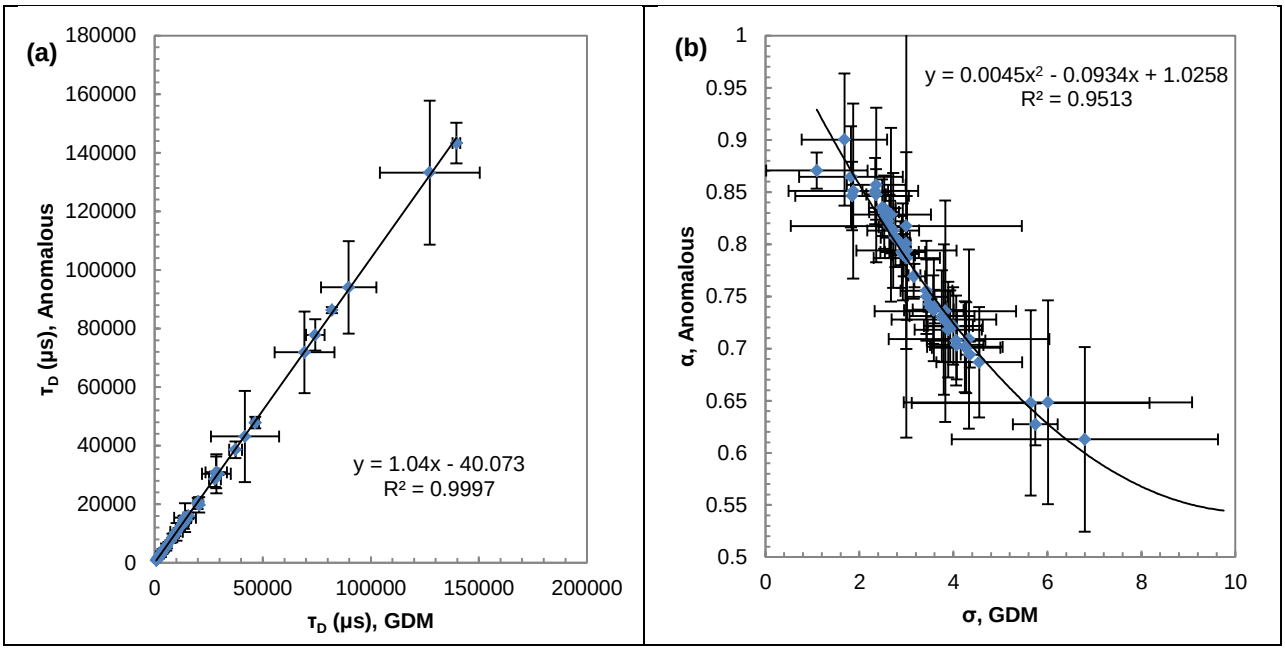

Figure 3.19. Correspondence of (a) the diffusion cross-over time τ_D and (b) anomaly coefficient α or standard deviation σ between the 3D anomalous diffusion and GDM models fits, respectively, of the mAb2 FCS ACFs across all tested mAb concentrations and co-solute formulations. All samples were measured in triplicate using dry-passivated slides at a focal depth of 3 μm, and correspond to the same data in Fig. 3.18.

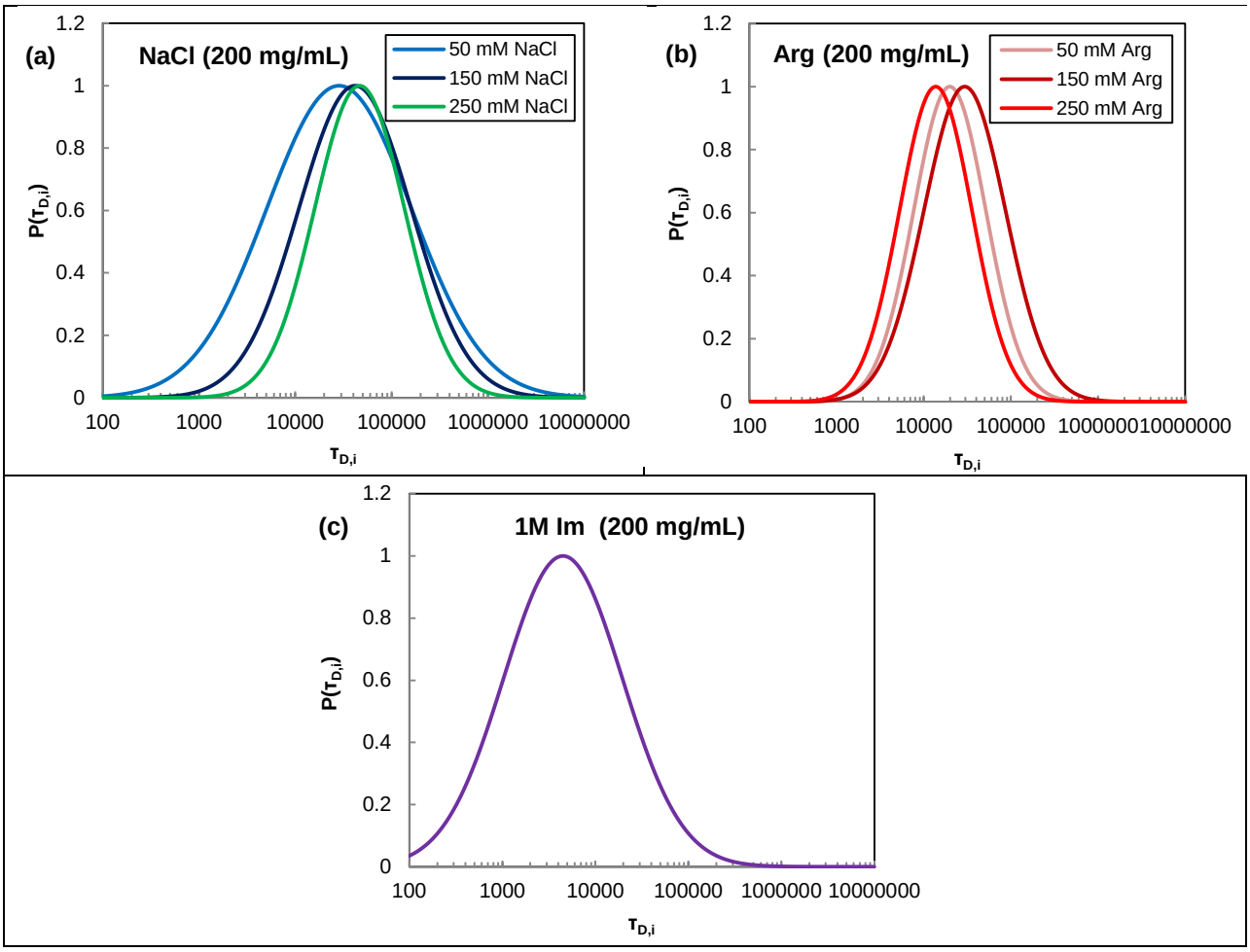

Figure 3.20. Probability distribution of τ_D for mAb2 at 200 mg/mL with (a) NaCl at 50, 150 and 250 mM, (b) Arg.HCl at 50, 150 and 250 mM and (c) 1 M Im(HCl) at pH 5.5, as determined from the Gaussian distribution model fit of the FCS ACFs.

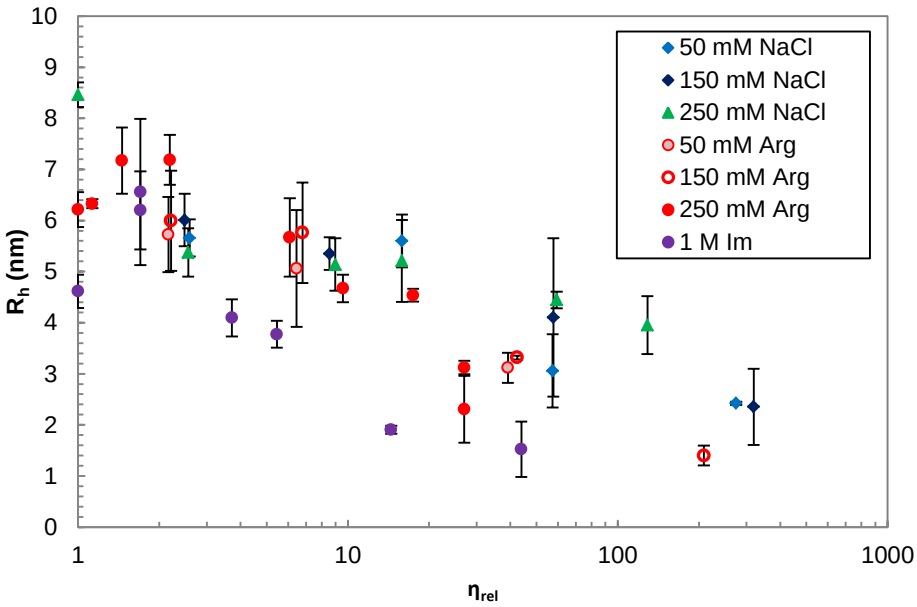

Figure 3.21. Dependence of the apparent hydrodynamic radii R_h on the relative viscosity for mAb2 in different co-solute formulations. R_h was calculated from the measured self-diffusion coefficient D_s fit from the τ_D obtained from FCS (GDM fit; 3 μm focal depth; dry-passivated slides) and from the solution viscosity using the Stokes-Einstein relation.

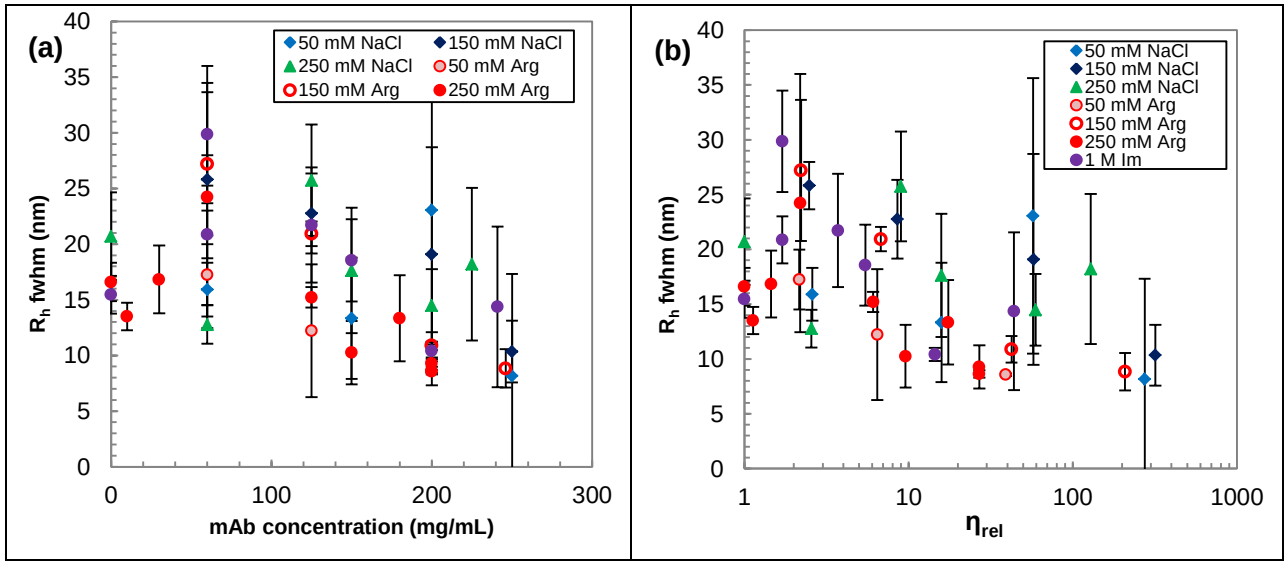

Figure 3.22. The full-width at half-maximum (fwhm) of the probability distribution function for R_h of mAb2 as a function of co-solute formulation versus (a) the mAb concentration and (b) the solution relative viscosity. The fwhm was calculated from σ (Fig. 3.18) obtained from the Gaussian distribution model fits of the FCS ACFs.

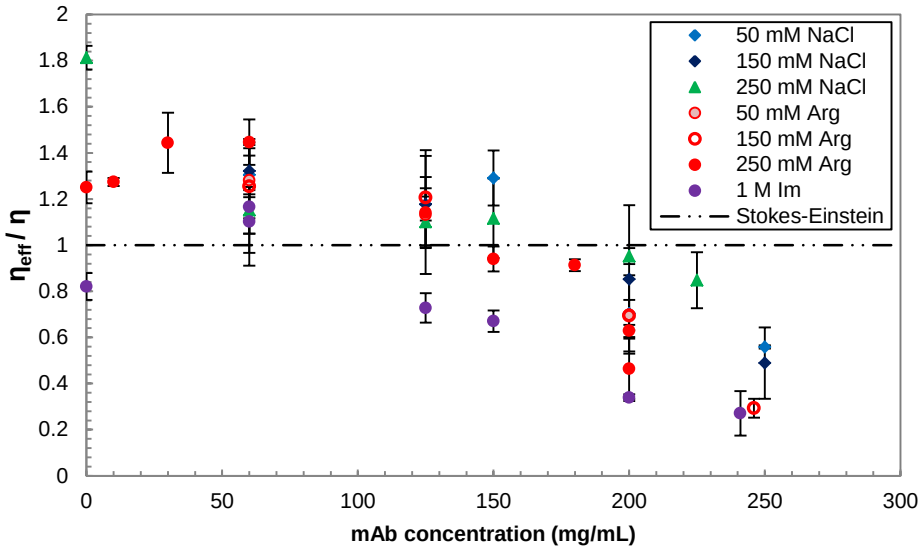

Figure 3.23. Concentration dependence of the effective viscosity normalized by the macroviscosity (η_{eff}/η) of mAb2 in different co-solute formulations. The effective viscosity η_{eff} was calculated from D_0/D_s following the length-scale dependent viscosity model[7] ($D_0/D_s = \eta_{eff}/\eta_0$) using D_s obtained from fits of the FCS ACFs to the Gaussian distribution model for 3D diffusion. Measurements were done in triplicate on dry-passivated glass slides at a focal depth of 3 μm.

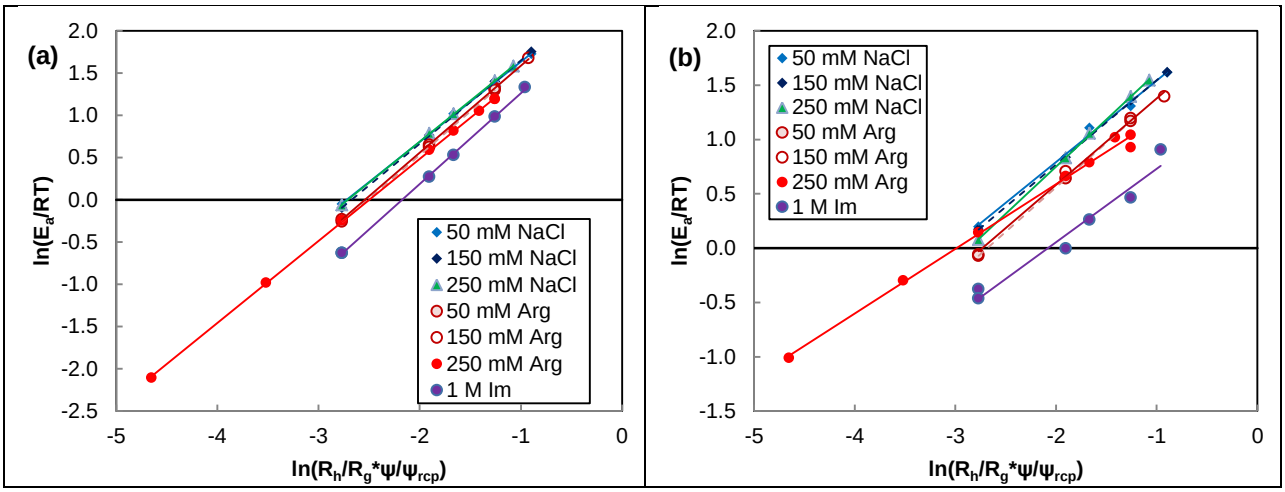

Figure 3.24. Linearized fits of the activation energy for viscous flow ($E_a/RT = \ln(\eta/\eta_0)$) to the LDV model, where E_a/RT was calculated from the **(a)** macroscopic relative viscosity η_{rel} and (b) microscopic relative viscosity ($= D_0/D_s$) for mAb2 in different co-solute formulations. These fits were used to obtain the hydrodynamic parameters a and interaction parameters b reported in Table 3.7.

	Fit to microviscosity (D_0/D_s)			Fit to macroviscosity (η_{rel})		
Formulation	**a**	**b**	**R^2 of fit**	**a**	**b**	**R^2 of fit**
50 mM NaCl	0.750	9.89	0.995	0.950	13.30	1.000
150 mM NaCl	0.777	10.21	1.000	0.986	13.99	1.000
250 mM NaCl	0.869	12.02	1.000	0.969	13.81	1.000
50 mM Arg.HCl	0.822	9.06	1.000	1.031	13.36	1.000
150 mM Arg.HCl	0.794	8.76	0.996	1.032	13.76	1.000
250 mM Arg.HCl	0.596	5.94	0.995	0.971	11.31	1.000
1 M Imid(HCl)	0.657	4.07	0.960	1.076	10.37	1.000

Table 3.7. Fit parameters from the the length-scale dependent viscosity model for both the microscopic and macroscopic viscosity for Fig. 3.24. Given the nearly identical slopes between formulations, an average *a* value 0.80 ± 0.05 and 0.99 ± 0.04 were used for further fits of the microscopic viscosity ($\eta_{eff}/\eta_0 = D_0/D_s$) and macroscopic viscosity, respectively, to the length-scale dependent viscosity model with fixed *a* (Table 3.3, Fig. 3.25, Fig. 3.8). The value of *a* was obtained by averaging over the first 6 rows in the table. Due to the unusual diffusion behavior of 1M Im, as well as the uncertainty and bias in the 250 mM Arg fit caused by the ultralow concentration (10 – 30 mg/mL) data points, the two systems were excluded from the average.

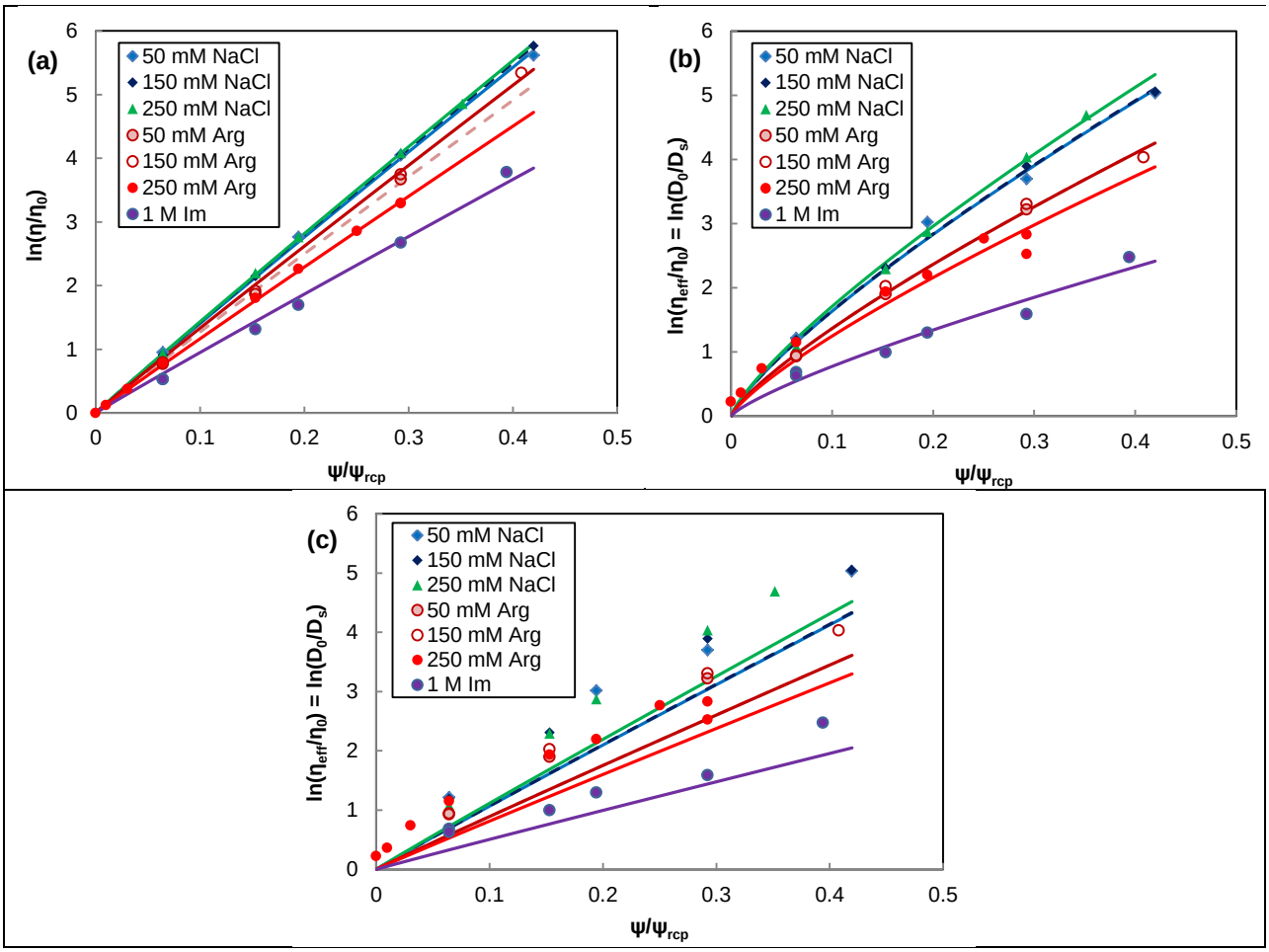

Figure 3.25. **(a)** Macroscopic relative viscosity and **(b)** micro (effective) relative viscosity and diffusion retardation as a function of the scaled concentration ψ/ψ_{rcp} for mAb2 in different co-solute formulations. The solid lines are fits of D_0/D_s to the length-scale dependent viscosity model with a fixed *a* of 0.99 and 0.80 for **(a)** and **(b)** respectively (Table 3.7) and formulation-dependent fitted values of b (Table 3.3). **(c)** Poor agreement between the best-fit of the microviscosity (D_0/D_s) to the LDV model using the average a fit from the macroscopic viscosity (0.99) and the experimental data.

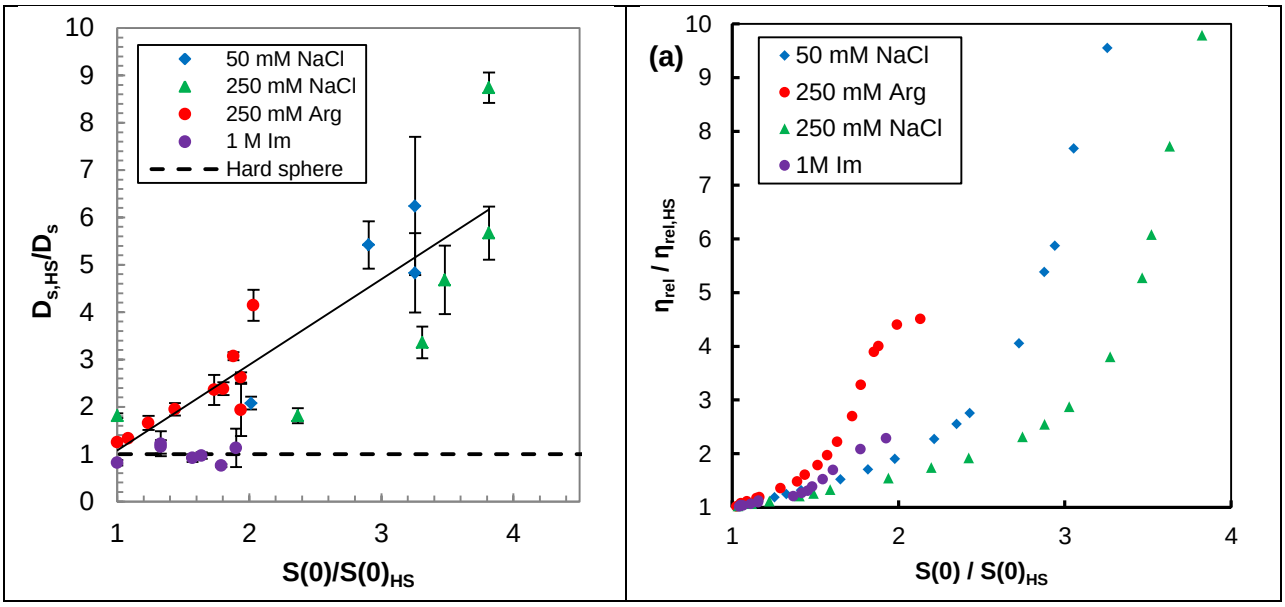

Figure 3.26. Correlation between the mAb2 hard-sphere normalized self-diffusion Ds,HS/Ds and the normalized structure factor S(0)/S(0)HS measured by SLS8 across multiple co-solute formulations and mAb concentrations from 60 – 200 mg/mL. The 1M Im data was excluded from the linear fit due to the ultrahigh ionic strength and resulting diffusion behavior. (b) Co-solute dependent relation between mAb2's solution relative viscosity ηrel and structure factor S(0), both normalized by the hard sphere (HS) values evaluated at the same concentration (volume fraction) as the mAb solution.

3.9 REFERENCES

1. Roberts CJ. Protein aggregation and its impact on product quality. Current Opinion in Biotechnology. 2014;30:211-7.
2. Roberts CJ. Therapeutic protein aggregation: mechanisms, design, and control. Trends in Biotechnology. 2014;32(7):372-80.
3. Shire SJ, Shahrokh Z, Liu J. Challenges in the Development of High Protein Concentration Formulations. J Pharm Sci. 2004;93(6):1390-402.
4. Hung JJ, Borwankar AU, Dear BJ, Truskett TM, Johnston KP. High concentration tangential flow ultrafiltration of stable monoclonal antibody solutions with low viscosities. J Membr Sci. 2016;508:113-26.
5. Baek Y, Singh N, Arunkumar A, Borys M, Li ZJ, Zydney AL. Ultrafiltration behavior of monoclonal antibodies and Fc-fusion proteins: Effects of physical properties. Biotechnol Bioeng. 2017;114(9):2057-65.
6. Binabaji E, Ma J, Rao S, Zydney AL. Theoretical analysis of the ultrafiltration behavior of highly concentrated protein solutions. J Membr Sci. 2015:JMS151044.

7. Burckbuchler V, Mekhloufi G, Giteau AP, Grossiord JL, Huille S, Agnely F. Rheological and syringeability properties of highly concentrated human polyclonal immunoglobulin solutions. Eur J Pharm Biopharm. 2010;76(3):351-6.

8. Allmendinger A, Fischer S, Huwyler J, Mahler H-C, Schwarb E, Zarraga IE, et al. Rheological characterization and injection forces of concentrated protein formulations: An alternative predictive model for non-Newtonian solutions. Eur J Pharm Biopharm. 2014;87(2):318-28.

9. Zarraga IE, Taing R, Zarzar J, Luoma J, Hsiung J, Patel A, et al. High shear rheology and anisotropy in concentrated solutions of monoclonal antibodies. J Pharm Sci. 2013;102(8):2538-49.

10. Buck PM, Chaudhri A, Kumar S, Singh SK. Highly Viscous Antibody Solutions Are a Consequence of Network Formation Caused by Domain-Domain Electrostatic Complementarities: Insights from Coarse-Grained Simulations. Mol Pharmaceutics. 2015;12(1):127-39.

11. Li L, Kumar S, Buck P, Burns C, Lavoie J, Singh S, et al. Concentration Dependent Viscosity of Monoclonal Antibody Solutions: Explaining Experimental Behavior in Terms of Molecular Properties. Pharm Res. 2014;31(11):3161-78.

12. Chaudhri A, Zarraga IE, Kamerzell TJ, Brandt JP, Patapoff TW, Shire SJ, et al. Coarse-Grained Modeling of the Self-Association of Therapeutic Monoclonal Antibodies. J Phys Chem B. 2012;116(28):8045-57.

13. Chaudhri A, Zarraga IE, Yadav S, Patapoff TW, Shire SJ, Voth GA. The Role of Amino Acid Sequence in the Self-Association of Therapeutic Monoclonal Antibodies: Insights from Coarse-Grained Modeling. J Phys Chem B. 2013;117(5):1269-79.

14. Kastelic M, Dill KA, Kalyuzhnyi YV, Vlachy V. Controlling the viscosities of antibody solutions through control of their binding sites. Journal of Molecular Liquids. 2017.

15. Godfrin PD, Zarraga IE, Zarzar J, Porcar L, Falus P, Wagner NJ, et al. Effect of Hierarchical Cluster Formation on the Viscosity of Concentrated Monoclonal Antibody Formulations Studied by Neutron Scattering. J Phys Chem B. 2016;120(2):278-91.

16. Lilyestrom WG, Yadav S, Shire SJ, Scherer TM. Monoclonal Antibody Self-Association, Cluster Formation, and Rheology at High Concentrations. J Phys Chem B. 2013;117(21):6373-84.

17. Wang W, Lilyestrom WG, Hu ZY, Scherer TM. Cluster Size and Quinary Structure Determine the Rheological Effects of Antibody Self-Association at High Concentrations. J Phys Chem B. 2018;122(7):2138-54.

18. Yearley Eric J, Godfrin Paul D, Perevozchikova T, Zhang H, Falus P, Porcar L, et al. Observation of Small Cluster Formation in Concentrated Monoclonal Antibody Solutions and Its Implications to Solution Viscosity. Biophys J. 2014;106(8):1763-70.

19. Schmit JD, He F, Mishra S, Ketchem RR, Woods CE, Kerwin BA. Entanglement Model of Antibody Viscosity. J Phys Chem B. 2014;118(19):5044-9.

20. Yadav S, Liu J, Shire SJ, Kalonia DS. Specific Interactions in High Concentration Antibody Solutions Resulting in High Viscosity. J Pharm Sci. 2010;99(3):1152-68.

21. Yadav S, Shire SJ, Kalonia DS. Factors Affecting the Viscosity in High Concentration Solutions of Different Monoclonal Antibodies. J Pharm Sci. 2010;99(12):4812-29.

22. Yadav S, Shire SJ, Kalonia DS. Viscosity behavior of high-concentration monoclonal antibody solutions: Correlation with interaction parameter and electroviscous effects. J Pharm Sci. 2012;101(3):998-1011.

23. Kanai S, Liu J, Patapoff TW, Shire SJ. Reversible Self-Association of a Concentrated Monoclonal Antibody Solution Mediated by Fab-Fab Interaction That Impacts Solution Viscosity. J Pharm Sci. 2008;97(10):4219-27.

24. Hung JJ, Dear BJ, Karouta CA, Godfrin PD, Bollinger JA, Nieto MP, et al. Protein-Protein Interactions of Highly Concentrated Monoclonal Antibody Solutions via Static Light Scattering and Influence on the Viscosity. J Phys Chem B. (under review).

25. Dear BJ, Bollinger JA, Chowdhury A, Hung JJ, Wilks LR, Karouta CA, et al. X-Ray Scattering and Coarse-Grained Simulations for Protein-Protein Interactions of Monoclonal Antibodies. J Phys Chem B. (under preparation).

26. Chari R, Jerath K, Badkar AV, Kalonia DS. Long- and Short-Range Electrostatic Interactions Affect the Rheology of Highly Concentrated Antibody Solutions. Pharm Res. 2009;26(12):2607-18.

27. Yadav S, Laue TM, Kalonia DS, Singh SN, Shire SJ. The Influence of Charge Distribution on Self-Association and Viscosity Behavior of Monoclonal Antibody Solutions. Mol Pharmaceutics. 2012;9(4):791-802.

28. Yadav S, Sreedhara A, Kanai S, Liu J, Lien S, Lowman H, et al. Establishing a Link Between Amino Acid Sequences and Self-Associating and Viscoelastic Behavior of Two Closely Related Monoclonal Antibodies. Pharm Res. 2011;28(7):1750-64.

29. Du W, Klibanov AM. Hydrophobic salts markedly diminish viscosity of concentrated protein solutions. Biotechnol Bioeng. 2011;108(3):632-6.

30. Guo Z, Chen A, Nassar R, Helk B, Mueller C, Tang Y, et al. Structure-Activity Relationship for Hydrophobic Salts as Viscosity-Lowering Excipients for Concentrated Solutions of Monoclonal Antibodies. Pharm Res. 2012;29(11):3102-9.

31. Larson AM, Weight AK, Love K, Bonificio A, Wescott CR, Klibanov AM. Bulky Polar Additives That Greatly Reduce the Viscosity of Concentrated Solutions of Therapeutic Monoclonal Antibodies. J Pharm Sci. 2017;106(5):1211-7.

32. Calero-Rubio C, Ghosh R, Saluja A, Roberts CJ. Predicting protein-protein interactions of concentrated antibody solutions using dilute solution data and coarse-grained molecular models. J Pharm Sci. 2017.

33. Calero-Rubio C, Saluja A, Roberts CJ. Coarse-Grained Antibody Models for "Weak" Protein-Protein Interactions from Low to High Concentrations. J Phys Chem B. 2016;120(27):6592-605.

34. Whitaker N, Xiong J, Pace SE, Kumar V, Middaugh CR, Joshi SB, et al. A Formulation Development Approach to Identify and Select Stable Ultra–High-Concentration Monoclonal Antibody Formulations With Reduced Viscosities. J Pharm Sci. 2017;106(11):3230-41.

35. Wang S, Zhang N, Hu T, Dai W, Feng X, Zhang X, et al. Viscosity-Lowering Effect of Amino Acids and Salts on Highly Concentrated Solutions of Two IgG1 Monoclonal Antibodies. Mol Pharmaceutics. 2015;12(12):4478-87.

36. Connolly Brian D, Petry C, Yadav S, Demeule B, Ciaccio N, Moore Jamie MR, et al. Weak Interactions Govern the Viscosity of Concentrated Antibody Solutions: High-Throughput Analysis Using the Diffusion Interaction Parameter. Biophys J. 2012;103(1):69-78.

37. Johnston KP, Maynard JA, Truskett TM, Borwankar AU, Miller MA, Wilson BK, et al. Concentrated Dispersions of Equilibrium Protein Nanoclusters that Reversibly Dissociate into Active Monomers. ACS Nano. 2012;6(2):1357-69.

38. Liu J, Nguyen MDH, Andya JD, Shire SJ. Reversible Self-Association Increases the Viscosity of a Concentrated Monoclonal Antibody in Aqueous Solution. J Pharm Sci. 2005;94(9):1928-40.

39. Ghosh R, Calero-Rubio C, Saluja A, Roberts CJ. Relating protein-protein interactions and aggregation rates from low to high concentrations. J Pharm Sci. 2016;105(3):1086-96.

40. Scherer TM, Liu J, Shire SJ, Minton AI. Intermolecular Interactions of IgG1 Monoclonal Antibodies at High Concentrations Characterized by Light Scattering. J Phys Chem B. 2010;114(40):12948-57.

41. Scherer TM. Role of Cosolute–Protein Interactions in the Dissociation of Monoclonal Antibody Clusters. J Phys Chem B. 2015;119(41):13027-38.

42. Kheddo P, Tracka M, Armer J, Dearman RJ, Uddin S, van der Walle CF, et al. The effect of arginine glutamate on the stability of monoclonal antibodies in solution. International journal of pharmaceutics. 2014;473(1–2):126-33.

43. Kheddo P, Cliff MJ, Uddin S, van der Walle CF, Golovanov AP. Characterizing monoclonal antibody formulations in arginine glutamate solutions using 1H NMR spectroscopy. mAbs. 2016;8(7):1245-58.

44. Dear BJ, Hung JJ, Truskett TM, Johnston KP. Contrasting the Influence of Cationic Amino Acids on the Viscosity and Stability of a Highly Concentrated Monoclonal Antibody. Pharm Res. 2017;34(1):193-207.

45. Borwankar AU, Dear BJ, Twu A, Hung JJ, Dinin AK, Wilson BK, et al. Viscosity Reduction of a Concentrated Monoclonal Antibody with Arginine·HCl and Arginine·Glutamate. Ind Eng Chem Res. 2016;55(43):11225-34.

46. Inoue N, Takai E, Arakawa T, Shiraki K. Specific Decrease in Solution Viscosity of Antibodies by Arginine for Therapeutic Formulations. Mol Pharmaceutics. 2014;11(6):1889-96.

47. Fukuda M, Moriyama C, Yamazaki T, Imaeda Y, Koga A. Quantitative Correlation between Viscosity of Concentrated MAb Solutions and Particle Size Parameters Obtained from Small-Angle X-ray Scattering. Pharm Res. 2015;32(12):3803-12.

48. Fukuda M, Watanabe A, Hayasaka A, Muraoka M, Hori Y, Yamazaki T, et al. Small-scale screening method for low-viscosity antibody solutions using small-angle X-ray scattering. Eur J Pharm Biopharm. 2017;112:132-7.

49. Binabaji E, Ma J, Zydney A. Intermolecular Interactions and the Viscosity of Highly Concentrated Monoclonal Antibody Solutions. Pharm Res. 2015;32(9):3102-9.

50. Wang G, Varga Z, Hofmann J, Zarraga IE, Swan JW. Structure and Relaxation in Solutions of Monoclonal Antibodies. J Phys Chem B. 2018;122(11):2867-80.

51. Corbett D, Hebditch M, Keeling R, Ke P, Ekizoglou S, Sarangapani P, et al. Coarse-Grained Modeling of Antibodies from Small-Angle Scattering Profiles. J Phys Chem B. 2017;121(35):8276-90.
52. Sablani SS, Goosen MFA, Al-Belushi R, Wilf M. Concentration polarization in ultrafiltration and reverse osmosis: a critical review. Desalination. 2001;141(3):269-89.
53. Holyst R, Bielejewska A, Szymanski J, Wilk A, Patkowski A, Gapinski J, et al. Scaling form of viscosity at all length-scales in poly(ethylene glycol) solutions studied by fluorescence correlation spectroscopy and capillary electrophoresis. Physical Chemistry Chemical Physics. 2009;11(40):9025-32.
54. Dharmaraj VL, Godfrin PD, Liu Y, Hudson SD. Rheology of clustering protein solutions. Biomicrofluidics. 2016;10(4):043509.
55. Yadav S, Scherer TM, Shire SJ, Kalonia DS. Use of dynamic light scattering to determine second virial coefficient in a semidilute concentration regime. Analytical biochemistry. 2011;411(2):292-6.
56. Sorret Lea L, DeWinter Madison A, Schwartz Daniel K, Randolph Theodore W. Challenges in Predicting Protein-Protein Interactions from Measurements of Molecular Diffusivity. Biophys J. 2016;111(9):1831-42.
57. Neergaard MS, Kalonia DS, Parshad H, Nielsen AD, Møller EH, van de Weert M. Viscosity of high concentration protein formulations of monoclonal antibodies of the IgG1 and IgG4 subclass – Prediction of viscosity through protein–protein interaction measurements. European Journal of Pharmaceutical Sciences. 2013;49(3):400-10.
58. Nicoud L, Jagielski J, Pfister D, Lazzari S, Massant J, Lattuada M, et al. Kinetics of Monoclonal Antibody Aggregation from Dilute toward Concentrated Conditions. J Phys Chem B. 2016.
59. Nicoud L, Lattuada M, Yates A, Morbidelli M. Impact of aggregate formation on the viscosity of protein solutions. Soft Matter. 2015.
60. Le Bon C, Nicolai T, Kuil ME, Hollander JG. Self-Diffusion and Cooperative Diffusion of Globular Proteins in Solution. J Phys Chem B. 1999;103(46):10294-9.
61. Zettl U, Hoffmann ST, Koberling F, Krausch G, Enderlein J, Harnau L, et al. Self-Diffusion and Cooperative Diffusion in Semidilute Polymer Solutions As Measured by Fluorescence Correlation Spectroscopy. Macromolecules. 2009;42(24):9537-47.
62. Banchio AJ, Nägele G. Short-time transport properties in dense suspensions: From neutral to charge-stabilized colloidal spheres. The Journal of Chemical Physics. 2008;128(10):104903.
63. Cichocki B, Felderhof BU. Sedimentation and self-diffusion in suspensions of spherical particles. Physica A: Statistical Mechanics and its Applications. 1989;154(2):213-32.
64. Heinen M, Zanini F, Roosen-Runge F, Fedunova D, Zhang F, Hennig M, et al. Viscosity and diffusion: crowding and salt effects in protein solutions. Soft Matter. 2012;8(5):1404-19.
65. van Blaaderen A, Peetermans J, Maret G, Dhont JKG. Long-time self-diffusion of spherical colloidal particles measured with fluorescence recovery after photobleaching. The Journal of Chemical Physics. 1992;96(6):4591-603.
66. Tokuyama M, Oppenheim I. Dynamics of hard-sphere suspensions. Phys Rev E. 1994;50(1):R16-R9.

67. He F, Woods C, Litowski J, Roschen L, Gadgil H, Razinkov V, et al. Effect of Sugar Molecules on the Viscosity of High Concentration Monoclonal Antibody Solutions. Pharm Res. 2011;28(7):1552-60.
68. Josephson LL, Furst EM, Galush WJ. Particle tracking microrheology of protein solutions. Journal of Rheology. 2016;60(4):531-40.
69. Bauer KC, Suhm S, Wöll AK, Hubbuch J. Impact of additives on the formation of protein aggregates and viscosity in concentrated protein solutions. International Journal of Pharmaceutics. 2017;516(1):82-90.
70. Szymański J, Patkowski A, Wilk A, Garstecki P, Holyst R. Diffusion and Viscosity in a Crowded Environment: from Nano- to Macroscale. J Phys Chem B. 2006;110(51):25593-7.
71. Kalwarczyk T, Ziębacz N, Bielejewska A, Zaboklicka E, Koynov K, Szymański J, et al. Comparative Analysis of Viscosity of Complex Liquids and Cytoplasm of Mammalian Cells at the Nanoscale. Nano Letters. 2011;11(5):2157-63.
72. Kalwarczyk T, Sozanski K, Jakiela S, Wisniewska A, Kalwarczyk E, Kryszczuk K, et al. Length-scale dependent transport properties of colloidal and protein solutions for prediction of crystal nucleation rates. Nanoscale. 2014;6(17):10340-6.
73. Kalwarczyk T, Sozanski K, Ochab-Marcinek A, Szymanski J, Tabaka M, Hou S, et al. Motion of nanoprobes in complex liquids within the framework of the length-scale dependent viscosity model. Advances in Colloid and Interface Science. 2015;223:55-63.
74. Nicoud L, Lattuada M, Lazzari S, Morbidelli M. Viscosity scaling in concentrated dispersions and its impact on colloidal aggregation. Physical Chemistry Chemical Physics. 2015;17(37):24392-402.
75. Wang Y, Li C, Pielak GJ. Effects of Proteins on Protein Diffusion. Journal of the American Chemical Society. 2010;132(27):9392-7.
76. Sozański K, Wiśniewska A, Kalwarczyk T, Hołyst R. Activation Energy for Mobility of Dyes and Proteins in Polymer Solutions: From Diffusion of Single Particles to Macroscale Flow. Phys Rev Lett. 2013;111(22):228301.
77. Odijk T. Depletion Theory of Protein Transport in Semi-Dilute Polymer Solutions. Biophys J. 2000;79(5):2314-21.
78. Bucciarelli S, Myung JS, Farago B, Das S, Vliegenthart GA, Holderer O, et al. Dramatic influence of patchy attractions on short-time protein diffusion under crowded conditions. Science Advances. 2016;2(12).
79. Balbo J, Mereghetti P, Herten D-P, Wade Rebecca C. The Shape of Protein Crowders is a Major Determinant of Protein Diffusion. Biophys J. 2013;104(7):1576-84.
80. Horn FM, Richtering W, Bergenholtz J, Willenbacher N, Wagner NJ. Hydrodynamic and Colloidal Interactions in Concentrated Charge-Stabilized Polymer Dispersions. Journal of Colloid and Interface Science. 2000;225(1):166-78.
81. Roos M, Ott M, Hofmann M, Link S, Rössler E, Balbach J, et al. Coupling and Decoupling of Rotational and Translational Diffusion of Proteins under Crowding Conditions. Journal of the American Chemical Society. 2016;138(32):10365-72.
82. Roosen-Runge F, Hennig M, Seydel T, Zhang F, Skoda MWA, Zorn S, et al. Protein diffusion in crowded electrolyte solutions. Biochim Biophys Acta, Proteins Proteomics. 2010;1804(1):68-75.

83. Roosen-Runge F, Hennig M, Zhang F, Jacobs RMJ, Sztucki M, Schober H, et al. Protein self-diffusion in crowded solutions. Proc Natl Acad Sci U S A. 2011;108(29):11815.

84. Cardinaux F, Zaccarelli E, Stradner A, Bucciarelli S, Farago B, Egelhaaf SU, et al. Cluster-Driven Dynamical Arrest in Concentrated Lysozyme Solutions. J Phys Chem B. 2011;115(22):7227-37.

85. Grimaldo M, Roosen-Runge F, Zhang F, Seydel T, Schreiber F. Diffusion and Dynamics of γ-Globulin in Crowded Aqueous Solutions. J Phys Chem B. 2014;118(25):7203-9.

86. Grimaldo M, Roosen-Runge F, Hennig M, Zanini F, Zhang FJ, Zamponi M, et al. Salt-Induced Universal Slowing Down of the Short-Time Self-Diffusion of a Globular Protein in Aqueous Solution. J Phys Chem Lett. 2015;6(13):2577-82.

87. Schwille P, Haustein E. Fluorescence Correlation Spectroscopy - An Introduction to its Concepts and Applications2001.

88. Woll D. Fluorescence correlation spectroscopy in polymer science. RSC Advances. 2014;4(5):2447-65.

89. Weiss M, Hashimoto H, Nilsson T. Anomalous Protein Diffusion in Living Cells as Seen by Fluorescence Correlation Spectroscopy. Biophys J. 2003;84(6):4043-52.

90. Malchus N, Weiss M. Elucidating Anomalous Protein Diffusion in Living Cells with Fluorescence Correlation Spectroscopy—Facts and Pitfalls. Journal of Fluorescence. 2010;20(1):19-26.

91. Stachowiak JC, Hayden CC, Sasaki DY. Steric confinement of proteins on lipid membranes can drive curvature and tubulation. Proc Natl Acad Sci U S A. 2010;107(17):7781.

92. Busch DJ, Houser JR, Hayden CC, Sherman MB, Lafer EM, Stachowiak JC. Intrinsically disordered proteins drive membrane curvature. Nature Communications. 2015;6:7875.

93. Houser JR, Busch DJ, Bell DR, Li B, Ren P, Stachowiak JC. The impact of physiological crowding on the diffusivity of membrane bound proteins. Soft Matter. 2016;12(7):2127-34.

94. Snead WT, Hayden CC, Gadok AK, Zhao C, Lafer EM, Rangamani P, et al. Membrane fission by protein crowding. Proc Natl Acad Sci U S A. 2017;114(16):E3258.

95. Chandradoss SD, Haagsma AC, Lee YK, Hwang J-H, Nam J-M, Joo C. Surface Passivation for Single-molecule Protein Studies. Journal of Visualized Experiments : JoVE. 2014(86):50549.

96. Blümmel J, Perschmann N, Aydin D, Drinjakovic J, Surrey T, Lopez-Garcia M, et al. Protein repellent properties of covalently attached PEG coatings on nanostructured SiO2-based interfaces. Biomaterials. 2007;28(32):4739-47.

97. Yang Z, Galloway JA, Yu H. Protein Interactions with Poly(ethylene glycol) Self-Assembled Monolayers on Glass Substrates: Diffusion and Adsorption. Langmuir. 1999;15(24):8405-11.

98. Müller CB, Loman A, Richtering W, Enderlein J. Dual-Focus Fluorescence Correlation Spectroscopy of Colloidal Solutions: Influence of Particle Size. J Phys Chem B. 2008;112(28):8236-40.

99. Engelke H, Dorn I, Radler JO. Diffusion and molecular binding in crowded vesicle solutions measured by fluorescence correlation spectroscopy. Soft Matter. 2009;5(21):4283-9.

100. Lehmann S, Seiffert S, Richtering W. Refractive Index Mismatch Can Misindicate Anomalous Diffusion in Single-Focus Fluorescence Correlation Spectroscopy. Macromolecular Chemistry and Physics. 2015;216(2):156-63.

101. Banachowicz E, Patkowski A, Meier G, Klamecka K, Gapiński J. Successful FCS Experiment in Nonstandard Conditions. Langmuir. 2014;30(29):8945-55.

102. Wang F, Shi Y, Luo S, Chen Y, Zhao J. Conformational Transition of Poly(N-isopropylacrylamide) Single Chains in Its Cononsolvency Process: A Study by Fluorescence Correlation Spectroscopy and Scaling Analysis. Macromolecules. 2012;45(22):9196-204.

103. Kalwarczyk T, Kwapiszewska K, Szczepanski K, Sozanski K, Szymanski J, Michalska B, et al. Apparent Anomalous Diffusion in the Cytoplasm of Human Cells: The Effect of Probes' Polydispersity. J Phys Chem B. 2017;121(42):9831-7.

104. Pal N, Verma SD, Singh MK, Sen S. Fluorescence Correlation Spectroscopy: An Efficient Tool for Measuring Size, Size-Distribution and Polydispersity of Microemulsion Droplets in Solution. Analytical Chemistry. 2011;83(20):7736-44.

105. Khan MF, Singh MK, Sen S. Measuring Size, Size Distribution, and Polydispersity of Water-in-Oil Microemulsion Droplets using Fluorescence Correlation Spectroscopy: Comparison to Dynamic Light Scattering. J Phys Chem B. 2016;120(5):1008-20.

106. Hassan PA, Rana S, Verma G. Making Sense of Brownian Motion: Colloid Characterization by Dynamic Light Scattering. Langmuir. 2014.

107. Reitan NK, Juthajan A, Lindmo T, de Lange Davies C. Macromolecular diffusion in the extracellular matrix measured by fluorescence correlation spectroscopy. BIOMEDO. 2008;13(5):054040--9.

108. Banks DS, Fradin C. Anomalous Diffusion of Proteins Due to Molecular Crowding. Biophys J. 2005;89(5):2960-71.

109. Widengren J, Mets U, Rigler R. Fluorescence correlation spectroscopy of triplet states in solution: a theoretical and experimental study. The Journal of Physical Chemistry. 1995;99(36):13368-79.

110. Chowdhury PK. Fluorescence Correlation Spectroscopy: A Brief Review of Techniques and Applications to Biomolecules and Biosystems. Journal of Proteins & Proteomics. 2011;2(2):145-69.

111. Torquato S, Truskett TM, Debenedetti PG. Is Random Close Packing of Spheres Well Defined? Phys Rev Lett. 2000;84(10):2064-7.

112. Minton AP. Static Light Scattering from Concentrated Protein Solutions, I: General Theory for Protein Mixtures and Application to Self-Associating Proteins. Biophys J. 2007;93(4):1321-8.

113. Yajima H, Yamamoto H, Nagaoka M, Nakazato K, Ishii T, Niimura N. Small-angle neutron scattering and dynamic light scattering studies of N- and C-terminal fragments of ovotransferrin. Biochim Biophys Acta, Gen Subj. 1998;1381(1):68-76.

114. Porcar L, Falus P, Chen W-R, Faraone A, Fratini E, Hong K, et al. Formation of the Dynamic Clusters in Concentrated Lysozyme Protein Solutions. J Phys Chem Lett. 2009;1(1):126-9.

115. Starr TE, Thompson NL. Local Diffusion and Concentration of IgG near Planar Membranes: Measurement by Total Internal Reflection with Fluorescence Correlation Spectroscopy. J Phys Chem B. 2002;106(9):2365-71.

116. Soraruf D, Roosen-Runge F, Grimaldo M, Zanini F, Schweins R, Seydel T, et al. Protein cluster formation in aqueous solution in the presence of multivalent metal ions - a light scattering study. Soft Matter. 2014;10(6):894-902.

117. Tuteja A, Mackay ME, Narayanan S, Asokan S, Wong MS. Breakdown of the Continuum Stokes−Einstein Relation for Nanoparticle Diffusion. Nano Letters. 2007;7(5):1276-81.

118. Braun MK, Grimaldo M, Roosen-Runge F, Hoffmann I, Czakkel O, Sztucki M, et al. Crowding-Controlled Cluster Size in Concentrated Aqueous Protein Solutions: Structure, Self- and Collective Diffusion. J Phys Chem Lett. 2017;8(12):2590-6.

119. Falus P, Porcar L, Fratini E, Chen W-R, Faraone A, Hong K, et al. Distinguishing the monomer to cluster phase transition in concentrated lysozyme solutions by studying the temperature dependence of the short-time dynamics. Journal of Physics: Condensed Matter. 2012;24(6):064114.

120. Shukla A, Mylonas E, Di Cola E, Finet S, Timmins P, Narayanan T, et al. Absence of equilibrium cluster phase in concentrated lysozyme solutions. Proc Natl Acad Sci U S A. 2008;105(13):5075.

121. Piazza R, Iacopini S. Transient clustering in a protein solution. The European Physical Journal E. 2002;7(1):45-8.

122. Kern W. The Evolution of Silicon Wafer Cleaning Technology. Journal of The Electrochemical Society. 1990;137(6):1887-92.

Chapter 4: Improving viscosity and stability of a highly concentrated monoclonal antibody solution with concentrated proline[3]

Jessica J. Hung, Barton J. Dear, Aileen K. Dinin, Ameya U. Borwankar, Sumarth K. Mehta, Thomas T. Truskett, Keith P. Johnston

4.1 ABSTRACT

Purpose. To explain the effects of the osmolyte proline on the protein-protein interactions (PPI), viscosity and stability of highly concentrated antibody solutions in contrast to other neutral osmolytes.

Methods. The viscosity of ~225 mg/mL mAb solutions was measured with proline, glycine and trehalose as a function of pH and co-solute concentration up to 1.3M. The stability was assessed via turbidity as well as size exclusion chromatography after 4 weeks storage at 40°C. The PPI strength was assessed qualitatively via the high concentration diffusion rate by dynamic light scattering.

Results. Increasing proline significantly reduced the mAb viscosity and increased the colloidal stability at pH 6, but not at pH 5 further from the mAb pI. In contrast, glycine and trehalose did not improve the viscosity nor stability. The normalized diffusion coefficient at high concentration, which is inversely proportional to the attractive PPI strength, increased with proline concentration but decreased with increasing glycine.

Conclusions. Proline demonstrated greater efficacy for improving mAb viscosity and stability in contrast to glycine and trehalose due to its amphipathic structure and partial charge on the pyrrolidine side chain. These properties likely allow proline to screen the attractive electrostatic and hydrophobic interactions that promote self-association and high viscosities.

[3] The first-author was responsible for the design and execution of the experiments, data analysis and interpretation, intellectual development and writing of the manuscript.

4.2 INTRODUCTION

Formulation strategies to reduce the viscosity and enhance the stability of highly concentrated monoclonal antibody solutions are of great interest in the field of drug delivery. For the preferred delivery route of subcutaneous injection, antibodies often must be formulated at concentrations of 200 mg/mL or higher in order to deliver the required dosage in a limited injection volume of 1 – 1.5 ml (1). However, attractive short-ranged protein-protein interactions (PPI) become dominant at these concentrations (2, 3) due to small spacings between protein molecules on the order of the molecular diameter (2). These interactions can lead to self-association (3) and high viscosities above the 15 – 20 cP limit for subcutaneous injection (1). The concentration-dependent viscosity increase is thought to arise from reversible protein self-association via attractive multibody interactions mediated by short-ranged PPI (4, 5). Strategies to modify or disrupt these oligomers and reduce the solution viscosity therefore require an understanding of the complex landscape of PPI at high concentrations (6).

The viscosity and colloidal stability of concentrated protein solutions is determined by an intricate balance of long-ranged and local anisotropic electrostatic and hydrophobic interactions. In addition to long-ranged electrostatic repulsion between molecules due to the protein net charge (7), protein molecules in close proximity also experience strong, short-ranged anisotropic electrostatic attraction from the alignment of local charges and dipoles (8, 9) or via charge-dipole and dipole-dipole interactions (7, 10). As the magnitude of the difference between the pH and isoelectric point increases, the long ranged electrostatic repulsion becomes stronger. The local electrostatic attraction also becomes weaker, as more of the charges on the protein surface have the same sign, resulting in a smaller probability of attractive electrostatic contact between oppositely charged residues (7). Unfavorable hydrophobic interactions also promote self-association that may result in higher solution viscosities (11).

A strategy for lowering the solution viscosity is to weaken the attractive PPI and disrupt protein self-association. In some cases this has been accomplished by charge screening via salt

addition (10). For example, chaotropic salts have been found to afford greater viscosity reductions than neutral salts such as NaCl (12), as the greater disorder in the water structure weakens hydrophobic PPI (13). Similarly, hydrophobic salts in some cases have produced marked viscosity reductions in concentrated antibody solutions (11) by charge screening and also weakening of the hydrophobic interactions. It is also possible to reduce the viscosity by modifying the hydrophobic interactions with uncharged hydrophobic amino acids such as glycine, alanine and phenylalanine (14). Charged amino acids such as protonated arginine and histidine have been found to markedly improve the viscosity of antibodies at high concentration (2, 15) in addition to suppressing self-association (16, 17). It appears that arginine and histidine interact with hydrophobic residues on the protein surface via cation-π interactions (18) as well as with charged residues via their guanidyl (9) and imidazole functionalities (19). In this manner, arginine and histidine are able to modify both electrostatic and hydrophobic interactions to reduce protein viscosity and self-association. Furthermore, hydrophobic interactions can be minimized by stabilizing proteins in the native folded state at high concentration by depletion attraction (20) via the addition of osmolyte depletants such as polymers and polysaccharides. The addition of preferentially-excluded osmolytes such as proline, glycine and trehalose would therefore favor the folded state of the protein to minimize the excluded volume, surface area and thus free energy at high concentration (20, 21). Similarly, the attachment of protein or peptide tags, such as Cherry-RedTM can improve the thermal stability and solubility of proteins, which was demonstrated from molecular dynamics simulations to be due to modification of the protein surface net charge and hydrophobicity along with steric hindrance effects (22).

Proline has been shown to solubilize poorly-soluble proteins and suppress aggregation during protein refolding (23, 24). Interestingly, proline is the most water-soluble of the common amino acids (7 M) at room temperature (25) and is often found on the solvent-exposed protein surface, despite possessing a cyclic side chain structure with three hydrophobic C_H2 groups (26).

Additionally, proline has been observed to cause a sharp increase in emission intensity and strong blue-shift in the emission spectra of ANS (8-anilinonaphthalene-1-sulfonic acid) dye at high concentrations, suggesting the creation of hydrophobic surfaces (24). Based on these observations, proline has been hypothesized to form amphipathic supramolecular assemblies (23, 24). As a result of its amphipathic nature, proline can act as a hydrotrope in solubilizing hydrophobic proteins (23). Proline is excluded from the protein backbone (21, 27) but also interacts favorably with the protein side chains (21, 27), allowing it to improve protein stability by promoting refolding of chemically-denatured protein (27) and suppressing aggregation during refolding events (27). Although proline has been seen in some instances to reduce the viscosity of commercial antibodies (14, 28), this effect has received little attention, and to our knowledge has not been studied systematically versus pH and co-solute concentration.

Herein, we compare the efficacy of the nonelectrolyte osmolytes proline (Pro), glycine (Gly) and trehalose (Tre) for reducing the viscosity and increasing the colloidal stability of concentrated mAb 1 solutions. Trehalose was chosen over the more widely used sucrose in order to facilitate comparison with our previous studies of depletant effects (using trehalose) on the viscosity of the mAb in this study (29, 30). We demonstrate that proline improves the viscosity and colloidal stability of mAb 1 solutions (measured by size exclusion chromatography) as a function of pH and Pro concentration between 250 and 1300 mM. In contrast, these improvements are not observed for the common osmolytes glycine (up to 1300 mM) and trehalose (up to 580 mM). Proline may thus bind more strongly to the mAb than glycine and trehalose due to its more favorable interactions with the protein side chains (21) and weaken local anisotropic electrostatic attraction and hydrophobic interactions more effectively. Unlike the protonated bases arginine, histidine and imidazole, a potential advantage of the neutral co-solute proline is that it does not influence the ionic strength and does not require added counterions. Notably, we show that a binary system with Pro and His at a total co-solute

concentration of 500 mM generates a greater viscosity reduction than 500 mM His alone, while greatly reducing the solution osmolarity and ionic strength due to reduced counterion levels.

4.3 MATERIALS AND METHODS

4.3.1 Materials

The monoclonal antibody used in this study (mAb 1) is an IgG1 antibody with an isoelectric point (pI) of 9.3. mAb 1 was supplied by AbbVie at ~120 mg/mL in a proprietary buffer composition, and is the same mAb as in Hung et al. (31), Borwankar et al. (32) and Dear et al. (33). L-glycine, L-histidine, L-histidine hydrochloride monohydrate, hydrochloric acid, and imidazole were purchased from Fisher Scientific, Fairlawn, NJ. L-proline was purchased from Alpha Aesar, Ward Hill, MA. α-trehalose dihydrate (Tre) was purchased from Ferro Pfanstiehl Laboratories Inc., Waukegan, IL. Amicon Ultra-15 Ultracel – 30K centrifugal filters were purchased from Merck Millipore Ltd. Ireland. Disposable 0.22 μm polyethersulfone (PES) bottle top filters and 13 mm syringe sterile filters were obtained from Celltreat Scientific Products, Shirley, MA (product codes 229717 and 229746).

4.3.2 Centrifugal Diafiltration and Ultrafiltration (CF)

The concentrated mAb solutions were prepared by centrifugation filtration as described previously (31-33). The co-solute buffers were prepared as described previously (33), where the reported co-solute concentration in the retentate, $C_{C,R}$, depends on the concentration in the buffer feed, $C_{C,F}$ as a result of volume exclusion effects.

$$C_{C,R} = C_{C,F} * \left(1 - \bar{v}_p * C_P\right) \tag{4.1}$$

Here, C_P is the targeted mAb concentration (230 mg/mL) and $\bar{v}_p$ is the protein partial volume (0.7407 mL/g (34)). Consequently, in this study the final co-solute concentrations reported as 250, 400, 750 and 1300 mM correspond to feed concentrations of 300, 480, 905 and

1565 mM respectively. The buffers were sterile filtered with the Celltreat bottle top PES filters and then degassed under vacuum for 30 minutes.

4.3.3 Lyophilization Dilution (LD)

Lyophilized mAb 1 powder was prepared as described previously (33) with Pro or Tre added as a cryoprotectant and osmolyte in a 0.25:1 osmolyte:mAb mass ratio. The mAb powder was then reconstituted in concentrated aqueous buffers of His, Im or additional Pro to obtain ~100 μL of a 250 mg/mL mAb dispersion at the desired co-solute concentration.

4.3.4 mAb concentration determination and turbidity by UV-Vis spectroscopy

The mAb concentration was measured in duplicate at 500x dilution using a Cary 60 UV-Vis spectrophotometer (Agilent Technologies, Santa Clara, CA), as described previously (31-33) with an extinction coefficient of 1.42 ml/mg/cm. The turbidity of the concentrated, unfiltered mAb solutions was measured at 350 nm in a micro volume size cell (A54094; Beckman Coulter, Indianapolis, IN) with a 0.2 cm path length. The turbidity was determined by subtracting the A350 of the protein-free solvent from the A350 of the sample and normalized to a 1 cm path length.

4.3.5 Viscosity measurements

The solvent viscosity was measured in triplicate at 25°C using a size 50 Cannon-Fenske routine viscometer (Cannon Instrument Company, State College, PA) and averaged. The mAb viscosity was measured in triplicate using a customized capillary syringe viscometer as described previously (31-33).

The viscosity of protein solutions increases exponentially with protein concentration as described by colloidal viscosity models such the Ross-Minton equation (4, 35). Due to small differences in sample mAb concentration between the different co-solute systems in this work,

the viscosities were instead normalized by the protein concentration through the inherent viscosity

$$\eta_{inh} \equiv \frac{\ln(\eta/\eta_0)}{c} \tag{4.2}$$

in order to more directly compare the effects of different co-solute formulations on the viscosity. Here η is the solution viscosity, η_0 is the solvent viscosity and c is the protein concentration (36). Unlike η, η_{inh} increases linearly with concentration. Reported errors in η_{inh} were calculated from propagation of error in concentration and viscosity measurements. Qualitatively, the inherent viscosity increases with the strength of the PPI. Given the modest variation in mAb concentrations in this study, the results were also normalized and presented as a calculated viscosity at a reference mAb concentration of 225 mg/mL, as determined using Eqn. 4.2. Although η_{inh} is expected to change by up to about 1.5 mL/g over the concentration range 205 to 230 mg/mL (31), for simplicity we assume a constant η_{inh} for predicting the viscosity.

4.3.6 Dynamic light scattering

The collective diffusion coefficient Dc of mAb 1 at high concentration in the different formulation conditions was measured by DLS using a Malvern Zetasizer Nano ZS equipped with a 633 nm laser (Malvern Instruments, Malvern, Worcestershire, United Kingdom). The Dc was determined by fitting the autocorrelation function (ACF) with the quadratic cumulant algorithm. However, the 750 and 1300 mM proline measurements were fit with a stretched double exponential function (37) (Eqn. 4.3) due to the presence of a visible second decay mode, with the first (fast) decay mode attributed to the diffusion of the protein.

$$G_2(\tau) = \sigma^2 * \left(A_1 * \exp\left(-\frac{\tau}{\tau_1}\right) + (1 - A_1) * \exp\left(-\frac{\tau}{\tau_2}\right)^{\beta}\right)^2 \tag{4.3}$$

Here, σ^2 is an instrument-specific prefactor, A_1 is the weighting factor by intensity for the fast decay mode, τ_1 and τ_2 are the characteristic relaxation times of the fast and slow decay modes respectively, and β is a stretch exponent to capture the shape of the slower exponential decay. The diffusion coefficients D_i were determined from τ_i via Eqn. 4.4, where q is the scattering vector (Eqn. 4.5) of the DLS measurement (36):

$$\frac{1}{\tau} = q^2 D \tag{4.4}$$

$$q = \frac{4\pi n}{\lambda} \sin\left(\frac{\theta}{2}\right) \tag{4.5}$$

where λ is the incident laser wavelength, n is the solvent refractive index (RI), and θ is the scattering angle. The samples were sterile filtered through a 0.22 μm PES syringe filter (Celltreat Scientific Products, Shirley, MA) prior to DLS. The DLS measurements were made at 25°C in the back-scattering mode (scattering angle of 173°). Each sample was measured in triplicate for one minute per replicate, consisting of four 15-second scans which were averaged.

4.3.7 Accelerated storage stability study

50 μL aliquots of the final mAb solution were stored in capped 300 μL HPLC vial inserts inside 1 ml HPLC vials (Thermo Fisher Scientific, Waltham, MA). The vials were sealed with three alternating layers of Parafilm and aluminum in order to minimize evaporative losses. The sealed vials were stored in a Boekel convection oven (model number 107905; Boekel Industries, Feasterville, PA) at 40°C for 4 weeks. The samples were diluted to 2 mg/mL for SEC analysis.

4.3.8 Size exclusion chromatography (SEC)

The relative level of irreversible soluble aggregates in the final solutions before and after accelerated storage stability studies was quantified by SEC after dilution of the mAb solution to

2 mg/mL in the mobile phase (200 mM NaHPO4, 50 mM NaCl (pH 7)) and sterile filtration through a 0.22 μm PES syringe filter (Celltreat Scientific Products, Shirley, MA). As sterile filtration removes large insoluble aggregates, this method only quantifies the level of soluble aggregates, rather than total aggregates. The standard solution was prepared by diluting freshly-thawed mAb monomer stock (as provided at 120 mg/mL) in the mobile phase. A 10 μL injection of each sample was analyzed with a Waters Breeze HPLC (Waters Corporation, Milford, MA) equipped with a Tosoh Biosciences TSKgel3000SWXL column (Tosoh Corporation, Tokyo, Japan), operating at a flow rate of 0.5 ml/min. The eluate was monitored by the UV absorbance at 214 nm and 280 nm using a Waters 2489 UV/Visible detector (Waters Corporation, Milford, MA), which has a baseline noise level of < 5 μAU. Typical peak heights in the spectrograph were 0.20 AU. The soluble aggregate level ("% soluble aggregates") was quantified by the peak area ratio of the aggregate peak to the monomer + aggregate peaks for the diluted samples, which is equivalent to the mass fraction of soluble protein that is incorporated in the irreversible soluble aggregates. Throughout the rest of this study, the terms "monomer retention" or "percent monomer" refer specifically to the mass fraction of soluble protein that remains monomeric, and is not equivalent to the total monomer recovery after incubation, as this method does not account for the monomer loss to formation of insoluble aggregates. Due to limited sample amounts, measurements were made without duplicates. However, the systematic instrument error was confirmed to be very small, as the standard deviation in the measured percent monomer (relative to total soluble protein content) for the mAb standard solution across 9 replicate measurements from multiple sample sets was less than 0.1% (for an average value of 99.7%).

4.4 RESULTS

4.4.1 Increasing viscosity reduction with increasing proline concentration

In order to investigate the effect of co-solutes on mAb 1's viscosity, control experiments were first performed at 50 mM His-HCl (pH 5, 6). As seen in Table 4.1, 205 and 208 mg/mL mAb 1 solutions had viscosities of 21 and 57 cP at pH 5 and 6, respectively, corresponding to inherent viscosities of 15.0 and 20.0 mL/g (Fig. 4.1a, Table 4.1). In order to more directly compare different formulations, the mAb viscosity was calculated for a reference concentration of 225 mg/mL from Eqn. 4.2 using the empirical inherent viscosity (measured at 200 –230 mg/mL mAb 1). Although η_{inh} increases modestly with mAb concentration (Eqn. 4.9), by up to 1.7 mL/g between 190 and 230 mg/mL (31), we assumed that η_{inh} for a given formulation remains constant between 200 – 225 mg/mL for comparison purposes. As seen in Fig. 4.1b, the viscosity was calculated to increase to >80 cP at 225 mg/mL and pH 6. For a phosphate (Phos) buffered system at the same pH, a higher viscosity of 80 cP was observed at 209 mg/mL mAb 1 (Table 4.4) with a calculated viscosity of 110 cP at 225 mg/mL (Fig. 4.1b).

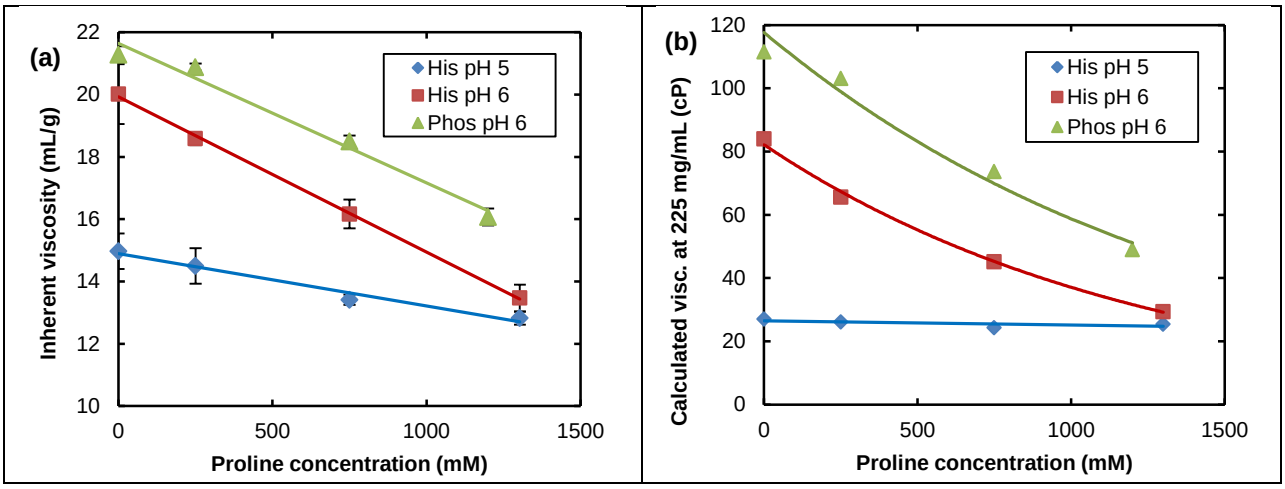

Figure 4.1. Dependence of (A) measured inherent viscosity of concentrated 200 – 250 mg/ml mAb solutions and (B) calculated viscosity at 225 mg/mL mAb on proline concentration. Samples are buffered with 50 mM of histidine HCl or phosphate buffer. The corresponding viscosity data is shown in Table 4.1 and Table 4.4, and the colored lines are a guide to the eye.

mAb conc (mg/ml)	pH	Proline conc		η (cP)	η_0 (cP)	η_{inh} (ml/g)	A_{350} ($AU*cm^{-1}$)
		mg/ml	mM				
pH 5							
208 ± 4.3	4.93	0	0	21 ± 2.1	0.93	15.0 ± 0.6	0.293
225 ± 2.2	5.12	29	250	26 ± 3.2	1.00	14.5 ± 0.6	0.272
239 ±1.0	5.15	86	750	29 ± 1.0	1.19	13.4 ± 0.2	0.427
209 ± 0.9	5.27	150	1300	21 ± 0.9	1.42	12.8 ± 0.2	0.431
pH 6							
205 ± 9.6	5.96	0	0	57 ± 2.4	0.93	20.0 ± 1.0	0.327
205 ± 0.4	5.94	29	250	45 ± 1.9	1.00	18.6 ± 0.2	0.380
205 ± 2.9	6.05	86	750	33 ± 2.7	1.19	16.2 ± 0.5	0.511
195 ± 1.3	6.07	150	1300	20 ± 1.6	1.42	13.5 ± 0.4	0.525

Table 4.1. Dependence of mAb viscosity on proline concentration at pH 5 and 6 with 50 mM His(HCl) for mAb solutions formed by centrifugation filtration.

In an attempt to reduce the mAb viscosity at pH 6 to acceptably low levels for subcutaneous injection, Pro was added at concentrations from 250 to 1300 mM. The highest concentration of 1300 mM was chosen to approach the threshold concentration of 1.5 M, above

which proline has been shown to solubilize poorly-soluble proteins and suppress aggregation during protein refolding (23). While the highest co-solute concentration of 1300 mM is too high to be practical, the intermediate Pro concentration of 750 mM used here is still within the osmolarity threshold for acceptable levels of pain during injection (2x – 3x iso-osmolarity, according to various biopharmaceutical experts, and corresponding to 600 – 900 mM Pro). Given the small variation in mAb concentrations between samples, and considering the exponential dependence of viscosity on protein concentration, it is more meaningful to compare η_{inh} rather than absolute viscosities, as explained in the Methods section on viscosity. As the Pro concentration was increased, similar large decreases in η_{inh} of up to 6 mL/g for the mAb solution were observed in both the 50 mM His and Phos buffers (Fig. 4.1a; Table 4.1; Table 4.4). The corresponding mAb viscosity in His and Phos buffer decreased by 3-fold to 20 cP at 195 mg/mL and 48 cP at 224 mg/mL, respectively (Fig. 4.1b; Table 4.1; Table 4.4). In contrast, at pH 5 the addition of Pro in 50 mM His buffer caused a smaller reduction in η_{inh} (Fig. 4.1a, Table 4.1). As a consequence of the simultaneous increase in solvent viscosity and decrease in inherent viscosity with increasing Pro concentration, the calculated mAb viscosity at 225 mg/mL remained constant at ~25 cP over the entire concentration range (Fig. 4.1b). It is interesting to note that the addition of high concentrations of Pro at pH 6 reduces the mAb viscosity and inherent viscosity to approach the same value as at pH 5.

4.4.2 Lack of viscosity reduction from preferential exclusion with glycine and trehalose

To further probe the effects of neutral, preferentially excluded (20, 21) osmolytes on protein viscosity, glycine and trehalose were studied. Glycine in some cases can greatly reduce the viscosity of mAb solutions (14). However, we found that at pH 5 Gly mildly increased η_{inh} for mAb 1, by up to ~3 mL/g at the highest concentration of 1300 mM relative to the 50 mM His control (Fig. 4.2a, Table 4.2). At pH 6, 250 mM Gly appears to cause a modest reduction in η_{inh} relative to the control, even at a higher mAb concentration (Table 4.2, 4.5). However, further

increasing the Gly concentration to 1300 mM increased η_{inh} relative to the control, even at a lower mAb concentration (Table 4.2, 4.5). Consequently, whereas the addition of Pro caused a large reduction in the calculated mAb viscosity at pH 6, Gly caused a significant increase in the calculated viscosity at both pH 5 and 6, as seen in Fig. 4.2b.

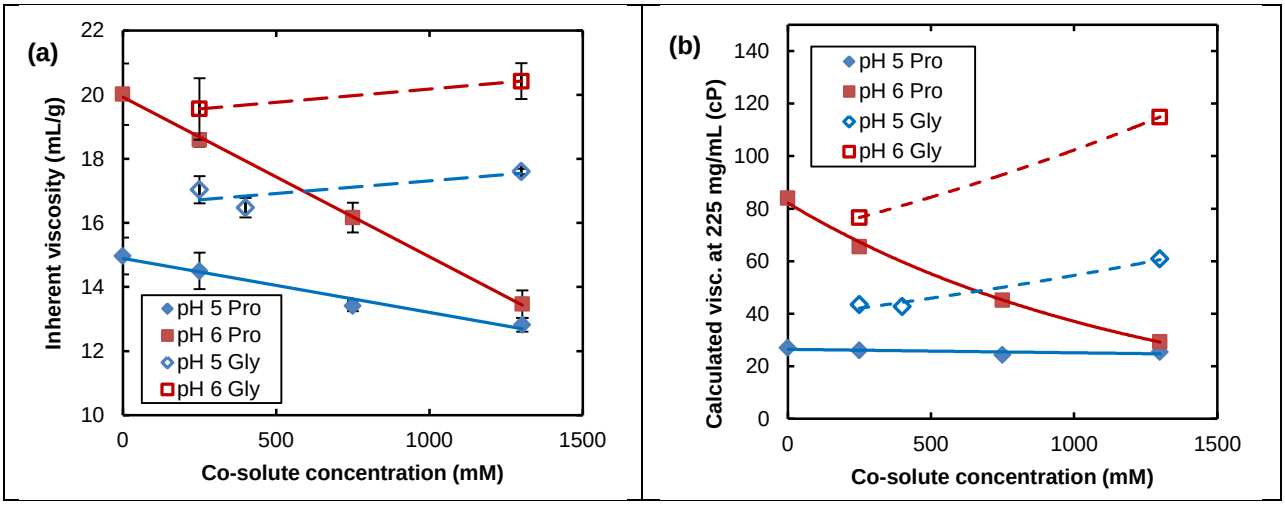

Figure 4.2. Dependence of (A) measured inherent viscosity of concentrated 200 – 250 mg/ml mAb solutions and (B) corresponding calculated viscosity at 225 mg/mL mAb on co-solute choice (proline, glycine) and co-solute concentration. The proline data from Fig. 4.1 is reproduced here for visual comparison against the glycine viscosity data. Samples are buffered with 50 mM histidine HCl. The corresponding viscosity data is shown in Table 4.1 and Table 4.2, and the colored lines are a guide to the eye.

mAb conc (mg/ml)	pH	Glycine conc		η (cP)	η_0 (cP)	η_{inh} (ml/g)	A_{350} ($AU*cm^{-1}$)
		mg/ml	mM				
pH 5							
232 ± 3.6	5.11	19	250	49 ± 3.8	0.94	17.0 ± 0.4	0.318
233 ± 4.1	5.12	30	400	49 ± 0.8	1.05	16.5 ± 0.3	0.286
207 ± 0.0	5.38	98	1300	45 ± 0.8	1.16	17.6 ± 0.1	0.397
pH 6							
223 ± 1.9	5.96	19	250	74 ± 8.7	0.94	19.6 ± 0.6	0.318
193 ± 1.3	6.10	98	1300	59 ± 2.8	1.16	20.4 ± 0.3	0.401

Table 4.2. Dependence of mAb viscosity on glycine concentration at pH 5 – 6 with 50 mM His(HCl).

Similar to the case for Gly, the addition of Tre up to 580 mM did not reduce the mAb viscosity at pH 6 (Table 4.5, 4.6). For mAb solutions buffered in 30 mM His, the addition of up to 220 mM Tre produced a mild increase in η_{inh} relative to the Tre-free control (Table 4.5; control in row 1). However, the modest increase in η_{inh} of up to ~1.0 mL/g may be accounted for in part by the higher corresponding mAb concentrations. Similarly, the addition of up to 580 mM Tre did not significantly change η_{inh} for mAb solutions buffered with 50 mM Phos (Table 4.6) relative to the Tre-free phosphate control (row 1 in Table 4.6). Unlike for Gly, which modestly reduces the viscosity at pH 6 and low Gly concentration, Tre does not appear to reduce the viscosity at any concentration between 150 – 580 mM.

The results for Gly and Tre indicate that depletion attraction produced by a neutral co-solute does not produce a general viscosity reduction, as was proposed in an earlier study based upon a theoretical model (30). The greater viscosity reduction for Pro versus Gly or Tre may be influenced by the stronger interactions between the Pro and protein side chains. Furthermore, the larger size of Pro compared to Gly may also contribute to greater depletion attraction at the same

co-solute concentration, which in turn promotes a more compact, folded conformation for the mAb (20) and minimizes the number of solvent-exposed self-association sites.

4.4.3 Viscosity reduction with binary co-solutes: proline with histidine or imidazole

To attempt to modulate the electrostatic and hydrophobic PPI to further reduce the viscosity, we also examined binary systems of Pro with protonated His or Im. Histidine is a pharmaceutically-acceptable co-solute that has been shown to reduce the viscosity of several mAbs (33, 38, 39), likely through preferential interactions of His with aromatic residues via its imidazole side chain as has been seen in simulations (18, 19), which may screen hydrophobic interactions. Imidazole was also investigated for its same favorable preferential interactions with aromatic residues, but was also chosen due to its smaller size compared to His (it lacks the amino acid backbone of His). Due to the similar mechanisms by which the two co-solutes modify protein interactions, at 250 mM both reduced the mAb inherent viscosity at ~230 mg/mL and pH 6 by 3 – 4 mL/g relative to the 50 mM His control (Table 4.7), indicating a weakening of attractive PPI. The reduction in inherent viscosity is slightly greater for His compared to Imid, but the higher solvent viscosity for His caused the net change in viscosity to be identical between His and Imid (Table 4.7). The addition of 250 mM Pro further reduced η_{inh} at ~230 mg/mL from 16 – 17 mL/g without Pro (Table 4.7) to 14.8 and 14.3 mL/g at ~225 mg/mL for the His and Im systems, respectively (Fig. 4.3a, Table 4.8), with the corresponding calculated viscosity at 225 mg/mL decreasing by nearly 1.5-fold from 40 – 45 cP without Pro to 25 – 30 cP (Fig. 4.3b). However, the addition of Pro in the binary systems at pH 5 did not further reduce η_{inh} (Fig. 4.3a, Table 4.8) or viscosity (Fig. 4.3b) significantly. A summary of the lowest-viscosity proline formulations are presented in Fig. 4.4.

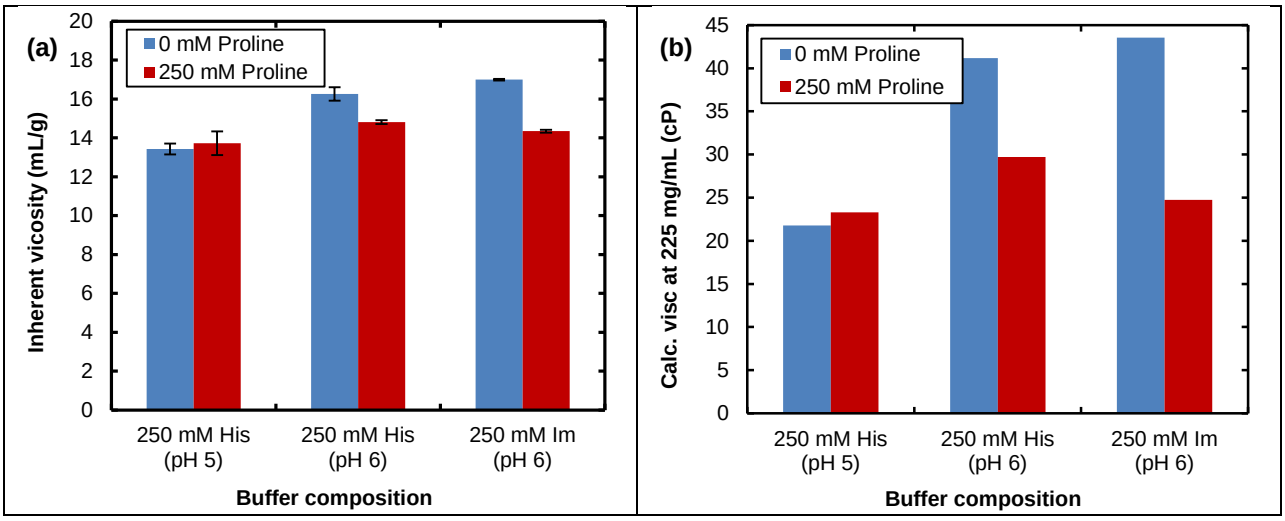

Figure 4.3. (A) Measured inherent viscosity and (B) calculated viscosity of 225 mg/mL mAb solutions containing 250 mM histidine or imidazole with no proline (blue bars) or an additional 250 mM proline (red bars).

Impressively, the use of binary Pro-His systems will now be shown to lower viscosities more than His-only formulations at the same 'active' co-solute concentration (i.e. not counting the counterions) but at a lower solution osmolarity. For example, the calculated viscosity of this mAb at 225 mg/mL and pH 6 was 40 cP in 250 mM His (Fig. 4.3b; also Fig. S11 from Dear et al. (33)). Further increases in His concentration to 500 mM led to a small reduction in the calculated viscosity to 35 cP (Table 4.10), but at a total co-solute osmolarity of 810 mM. In contrast, the 250:250 mM His:Pro binary system reduced the expected (calculated) viscosity at 225 mg/mL to 31 cP, at a lower total co-solute osmolarity of 655 mM. An intermediate His concentration of 360 mM (osmolarity = 583 mOsm/L), closer to the osmolarity of the binary Pro-His system, actually caused a small increase in the calculated viscosity (Table 4.10) to 44 cP, but the change is small and may be caused in part by the sample drift to a slightly higher final solution pH.

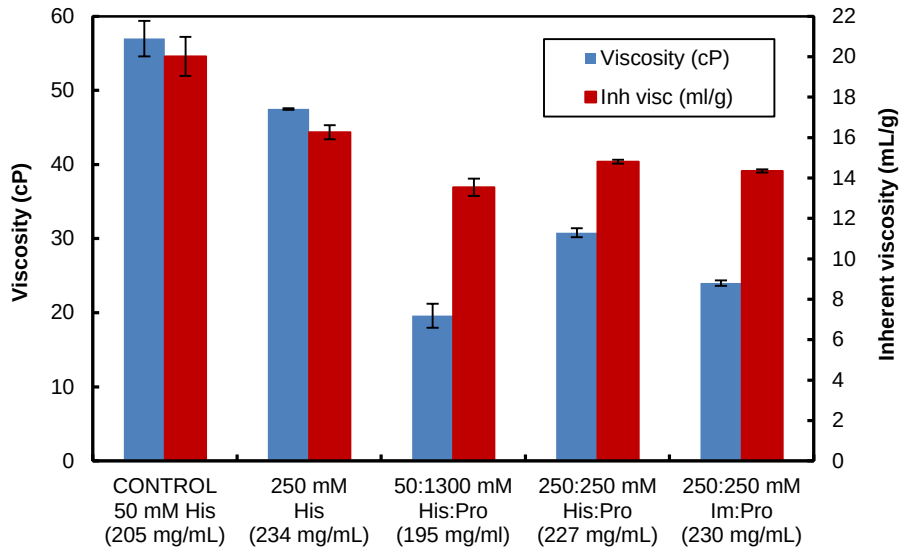

Figure 4.4. Viscosity reductions for select 200 – 230 mg/mL solutions at pH 6 after the addition of high concentrations of proline to the mAb solution in histidine or imidazole buffer. The exact mAb and buffer concentrations are listed in mg/mL and mM, respectively.

While binary systems of Pro with His offer larger viscosity reductions that His-only at the same total co-solute concentration, both co-solutes are much less effective than Arg for the reducing the viscosity of mAb 1 at pH 6. As seen from Fig. S11 of an earlier study with this mAb (33), the addition of 250 mM Arg.HCl at pH 6 reduces the viscosity at 225 mg/mL to 26 cP. Increasing the Pro conc at pH 6 does reduce the viscosity to this same low value, but requires over 1300 mM to do so (Fig. 4.1b). Similarly, the same study showed that over 800 mM His would be needed at pH 6 to reduce the viscosity to ~26 cP. It is clear that at least for this mAb at pH 6, Arg is far more effective on a molar basis for reducing the mAb viscosity.

For practical formulation development applications, Pro as the main viscosity modifier may thus not be as desirable or advantageous as Arg due to its lower molar efficacy for reducing viscosity. However, there may be certain situations where Pro may be advantageous over Arg due to its neutrality, as will be explained in the Discussion section below. Furthermore, the fundamental insight gained from contrasting the effects of Pro on the mAb viscosity and stability

relative to Arg and His may provide guidelines for the future selection and design of highly potent viscosity-reducing co-solutes for a wide variety of mAbs.

4.4.4 Effects of osmolytes on mAb stability against aggregation

To characterize the mAb colloidal stability under thermal stress, the level of irreversible soluble aggregates after 4 weeks of storage at 40°C was quantified by SEC. The pre-storage stability of the mAb was excellent across all tested formulations, with a monomer content of over 99% (relative to the total soluble protein content), as seen from Fig. 4.5a. However, mAb 1 showed a significant loss in soluble monomer content after 4 weeks of storage at 40°C at both pH 5 and 6 in 30 mM His(HCl) control buffers, as seen in Dear et al. (33) and Fig. 4.5b, 4.5c. The monomer content of the mAb 1 pH 5 and 6 controls were 92.0 and 88.2% respectively. The addition of 220 mM Tre suppressed aggregation of mAb 1, yielding 99.5% monomer (33), consistent with protein stabilization by a general osmotic depletion effect to favor folding (20, 21). Similarly, both Pro and Gly suppressed soluble mAb aggregation at all tested co-solute concentrations. As seen in Fig. 4.5b and 4.5c, the relative monomer content of the mAb 1 solutions in 50 mM His with 250 – 1300 mM Pro or Gly were greater than 96.5% after storage, compared to the 30 mM His controls with less than 92.0% monomer content. Increasing Pro concentration between 250 and 1300 mM progressively inhibited post-storage aggregation at both pH 5 (Fig. 4.5b) and 6 (Fig. 4.5c; Table 4.11). However, the overall effect of Pro on both viscosity and stability at pH 5 is weak. The pH 6 Pro systems are all at comparable mAb concentrations of 195 – 205 mg/mL, and show a clear correlation between higher Pro levels and increased storage stability.

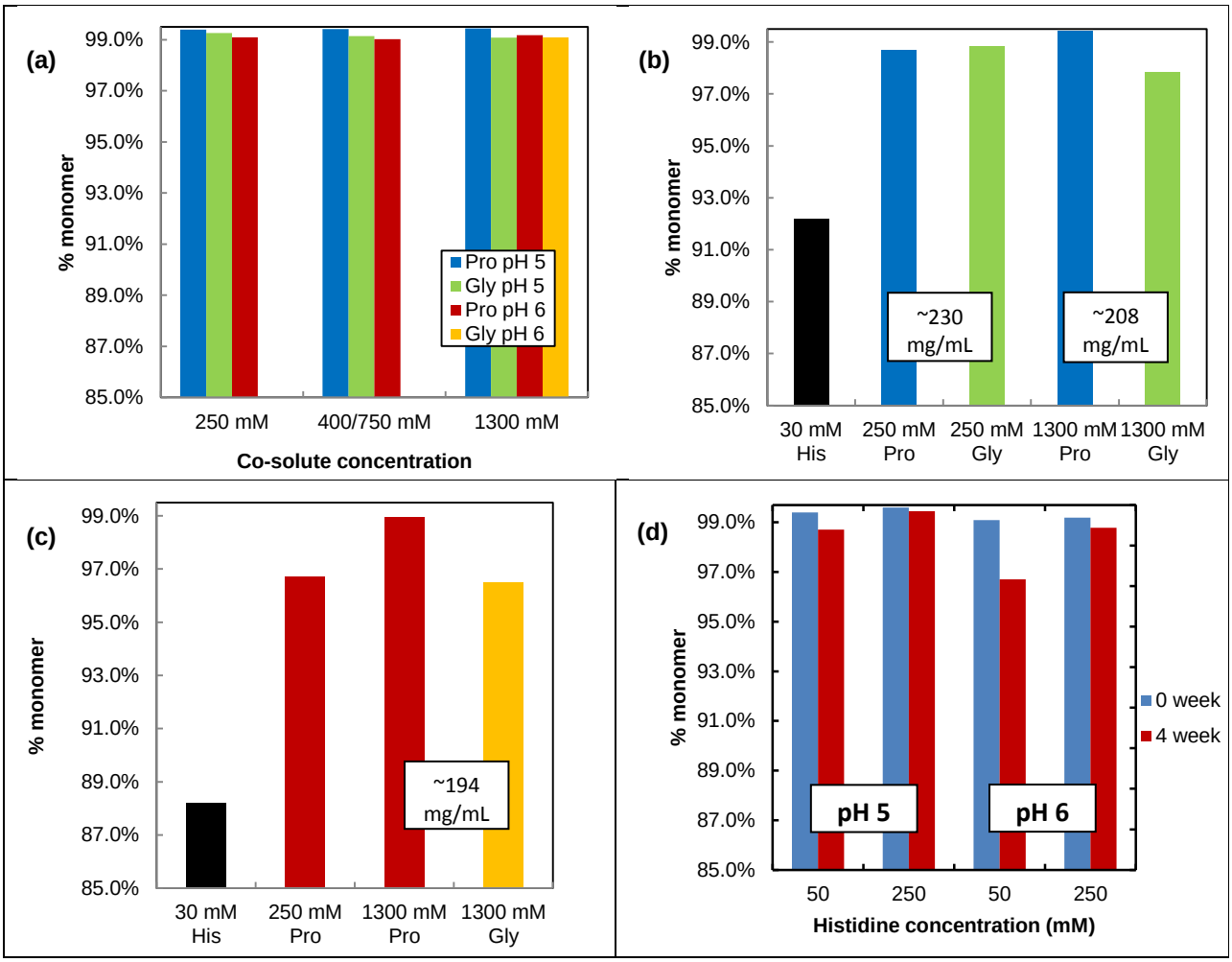

Figure 4.5. Accelerated storage stability of 193 - 232 mg/mL mAb solutions with addition of proline, glycine or histidine. (A) Monomer fraction (of total soluble protein content) before storage as a function of co-solute and pH. The intermediate co-solute concentration is 750 mM for both Pro systems (pH 5 and 6), and 400 mM for Gly (pH 5). No initial stability measurements were made for 250 or 400 mM Gly at pH 6. (B) Monomer fraction after 4-weeks storage at 40°C as a function of co-solute formulation at pH 5. (C) Monomer fraction after 4-weeks storage at 40°C as a function of co-solute formulation at pH 6. The 30 mM His(HCl) 4-week storage controls shown by black bars were reproduced from an earlier study on the same mAb, as reported in Dear et al. (33), where the pH 5 control was at 242 mg/mL, and the pH 6 control was at 224 mg/mL. (D) Monomer fraction before (blue bars) and after (red bars) 4 weeks of storage with histidine at pH 5 and 6 with an additional 250 mM proline. All sample concentrations are shown in Tables 3.S8 – 3.S10. The approximate sample concentrations for each pH/co-solute concentration pair in (B) and (C) are also shown in text boxes on each figure. The monomer fraction was measured by SEC after dilution of the storage samples to 2 mg/mL in the SEC mobile phase.

In contrast, the stabilizing effects of Gly at pH 5 were diminished at 1300 mM relative to 250 mM (Fig. 4.5b, Table 4.12). Similarly, 1300 mM Gly at pH 6 did not increase the post-storage stability as much as 1300 mM Pro (Fig. 4.5c, Table 4.11, 4.12). Thus, while both Pro and Gly imparted overall stabilizing effects on mAb 1 relative to 30 mM His, Gly addition beyond 250 mM proved to be less beneficial. These differing trends can be explained in the context of the net effect of Gly and Pro on the protein stability resulting from a competition between stabilization of the peptide backbone through crowding effects and destabilization of the hydrophobic residue side chains through preferential co-solute interactions, which lead to favorable solvation energies for the side chains (20, 21, 40). CH-π interactions between Gly/Pro and aromatic residues create favorable solvation energies for hydrophobic side chains (40, 41) and destabilize them (conformational instability). However, Pro may contribute more steric repulsion or crowding for greater colloidal stability due to its larger size and rigid side chain structure, which helps to compensate for the increased conformational instability. In contrast, Gly's small size results in less steric repulsion to counteract the increased conformational instability, such that the net effect is reduced overall protein stability relative to 250 mM Gly (but still more stable than the 30 mM His control).

Interestingly, the enhancement of mAb 1's stability with increasing Pro concentration was more pronounced at pH 6, with a 12-fold reduction in monomer loss from 2.4% down to 0.2% at the highest Pro concentration of 1300 mM (Fig. 4.5c, Table 4.11). Proline at the same concentration also nearly eliminated aggregation at pH 5, with a monomer loss of 0.01% (Table 4.11). However, aggregation was less of an issue overall at pH 5, given the much smaller monomer loss at pH 5 relative to pH 6 at each Pro concentration studied (Table 4.11).

Similar to Pro, His improved mAb 1's stability with increasing co-solute concentration, as seen in Fig. 4.5d. An increase in His concentration from 50 to 250 mM in the presence of 250 mM Pro caused a nearly five-fold reduction in monomer loss at both pH 5 and 6, down to as low

as 0.2% and 0.4% respectively (Table 4.12). As was also the case for the Pro systems (Fig. 4.5b, 4.5c), the increased His concentration had a much larger effect on mAb stability at pH 6 than at pH 5, maintaining 99% monomer retention (relative to the total soluble protein content) after 4 weeks of accelerated storage, as opposed to 96.5% at 50 mM His (Fig. 4.5d). Furthermore at pH 6, 250 mM His stabilized the protein more effectively than Pro at the same concentration.

4.4.5 Contrasting effects of proline and glycine on mAb dynamics at high concentration

The collective diffusion coefficient D_c of the mAb at high concentration, as measured by DLS, is strongly influenced by protein-protein interactions via the osmotic compressibility $d\pi/dc$ (Eqn. 4.6), where ϕ is the mAb volume fraction and $f_{sp}c_s$ is a protein-solvent friction term (42).

$$D_c = \frac{(1-\phi)^2}{f_{sp}c_s} * \frac{d\pi}{dc} \tag{4.6}$$

As such, osmolyte effects on D_c can be related to change in the strength of the protein-protein interactions, where $d\pi/dc$ is inversely proportional to the PPI strength (43). The effects of proline and glycine on D_c (Table 4.3) and viscosities (Tables 4.1-4.2) were correlated. The parameters used to fit D_c are given in Table 4.14.

Co-solute conc (mM)	mAb conc (mg/mL)	D_0*10^7 (cm^2/s)	D_c*10^7 (cm^2/s)	D_c/D_0	PDI	β
Proline						
250	228	4.16	3.70 ± 0.11	0.89 ± 0.03	0.191 ± 0.004	---
750	236	3.50	3.54 ± 0.03	1.01 ± 0.010	---	0.37 ± 0.03
1300	228	2.92	3.53 ± 0.01	1.21 ± 0.005	---	0.37 ± 0.05
Glycine						
250	241	4.44	3.31 ± 0.12	0.75 ± 0.027	0.188 ± 0.007	---
750	243	3.95	3.18 ± 0.03	0.81 ± 0.007	0.192 ± 0.006	---
1300	235	3.60	2.56 ± 0.03	0.71 ± 0.008	0.212 ± 0.003	---

Table 4.3. D_c/D_0 of mAb1 at pH 6 with Pro or Gly in 50 mM His(HCl). The ACFs were fit with the quadratic cumulant algorithm except for 750 and 1300 mM proline, which showed secondary decays and were fit to a double exponential (with stretch exponent β). The DLS fit parameters are given in Table 4.12.

Interestingly, a prominent second decay mode was observed for 750 and 1300 mM proline (Fig. 4.9) even though the samples had already been filtered through 0.22 um filters prior to DLS to remove large aggregates. The origin of the second decay mode is unclear, although measurements of the mAb-free Pro solvents suggest that the decay mode may correspond with entities formed only at ultrahigh Pro concentrations, as discussed in the Supporting Info. The ACFs were therefore fit to a stretched double exponential function (Table 4.14). To account for differences in mAb 1's diffusivity due to the formulation solvent viscosities, D_c was normalized as D_c/D_0, where D_0 is measured at infinite dilution in the given solvent. The value of D_0 was determined from a previous measurement for the same mAb in a 30 mM His buffer (33) and corrected for η_0 of each formulation using the Stokes-Einstein relation (Eqn. 4.7).

$$D_0 = \frac{k_B T}{6\pi\eta_0 R_H} \tag{4.7}$$

The D_c/D_0 of mAb 1 increased with proline concentration to above 1.0, whereas it decreased very slightly from 0.75 to 0.71 with increasing glycine concentration (Table 4.3). The PDI of D_c also increased with glycine concentration, although the values for proline and glycine at 250 mM were comparable. The second decay mode of 750 and 1300 mM proline corresponded to a very slow-moving entity/relaxation mode, with D_{eff}/D_0 of ~0.006 (Table 4.14). However, the relative contribution of this slower decay mode to the overall ACF was small (~30% by intensity; Table 4.14). This secondary decay was not observed for glycine (Fig. 4.9b) even at the highest glycine concentration of 1300 mM. At the same mAb concentration, the increasingly faster D_c/D_0 with proline can be attributed to more repulsive (or less attractive) protein-protein interactions via the $d\pi/dc$ contribution to D_c (42). The increase in D_c with proline concentration therefore suggests a progressive weakening of the attractive protein-protein net interactions, which is in line with the observed reduction in mAb viscosity. In contrast, the negligible change in D_c/D_0 with increasing glycine concentration suggests that glycine has no discernible effect on the protein interactions.

The possible causes for the greatly differing effects of proline and glycine on the mAb interactions, viscosity, and stability will be explored further in the Discussion section below.

4.5 DISCUSSION

4.5.1 Proline as an alternative viscosity modifier to ionic co-solutes such as Arg and His

The high concentrations of Pro needed to achieve an acceptable level of viscosity reduction for this mAb at pH 6 are impractical, but it will be shown below to be practical in mixtures with histidine and imidazole. Since cryoprotectants are already included in most lyophilized formulations, proline can be used in place of other cryoprotectants (such as sucrose, mannitose, etc.), with the added benefit of improving the viscosity and stability of the reconstituted protein at high concentration. Using a cryoprotectant that also functions as a viscosity modifier will help to reduce the total osmolality of the mAb drug product, as less Arg, His etc. is needed to maintain low viscosities. Pro has also been approved for use in parenteral formulations (12), and thus it would be helpful to compare its performance as a viscosity modifier against other co-solutes such as Arg and His. Pro shares some physical characteristics with Arg – it is an amphipathic molecule whose side chain (pyrrolidine) has been shown in simulations to preferentially interact with hydrophobic residues via CH-π interactions (13).

An important advancement of this work is the demonstration of greater reductions of viscosity for a Pro-His(HCl) mixture relative to pure His(HCl). As discussed earlier, the 250:250 mM His(HCl):Pro binary system was able to reduce the calculated mAb viscosity at 225 mg/mL and pH 5 even relative to 500 mM His(HCl) (same total co-solute concentration, not including the Cl- counterions), while also providing for a lower co-solute osmolarity of 655 mOsm/L, compared to 810 mOsm/L for 500 mM His(HCl) (Table 4.10). An osmolarity of 655 mOsm/L may be low enough for injection based on various biopharmaceutical experts. Since Pro is a neutral molecule, it is compatible with other ionic co-solutes, creating a large formulation space

for binary Pro systems. However, binary Pro-Arg systems were not explored in this work since Pro-Arg systems require a third solvent component (a buffering agent), as Arg is a poor buffering agent at clinically relevant pH values (pH 5 – 6), leading to a more complicated formulation.

Furthermore, there are some situations where Pro may be advantageous over ionic co-solutes such as Arg and His. For example, in formulation conditions where the mAb has a strong net charge (ex. low pH far from the pI), increasing the ionic strength may screen out the electrostatic repulsion and actually increase the net attraction (1, 17, 18), which has in one case led to phase separation (1). It may therefore be preferable to use a neutral viscosity modifier such as Pro instead of ionic co-solutes such as Arg and His in order to weaken the non-electrostatic PPI without screening out the beneficial electrostatic repulsion.

4.5.2 Inferring protein-protein interaction from viscosity and stability

Although protein-protein interactions are commonly measured at low concentration, they have rarely been measured at concentrations above 200 mg/mL, even without added co-solutes. More recently, neutron scattering (44) and light scattering (3, 4, 45) at high concentration have given some insight into how charged co-solutes modify mAb self-association to lower the mAb viscosity, as well as demonstrated differences in co-solute binding to the protein surface (46). Despite the limited information, it may also be possible to begin to infer how co-solutes influence PPI from the degree by which they modify the viscosity, presumably by weakening the PPI. For example, Arg+ is known to bind to hydrophobic sites (47). Arg+ is also known to reduce the viscosity of highly concentrated mAbs significantly more than inorganic salts such as NaCl (15), which do not modify hydrophobic interactions.

The pH-dependent effect of His and Im on viscosity and stability (Table 4.7, Fig. 4.5d) can be explained in terms of the protein net charge and charge distribution, which change with pH. Since the mAb pI is 9.3, the mAb has a smaller net positive charge and a greater degree of charge anisotropy at pH 6 than at pH 5, where the charge distribution balance is shifted towards

positive charges. As a result, the increase in pH from 5 to 6 both weakens the long-ranged electrostatic repulsion between mAb molecules and strengthens the local anisotropic electrostatic attraction (due to a higher number and probability of attractive electrostatic contacts between oppositely-charged sites on neighboring mAb molecules), leading to stronger protein self-association and higher viscosities. Protonated His and Im may be able to neutralize negative residues via ion pairing, and may also make neutral and positive residues more strongly positive via interactions between the imidazole functionality and the imidazole/guanidyl side chains of the His and Arg residues, respectively (19). As a result, His may be able to increase the protein net charge and reduce surface charge anisotropy, thus strengthening global electrostatic repulsion while weakening local anisotropic electrostatic attraction. Changes in the mAb net charge at high concentration caused by co-solute binding may be quantified in future studies from zeta potential measurements, although extremely low protein electrophoretic mobilities at high ionic strength and/or concentration may prove challenging for obtaining meaningful measurements. Since the mAb has a smaller net charge and greater charge anisotropy at pH 6, modification of the mAb charge and charge distribution by His is expected to have a larger effect on the mAb viscosity and stability than at pH 5, where there are fewer anisotropic attractive interactions to neutralize. The significant differences in the reduction of aggregation and viscosity (η_{inh}) by His at pH 5 and 6 (Table 4.7, Fig. 4.5d) are in agreement with this hypothesis, and are indicative of histidine's effect on the electrostatic PPI. The modestly larger reduction in inherent viscosity by His compared to Imid may potentially be attributed to its larger molecular size, which allows it to contribute more steric repulsion and molecular crowding than Imid at the same molar concentration, favoring a more compact folded mAb conformation (20) that leads to fewer surface-exposed attraction sites. Correspondingly, the larger reduction in η_{inh} for Imid with added Pro, compared to for His, may likely be attributed to the smaller size of Imid which results in less steric hindrance for Pro molecules to approach and interact with the attractive sites on the mAb

surface. In addition, the relative increase in added steric repulsion from Pro is greater for Imid compared to His, given the smaller occupied volume by Imid. However, the differences in viscosity between His and Imid with Pro are not significant enough to support any conclusive statements regarding differences in the two co-solutes' effects on the PPI.

We now address the pH-dependent effects of Pro on the mAb viscosity and stability. Polyol and sugar osmolytes are known to have a pH-dependent effect on protein conformational stability at low pH (~2 – 5) (48) due to changes in the protonation state of the carboxylic acid side chains (pKa ~ 4) in the aspartic acid and glutamic acid residues. The resulting change in protein hydrophobicity (49) modifies the degree of osmolyte exclusion due to repulsion between the polar osmolyte OH- groups and hydrophobic protein surface. However, given the lack of OH- groups in Pro and the higher pH (5 – 6) in this study, the preferential exclusion mechanism cannot explain proline's pH-dependent effects on the mAb viscosity and stability. Instead, it is likely that Pro reduces mAb viscosity and aggregation by modifying the local attractive hydrophobic and/or electrostatic interactions directly. Although the pH dependence may reflect changes in protein hydrophobicity with pH, the similarity between proline and histidine's beneficial effects on these properties with increasing pH may also indicate modification of the electrostatic PPI by Pro, despite proline's net neutrality between pH 5 and 6.

It is possible that the partial positive charge on the pyrrolidine ring side chain (41) as well as the polar groups in Pro may interact with charged mAb residues. The greater molar efficacy of His for reducing viscosity and aggregation relative to Pro may be due to the larger positive charge on its side chain. For example, nearly three times as much Pro as His (750 vs 250 mM respectively; Fig. 4.1b; Table 4.7) is needed to reduce the viscosity at 225 mg/mL and pH 6 to 40 cP. Similarly, the addition of 1050 mM Pro to a reference condition (50:250 mM His:Pro; pH 6) was needed to achieve the same level of aggregation suppression as adding 200 mM His (Fig. 4.5c, 4.5d). However, although Pro reduces viscosity and aggregation at a lower

molar efficiency than His, the observation that it does so in a similar pH-dependent basis (suggesting modification of electrostatic PPI) is surprising given its zero net charge.

4.5.3 Proline amphipathic behavior and modification of hydrophobic PPI

Proline has been observed to bind to aromatic residues by X-ray crystallography (50). Simulations show that Pro interacts with (and binds to) those residues through its pyrrolidine ring side chain via CH-π interactions (41). As a result, Pro can potentially shield aromatic residues and disrupt hydrophobic PPI via preferential hydration of the protein surface through its zwitterionic functionality (51). The stabilization and twofold viscosity reduction of a 200 mg/mL polyclonal IgG solution by 250 mM Pro observed in literature (28) has been attributed to this effect. However, Pro lowered the viscosity of two other mAbs at low concentration but increased the viscosity for one mAb at > 200 mM Pro (52), in contrast to the monotonic behavior (up to 1300 mM Pro) for the mAb in this study. This variability likely reflects the different distributions of hydrophobic and charged interactions sites between the different mAbs. Once the interacting sites are saturated or fully screened by the Pro molecules, the addition of further Pro only serves to increase the solvent viscosity and therefore the solution viscosity.

At high proline concentration, proline's ability to disrupt hydrophobic interactions may also be enhanced by the hypothesized formation of dimers with hydrophobic "pockets" (26) or of supramolecular aggregates (23, 24) via alignment of the pyrrolidine rings. In both cases, the resulting Pro aggregate is strongly amphipathic, with a hydrophilic face (the carboxyl and amino groups) and a hydrophobic face (the stacked pyrrolidine rings). This amphipathic structure may explain why Pro at 2 M or higher has been shown to be a potent hydrotrope (23), as Pro may act as a surfactant to bridge the exposed hydrophobic mAb residues and the solvent molecules, subsequently weakening the attractive hydrophobic PPI. The unexpected observed increase in the mAb solution turbidity with decreasing viscosity at high Pro concentration (Supporting Info) may be attributed in part to the potential formation of Pro aggregates. Similarly, the development

of a much slower secondary relaxation mode in the DLS ACFs for 750 and 1300 mM proline, which was not present for glycine at the same co-solute concentration nor at 250 mM proline, may also indicate structuring of the proline at high concentration and interactions of the mAb with the proline superstructure. It is unlikely that this second decay mode is caused by large mAb aggregates, as the samples were filtered in order to remove aggregates prior to DLS. There was also less irreversible aggregation observed by SEC (Fig. 4.5c) than at 250 mM proline, where the second decay was not present. Similarly, although a secondary decay mode is often indicative of glassy fluids (53) or percolating networks (54), it is unlikely that the high proline mAb solution is approaching a glassy state, given the low viscosities. Instead, the appearance of the secondary slow decay mode corresponds to a large reduction in mAb viscosity and increase in 4-week storage stability, suggesting that this decay mode corresponds to a beneficial entity/mechanism, such as the proposed formation of proline supramolecular aggregates at ultrahigh co-solute concentration. However, further investigation with spectroscopic and other orthogonal techniques would be warranted to validate this hypothesis in future studies.

4.5.4 Favorable side-chain interactions: relation to viscosity and stability

The larger viscosity reductions for Pro relative to the other two osmolytes may be explained in part by the strength of the interactions between the osmolytes and protein residue side chains. Although all three osmolytes are preferentially excluded from the protein backbone, they interact differently with the side chains (21). Trehalose is considered to have the weakest side chain interactions of the three, given the small overall free energy change for side chain transfer into a 1 M osmolyte solution. In contrast, Pro exhibits strongly favorable side chain interactions given the large negative transfer energies (21). More specifically, the transfer energies for apolar (hydrophobic) side chains into Tre solutions are positive (unfavorable), whereas they are significantly negative (favorable) in Pro solutions (21). The favorable side chain interactions of Pro are due to the pyrrolidine ring, which preferentially interacts with

aromatic residues and may allow Pro to shield the hydrophobic residues (26, 41). Glycine can also interact with aromatic residues via CH-π interactions (41), but to a much weaker extent than Pro given the fewer CH-groups available. The stronger side chain interactions may contribute to proline's greater efficacy for weakening local attractive PPI and reducing the mAb viscosity compared to Tre and Gly.

The differences in Pro and Gly's interactions with the protein side chain may also explain their different effects on the colloidal stability of mAb 1. An increase in osmolyte concentration is expected to improve mAb conformational stability due to osmotic depletion (20), which in turn maintains the mAb in the native folded state and minimizes self-association between hydrophobic sites. However, at high total solute (protein + osmolyte) concentrations, the increased proximity of the protein molecules to each other in the crowded system may enhance local electrostatic and hydrophobic attraction, leading to increased self-association despite the greater conformational stability. Proline appears to weaken these attractive interactions, evidenced by its efficacy for reducing the viscosity. In contrast, Gly does not appear to do so, as indicated by its unfavorable effect on the viscosity. This difference may explain why Pro progressively stabilizes mAb 1 with increasing osmolyte concentration (Fig. 4.5b, 4.5c; Table 4.11), while Gly has the opposite effect (Fig. 4.5b, 4.5c; Table 4.12).

4.6 CONCLUSIONS

Proline reduces the viscosity of a concentrated 225 mg/mL mAb 1 solution by up to 3-fold down to 25 cP at pH 6, but has no effect at pH 5. More interestingly, a 250:250 mM His(HCl):Pro binary system causes a greater viscosity reduction at pH 6 (from 84 cP to 31 cP at 225 mg/mL (calculated)) compared to a His system at the same total co-solute concentration (500 mM; 35 cP at 225 mg/mL). Notably, the osmolarity of the His-Pro binary system is 655 mOsm/L, which may be considered within the acceptable range, below that of the His-only system (810 mOsm/L), as Pro does not contribute any counterions to the solution. The lack of

charge or counterions for Pro may also make it more advantageous than ionic viscosity-modifiers such as Arg and His in certain systems with strong electrostatic repulsion (ex. pH far from pI; strongly repulsive B22's etc.), where increasing the ionic strength through addition of ionic co-solutes may lead to stronger attraction and eventual phase instability (55). Pro similarly progressively increases the protein 4-week 40°C storage stability in terms of the soluble monomer content from 92.0% and 88.2% without added co-solute at pH 5 and 6 respectively, to ≥99% at 1300 mM Pro for both pH values. The reductions in viscosity and aggregation are not simply due to osmotic depletion, as two other neutral osmolytes, Gly and Tre, raise both properties. The viscosity of the mAb solution decreased from pH 6 to pH 5 without added co-solute, which may be attributed to the mAb's larger positive net charge, reduced surface charge anisotropy, and weaker local anisotropic electrostatic attraction. It is likely that at pH 6, proline also weaken these interactions by modifying charged sites on the protein surface, given the large dipole moment of its zwitterionic functionality. Furthermore, the hydrophobic part of the pyrrolidine ring may bind to hydrophobic sites on the protein surface and weaken hydrophobic attraction. The faster normalized collective diffusion of mAb 1 at high proline concentration also suggests a weakening of attractive protein interactions. Although co-solute effects on protein morphology have rarely been studied at high protein concentrations, they would be warranted in the future to better understand how changes in morphology and PPI influence viscosity.

4.7 ACKNOWLEDGMENTS

AbbVie provided financial support and the antibody used in this study. The University of Texas at Austin received research funds from AbbVie Inc. to conduct the study. This work was also supported by the Welch Foundation (F-1319, F-1696) and National Science Foundation (CBET-1247945, DGE-1110007). Any opinion, findings, and conclusions or recommendations expressed in this material are those of the authors(s) and do not necessarily reflect the views of the National Science Foundation.

4.8 SUPPORTING INFORMATION

4.8.1 Capillary syringe viscometry

150 uL of the mAb solution was transferred into a 0.1 ml conical glass vial (Wheaton, Millville, NJ), and the flow rate of the solution through a 25-gauge (0.26 mm ID), 1.5" (4 cm) Precision Glide needle attached to a 1 ml Luer-LokTM syringe (Becton Dickinson & Co., Franklin Lakes, NJ), with the syringe plunger held at the 1 ml mark, was captured by video (Kodak Z812 IS zoom digital camera at a frame rate of 30 frames per second) and determined from ImageJ image analysis (56). The derivation of the correlation between the liquid volume and liquid height in the vial, as well as ΔP across the needle was described previously (31). The applied shear rate during each measurement depends on the viscosity of the sample, as described previously (31). For the range of viscosities measured in this study (20 – 100 cP), the corresponding applied shear rates range from 1300 to 260 s^{-1}, respectively.

4.8.2 Dependence of inherent viscosity on mAb concentration

The inherent viscosity increase is expected to increase with the mAb concentration, as can be seen from Eqn. 4.9, derived from combining the definition of the inherent viscosity (Eqn. 4.3) with the Ross-Minton viscosity model (35, 57) (Eqn. 4.8)

$$\frac{\eta}{\eta_0} = exp\left(\frac{[\eta]c}{1-[\eta]\frac{k}{\nu}c}\right) \tag{4.8}$$

$$\eta_{inh} = \frac{[\eta]}{1-[\eta]\frac{k}{\nu}c} \tag{4.9}$$

where [η] is the mAb intrinsic viscosity, c is the mAb concentration, k is the crowding factor, and ν is the Simha shape parameter (35, 57, 58).

The dependence of the inherent viscosity on the mAb concentration has also been observed experimentally, with the inherent viscosity increasing by between 0.02 to 0.06 mL/g per 1 mg/mL mAb (31). The rate of increase in inherent viscosity depends strongly on the co-solute composition, as seen in previous studies with mAb 1 (31, 33).

4.8.3 Binary co-solute systems with proline and histidine/imidazole

The binary 250:250 mM Im:Pro and His:Pro systems afforded the second lowest inherent viscosities for pH 6 in the entire study, with corresponding viscosities of 24 cP and 30 cP at 230 mg/mL, respectively (Fig. 4.4). The lowest η_{inh} of 13.5 mL/g was obtained at a high Pro concentration of 1300 mM buffered with 50 mM His. However, although the addition of 1300 mM Pro yielded the greatest reduction in η_{inh}, the binary His-Pro and Im-Pro systems at half the co-solute concentration are more practical for subcutaneous injection in terms of tonicity.

A second process, dilution of lyophilized powder (LD), was utilized to complement the above data (from centrifugation filtration, CF) at pH 6. The LD process has an advantage in that the final co-solute composition is fully defined from gravimetric analysis. In the CF process, there is some uncertainty in this composition due to excluded volume effects, Donnan equilibrium and membrane/co-solute interactions during filtration (59, 60). As seen for binary co-solute systems with Pro and 240 mM His produced by LD (Table 4.9), η_{inh} decreased modestly by 0.5 mL/g with the increase in Pro concentration between 435 to 870 mM, but remained relatively constant between 870 and 1300 mM. The inherent viscosities are comparable to that of the binary system with 250:250 mM Pro:His made by CF (Table 4.8). We chose to study higher protein concentrations by LD, which may explain in part the slightly higher inherent viscosities of the LD systems (Table 4.9), as η_{inh} may be expected to increase about 0.5 – 0.75 mL/g at 250 mg/mL mAb versus 225 mg/mL (Supporting Info).

4.8.4 Dynamic light scattering of the 1300 mM Pro (mAb-free) buffer

To determine whether the secondary relaxation mode in the ACFs of the 750 and 1300 mM Pro system indicated any unusual structures in the mAb solution, or if it arose from the concentrated proline itself, the ACF of a placebo buffer with 1300 mM Pro and 50 mM His (to replicate the solvent conditions of the highest-Pro conc mAb sample, where the secondary decay was most prevalent) was measured in triplicate. As can be seen from Fig. 4.10, the buffer-only ACF is very noisy due to the low count rates (~7 kcps), and there is no clear decay. However, an approximate, extremely depressed correlation relaxation mode may be discerned, with a possible relaxation time of ~1000 us, in the same delay time range as the second relaxation mode in the ACFs of the 750 and 1300 mM Pro systems with mAb. It is possible that the ultraconcentrated Pro forms some unusual structures, such as the supramolecular Pro aggregates proposed in the literature (23, 24), that are responsible for the second decay in the 750 and 1300 mM Pro mAb samples. However, the placebo buffer count rates are extremely low (~7 kcps, even at max laser power with no attenuation) on the order of solvent background scattering. In contrast, the mAb scattering contributes count rates on the order of 500 kcps. As such, it is unclear whether the concentrated Pro would have any significant effects on the ACF of the mAb solution, as the photon count rates from the Pro is on the same order of magnitude as the background noise.

4.8.5 Effect of high concentrations of proline, glycine and histidine on mAb turbidity

Unlike the case for SEC, which is performed at dilute conditions, protein self-association may be characterized at high concentration in terms of the solution turbidity (61). An elevated turbidity is typically correlated with increased protein aggregation (61, 62) and subsequent viscosity increase (4, 63-65). As shown in Table 4.1 at pH 5 and 6, the A350 values (normalized to 1 cm) were higher at 500 and 1300 mM Pro than for either 0 or 250 mM Pro, despite the lower corresponding viscosities. However, even the highest measured turbidity of 0.5 cm^{-1} at 195 mg/mL and pH 6 with 1300 mM Pro (Table 4.1) is relatively low, comparable to the turbidity of

70 – 100 mg/mL mAb solutions formed by tangential flow ultrafiltration under optimized conditions (66-68). Given the expected increase in turbidity with mAb concentration (62), the comparable turbidities in this study but at much higher concentrations (>200 mg/mL) indicate a low level of insoluble aggregates. Due to small variations in the mAb concentrations, the A_{350} was also normalized by the protein concentration (A_{350}/c), as shown in Fig. 4.6. The shapes of the A_{350}/c versus proline concentration curves were similar, reaching a plateau. However, the values were modestly higher at pH 6 (Fig. 4.6), which may indicate greater aggregation (61, 62). At a given proline concentration, the A_{350}/c, the corresponding amount of aggregates from SEC and viscosities were higher at pH 6 than at pH 5. However, at a given pH, the slight increase in A_{350}/c with proline concentration was unexpected, given the corresponding decrease in inherent viscosity (Fig. 4.7a) and increase in % monomer from SEC (Fig. 4.7b), as discussed below.

In contrast, the elevated inherent viscosities and reduced mAb stability of the glycine-containing formulations were found to correlate directly with the initial (pre-storage) normalized solution turbidity, as seen in Figs. S3a and S3b respectively. The concurrent viscosity and aggregation increase with elevated solution turbidities is consistent with the formation of protein aggregates (4, 61-65, 69).

The elevated turbidities observed for the systems with 750 and 1300 mM Pro (Table 4.1, Fig. 4.6), relative to 250 mM Pro (Table 4.1, 4.5), Gly (Table 4.2) or His (Table 4.7), are suggestive of the presence of Pro aggregates in the mAb solution, which are hypothesized to form at high Pro concentration based on simulations (26) and indirect evidence (23, 24, 70). As mentioned earlier, the unexpected inverse correlation between the turbidity and viscosity (Fig. 4.7a) or stability (Fig. 4.7b) of the high Pro concentration solutions is the opposite of the correlation seen for Gly (Fig. 4.8a, 4.8b), which exhibits a typical increase in turbidity with viscosity due to the presence of viscosity-raising reversible oligomers (4, 63). It is thus possible

that the elevated turbidity of the 750 and 1300 mM Pro solutions was caused by the formation of viscosity-lowering amphipathic Pro aggregates rather than by protein self-association.

The formation of Pro super-aggregates is hypothesized to occur at concentrations of 1.5 M or higher, based on indirect experimental evidence (23, 24, 70). As such, it may seem unlikely that proline aggregation occurs at the concentrations (0.25 – 1.3 M) in this study. However, proline aggregates may potentially still form due to the crowded environment in the concentrated proline-protein solution, given that the protein contributes to the osmotic depletion of Pro. Previously, a sharp and unusual change in proline's physical properties and its potency as a protein solubilizer and stabilizer (as assessed by turbidity reduction for denatured protein solutions) was observed at ~1.5 M (23, 24, 70), corresponding to mass concentration and volume fractions of 170 mg/mL and 0.17, respectively. In our ~220 mg/mL mAb solutions with 750 – 1300 mM Pro, the combined mass concentration and volume fraction of the mAb and Pro were 300+ mg/mL and 0.30, respectively. Thus, the total solute concentration may be sufficient to produce enough osmotic depletion to form proline aggregates at 750 and 1300 mM Pro.

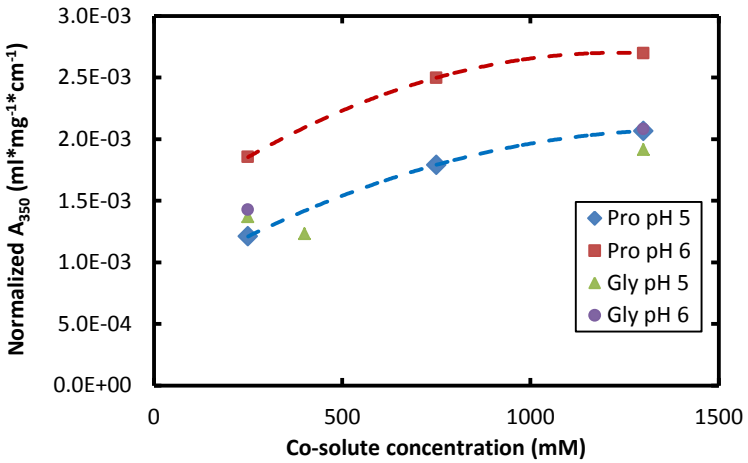

Figure 4.6. 'Normalized' turbidity of ~220 mg/mL mAb solutions with proline or glycine as a function of the co-solute concentration and pH. The normalized turbidity was calculated by dividing the measured solution turbidity by the mAb concentration. The colored lines are a guide to the eye.

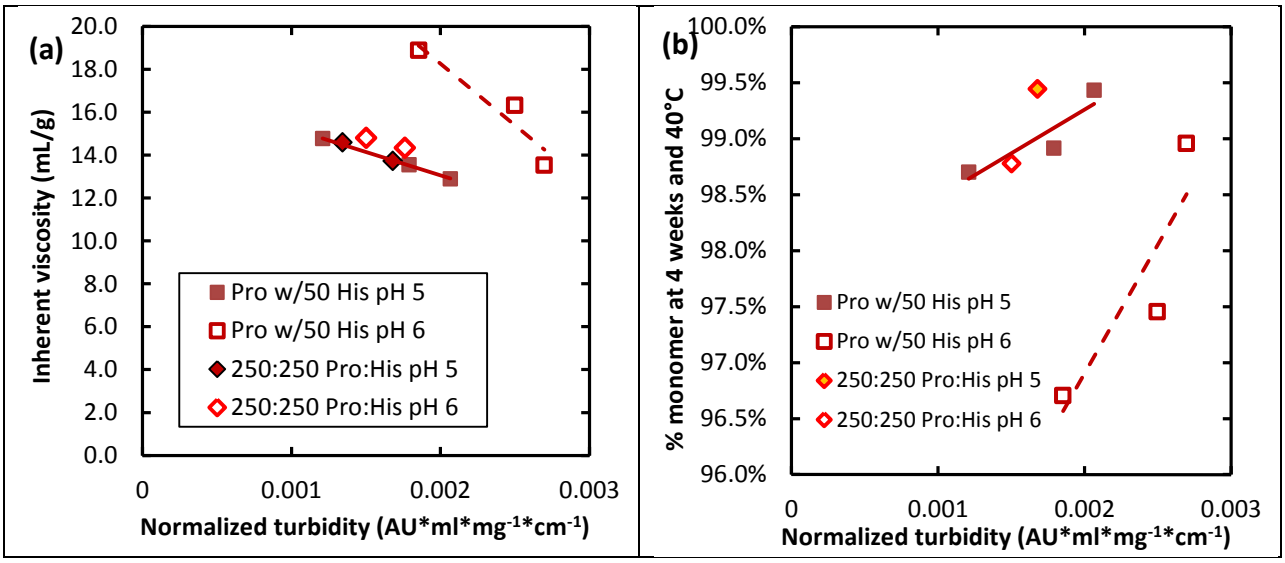

Figure 4.7. (a) Inherent viscosity and (b) monomer retention after 4 weeks of storage at 40°C as a function of initial (pre-storage) concentration-normalized turbidity for mAb solutions with 250 – 1300 mM proline in 50 mM His(HCl) buffer at pH 5 – 6. The normalized turbidity was calculated by dividing the solution turbidity at 350 nm by the mAb concentration. The colored lines are a guide to the eye.

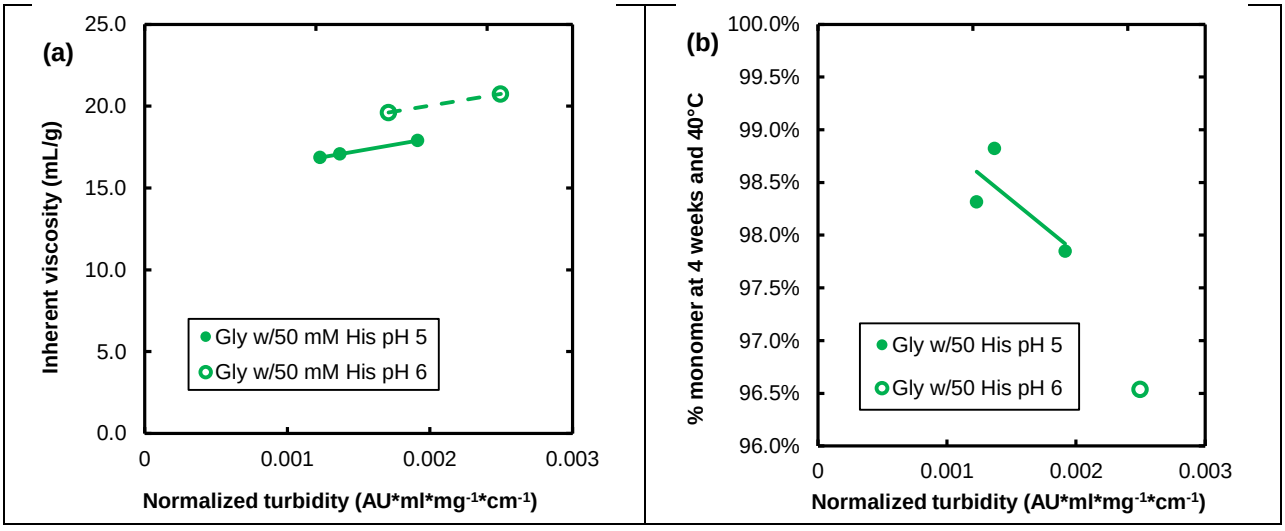

Figure 4.8. (a) Inherent viscosity and (b) monomer retention after 4 weeks of storage at 40°C as a function of initial (pre-storage) concentration-normalized turbidity for mAb solutions with 250 – 1300 mM glycine in 50 mM His(HCl) buffer at pH 5 – 6. The normalized turbidity was calculated by dividing the solution turbidity at 350 nm by the mAb concentration. The colored lines are a guide to the eye.

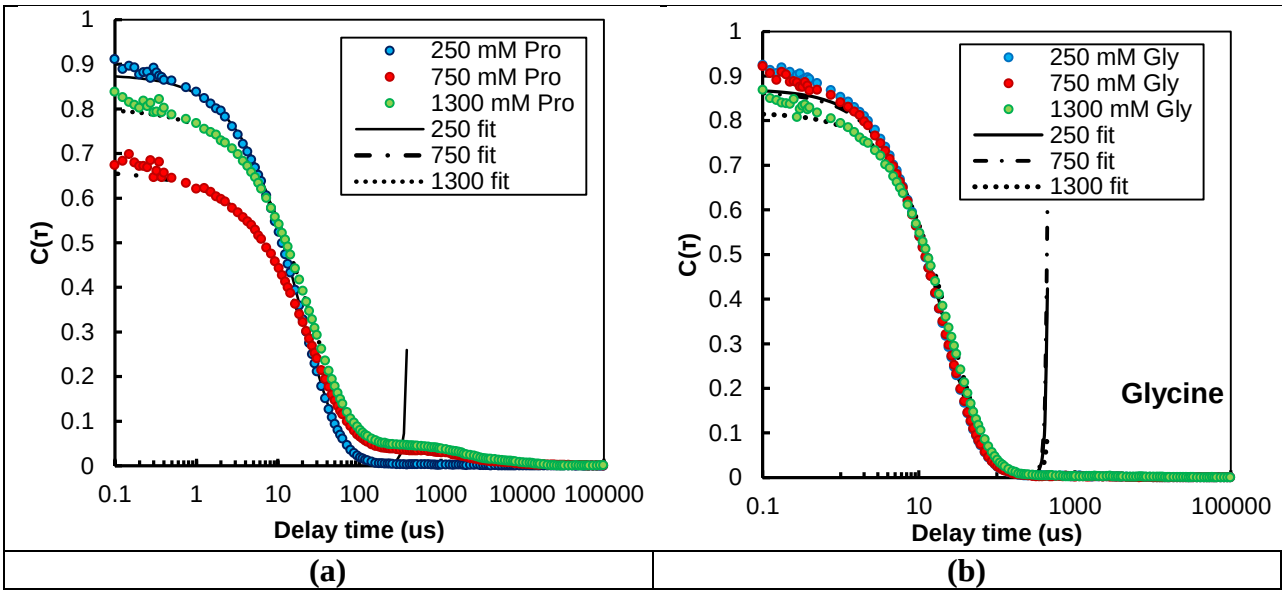

Figure 4.9. DLS ACFs of mAb1 with (a) 250, 750 and 1300 mM proline or (b) 250, 750 and 1300 mM glycine at pH 6 in 50 mM His(HCl). The data is shown as discrete points, while the double exponential fits (750 and 1300 mM proline) and quadratic cumulant fits (all others) are shown by the dashed lines.

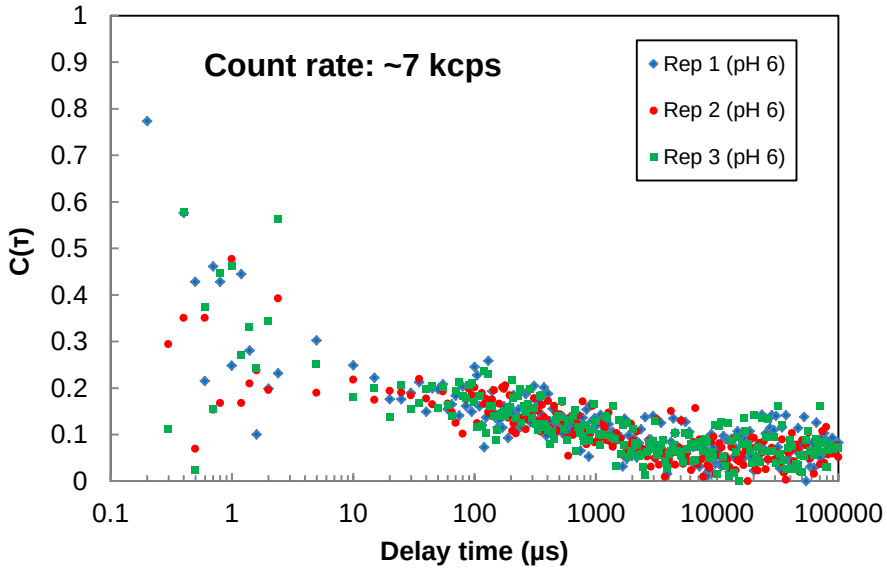

Figure 4.10. DLS autocorrelation function of the 50:1300 mM His(HCl):Pro (pH 6) background buffers. The average photon count rate was ~7 kcps across all replicate measurements.

mAb conc (mg/mL)	pH	Proline conc		η (cP)	η_0 (cP)	η_{inh} (mL/g)	A_{350} ($AU*cm^{-1}$)
		mg/mL	mM				
209 ± 0.3	6.07	0	0	80 ± 4.6	0.93	21.3 ± 0.3	0.530
226 ± 0.5	6.15	29	250	106 ± 2.3	0.94	20.9 ± 0.1	0.806
214 ± 1.9	6.06	86	750	60.0 ± 1.3	1.15	18.5 ± 0.2	0.963
224 ± 0.3	6.04	138	1200	48 ± 2.9	1.31	16.1 ± 0.3	0.352

Table 4.4. Dependence of mAb viscosity on proline concentration at pH 6 with 50 mM sodium phosphate for mAb solutions formed by centrifugation filtration.

mAb conc (mg/mL)	pH	Tre conc		η (cP)	η_0 (cP)	η_{inh} (mL/g)
		mg/mL	mM			
225 ± 0.1[a]	6.04	0	0	102 ± 1.1	0.93	20.9 ± 0.0
248 ± 3.8	6.13	56	147	277 ± 43.4	1.10	22.3 ± 0.7
243 ± 2.2	6.10	51	134	176 ± 1.8	1.08	21.0 ± 0.2
261 ± 5.6[a]	6.05	83	220	329 ± 18.8	1.05	22.0 ± 0.5
196 ± 2.0[a]	6.05	83	220	58 ± 4.1	1.05	20.5 ± 0.4

a. Data from Dear et al ., *Pharm. Res.* (2017) (33)

Table 4.5. Dependence of mAb viscosity on trehalose concentration at pH 6 with 30 mM His(HCl). The sample in row 5 was obtained by diluting the 260 mg/mL solution in row 4 with same-formulation buffer.

mAb conc (mg/mL)	pH	Tre conc		η (cP)	η_0 (cP)	η_{inh} (mL/g)
		mg/mL	mM			
209	6.1	0	0	80	0.93	21.3
219	6.4	100	264	151	1.22	22.0
244	6.3	200	529	356	1.40	22.7
218	6.4	220	582	94	1.46	19.1

Table 4.6. Dependence of mAb viscosity on trehalose concentration at pH 6 with 50 mM sodium phosphate buffer. The mAb solutions were formed by the lyophilization dilution (LD) technique.

mAb conc (mg/mL)	pH	Buffer	Buffer conc (mM)	η (cP)	η_0 (cP)	η_{inh} (mL/g)	A_{350} ($AU*cm^{-1}$)
pH 5							
208 ± 4.3	4.93	His	50	21 ± 2.1	0.93	15.0 ± 0.6	0.293
210 ± 4.0	5.00	His	250	18 ± 0.4	1.06	13.4 ± 0.3	0.422
pH 6							
205 ± 9.6	5.96	His	50	57 ± 2.4	0.93	20.0 ± 1.0	0.327
234 ± 5.0	6	His	250	48 ± 0.1	1.06	16.2 ± 0.3	0.293
230 ± 0.2	6.17	Im	250	47 ± 0.4	0.95	17.0 ± 0.0	0.369

Table 4.7. Dependence of mAb viscosity on the concentration of buffer species, histidine or imidazole (titrated with HCl to pH 5 - 6) for mAb solutions formed by centrifugation filtration.

mAb conc (mg/mL)	pH	Buffer	Proline conc		η (cP)	η_0 (cP)	η_{inh} (mL/g)	A_{350} ($AU*cm^{-1}$)
			mg/mL	mM				
pH 5								
201 ± 1.0	4.96	His	29	250	17 ± 2.1	1.06	13.7 ± 0.6	0.338
pH 6								
227 ± 0.8	5.92	His	29	250	31 ± 0.6	1.06	14.8 ± 0.1	0.342
223 ± 0.3	6.11	Im	29	250	24 ± 0.4	0.98	14.3 ± 0.1	0.393

Table 4.8. Viscosity of binary co-solute systems at pH 5 – 6 with 250 mM proline and 250 mM His(HCl) or Im(HCl) for mAb solutions formed by centrifugation filtration. The results for His and Im without proline are given in Table 4.7.

mAb conc (mg/mL)	Proline conc		η (cP)	η_0 (cP)	η_{inh} (mL/g)
	mg/mL	mM			
260 ± 4.0	50	435	59 ± 0.4	1.12	15.2 ± 0.2
257 ± 0.8	100	870	55 ± 2.9	1.29	14.6 ± 0.2
265 ± 0.7	100	870	64 ± 3.3	1.29	14.7 ± 0.2
238 ± 1.0	150	1300	48 ± 2.6	1.53	14.5 ± 0.2
246 ± 0.3	150	1300	68 ± 3.8	1.53	15.4 ± 0.2

Table 4.9. Dependence of mAb viscosity on proline concentration at pH 6 with 240 mM His(HCl) for mAb solutions made by lyophilization dilution.

Formulation	Meas. pH	His buffer pH	Osmolarity (mOsm/L)	Meas. mAb conc (mg/mL)	η_{inh} (mL/g)	η_0 (cP)	Calc visc at 225 mg/mL (cP)
250:250 mM His(HCl):Pro	5.9	6.0	655	227	14.8	1.06	31
360 mM His(HCl)	6.2	6.0	583	236	15.1	1.25	44
500 mM His(HCl)	6.0	6.0	810	232	14.2	1.3	35

Table 4.10. Comparison of the binary Pro-His system (pH 5.9; Table 4.8) with His-only systems for the same mAb from Dear et al. at high osmolarities and pH ~6. The samples were prepared in pH 6 His(HCl) buffer, with a HCl:His mole ratio of 0.62. The co-solute osmolarity was calculated using the known His and Pro concentrations, along with the HCl concentration calculated with the buffer HCl:His mole ratio. The expected viscosity at 225 mg/mL for each system was calculated from the measured η_{inh} (at 219 – 246 mg/mL) (Eqn. 4.2). The first row (Pro-His binary system) is replicated from Table 4.8 of this work. All remaining inherent viscosity data is reproduced from Table SIII and Figure S14 of Dear et al. (33).

mAb conc (mg/mL)	pH	Proline conc		% monomer by SEC after storage at 40°C		% monomer loss after 4 weeks
		mg/mL	mM	0 weeks	4 weeks	
pH 5						
225 ± 2.2	5.12	29	250	99.4%	98.7%	0.7%
239 ±1.0	5.15	86	750	99.4%	98.9%	0.5%
209 ± 0.9	5.27	150	1303	99.4%	99.4%	0.0%
pH 6						
205 ± 0.4	5.94	29	250	99.1%	96.7%	2.4%
205 ± 2.9	6.05	86	750	99.0%	97.5%	1.5%
195 ± 1.3	6.07	150	1303	99.2%	99.0%	0.2%

Table 4.11. mAb soluble aggregation rate and monomer retention under accelerated storage at 40°C and pH 5 – 6 with 50 mM His(HCl) as a function of proline concentration.

mAb conc (mg/mL)	pH	Glycine conc		% monomer by SEC after storage at 40°C		% monomer loss after 4 weeks
		mg/mL	mM	0 weeks	4 weeks	
pH 5						
232 ± 3.6	5.16	19	250	99.3%	98.8%	0.5%
233 ± 4.1	5.18	30	400	99.1%	98.3%	0.8%
207 ± 0.0	5.38	98	1300	99.1%	97.9%	1.2%
pH 6						
223 ± 1.9	5.96	19	250	---	---	---
193 ± 1.3	6.10	98	1300	99.1%	96.5%	2.5%

Table 4.12. mAb soluble aggregation rate and monomer retention under accelerated storage at 40°C and pH 5 – 6 with 50 mM His(HCl) as a function of glycine concentration.

mAb conc (mg/mL)	pH	His conc (mM)	Proline conc		% monomer by SEC after storage at 40°C		% monomer loss after 4 weeks
			mg/mL	mM	0 weeks	4 weeks	
pH 5							
225 ± 2.2	5.12	50	29	250	99.4%	98.7%	0.7%
201 ± 1.0	4.96	250	29	250	99.6%	99.4%	0.2%
pH 6							
205 ± 0.4	5.94	50	29	250	99.1%	96.7%	2.4%
227 ± 0.8	5.92	250	29	250	99.2%	98.8%	0.4%

Table 4.13. mAb soluble aggregation rate and monomer retention under accelerated storage at at 40°C and pH 5 – 6 with 250 mM proline as a function of histidine(HCl) concentration.

Co-solute conc (mM)	η_0 (cP)	Solvent RI	q (cm^{-1})	τ_d (μs)	τ_{slow} (μs)	A_1	D_{slow}/D_0
Proline							
250	1.00	1.338	265087	38 ± 1.2	---	---	---
750	1.19	1.347	266992	40 ± 0.4	6346 ± 1115	0.66 ± 0.02	0.0063 ± 0.0011
1300	1.42	1.358	269087	39 ± 0.2	7194 ± 501	0.68 ± 0.01	0.0066 ± 0.0005
Glycine							
250	0.94	1.336	264797	43 ± 1.5	---	---	---
750	1.05	1.343	266121	44 ± 0.4	---	---	---
1300	1.16	1.350	267577	54 ± 0.6	---	---	---

Table 4.14. DLS autocorrelation fit parameters for mAb 1 at pH 6 with proline or glycine in 50 mM His(HCl). All formulations were fit with the quadratic cumulant algorithm (with associated polydispersity index PDI), except for 750 and 1300 mM proline, which were fit to a double exponential function.

4.9 REFERENCES

1. Shire SJ, Shahrokh Z, Liu J. Challenges in the Development of High Protein Concentration Formulations. J Pharm Sci. 2004;93(6):1390-402.
2. Connolly Brian D, Petry C, Yadav S, Demeule B, Ciaccio N, Moore Jamie MR, et al. Weak Interactions Govern the Viscosity of Concentrated Antibody Solutions: High-Throughput Analysis Using the Diffusion Interaction Parameter. Biophys J. 2012;103(1):69-78.
3. Scherer TM, Liu J, Shire SJ, Minton AI. Intermolecular Interactions of IgG1 Monoclonal Antibodies at High Concentrations Characterized by Light Scattering. J Phys Chem B. 2010;114(40):12948-57.
4. Lilyestrom WG, Yadav S, Shire SJ, Scherer TM. Monoclonal Antibody Self-Association, Cluster Formation, and Rheology at High Concentrations. J Phys Chem B. 2013;117(21):6373-84.
5. Arora J, Hu Y, Esfandiary R, Sathish HA, Bishop SM, Joshi SB, et al. Charge-mediated Fab-Fc interactions in an IgG1 antibody induce reversible self-association, cluster formation, and elevated viscosity. mAbs. 2016;8(8):1561-74.
6. Quang LJ, Sandler SI, Lenhoff AM. Anisotropic Contributions to Protein–Protein Interactions. J Chem Theory Comput. 2014;10(2):835-45.
7. Chari R, Jerath K, Badkar AV, Kalonia DS. Long- and Short-Range Electrostatic Interactions Affect the Rheology of Highly Concentrated Antibody Solutions. Pharm Res. 2009;26(12):2607-18.
8. Yadav S, Laue TM, Kalonia DS, Singh SN, Shire SJ. The Influence of Charge Distribution on Self-Association and Viscosity Behavior of Monoclonal Antibody Solutions. Mol Pharmaceutics. 2012;9(4):791-802.

9. Buck PM, Chaudhri A, Kumar S, Singh SK. Highly Viscous Antibody Solutions Are a Consequence of Network Formation Caused by Domain-Domain Electrostatic Complementarities: Insights from Coarse-Grained Simulations. Mol Pharmaceutics. 2015;12(1):127-39.

10. Yadav S, Liu J, Shire SJ, Kalonia DS. Specific Interactions in High Concentration Antibody Solutions Resulting in High Viscosity. J Pharm Sci. 2010;99(3):1152-68.

11. Du W, Klibanov AM. Hydrophobic salts markedly diminish viscosity of concentrated protein solutions. Biotechnol Bioeng. 2011;108(3):632-6.

12. Kanai S, Liu J, Patapoff TW, Shire SJ. Reversible Self-Association of a Concentrated Monoclonal Antibody Solution Mediated by Fab-Fab Interaction That Impacts Solution Viscosity. J Pharm Sci. 2008;97(10):4219-27.

13. Salvi G, De Los Rios P, Vendruscolo M. Effective interactions between chaotropic agents and proteins. Proteins: Struct, Funct, Bioinf. 2005;61(3):492-9.

14. Chang BS, inventor; Integritybio Inc., assignee. Protein formulations containing amino acids patent WO2013063510 A1. 2013.

15. Inoue N, Takai E, Arakawa T, Shiraki K. Specific Decrease in Solution Viscosity of Antibodies by Arginine for Therapeutic Formulations. Mol Pharmaceutics. 2014;11(6):1889-96.

16. Arakawa T, Ejima D, Tsumoto K, Obeyama N, Tanaka Y, Kita Y, et al. Suppression of protein interactions by arginine: A proposed mechanism of the arginine effects. Biophys Chem. 2007;127(1–2):1-8.

17. Chen B, Bautista R, Yu K, Zapata GA, Mulkerrin MG, Chamow SM. Influence of histidine on the stability and physical properties of a fully human antibody in aqueous and solid forms. Pharm Res. 2003;20(12):1952-60.

18. Liao SM, Du QS, Meng JZ, Pang ZW, Huang RB. The multiple roles of histidine in protein interactions. Chem Cent J. 2013;7.

19. Heyda J, Mason PE, Jungwirth P. Attractive Interactions between Side Chains of Histidine-Histidine and Histidine-Arginine-Based Cationic Dipeptides in Water. J Phys Chem B. 2010;114(26):8744-9.

20. Arakawa T, Timasheff SN. The stabilization of proteins by osmolytes. Biophys J. 1985;47(3):411-4.

21. Auton M, Rösgen J, Sinev M, Holthauzen LMF, Bolen DW. Osmolyte effects on protein stability and solubility: A balancing act between backbone and side-chains. Biophys Chem. 2011;159(1):90-9.

22. Baumann P, Schermeyer M-T, Burghardt H, Dürr C, Gärtner J, Hubbuch J. Prediction and characterization of the stability enhancing effect of the Cherry-Tag™ in highly concentrated protein solutions by complex rheological measurements and MD simulations. International Journal of Pharmaceutics. 2017;531(1):360-71.

23. Samuel D, Kumar TKS, Jayaraman G, Yang PW, Yu C. Proline is a protein solubilizing solute. Biochem Mol Biol Int. 1997;41(2):235-42.

24. Kumat TKS, Samuel D, Jayaraman G, Srimathi T, Yu C. The role of proline in the prevention of aggregation during protein folding in vitro. IUBMB Life. 1998;46(3):509-17.

25. Amend JP, Helgeson HC. Solubilities of the common L-α-amino acids as a function of temperature and solution pH. Pure Appl Chem. 1997;69(5):935-42.

26. Busch S, Lorenz CD, Taylor J, Pardo LC, McLain SE. Short-Range Interactions of Concentrated Proline in Aqueous Solution. J Phys Chem B. 2014;118(49):14267-77.
27. Ignatova Z, Gierasch LM. Inhibition of protein aggregation in vitro and in vivo by a natural osmoprotectant. Proc Natl Acad Sci U S A. 2006;103(36):13357-61.
28. Maeder W, Lieby P, Sebald A, Spycher M, Bolli R. Stability over 24 Months and Tolerability of a New 20% Proline-stabilized Polyclonal Immunoglobulin for Subcutaneous Administration (SCIG). J Allergy Clin Immunol. 2010;125(2, Supplement 1):AB142.
29. Borwankar AU, Dinin AK, Laber JR, Twu A, Wilson BK, Maynard JA, et al. Tunable equilibrium nanocluster dispersions at high protein concentrations. Soft Matter. 2013;9(6):1766.
30. Johnston KP, Maynard JA, Truskett TM, Borwankar AU, Miller MA, Wilson BK, et al. Concentrated Dispersions of Equilibrium Protein Nanoclusters that Reversibly Dissociate into Active Monomers. ACS Nano. 2012;6(2):1357-69.
31. Hung JJ, Borwankar AU, Dear BJ, Truskett TM, Johnston KP. High concentration tangential flow ultrafiltration of stable monoclonal antibody solutions with low viscosities. J Membr Sci. 2016;508:113-26.
32. Borwankar AU, Dear BJ, Twu A, Hung JJ, Dinin AK, Wilson BK, et al. Viscosity Reduction of a Concentrated Monoclonal Antibody with Arginine·HCl and Arginine·Glutamate. Ind Eng Chem Res. 2016;55(43):11225-34.
33. Dear BJ, Hung JJ, Truskett TM, Johnston KP. Contrasting the Influence of Cationic Amino Acids on the Viscosity and Stability of a Highly Concentrated Monoclonal Antibody. Pharm Res. 2017;34(1):193-207.
34. Zhao H, Brown Patrick H, Schuck P. On the Distribution of Protein Refractive Index Increments. Biophys J. 2011;100(9):2309-17.
35. Liu J, Nguyen MDH, Andya JD, Shire SJ. Reversible Self-Association Increases the Viscosity of a Concentrated Monoclonal Antibody in Aqueous Solution. J Pharm Sci. 2005;94(9):1928-40.
36. Heimenz PC, Rajagopalan R. Principles of Colloid and Surface Chemistry. 3rd ed. New York: Marcel Dekker, Inc.; 1997.
37. Dharmaraj VL, Godfrin PD, Liu Y, Hudson SD. Rheology of clustering protein solutions. Biomicrofluidics. 2016;10(4):043509.
38. Wang S, Zhang N, Hu T, Dai W, Feng X, Zhang X, et al. Viscosity-Lowering Effect of Amino Acids and Salts on Highly Concentrated Solutions of Two IgG1 Monoclonal Antibodies. Mol Pharmaceutics. 2015;12(12):4478-87.
39. Whitaker N, Xiong J, Pace SE, Kumar V, Middaugh CR, Joshi SB, et al. A Formulation Development Approach to Identify and Select Stable Ultra–High-Concentration Monoclonal Antibody Formulations With Reduced Viscosities. J Pharm Sci. 2017;106(11):3230-41.
40. Auton M, Bolen DW, Rosgen J. Structural thermodynamics of protein preferential solvation: Osmolyte solvation of proteins, aminoacids, and peptides. Proteins: Struct, Funct, Bioinf. 2008;73(4):802-13.
41. Zondlo NJ. Aromatic-Proline Interactions: Electronically Tunable CH/pi Interactions. Acc Chem Res. 2013;46(4):1039-49.

42. Nicoud L, Jagielski J, Pfister D, Lazzari S, Massant J, Lattuada M, et al. Kinetics of Monoclonal Antibody Aggregation from Dilute toward Concentrated Conditions. J Phys Chem B. 2016.

43. Svergun DI, Koch MH, Timmins PA, May RP. Small angle X-ray and neutron scattering from solutions of biological macromolecules. New York: Oxford University Press; 2013. 368 p.

44. Godfrin PD, Zarzar J, Zarraga IE, Porcar L, Falus P, Wagner NJ, et al. The Effect of Hierarchical Cluster Formation on the Viscosity of Concentrated Monoclonal Antibody Formulations Studied by Neutron Scattering. J Phys Chem B. 2015.

45. Lilyestrom WG, Shire SJ, Scherer TM. Influence of the Cosolute Environment on IgG Solution Structure Analyzed by Small-Angle X-ray Scattering. J Phys Chem B. 2012;116(32):9611-8.

46. Scherer TM. Role of Cosolute–Protein Interactions in the Dissociation of Monoclonal Antibody Clusters. J Phys Chem B. 2015;119(41):13027-38.

47. Shukla D, Trout BL. Interaction of Arginine with Proteins and the Mechanism by Which It Inhibits Aggregation. J Phys Chem B. 2010;114(42):13426-38.

48. Haque I, Singh R, Moosavi-Movahedi AA, Ahmad F. Effect of polyol osmolytes on ΔGD, the Gibbs energy of stabilisation of proteins at different pH values. Biophys Chem. 2005;117(1):1-12.

49. Kuhn LA, Swanson CA, Pique ME, Tainer JA, Getzoff ED. Atomic and residue hydrophilicity in the context of folded protein structures. Proteins: Struct, Funct, Bioinf. 1995;23(4):536-47.

50. Pemberton TA, Still BR, Christensen EM, Singh H, Srivastava D, Tanner JJ. Proline: Mother Nature's cryoprotectant applied to protein crystallography. Acta Crystallogr, Sect D: Biol Crystallogr. 2012;68(Pt 8):1010-8.

51. Jiang SY, Cao ZQ. Ultralow-Fouling, Functionalizable, and Hydrolyzable Zwitterionic Materials and Their Derivatives for Biological Applications. Adv Mater. 2010;22(9):920-32.

52. Wang S, Zhang N, Hu T, Dai WG, Feng X, Zhang X, et al. Viscosity-Lowering Effect of Amino Acids and Salts on Highly Concentrated Solutions of two IgG1 Monoclonal Antibodies. Mol Pharmaceutics. 2015.

53. Saha D, Joshi YM, Bandyopadhyay R. Characteristics of the secondary relaxation process in soft colloidal suspensions. Epl. 2015;112(4).

54. Richter S, Boyko V, Schröter K. Gelation Studies on a Radical Chain Cross-Linking Copolymerization Process: Comparison of the Critical Exponents Obtained by Dynamic Light Scattering and Rheology. Macromolecular Rapid Communications. 2004;25(4):542-6.

55. Woldeyes MA, Calero-Rubio C, Furst EM, Roberts CJ. Predicting Protein Interactions of Concentrated Globular Protein Solutions Using Colloidal Models. J Phys Chem B. 2017;121(18):4756-67.

56. Schneider CA, Rasband WS, Eliceiri KW. NIH Image to ImageJ: 25 years of image analysis. Nat Meth. 2012;9(7):671-5.

57. Ross PD, Minton AP. HARD QUASI-SPHERICAL MODEL FOR VISCOSITY OF HEMOGLOBIN SOLUTIONS. Biochem Biophys Res Commun. 1977;76(4):971-6.

58. Burckbuchler V, Mekhloufi G, Giteau AP, Grossiord JL, Huille S, Agnely F. Rheological and syringeability properties of highly concentrated human polyclonal immunoglobulin solutions. Eur J Pharm Biopharm. 2010;76(3):351-6.

59. Miao F, Velayudhan A, DiBella E, Shervin J, Felo M, Teeters M, et al. Theoretical analysis of excipient concentrations during the final ultrafiltration/diafiltration step of therapeutic antibody. Biotechnol Prog. 2009;25(4):964-72.

60. Teeters M, Bezila D, Benner T, Alfonso P, Alred P. Predicting diafiltration solution compositions for final ultrafiltration/diafiltration steps of monoclonal antibodies. Biotechnol Bioeng. 2011;108(6):1338-46.

61. Chaudhuri R, Cheng Y, Middaugh CR, Volkin D. High-Throughput Biophysical Analysis of Protein Therapeutics to Examine Interrelationships Between Aggregate Formation and Conformational Stability. AAPS J. 2014;16(1):48-64.

62. Cromwell MEM, Hilario E, Jacobson F. Protein aggregation and bioprocessing. AAPS J. 2006;8(3):E572-E9.

63. Castellanos MM, Pathak JA, Colby RH. Both protein adsorption and aggregation contribute to shear yielding and viscosity increase in protein solutions. Soft Matter. 2014;10(1):122-31.

64. Pathak Jai A, Sologuren Rumi R, Narwal R. Do Clustering Monoclonal Antibody Solutions Really Have a Concentration Dependence of Viscosity? Biophys J. 2013;104(4):913-23.

65. Yearley Eric J, Godfrin Paul D, Perevozchikova T, Zhang H, Falus P, Porcar L, et al. Observation of Small Cluster Formation in Concentrated Monoclonal Antibody Solutions and Its Implications to Solution Viscosity. Biophys J. 2014;106(8):1763-70.

66. Rosenberg E, Hepbildikler S, Kuhne W, Winter G. Ultrafiltration concentration of monoclonal antibody solutions: Development of an optimized method minimizing aggregation. J Membr Sci. 2009;342(1-2):50-9.

67. Fesinmeyer RM, Hogan S, Saluja A, Brych S, Kras E, Narhi L, et al. Effect of Ions on Agitation- and Temperature-Induced Aggregation Reactions of Antibodies. Pharm Res. 2009;26(4):903-13.

68. Matheus S, Friess W, Schwartz D, Mahler H-C. Liquid high concentration IgG1 antibody formulations by precipitation. J Pharm Sci. 2009;98(9):3043-57.

69. Yearley EJ, Zarraga IE, Shire SJ, Scherer TM, Gokarn Y, Wagner NJ, et al. Small-Angle Neutron Scattering Characterization of Monoclonal Antibody Conformations and Interactions at High Concentrations. Biophys J. 2013;105(3):720-31.

70. Samuel D, Kumar TK, Ganesh G, Jayaraman G, Yang PW, Chang MM, et al. Proline inhibits aggregation during protein refolding. Protein Sci. 2000;9(2):344-52.

Chapter 5: High Concentration Tangential Flow Ultrafiltration of Stable Monoclonal Antibody Solutions with Low Viscosities[4]

Jessica J. Hung, Ameya U. Borwankar, Barton J. Dear, Thomas M. Truskett and Keith P. Johnston

5.1 ABSTRACT

During production of concentrated monoclonal antibody formulations by tangential flow ultrafiltration (TFF), high viscosities and aggregation often cause extensive membrane fouling, flux decay and low product yields. To address these challenges, the co-solutes histidine or imidazole were added at high concentrations from 250 to 320 mM to reduce the viscosity by up to ten-fold relative to conventional low co-solute formulations, to as low as 40 cP at 250 mg/mL. At high mAb concentrations of up to 280 mg/mL, the transmembrane flux was increased threefold by adding high concentrations of co-solutes that also lowered the viscosity. Furthermore, the co-solutes also increased the mAb gel point concentration c_g by up to 100 mg/mL mAb and thus enhanced concentration polarization-driven back-diffusion of the mAb at the membrane wall, which led to increased fluxes. The low viscosity and hollow fiber filter modules with straight flow paths enabled more uniform TMP and wall shear stress τ_w profiles, which mitigated the reversible flux decay that results from an axial decline in the local TMP. The concentrated mAb was stable by SEC before and after extended storage at 4°C and 37°C.

5.2 INTRODUCTION

For subcutaneous (subQ) delivery of monoclonal antibodies (mAb) and other protein therapeutics, the desired dosage often requires protein concentrations of 150 mg/mL or higher

[4] This chapter was previously published as Hung, JJ, Borwankar AU, Dear BJ, Truskett TM, Johnston KP. "High concentration tangential flow ultrafiltration of stable monoclonal antibody solutions with low viscosities" *J. Membr. Sci.*, 2016; 508:113-126. The first-author was responsible for the design and execution of the experiments, data analysis and interpretation, intellectual development and writing of the manuscript.

given the small injection volume of 1.5 mL (1). At these concentrations, attractive short-ranged interactions between proteins may produce aggregation (2) and/or high viscosities (3, 4) above the desired limit of 20 – 50 cP for subQ injection (5). Even though tangential flow filtration (TFF) is used commonly for manufacturing concentrated proteins, relatively few publications have reported results for concentrations above 150 mg/mL. Here, low fluxes in TFF and concentration polarization resulting from high viscosities (3, 4, 6) may result in protein gelation, membrane fouling and protein aggregation (7). Thus, novel concepts would be highly beneficial for weakening protein interactions to reduce viscosity and aggregation, both to improve TFF ultrafiltration and to advance subcutaneous injection at high concentrations.

Several studies of TFF have optimized the transmembrane pressure (TMP), cross-flow rates and shear stress to reach concentrations of 150 to 200 mg/mL (6, 8-12). These studies have attempted to minimize protein aggregation during filtration (6, 8, 13) and to avoid large viscosity increases and the associated flux decay (6, 8, 14-17) and large axial pressure drops ΔP (3, 12), both of which limit the maximum achievable mAb concentration. The large pressure drops may exceed pump capacity (3, 4) and increase axial variation in TMP, with undesirably high TMP values at the influent port (12, 15, 16) and back-filtration near the effluent port where the TMP is negative (12). The TMP is typically optimized based on the transition point between the pressure-dependent and pressure-independent regions of the flux-TMP profile, which is also known as the 'knee-point TMP.' To maximize the membrane flux while minimizing the risk of protein gelation, the TMP should be maintained near this optimal value (6). As protein concentration increases, it was found that the optimal TMP decreases (6). The low optimal TMP is problematic since high TMPs would be desirable to overcome losses in protein fluxes at high concentrations resulting from concentration polarization and fouling. In an alternative approach, single-pass TFF has been used to reach a final mAb concentration of 225 mg/mL by eliminating the recirculation loop to minimize mAb exposure to high shear stresses in the pump head (13).

In TFF, fouling and concentration polarization may be mitigated by applying an appropriate wall shear stress τ_w or shear rate γ_w to sweep protein molecules near the wall back into the bulk flow (14, 18). If the shear stress is too large, it may cause protein denaturation and aggregation (19), especially in the presence of air-solution and solution-solid interfaces (20, 21). For proteins, flat sheet cassettes (filter modules) are typically used for TFF due to facile scalability and high fluxes (6, 8-10, 13, 22, 23). However, given the serpentine flow path, a high local τw is required in the stagnation zones in the 90-degree bends to mitigate protein fouling and concentration polarization, but this may cause protein denaturation and aggregation. For example, an average τ_w of 200 – 300 Pa is recommended for ultrafiltration of concentrated mAb solutions at typical feed flow rates of 300 – 400 LMH (liters per square meter per hour) with the flat sheet geometry (6, 8). In contrast, more uniform flow in the hollow fiber geometry may avoid the possibility of high local values of τw to minimize shear-induced protein aggregation, particularly at high concentrations. Recent advancement in the design of asymmetric hollow fiber membranes make them more attractive for protein separations given improved fluxes (14, 24).

The design of mAb formulations with lower viscosities at high concentrations would be highly beneficial for advancing ultrafiltration in TFF. In TFF, lower viscosities would enable higher fluxes, lower axial ΔP, and better control of the TMP for lower values of τ_w. The solution viscosity exhibits an exponential dependence on the mAb concentration, as described by the Ross-Minton equation (4, 25) (Eqn. 5.1),

$$\eta = \eta_0 * \exp((c[\eta])/(1-k/v*c[\eta])) \quad (5.1)$$

where η is the solution viscosity, η_0 is the solvent viscosity, c is the mAb concentration, [η] is the intrinsic viscosity, k is the crowding factor and ν is the Simha shape factor. To first order, the intrinsic viscosity [η] is an effective specific volume of the mAb molecule at infinite dilution (4, 26), whereby the viscosity increases with [η]. Furthermore, the effect of pair-wise interparticle

interactions on η may be captured by [η], as described in a virial expansion of viscosity as a function of mAb concentration (4). The level of the exponential increase in viscosity may be ameliorated by weakening attractive intermolecular interactions at higher concentrations to lower [η]. Even when protein-protein interactions are repulsive at dilute conditions, they may become attractive at high concentrations (2, 4) due to anisotropic short-ranged electrostatic and hydrophobic interactions (27) at small protein separation distances <5 nm (28). The anisotropic nature of these interactions arises from the heterogeneous distribution of charged and hydrophobic residues on the protein surface (29-31).

Recently, strategies to lower the solution viscosity and improve mAb stability by the addition of high concentrations (150 – 1000 mM) of co-solutes are gaining attention. In some cases, electrostatic interactions can be modulated by the addition of salts to screen the protein charge and minimize attractive local anisotropic interactions (4, 11, 32-35). Furthermore, hydrophobic salts have been hypothesized to adsorb on hydrophobic sites and further screen hydrophobic interactions, resulting in large viscosity reductions (36, 37). The amino acids arginine (5, 28, 38-43) and histidine (44) in the protonated form have been shown to produce significant viscosity reductions at high co-solute concentrations without adversely impacting the mAb stability. The two are hypothesized to screen both electrostatic and hydrophobic interactions via a similar binding mechanism (39, 45, 46). Alternatively, we introduced a concept of adding a high concentration of a nonionic crowding agent, for example the disaccharide trehalose (47, 48) to provide a depletion attraction force (49, 50) to osmotically compress proteins to attempt to raise the stability. According to a free energy model, the compression generates nanoclusters of primary colloidal charged spheres, whereby the protein may adopt a more stable conformation through a self-crowding mechanism (51, 52). Despite the benefits of co-solutes on protein viscosity and stability, to our knowledge, protein solutions with elevated concentrations of co-solutes have not been formed by TFF.

Herein we utilize high concentrations of histidine or imidazole with trehalose as co-solutes to form stable solutions of a human IgG1 mAb by TFF with viscosities as low as 70 and 40 cP at 280 and 255 mg/mL, respectively. Histidine at low concentrations is a common pharmaceutical buffer that may preferentially bind to and shield interaction-prone mAb residues to mitigate protein network formation (reversible aggregates) and possibly reduce the viscosity significantly. In control experiments with low co-solute concentrations, the solutions gelled and were ~10 times more viscous than the formulations with high concentrations of co-solute, resulting in poor transmembrane fluxes. The low viscosities of the solutions and the choice of the hollow fiber geometry are shown to provide for low axial ΔP, resulting in a relatively uniform and small wall shear stress and more uniform TMP. The high concentrations of co-solute also enhance concentration polarization-driven back-diffusion of the mAb near the membrane wall at high mAb concentration by increasing the mAb gel point concentration c_g. Because these factors mitigate flux decay from stagnation at the membrane wall and from axial decline in the local TMP, it became possible to achieve relatively low losses in membrane flux (low permeation resistance). A secondary objective was to show that the TFF process is well suited for forming concentrated protein solutions with high co-solute levels and low viscosities to complement previous techniques (11, 36, 37, 41-43, 47, 48). The mAb solutions were diluted and studied by SEC before and after extended storage at 4°C to show that the formation of irreversible aggregates was minimal.

5.3 MATERIALS AND METHODS

5.3.1 Materials

The IgG1 mAb used in this study was provided by AbbVie as a concentrated solution at 130 mg/mL in a proprietary buffer containing 10 mM histidine, 4% mannitol and 0.1% Tween-80 at pH 5.8 (referred to as the “freezing buffer”). The mAb solution was aliquoted into 5 ml

sub-samples into 5-mL cryogenic vials (Corning Incorporated, Corning, NY) and frozen using a dry ice-ethanol freezing mixture for extended storage at -80°C. α-trehalose dihydrate (Tre) was purchased from Ferro Pfanstiehl Laboratories Inc., Waukegan, IL. All other chemicals (L-histidine (His), imidazole (Im), citric acid monohydrate (CitrA), hydrochloric acid (HCl), o-phosphoric acid (PhosA)) were purchased from Thermo Fisher Scientific, Fair Lawn, NJ. Disposable 0.22 μm polyethersulfone (PES) bottle top and 13 mm syringe sterile filters were obtained from Celltreat Scientific Products, Shirley, MA (product codes 229717 and 229746). Disposable 50 kDa PES MidiKros hollow fiber filter modules with a length of 20 cm and an ID of 0.5 mm (36 fibers and 115 cm2 area, part no. D02-E050-05-N) or 1.0 mm (12 fibers and 75 cm2 area, part no. D02-E050-10-N from Spectrum Labs, Rancho Dominguez, CA) were utilized for TFF. Amicon Ultra-15 Ultracel – 30K centrifugal filters were purchased from Merck Millipore Ltd. Ireland.

5.3.2 Diafiltration and ultrafiltration to 250 mg/mL by TFF

Buffers were prepared at the desired co-solute composition and sterile filtered with the Celltreat bottle top PES filters and then degassed under vacuum for 30 minutes. The frozen mAb stock (25 mL in 5 vials) was thawed in a 4°C water bath and diluted with an equal volume (25 mL) of the buffer, resulting in a mAb concentration of 65 mg/mL. The diluted mAb solution was gently mixed in a 50-mL centrifuge tube, which served as the retentate reservoir during the TFF experiments. In two of the experiments, the buffer exchange was done at a lower concentration of 20 mg/mL to attempt to form less turbid solutions. In one of these experiments, the diluted mAb solution was additionally sterile-filtered using the 0.22 μm bottle top filters and degassed prior to buffer exchange.

The diluted mAb solution was buffer-exchanged at constant concentration with permeation of six diavolumes (150 mL) of the desired formulation buffer with a KrosFlo Research II TFF system (Spectrum Labs, Rancho Dominguez, CA) operated in a constant-

volume mode. A schematic of the TFF setup is given in Fig. 5.6. The TMP was maintained at 0.80 bar using a KrosFlo automatic backpressure valve (Spectrum Labs, Rancho Dominguez, CA), which regulated the pressure by constricting the retentate line. The feed cross-flow rate was set at 100 mL/min for the 1.0 mm ID filter module and 220 mL/min for the 0.5 mm ID filter module, corresponding to calculated wall shear rates inside each fiber of 1415 and 8300 s^{-1} respectively. The retentate reservoir was gently mixed throughout the process using a Vari Mix Platform Rocker (Thermo Fisher Scientific, Fair Lawn, NJ) set at the maximum speed and rocking angle along with periodic hand swirling. The buffer-exchanged solution was recovered and sterile filtered, then stored overnight at 4°C, after which it was concentrated to ~250 mg/mL the following day using the 1.0 mm ID filter module.

When the 1.0 mm ID filter module was used during diafiltration, the filter membrane was cleaned between diafiltration and ultrafiltration to recover membrane performance. When the 0.5 mm module was used for the diafiltration step, the corresponding ultrafiltration was performed with a new 1.0 mm ID module. The new filters were first flushed with 200 mL of DI water without recirculating or permeating any material in order to flush out residual glycerin impurities. Both the new and used membranes were then cleaned prior to filtration by permeating 4 mL DI water/cm^2 membrane area, circulating 0.5N NaOH for 30 minutes to decompose adsorbed protein, followed by permeating another 4 mL DI water/cm^2 membrane area to flush the residual NaOH and degraded protein out of the membrane pores. A normalized water permeability (NWP) test was then conducted to check the performance of the regenerated membrane prior to ultrafiltration. The NWP was also determined for the fouled membrane after both diafiltration and ultrafiltration.

The buffer-exchanged mAb solution was concentrated from 65 mg/mL to 250 mg/mL by ultrafiltration using the 1.0 mm ID hollow fiber module. The feed cross-flow rate was initially kept at 100 mL/min (corresponding to a cross-flow flux of 800 LMH) and the TMP was

maintained at 0.80 bar. When the mAb solution became too viscous (> 150 cP, the TMP could no longer be regulated. At this point, the TMP was maintained at 0.80 bar by partially restricting the permeate line (to increase the permeate back-pressure) and decreasing the feed cross-flow rate (to decrease ΔP across the filter module). The retentate was kept well-mixed using the rocker set at the maximum speed. The rocker angle for the Vari Mix Platform Rocker was gradually reduced over time as the fluid level in the retentate reservoir decreased in order to keep the feed and retentate return lines submerged. The retentate concentration at any given time was estimated based on the permeate mass, which was monitored in real time, assuming no permeation of mAb through the membrane, and was subsequently verified by UV-Vis spectroscopy via 150 μL aliquots. The instantaneous flux was also determined by the change in permeate mass in one-minute intervals. The final 250 mg/mL solution was recovered and mixed by gentle pipetting to homogenize the solution prior to characterization by DLS, UV-Vis spectroscopy and syringe capillary viscometry.

Low co-solute controls were also prepared by centrifugation filtration, as described in the Supporting Information, to place the results from TFF in perspective.

5.3.3 TFF membrane fouling characterization

The extent of membrane fouling at the end of ultrafiltration was assessed by measuring the percent reduction in the normalized water permeability (NWP). The DI water flux of the cleaned membrane was measured at room temperature (20°C) and a TMP of 0.25 bar, 0.50 bar and 0.8 bar before the start of ultrafiltration. The pre-ultrafiltration NWP in LMH (liters per square meter membrane area) per bar of applied TMP was calculated from the slope of the water flux vs TMP curve. The NWP of the fouled membrane after ultrafiltration was measured in the same way after the membrane was first washed by recirculating 200 mL DI at a cross-flow flux of 800 LMH for 10 minutes to recover reversibly adsorbed protein.

5.3.4 mAb concentration determination and turbidity by UV-Vis spectroscopy

The mAb concentration in the intermediate and final solutions was measured in duplicate at 500x dilution using a Cary 60 UV-Vis spectrophotometer (Agilent Technologies, Santa Clara, CA). The concentrated mAb solution was diluted in 50 mM pH 6.4 sodium phosphate buffer, and the absorbance at 280 nm was measured in a QS quartz cuvette (Hellma GmbH and Co, Mullheim, Germany) with a path length of 1 cm. The absorbance was converted to a mass concentration via the Beer-Lambert law using the provided mAb extinction coefficient of 1.42 mL/mg/cm. The turbidity of the buffer-exchanged 20 mg/mL mAb stock as well as of the concentrated mAb solution was measured undiluted using a Cary 60 UV-Vis spectrophotometer (Agilent Technologies, Santa Clara, CA) as described in the Supporting Information.

5.3.5 Syringe capillary viscometry

The viscosity of the mAb solution was measured at room temperature in triplicate using a custom syringe capillary viscometer as described previously (47). Briefly, a 25G (ID = 0.1 mm; L = 1.5") Precision Glide needle (Becton Dickinson & Co.) was attached to a 1.0 mL Luer-LokTM syringe (Becton Dickinson & Co.). A 100 – 125 μL aliquot of the solution was placed in a 0.1 mL conical vial (catalog no. 03-341-15; Wheaton, Millville, NJ). The solution was warmed to 25°C with a heating block (Thermo Scientific, Waltham, MA) and drawn into the syringe, and the flow rate of the solution through the needle was determined by ImageJ image analysis (53) of a video taken with a Kodak Z812 IS zoom digital camera. The change in the solution column height was tracked over time and correlated to the sample volume based on an established calibration curve, as described in the Supporting Information. The flow rate was correlated to a viscosity based on the Hagen-Poiseuille equation, using a calibration curve determined from a set of viscosity standard solutions. The viscosities measured at high concentration by the capillary viscometer correspond to an estimated shear rate of 25 - 500 s^{-1}, as demonstrated in the

Supporting Information, assuming a Newtonian shear response to fluid flow (n = 1 power-law dependence between viscosity and shear rate) (54).

5.3.6 Size exclusion chromatography

For characterization of soluble irreversible aggregate levels in the final solutions, the mAb solution was diluted to 2 mg/mL in the mobile phase (92 mM $NaHPO_4$, 211 mM Na_2SO_4, pH 7). The standard solution was prepared by diluting freshly-thawed mAb monomer stock (as provided in the original freezing buffer at 130 mg/mL) in the mobile phase. The diluted samples were sterile filtered through a 0.22 μm PES syringe filter (Celltreat Scientific Products, Shirley, MA). Duplicate 10 μL injections of each sample were analyzed with a Waters Breeze HPLC (Waters Corporation, Milford, MA) equipped with a Tosoh Biosciences TSKgel3000SWXL column (Tosoh Corporation, Tokyo, Japan) and operated at a mobile phase flow rate of 0.5 mL/min. The eluate was monitored by the UV absorbance at 214 nm and 280 nm. The soluble (small, irreversible) aggregate content was quantified by the percentage monomer as determined from the ratio of monomer and aggregate peak areas for the diluted samples. The insoluble (large, irreversible) aggregate content was quantified by the monomer recovery, which was determined from the ratio of the monomer peak areas for the dilute and concentrated solutions for the post-ultrafiltration samples, and for the pre and post-storage solutions for the storage stability tests.

5.3.7 Sample storage stability study

Small 150 μL aliquots of the final mAb solution were stored in capped 0.1 mL conical vials (Wheaton, Millville, NJ) sealed with Parafilm. The sealed vials were stored in a -40°C freezer, in a refrigerator at 4°C and in a water bath at 37°C for up to 8 weeks. To minimize evaporative losses, the samples stored at 37°C were additionally sealed with three additional alternating layers of aluminum foil and Parafilm. Individual aliquots were removed from storage

at 4 days, 1 week, 2 weeks, 4 weeks and 8 weeks and characterized by UV-Vis spectroscopy, syringe capillary viscometry and DLS measurements at a scattering angle of 90°. The samples were discarded after characterization, so that a fresh aliquot was used for each time point.

5.4 RESULTS AND DISCUSSION

5.4.1 Addition of high concentrations of co-solute reduces solution viscosity at 250 mg/mL mAb

We begin by describing control experiments with low co-solute concentrations. As seen in Table 5.1, these solutions formed by centrifugation filtration (CF) buffered with 10 mM His (freezing buffer) or 30 mM His were extremely viscous, exceeding 200 cP at 240 mg/mL and 400 cP at 270 mg/mL. These low co-solute controls had a large inherent viscosity

$$\eta_{inh} = \frac{\ln\left(\frac{\eta}{\eta_0}\right)}{c} \tag{5.2}$$

of ~22 mL/g. To some extent, η_{inh} normalizes the solution viscosity η for the mAb concentration c and solvent viscosity η_0 (55). The inherent viscosity qualitatively reflects the strength of attractive interactions that raise the viscosity in a similar manner as for $[\eta]$. The addition of 150 mM NaCl lowered η_{inh} to 18.0 mL/g, likely indicating a weakening of attractive interactions by electrostatic screening, as observed for certain mAbs previously (4, 11, 32). The same low co-solute solution in the freezing buffer was significantly more viscous when manufactured by TFF (Table 5.2), as will be explained below, increasing to 550 cP with a η_{inh} of 26 mL/g at 240 mg/mL mAb. Similarly high viscosities were obtained for a co-solute-free control mAb solution in DI water (Table 5.2, Fig. 5.1).

mAb conc (mg/mL)	Exc 1	Exc 1 conc (mM)	Exc 2	Exc 2 conc (mM)	Exc 3	Exc 3 conc (mM)	pH	η (cP)	η_0 (cP)	η_{inh} (mL/g)	Turbidity ($AU*cm^{-1}$)	DF time (min)	UF time (min)
281 ± 8.7	Freezing buffer (replicate 1)						6.1	424	0.98	21.6	0.376	0	75
271 ± 0.5	Freezing buffer (replicate 2)						6.1	460	0.98	22.7	0.388	0	75
238 ± 3.3	His	30	HCl	19	---	---	6.2	188	0.98	22.1	0.388	70	54
230 ± 2.8	His	30	HCl	19	NaCl	150	6.0	61	0.98	18.0	0.581	85	69

Table 5.1. Viscosity (η) and filtration times for low co-solute control solutions made by centrifugation filtration (CF). The diafiltration (DF) time corresponds to buffer exchange into 6 diavolumes and subsequent concentration to ~80 mg/mL mAb. The ultrafiltration (UF) time corresponds to concentration from ~80 mg/mL to 250 mg/mL. No diafiltration step was required for the controls in the freezing buffer. The inherent viscosity ηinh was calculated from η and the measured solvent viscosity η_0.

mAb conc ± stdev (mg/mL)	Tre conc (mg/mL)	Base	Base conc (mg/mL)	Acid	Acid conc (mg/mL)	pH	η (cP)	η_0 (cP)	η_{inh} (mL/g)	$[\eta]$ (mL/g)	k/v	DF time (min)	UF time (min)
242±2.5	Freezing buffer					6.4	559	0.98	26.2	16.3	0.095	0[a]	99
245±3.6	DI water					6.7	729	0.93	27.2	20.6	0.047	150	96
282±3.7[b,c]	40	His	50	CitrA	17	6	66	1.11	14.5	12.1	0.041	68[d]	373[e]
241±0.3[b]	40	His	50	CitrA	17	6	50	1.11	15.8	6.2	0.403	253	136
251±18.5	50	His	50	PhosA	12	6	80	1.12	17.0	13.5	0.056	270	100
252±0.5	50	Im	17	CitrA	10	7	86	1.07	17.4	11.1	0.132	284	145
262±4.5	50	Im	17	HCl	7	6.4	133	0.99	18.7	11.9	0.112	243	147

a. No diafiltration step was needed for the freezing buffer solution
b. The mAb solution was buffer exchanged at 20 mg/mL instead of 60 mg/mL
c. The mAb solution was additionally degassed before diafiltration and ultrafiltration (optimized TFF procedure)
d. Buffer exchanged using a 115 cm^2 area membrane (all other rows buffer exchanged with 75 cm^2 membrane), leading to faster permeation rate
e. Larger sample volume (250 mL at start of ultrafiltration) compared to other rows (50 mL at start of ultrafiltration)

Table 5.2. Viscosity (η) and filtration times of low and high co-solute solutions made by tangential flow filtration (TFF). The inherent viscosities (η_{inh}) were evaluated at the final mAb concentration (~250 mg/mL), while the intrinsic viscosity $[\eta]$ and combined crowding-Simha shape factor k/v were fit from the viscosity profile. Alternating shaded rows indicate different formulations. The 280 mg/mL replicate of the 40:50:17 mg/mL Tre:His:CitrA solution corresponds to Replicate 4 and the 241 mg/mL replicate corresponds to Replicate 1 (Fig. 5.2).

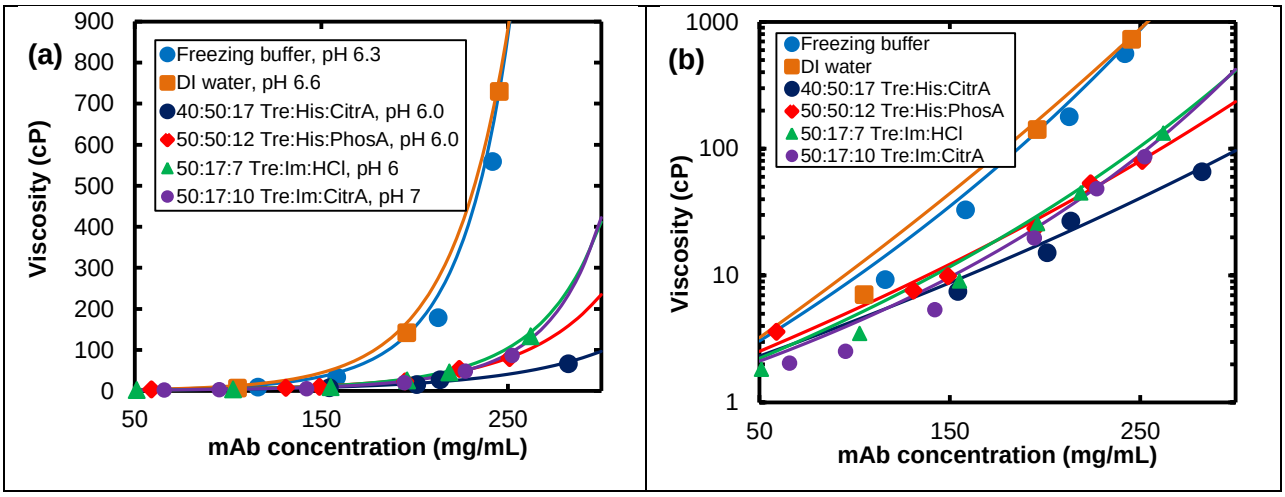

Figure 5.1. mAb solution viscosities during ultrafiltration to 250 mg/mL mAb by TFF plotted on a (a) linear and (b) log scale. The numbers in the formulation names represent concentration of each excipient in mg/mL. The solid lines represent two-parameter fits to the data by the Ross-Minton equation.

We now show that the addition of high concentrations of histidine (50 mg/mL = 320 mM) combined with trehalose (40 to 50 mg/mL = 105 – 130 mM) to the mAb solution resulted in a large reduction of the solution viscosity (η), particularly at the highest mAb concentrations. Remarkably, the high co-solute solutions manufactured by TFF were significantly less viscous than the low co-solute controls made by both TFF and CF. The high co-solute solutions remained below 50 cP with phosphoric acid (PhosA) up to 220 mg/mL and with citric acid (CitrA) all the way to ~260 mg/mL, corresponding to ηinh of 17.0 and 14.5 mL/g respectively (Fig. 5.1a, Table 5.2). On a semi-log plot (Fig. 5.1b), the slope of the viscosity profile gives a qualitative measure of [η] of the mAb in the given buffer, as described by the Ross-Minton model in Eqn. 5.1. The noticeably smaller slope for the high co-solute solutions (Fig. 5.1b) and two-parameter fits of the viscosity profiles to the Ross-Minton model (Fig. 5.7) both indicated a significant reduction in ηinh and [η] by the addition of high concentrations of co-solute (Table 5.2). Although the two formulations with high concentrations of His both resulted in low η at 250 mg/mL, the solution with CitrA as the counteracid was slightly less viscous, as shown in Fig. 5.1. Similarly low

viscosities were also observed when a structurally-analogous base, imidazole (Im), was used instead of His as the crowding agent, as shown in Fig. 5.1 and Table 5.2.

To further investigate whether trehalose or histidine generated the significant viscosity reduction, additional centrifugation filtration experiments were performed at pH 6 with high concentrations of either trehalose (Tre) alone or His-CitrA alone. The addition of 220 mM Tre to the formulation buffered with 30 mM His did not affect the mAb inherent viscosity, which was 22 mL/g (Table 5.1, 5.3). In contrast, the solutions with 320:80 mM His:CitrA had significantly lower inherent viscosities of 14.5 – 15.5 mL/g (Table 5.3), comparable to that of the Tre-His-CitrA solutions made by both CF (Table 5.3) and TFF (Table 5.2). Thus the large viscosity reductions observed by TFF in the high co-solute systems may be attributed to the His (and by extension, Im) rather than Tre. Histidine's effect on mAb viscosity has also been seen in a study by Chen et al. (44), where up to 60 mM His decreased the viscosity of an IgG2 mAb by up to 2x at 150 mg/mL mAb. However, although His and Im reduced the viscosity for the mAb's in Chen's study and ours, it does not mean that this effect may be generalized to other mAbs. Note that the large deviation in viscosity seen for the freezing buffer solutions prepared by TFF versus CF is not observed for the Tre-His-CitrA solution (Table 5.2, 5.3). It is likely that the low level of reproducibility for the freezing buffer solutions is caused by the ultrahigh viscosities at high mAb concentration, which results in significant pathway-dependent aggregation and gelation. In contrast, the much less viscous Tre-His-CitrA solutions that do not gel show better reproducibility between filtration techniques.

mAb conc ± stdev (mg/mL)	Exc 1	Exc 1 conc (mM)	Exc 2	Exc 2 conc (mM)	Exc 3	Exc 3 conc (mM)	pH	η (cP)	η_0 (cP)	η_{inh} (mL/g)	Turbidity (AU*cm^{-1})	DF time (min)	UF time (min)
261 ± 5.6	His	30	HCl	17	Tre	220	6.1	329	1.05	22.0	0.421	90	75
267 ± 2.0	His	322	CitrA	79	---	---	5.9	69	1.10	15.5	0.427	73	50
270 ± 0.5	His	322	CitrA	79	---	---	6.0	54	1.10	14.5	0.409	30	42
265 ± 6.1	His	322	CitrA	79	Tre	106	5.8	85	1.11	16.4	0.341	73	75
242 ± 0.2	His	322	CitrA	79	Tre	106	6.0	48	1.11	15.6	0.405	30	42

Table 5.3. Viscosity (η) and filtration times for high co-solute solutions made by centrifugation filtration (CF). The diafiltration (DF) time corresponds to buffer exchange into 6 diavolumes and subsequent concentration to ~80 mg/mL mAb. The ultrafiltration (UF) time corresponds to concentration from ~80 mg/mL to 250 mg/mL. The inherent viscosity η_{inh} was calculated from η and the measured solvent viscosity η_0.

The marked reduction in [η] and η_{inh} by addition of high concentrations of histidine and imidazole will now be shown to be consistent with a weakening of local attractive protein interactions. In the low co-solute (freezing buffer) and DI water formulations, the mAb exhibited an [η] of 16 and 20 mL/g, respectively, with a sharp increase in viscosity with mAb concentration. The viscosity was similar to that of an 'ill-behaved' viscous mAb with strong local protein-protein interactions from a study by Liu et al., where a sharp deviation from the Ross-Minton model (4) was observed with an assumed [η] of 6.3 mL/g. In contrast, the fits of the viscosity profiles of two 'well-behaved' non-viscous mAbs in the same study were excellent with this value of [η]. However, if both [η] and k/ν were fit by non-linear regression, [η] was found to be approximately 9 mL/g for the well-behaved antibodies, while the ill-behaved antibody exhibited a large [η] of 30 mL/g (4), similar to our results in the low co-solute and DI formulations. The addition of high concentrations of His and Im reduced [η] to 11 – 13 mL/g (Table 5.2), more closely approaching the [η] values of 8.4 – 8.6 mL/g seen in earlier studies for a non-viscous human IgG antibody (56) and a polyclonal antibody (26). Polyclonal antibodies are known to exhibit weaker interactions and lower viscosities in some cases than monoclonal

antibodies (11). On the basis of these studies, the reduction of [η] from 20 mL/g to as low as 11 mL/g in this study suggests that the addition of the co-solutes His/Im with Tre significantly weakened the attractive protein interactions. The viscosity behavior can be further characterized by the parameter k/ν (Table 5.2), which varied markedly between the low and high co-solute solutions, as discussed in the Supporting Information.

A gradual increase in η_{inh} with concentration was also observed for all of the mAb solutions, as seen in Fig. 5.8. However, the η_{inh} of the high co-solute solutions were consistently nearly two-fold lower than that of the low co-solute solutions at all mAb concentrations (Table 5.2, Fig. 5.8), likely indicating a significant reduction in attractive protein interactions by co-solute and mAb interactions, leading to the lower viscosities.

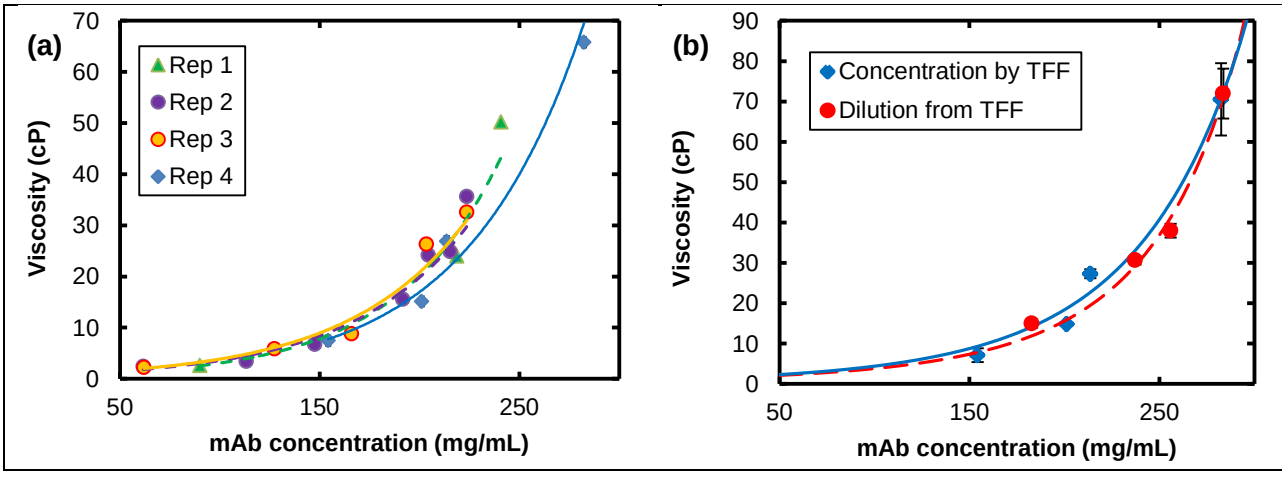

Figure 5.2. Relative reproducibility and reversibility of the 40:50:17 mg/mL Tre-His-CitrA mAb solution viscosity at pH 6. (a) Viscosity of the Tre-His-CitrA system as a function of four diafiltration conditions as described in Table 5.4. (b) Reversibility of Replicate 4 mAb solution viscosity between 150 and 280 mg/mL during concentration by TFF (—) and dilution in buffer (---). The colored lines are guides to the eye.

Low viscosities were obtained by ultrafiltration with four different TFF diafiltration conditions for the high co-solute Tre:His:CitrA formulation as shown in Table 5.4 and Fig. 5.2a. In replicates 2 and 3, buffer exchange was done at 65 mg/mL mAb with a wall shear rate of 1405

or 8200 s^{-1}, as indicated in Table 5.4. Replicate 3 was not relevant as it was highly turbid due to spallation from new tubing. Replicates 1 and 4 were buffer exchanged at the same shear rates as for 2 and 3, but with a lower concentration of 20 mg/mL and thus lower viscosity and shear stress. The concentration-normalized post-diafiltration turbidity of replicates 1, 2 and 4 increased linearly with the tubing wall shear stress*time, independent of the mAb concentration and applied wall shear stress (Fig. 5.9). The low turbidity of replicate 4 (due to the small tubing shear stress*time) indicates less irreversible aggregation during diafiltration; furthermore, it was the least viscous of the four replicates (Fig. 5.2a). There was also little hysteresis in the viscosity of replicate 4 upon dilution (Fig. 5.2b, Table 5.10), suggesting little gelation and irreversible aggregation during ultrafiltration, consistent with the lower turbidity (8). Since soluble low-MW aggregates may not be fully removed by sterile filtration of the buffer-exchanged stock before ultrafiltration, these oligomers could lead to enhanced protein network formation during ultrafiltration. Thus, the reduction in irreversible aggregation during diafiltration, as indicated by the lower turbidity, may contribute to less pathway-dependent gelation during ultrafiltration.

Sample	mAb conc during buffer exchange (mg/mL)	TMP (bar)	Filter wall shear rate (s^{-1})	Hollow fiber ID (mm)	Membrane mAb loading (g/m^2)	Tubing ID (mm)	Tubing wall shear rate (s^{-1})	Turbidity pre-sterile filtration ($AU*cm^{-1}$)
Replicate 1	22	0.8	1405	1.0	390	1.6	4145	0.380
Replicate 4	20	0.8	8200	0.5	407	3.1	1254	0.131
Replicate 2	65	0.8	1405	1.0	390	1.6	4145	0.953
Replicate 3	66	0.8	8250	0.5	254	3.1	1254	1.771

Table 5.4. Different TFF buffer exchange conditions for Replicates 1 – 4 of the 40:50:17 mg/mL Tre:His:CitrA solution (Fig. 5.2) and resulting turbidity. The thawed mAb stock was additionally sterile-filtered and degassed before diafiltration in Replicate 4. The 0.5 mm fiber ID modules have a higher water flux than the 1.0 mm fiber ID modules, as seen in Fig. 5.15, which may contribute to the higher permeate flux observed in the high-shear experiments (Replicates 3 and 4). The turbidity of the buffer-exchanged solution was measured as the absorbance at 350 nm for a 1 cm path length and corrected for the absorbance of the protein-free buffer.

5.4.2 TFF membrane flux decay at high concentration

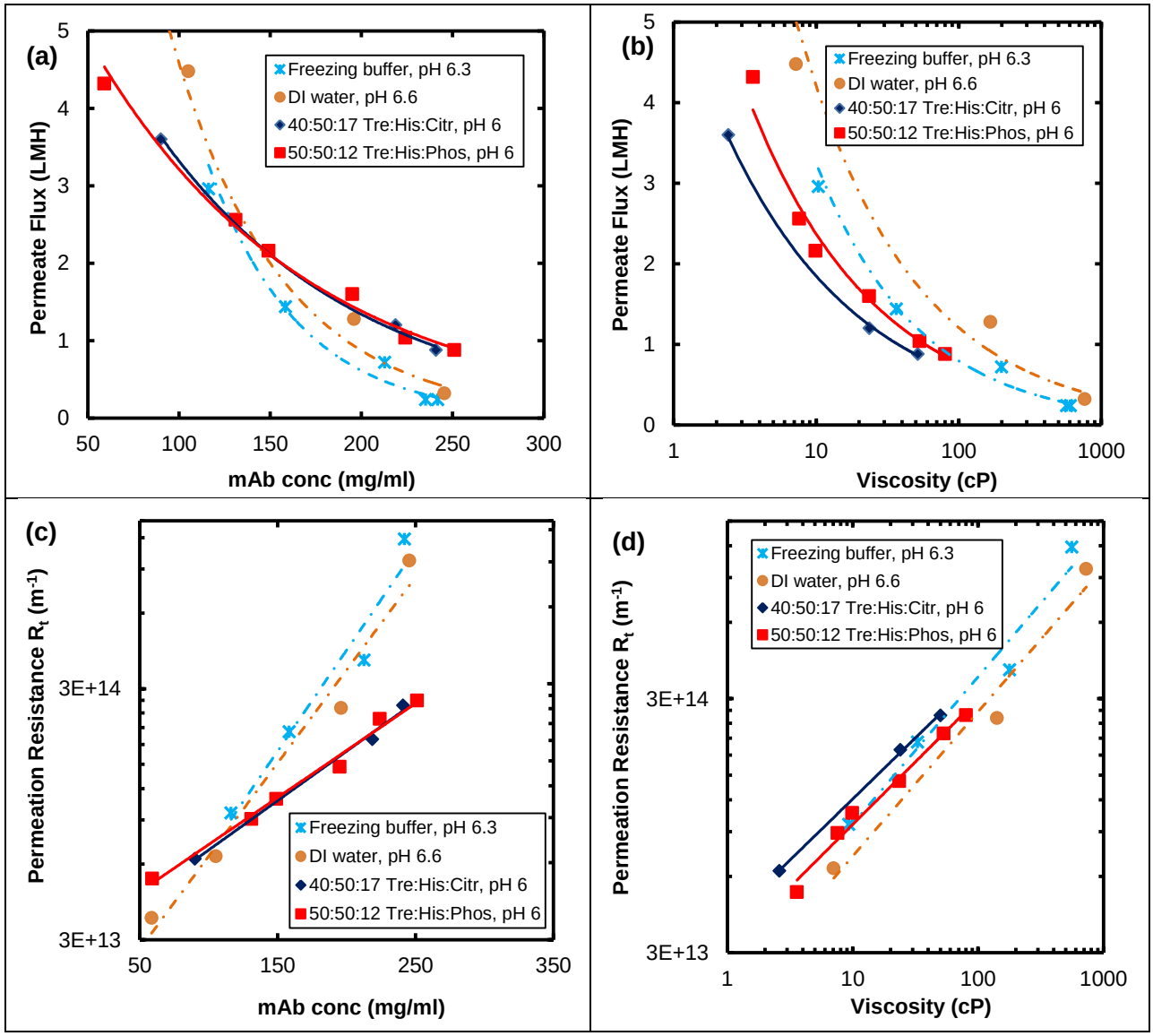

Figure 5.3. TFF membrane flux (in L/m^{2}h) as a function of (a) mAb concentration and (b) solution viscosity; and permeation flux resistance R_t (in m^{-1}) as a function of (c) mAb concentration and (d) solution viscosity during ultrafiltration to 250 mg/mL mAb for low co-solute (- - -) and high co-solute (—) solutions. The numbers in the formulation names represent concentration of each excipient in mg/mL. The flux and resistance curves for the 40:50:17 mg/mL Tre:His:Citr solution corresponds to Replicate 1. The colored lines are a guide to the eye, and correspond to the data series of the same color.

The high co-solute solutions will now be shown to exhibit significantly slower decay in membrane flux with increasing mAb concentration than the low co-solute solutions. The instantaneous flux was measured at the operating TMP of 0.80 bar. The permeate flux J of the low co-solute and His high co-solute solutions is plotted against the mAb concentration in Fig. 5.3a, and for the analogous Im high co-solute solutions in Fig. 5.10a. The low co-solute solutions started with a higher membrane flux than the high co-solute solutions, likely due to a lower η_0. However, a crossover in the flux between the low and high co-solute formulations was seen at 130 mg/mL due to the slower flux decay of the high co-solute systems. At the final mAb concentration of 250 mg/mL, the membrane flux for the high co-solute solutions was three times higher than that of the low co-solute systems. The flux decay from 60 to 250 mg/mL mAb was only 5-fold for the high co-solute solutions compared to the much larger 32-fold reduction for the low co-solute case. The membrane flux, J, was also normalized for differences in η_0 and plotted as the overall permeation resistance R_t according to Eqn. 5.3.

$$R_t = \frac{TMP}{J*\eta_0} \tag{5.3}$$

The resistance was found to increase exponentially with the mAb concentration, as seen in Fig. 5.3c and Fig. 5.10c. The smaller slopes of the resistance curves for the high co-solute formulations (plotted on a log scale in Fig. 5.3c; Fig. 5.10c) are consistent with the slower rate of flux decay. The crossover in R_t occurred at a slightly earlier mAb concentration of ~110 mg/mL than the flux crossover, and R_t was found to increase at a significantly slower rate for the high co-solute solutions.

Surprisingly, the low and high co-solute solutions were found to give similar fluxes as a function of the solution viscosity, as shown in Fig. 5.3b (imidazole shown in Fig. 5.10b). The low co-solute solutions again start at a higher flux at low viscosity, but no flux crossover is observed. Instead, the low and high co-solute flux profiles approximately converge at high

viscosities. When the flux was normalized for η_0 via the permeation resistance, the resistance curves nearly collapsed into a universal curve, as shown in Fig. 5.3d and Fig. 5.10d. This result is interesting since a given viscosity corresponded to greatly different mAb concentrations for the low and high co-solute solutions. The apparent correlation between the solution viscosity and flux may also reflect the effect of viscosity on the axial TMP profile and resultant flux, as will be discussed later.

The difference in flux decay between the low and high co-solute solutions will now be examined in terms of the components of flux decay – membrane fouling (pore blocking and cake formation) and concentration polarization. To investigate membrane fouling, we compared the post-ultrafiltration reduction in the membrane normalized water permeability (NWP) caused by irreversibly-adsorbed mAb. The fouled membrane was first flushed with DI water for ten minutes to wash off reversibly adsorbed mAb and remove the concentration polarization gel layer before the NWP measurement. For the low and high co-solute solutions, the NWP reduction due to fouling by irreversibly adsorbed mAb was comparable at ~60 – 70%, as seen in Table 5.5, with the exception of the Tre:His:CitrA solutions. The Tre:His:CitrA formulation, which was the least viscous formulation, consistently exhibited a smaller NWP reduction of ~ 30%. No clear trend was found between the mass of mAb lost to irreversible adsorption on the membrane (which varied between 100 and 300 mg mAb, based on the mass that was unaccounted for after recovery of the mAb in the solution and filter wash water) and the NWP reduction. The comparable NWP reductions suggest that the TFF filter membrane underwent similar degrees of fouling under both low and high co-solute conditions. Consequently, the large differences in the flux decline of the two types of solutions must be explained in part by concentration polarization.

Formulation	Pre-UF NWP (LMH/ bar)	Post-UF NWP (LMH/ bar)	% NWP reduction post-fouling	mAb recovered from filter wash (mg)	mAb recovered in soln (mg)	mAb in UF feed (mg)	mAb lost to filter adsorpt. (mg)	% mAb lost to irrevers. adsorption on filter
Freezing buffer	298	80	62	758	1565	2624	301	11.5
DI water	213	78	63	775	1480	2232	-23	-1.0
40:50:17 mg/mL Tre:His:CitrA (Replicate 4)	232	166	29	674	3080	4121	367	8.9
40:50:17 mg/mL Tre:His:CitrA (Replicate 1)	221	141	36	522	1445	2131	164	7.7
50:50:12 mg/mL Tre:His:PhosA	289	107	63	600	1745	2327	-18	-0.8
50:17:7 mg/mL Tre:Im:HCl	277	138	50	707	1503	2284	74	3.2
50:17:10 mg/mL Tre:Im:CitrA	267	57	79	573	1769	2606	264	10.1

Table 5.5. Membrane fouling and protein adsorption after ultrafiltration by TFF. The membrane normalized water permeability (NWP) was measured at room temperature (20 °C). The mass of mAb recovered during the filter wash was determined from the mAb concentration in the wash water after recirculation. The small calculated negative mAb mass losses for some formulations may be due to minor experimental error in concentration measurements.

The similar flux decay rates between the low and high co-solute solutions as a function of viscosity, η, (Fig. 5.3b) will now be explained in terms of concentration polarization. The expected transmembrane flux after accounting for concentration polarization is given by (6, 57)

$$J = \frac{D_v}{\delta} \ln\left(\frac{c_w}{c_b}\right) = k_c \ln\left(\frac{c_w}{c_b}\right) = k_c \ln(c_g) - k_c \ln(c_b) \tag{5.4}$$

where k_c is the mass transfer coefficient, c_b is the bulk protein concentration and c_w is the protein concentrations at the membrane wall, which at high protein concentrations is generally assumed to be equal to the gel limit c_g (58). As is apparent from Eqn. 5.4, the constants k_c and c_g may be obtained from a linear fit of the flux as a function of $\ln(c_b)$, where the slope is equal to $-k_c$ and the y-intercept is equal to $k_c \ln(c_g)$.

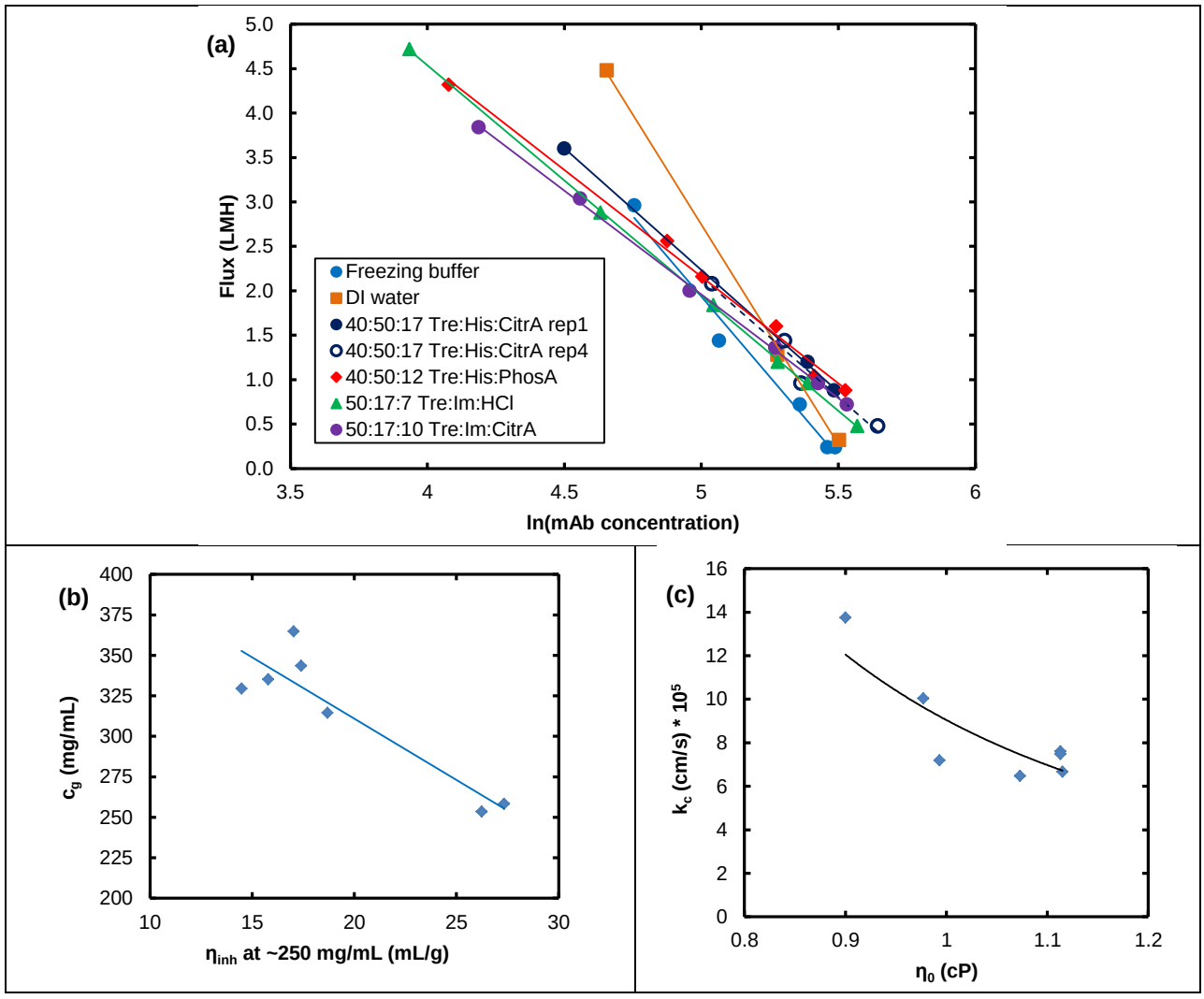

Figure 5.4. (a) TFF membrane flux (in L^2/m^2h) as a function of the natural logarithm of the mAb concentration. **(b)** Fitted gel point concentration c_g and corresponding mAb inherent viscosity at ~250 mg/mL. **(c)** Fitted mass transfer coefficient k_c and corresponding protein-free solvent viscosity. The lines are a guide to the eye.

From the linearized flux profiles (Fig. 5.4a), the c_g's were greater than 315 mg/mL (Table 5.6) for high co-solute concentrations compared to only 250 mg/mL at low concentrations. The c_g increased with a decrease in the inherent viscosity (Fig. 5.4b), as co-solutes weakened attractive PPI, reducing network formation and mAb viscosity. Interestingly, the k_c decreased slightly with increasing co-solute concentration as the solvent viscosity increased (Fig. 5.4c). As such, the larger flux of the high co-solute systems at high mAb concentration can be attributed in

part to the enhanced rate of back-diffusion near the membrane wall, which is directly correlated with the filtrate flux at system equilibrium (59), as a result of the higher c_g and therefore concentration polarization.

Sample	Slope	y-intercept	c_g (mg/ml)	k_c (cm/s)*10^5
Freezing buffer	-3.617	20.0	254	10.0
DI water	-4.952	27.5	258	13.8
Tre-His-Citr, Rep 1	-2.739	15.9	335	7.6
Tre-His-Citr, Rep 4	-2.696	15.6	330	7.5
Tre-His-Phos	-2.401	14.2	365	6.7
Tre-Im-HCl	-2.591	14.9	315	7.2
Tre-Im-CitrA	-2.334	13.6	344	6.5

Table 5.6. Mass transfer coefficient k_c and gel point c_g from linear fit of flux decay profile. The slope and y-intercept were obtained from linear fits of the flux decay profiles in Fig. 5.4a and used to calculate c_g and k_c (Eqn. 5.4)

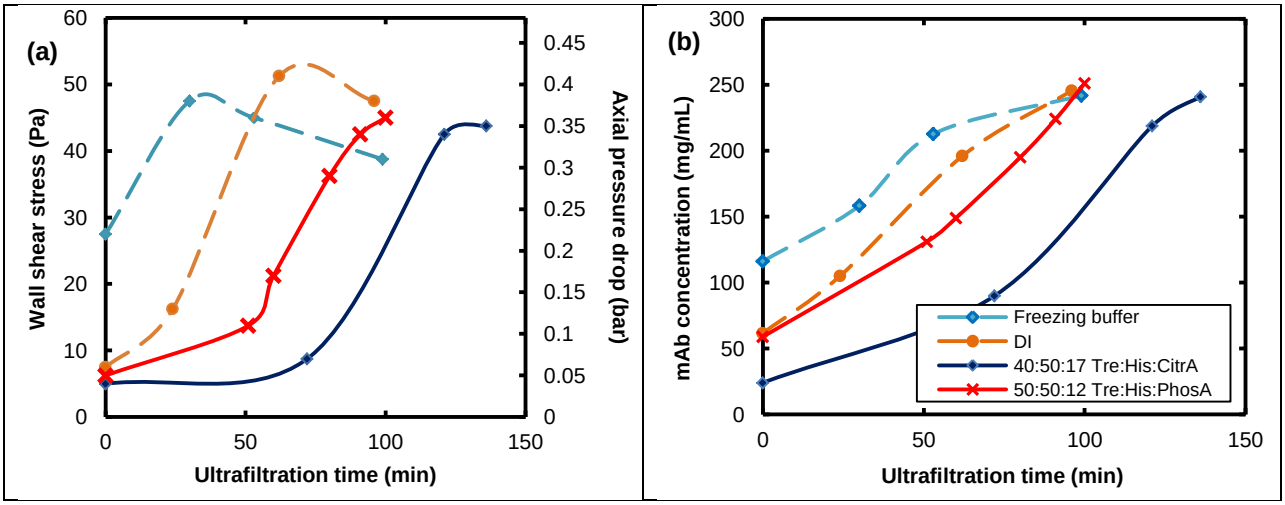

Figure 5.5. Time evolution of (a) pressure drop and wall shear stress and (b) mAb concentration during TFF ultrafiltration for low co-solute (---) and high co-solute solutions (—). The numbers in the formulation names represent conc of each excipient in mg/mL. The concentration and pressure/shear stress curves for the 40:50:17 mg/mL Tre:His:Citr solution corresponds to Replicate 1.

We now demonstrate that the low viscosity, high co-solute solutions additionally resulted in improved control of the wall shear stress, τ_w, during ultrafiltration. The τ_w was calculated from the measured ΔP (Eqn. 5.5)

$$\tau_w = \frac{d_H \Delta P}{4L} \tag{5.5}$$

where d_H is the hydrodynamic diameter of the flow channel and L is the axial length of the filter module. As seen in Fig. 5.5a, ΔP slowly increased from 0.04 bar to 0.05 – 0.12 bar during the first 60 minutes of ultrafiltration due to the increase in viscosity as the mAb was concentrated from 60 to 100 mg/mL (Fig. 5.5b), as follows from the Hagen-Poiseuille equation

$$\frac{\Delta P}{L} = \frac{8\eta Q}{\pi R^4} \tag{5.6}$$

where Q is the volumetric cross-flow rate and R is the diameter of the individual hollow fiber. The ΔP then increased rapidly to 0.35 bar due to the exponential viscosity increase between 100 and 200 mg/mL mAb. Once ΔP reached 0.35 bar, the cross-flow rate was gradually reduced to maintain a constant ΔP to prevent the pressure at the filter inlet from exceeding the module pressure rating. The corresponding τ_w increased slowly from 5 to 15 Pa, as seen in Fig. 5.5a, and then rapidly rose to a maximum value of 40 Pa before leveling off. In contrast, the τ_w for the low co-solute solution (freezing buffer) and DI water quickly increased to a maximum of 50 Pa at 150 – 160 mg/mL before decreasing with further increases in the mAb concentration, as discussed in the Supporting Information. The shear and concentration profiles of the Im systems are similar to those of the His systems, as seen in Fig. 5.11a and 5.11b. With the low viscosity of the high co-solute systems, τ_w stayed below 40 Pa up to 200 mg/mL, whereas this threshold was exceeded at only 150 – 160 mg/mL for the viscous, low co-solute systems.

The hollow fiber filter geometry will now be shown to enable a more uniform TMP and low wall shear stress τ_w for maintaining a high transmembrane flux. A low τ_w of 5 – 50 Pa was maintained throughout ultrafiltration to 250 mg/mL with the hollow fiber module (Fig. 5.5a), and

was sufficient to prevent rapid flux decline. In contrast, in TFF studies utilizing flat sheet cassettes, a higher τ_w of 200 – 400 Pa was applied to maximize membrane flux at mAb concentration greater than 50 mg/mL (6, 8) and maintain a high initial TMP. As described in the Supporting Information, the lower τ_w in this study may be attributed to the use of hollow fibers with a large inner diameter of 1.0 mm. In general, for the same bulk velocity and flow channel cross-sectional area in open flow channels, the hollow fiber may be expected to have higher pressure drops and wall shear stresses than cassettes by factors of 4.19 and 1.67 respectively. However, in screened cassettes, such as the commonly used Pellicon (Millipore) modules, additional parasitic pressure losses due to the screens as well as sharp turns in devices with serpentine flow paths may significantly increase ΔP and τ_w by up to a factor of ~5 relative to an open channel device (12, 60). As such, hollow fiber devices may actually offer comparable or potentially smaller overall ΔP and τ_w to screened cassette devices for the same flow velocity and channel cross-sectional area. Additionally, screened flat sheet cassettes have greater non-uniformity in their ΔP, τ_w and TMP profiles, given the serpentine flow path, which may create local areas of high TMP and τ_w that can contribute to protein aggregation. Since the soluble aggregate population was found to increase with τ_w between 100 and 300 Pa (6, 8), a method was developed for 'programming' the TMP throughout ultrafiltration. In this method, the TMP was maintained at its optimal value (the 'knee point') at any given mAb concentration. The optimal TMP was found to decrease with the mAb concentration (6). Concurrently, the cross-flow flux was adjusted between 290 and 450 LMH over the concentration range 5 - 90 mg/mL to maintain an appropriately low TMP and τ_w (6). However, it becomes difficult to maintain a sufficiently low optimal TMP at higher mAb concentrations, given the large η and ΔP, as shown in Eqn. 5.7,

$$TMP = \frac{(P_i + P_o)}{2} - P_p = P_o + \frac{\Delta P}{2} - P_p \tag{5.7}$$

where P_i and P_o are the filter inlet and outlet pressures, respectively, and P_p is the permeate pressure. In our case, the low viscosities of our concentrated solutions as well the hollow fiber geometry resulted in a small ΔP (Fig. 5.5a). Since ΔP was the controlling parameter for tuning the TMP and τ_w (Eqn. 5.5; Eqn. 5.7), the low ΔP led to a small τ_w, and more uniform axial TMP profile (Fig. 5.12). Consequently, we were able to maintain the TMP at a low level without the need to adjust the cross-flow rate throughout ultrafiltration.

The more uniform axial TMP profiles may also contribute to the higher fluxes for the high co-solute systems. As described by Binabaji et al. (12), a significant portion of the reversible flux decline at high concentration can be attributed to a steep decline in the local TMP near the back end of the filter device, resulting in reduced local fluxes. When the local TMP falls below the osmotic back-pressure, back-filtration significantly reduces the overall flux. In this study, the local TMP remained above the osmotic pressure at all mAb concentrations (Fig. 5.12), but a noticeable difference in the normalized TMP ($TMP_{local}/TMP_{average}$) profile can be seen between the high and low co-solute systems between 100 and 200 mg/mL mAb (Fig. 5.12a, 4.S7b). The local normalized TMP declined more quickly for the viscous, low co-solute systems below 1.0 (local TMP = average TMP when the normalized TMP = 1.0). The average TMP was set at the knee-point value of 0.8 bar, as described in the Supporting Information. Consequently, the local TMP for the low co-solute systems fell below the pressure-independent region (corresponding to normalized TMP < 1.0) more steeply in the rear section of the hollow fiber, which may explain the lower flux above 100 mg/mL mAb. However, while hollow fibers offer the advantage of more uniform flow paths and TMP profiles, they still have lower fluxes than flat sheet devices. The longer filtration times may be detrimental for maintaining protein quality.

5.4.3 Turbidity of high concentration mAb solution

The solution turbidity of the 40:50:17 mg/mL Tre:His:CitrA solution (replicate 4) was measured after 3 months of storage at 4°C, during which mild evaporative losses caused an

increase in the mAb concentration to 300 mg/mL. For a path length of 0.2 cm, the absorbance at 300 mg/mL at 350 nm was 0.165, corresponding to a turbidity of 0.826 AU*cm^{-1} and a concentration-normalized turbidity of 0.0027 AU*mL*mg^{-1}cm^{-1}, as reported in Table 5.7. The relatively low turbidity at 300 mg/mL in the current study likely resulted from the low solution η, axial ΔP and τ_w, which minimized the tendency for protein aggregation. The low levels of irreversible aggregation may also be favorable for reducing pore blocking and cake formation (61).

Sample ID	mAb conc (mg/mL)	η (cP)	η_{inh} (mL/g)	Absorbance at 350 nm (AU)	Turbidity at 350 nm (AU*cm^{-1})	Turbidity/c (AU*mL*mg^{-1}cm^{-1})
Before filtration	307	138	15.7	0.174	0.868	0.0028
After filtration	223	22	13.4	0.083	0.414	0.0019

Table 5.7. Turbidity (0.2 cm path length), turbidity/concentration (*c*) and viscosity (*η*) before and after syringe sterile filtration of Replicate 4 of the 40:50:17 mg/mL Tre:His:CitrA solution. The turbidity was corrected for the absorbance of the protein-free buffer.

Sterile filtration of the 300 mg/mL mAb solution resulted in a decrease in concentration to 223 mg/mL, due to the presence of entrained water in the washed syringe filter membrane. The resulting absorbance at 350 nm was 0.0743 AU, corresponding to a turbidity of 0.372 AU*cm^{-1} and a concentration-normalized turbidity of 0.0017 AU*mL*mg^{-1}cm^{-1} (Table 5.7). The two-fold reduction in turbidity corresponded with a decrease in ηinh from 15.7 to 13.4 mL/g, which may be explained in part by the dilution of the mAb. The normalized effective D_v from DLS increased from 0.26 to 0.31 after sterile filtration as indicated in Table 5.11, which may be due in part to the lower mAb concentration (62), but which may also suggest removal of larger aggregates, consistent with the smaller contribution to the DLS autocorrelation function at long times (Fig. 5.16). Although the removal of large aggregates by sterile filtration has been seen in

literature to reduce the low-shear (< ~300 s^{-1}) viscosity and eliminate the shear-thinning behavior of a concentrated IgG1 mAb (63) this does not appear to be the case for the Tre:His:CitrA solution. Both large irreversible (63) and small reversible aggregates (4, 11, 29, 30, 32, 64-66) are thought to promote protein network formation which leads to high viscosities. It is likely that in this case, network formation was sufficiently suppressed by the high His/Im levels (as will be described in the Discussion section), given the relatively low mAb viscosity.

5.4.4 pH shift during ultrafiltration

The high co-solute solutions underwent a negligible pH shift during ultrafiltration compared to the low co-solute solutions, remaining essentially constant during ultrafiltration from 60 to 250 mg/mL as shown in Fig. 5.13. Additionally, intermediate pH measurements during ultrafiltration of a representative high co-solute solution (50:17:10 mg/mL Tre:Im:CitrA) revealed a negligible difference in the pH of the retentate and permeate streams (shift of ~0.02 units), both of which remained constant at 7.0 as seen in Table 5.12. The matching, unchanging pH in the permeate and retentate streams over the entire mAb concentration range suggests that the charged buffer species (His, Im, counteracids) did not partition significantly across the membrane during filtration (9). The solution pH was in good agreement with the initial pH of the protein-free buffer, although a small shift of < 0.1 units was observed for the buffers prepared at pH 6.5 and 7 as seen in Table 5.13 due to the self-buffering capacity of the mAb (67). In contrast, a more noticeable pH shift of 0.2 units from 60 to 240 mg/mL was observed during filtration of the low co-solute solutions, suggesting partioning of the buffer species across the membrane due to the Donnan effect (9) or electrical double-layer volume exclusion (10, 68).

5.4.5 mAb stability in the ultraconcentrated solutions

The high co-solute solutions will now be shown to be stable against irreversible aggregation during manufacture and storage at 4°C, as assessed by size exclusion

chromatography (SEC). The monomer content was assessed as both (i) the ratio of monomer to monomer + soluble aggregates ("% monomer") and (ii) the mass ratio of recovered monomer for the post-TFF/storage to the pre-TFF/storage samples ("monomer recovery"). SEC measurements of the 250 mg/mL solutions after 2 – 4 weeks of storage at 4°C show similarly low levels of soluble irreversible aggregates for both the low and high co-solute solutions, with less than 1% soluble aggregates upon dilution to 2 mg/mL, as seen in Table 5.8. The only exception was the Tre:Im:CitrA solution, which showed 2.6% soluble aggregates when measured after 7 months of storage at 4°C. However, a significant difference in the insoluble aggregate content was seen between the low and high co-solute solutions, with monomer recoveries of ~90% with high co-solute and 60 – 80% with low co-solute formulations. Visible gel-like aggregates were observed during dilution of the concentrated low co-solute solutions. These large irreversible aggregates were filtered out during SEC sample preparation, but account for the significantly lower recoveries. The ultrahigh viscosity of the low co-solute solutions may explain the low monomer recoveries, as the viscous solutions may undergo greater pathway-dependent gelation and irreversible aggregation during ultrafiltration.

Formulation	% Monomer	Monomer recovery (%)
Concentrated solution from TFF		
mAb control (130 mg/mL)	99.7	100.0
40:50:17 mg/mL Tre:His:CitrA, pH 6 (280 mg/mL)	99.5	93.6
40:50:17 mg/mL Tre:His:CitrA, pH 6 (240 mg/mL)	99.9	88.9
50:50:12 mg/mL Tre:His:PhosA, pH 6 (250 mg/mL)	99.9	86.2
50:17:7 mg/mL Tre:Im:HCl, pH 6.3 (260 mg/mL)	99.0	91.8
50:17:10 mg/mL Tre:Im:CitrA, pH 7 (250 mg/mL)	97.4[a]	89.2
Freezing buffer (235 mg/mL)	99.5[b]	**83.7**
DI water (245 mg/mL)	99.4[b]	**62.6**
Dilution of 40:50:17 mg/mL Tre:His:CitrA solution (original 280 mg/mL)		
256 mg/mL dilution	99.5	90.8
237 mg/mL dilution	99.5	95.8
183 mg/mL dilution	99.5	97.2

a. After 7 months storage at 4°C
b. Visible ~1 mm gel-like clumps (aggregates) observed upon dilution to 2 mg/mL in mobile phase; removed by sterile filtration prior to SEC analysis

Table 5.8. Initial stability of mAb solutions by SEC. Samples were analyzed by SEC within two weeks of when the samples were manufactured except for the Tre:Im:CitrA solution, which was measured seven months after the solution was manufactured. All samples were stored at 4°C between manufacture and SEC measurements. The % monomer was determined from the ratio of the monomer to the combined monomer and aggregate peak areas, whereas the monomer recovery was determined from the ratio of the monomer peak areas for the post-ultrafiltration sample and the mAb control (unstressed 130 mg/mL mAb starting material in freezing buffer).

To more extensively test storage stability, Replicate 4 of the Tre:His:CitrA solution was stored over 8 weeks at -40°C, 4°C and 37°C. Due to evaporative losses during storage, especially at 37°C, the concentrations increased in some cases. Despite the high mAb concentrations, η remained below 100 cP for a majority of the stored samples and changes in $D_v/D_{v,o}$ were negligible as indicated in Table 5.14. The η_{inh} of the samples stored at -40°C and 4°C was relatively constant as seen in Fig. 5.14a, whereas η_{inh} at 37°C decreased from 16.9 mL/g at 4 days to 14.5 mL/g at 28 days (Table 5.9). At each temperature, the soluble aggregate content was

≤0.8% even after up to 4 weeks at 37°C and 8 weeks at -40°C and 4°C (Table 5.9; Fig. 5.14b). The monomer recovery after storage was also assessed relative to the original concentrated dispersion before accelerated storage tests. As seen in Table 5.9, the monomer recovery remained high at ~90% throughout the entire storage period of up to 8 weeks, even at the highest storage temperature of 37°C.

The concentrated high co-solute solutions also remained clear at low temperature, even after up to four months of storage at 4°C as shown in Fig. 5.14c. In contrast, the low co-solute solutions became cloudy and formed a rigid, opaque gel within minutes of exposure to the 4°C environment, as shown in Fig. 5.14d. Although the gelled solution returns to a liquid state upon being warmed to room temperature, irreversible phase separation was evident. It is likely that the concentrated co-solute shielded various charged patches and hydrophobic sites on the protein to inhibit gelation and the formation of aggregates during storage.

Time (days)	Storage temp (°C)	mAb conc (mg/mL)	η (cP)	η_{inh} (mL/g)	pH	% monomer by SEC	Monomer recovery (%)
4	-40	278 ± 5.3	92 ± 3.7	15.9	5.99	99.6	93.3
4	4	274 ± 6.6	88 ± 5.5	16.0	5.96	99.5	92.2
4	37	330 ± 2.7	297 ± 3.9	16.9	5.95	99.4	91.8
7	-40	263 ± 2.7	82 ± 3.7	16.4	5.98	99.5	97.7
7	4	266 ± 10.0	88 ± 2.3	16.4	5.97	99.6	84.3
7	37	260 ± 10.9	77 ± 0.6	16.3	5.97	99.4	98.3
14	-40	287 ± 5.1	101 ± 0.9	15.7	5.95	99.5	103.9[a]
14	4	288 ± 3.4	98 ± 5.7	15.6	5.98	99.5	96.7
14	37	454 ± 34.8	---[b]	---[b]	---[b]	99.2	96.3
28	-40	291 ± 3.5	132 ± 0.8	16.4	5.92	99.5	93.9
28	4	302 ± 6.4	133 ± 1.9	15.8	5.94	99.5	93.8
28	37	299 ± 4.2	86 ± 2.4	14.5	5.99	99.2	90.7
56	-40	279 ± 1.4	106 ± 2.6	16.3	5.95	99.4	85.0
56	4	272 ± 0.5	114 ± 6.1	17.1	5.96	---[c]	---[c]

a. Monomer recovery greater than 100% likely due to experimental error resulting in SEC sample being slightly more concentrated than 2 mg/mL

b. Sample became too concentrated and viscous to characterize by rheometry

c. Remaining sample volume after viscometry and concentration measurements was insufficient for SEC measurements

Table 5.9. Viscosity *(η)*, inherent viscosity *(η_{inh})* and SEC stability of Replicate 4 of the 40:50:17 mg/mL Tre:His:CitrA solution after up to 4-weeks of storage at -40°C, 4°C and 37°C. No 56-day sample at 37°C was available due to evaporative losses which rendered the sample too concentrated and viscous even for concentration measurements. The % monomer was determined from the ratio of the monomer to the combined monomer and aggregate peak areas, whereas the monomer recovery was determined from the ratio of the monomer peak areas for mAb solution before and after accelerated storage.

5.4.6 Mechanism of Viscosity Reduction

At concentrations of 250 mg/mL (~20% volume fraction) when the spacing between proteins is on the order of the molecular diameter (69), the relationship between viscosity and protein interactions is highly complex and not very well understood. Even with a range of techniques including SANS (32, 65, 70-73), SAXS (32), SLS (2), DLS (74-76), simulation (77-80), rheological studies (4, 11, 27-29, 63, 73, 81-84) and combinations thereof, relatively little is

known about the interactions and structure of protein solutions at high concentrations. From a rheological point of view, the significant reduction in [η] and η_{inh} of the concentrated mAb the high co-solute systems (Tables 5.1 – 5.3) may offer insight into the weakening of attractive protein interactions that contribute to high solution viscosities.

The significant reduction in viscosity for the mAb in this study resulting from the addition of histidine and imidazole (Fig. 5.1, Table 5.2 – 4.3) will now be examined in terms of modifications in the protein-protein interactions modified by these two co-solutes. The viscosity of antibody solutions has been shown to increase with the formation of small reversible low-density clusters or networks of interacting (28, 32, 64, 65) or physically entangled (85) mAb molecules. Network formation and aggregation may be mediated by local anisotropic attractive electrostatic and hydrophobic interactions. The addition of co-solutes may generate significant viscosity reductions by disruption of these interactions through shielding of charged (32, 65) and hydrophobic sites (36) on the protein surface. Inorganic salts such as NaCl have been shown in some cases to reduce mAb viscosity by weakening local attractive electrostatic interactions (4, 11, 32), but have also been found to increase the viscosity (41), likely by amplifying the strength of hydrophobic interactions (86). The charged amino acid arginine (Arg) is also known to both stabilize (87) and greatly reduce the viscosity for some proteins (28, 37, 41-43, 88) by shielding both electrostatic and hydrophobic residues on the protein surface (46, 87, 89, 90). The significant viscosity reduction from the addition of 300 mM His in this study (Fig. 5.1, Tables 4.2 – 4.3) may be caused by a similar mechanism as Arg, given their similar charge and molecular structure. In contrast, the addition of 150 mM NaCl caused a much smaller reduction in viscosity (Table 5.1), despite comparable solution ionic strengths. Recent membrane osmometry (43) and light scattering studies (45) suggest that co-solute effects on the viscosity of highly concentrated mAb occurs through modification of local rather than global interactions, and in some cases via co-solute binding to the mAb surface (45). The preferential interaction of

some co-solutes with the mAb may therefore explain the differences in co-solute effects on viscosity for co-solutes with similar charge and solution ionic strength.

The potent ability of histidine and imidazole to mitigate attractive protein-protein interactions and reduce the concentrated mAb viscosity by up to ten-fold (Fig. 5.1) will be explained in terms of their unique specific interactions with charged and hydrophobic residues on the protein surface. Histidine is positively charged below pH 6 and slightly hydrophobic with a Hopp-Woods hydrophobicity index of -0.5, where a negative index indicates an apolar residue in a protein sequence (91). Below pH 6, the cationic imidazole group is capable of shielding negatively-charged sites on the mAb surface via ion-pairing. Both His and Im also exhibit strong, selective binding affinities for the Arg and His residues on the protein surface (46). Molecular dynamics (MD) simulations have shown that positively-charged His is capable of pairing with both neutral and positively-charged His and Arg residues on the protein surface despite the Coulombic repulsion between like-charged pairs (46). The ability of His to form like-charged pairs with itself and Arg is thought to be due to stacking of the conjugated imidazole and guanidyl side chains respectively (46). As a result, His is capable of neutralizing negatively-charged residues through Coulombic attraction while blocking neutral and positively-charged His and Arg residues through stacking of the conjugated side chains, leading to its efficacy in screening anisotropic attractive electrostatic interactions. Beyond charge-shielding effects, His has also been shown via simulations to interact with hydrophobic aromatic residues via ion-π interactions through the imidazole group (92, 93). Due to the zwitterionic functional groups on His, the imidazole-aromatic interaction is effectively able to convert a hydrophobic surface patch to a hydrophilic one (94), weakening the hydrophobic interactions. In contrast, the inorganic salt NaCl does do not undergo specific binding with the protein and cannot mitigate local anisotropic interactions. The significantly greater viscosity reduction by His and Im (Fig. 5.1, Table 5.2 – 5.3), versus NaCl at comparable ionic strength (Table 5.1), therefore likely arose from more

efficient modulation of the local anisotropic attractive electrostatic and hydrophobic interactions. The very high concentrations of His and Im along with Tre also further perturb the electrostatic and hydrophobic interactions by the high degree of depletion attraction. In addition, the preferential exclusion of Tre from the surface favors folding for enhanced protein stability (95, 96).

5.5 CONCLUSIONS

For concentrated 250 to 280 mg/mL mAb solutions formed by TFF, the solution viscosity was reduced from 300 cP to 40 – 80 cP in systems containing high concentrations of the co-solutes histidine or imidazole. At the highest protein concentrations, the transmembrane fluxes were two to threefold higher with the high co-solute concentrations. This gain in transmembrane flux was due in part to a significant increase in the protein cg (gel point concentration) and the consequent enhancement of concentration polarization-driven back-diffusion near the membrane wall. The difference in the flux at high protein concentrations was not attributable to membrane fouling, as the normalized water permeability reductions were similar for high and low co-solute systems. For all co-solute concentrations, similar slopes were obtained for a wide range of systems on a log-log plot of permeation resistance (flux normalized by η_0 at constant TMP) versus viscosity over three orders of magnitude in viscosity, indicating the important role of viscosity in regards to flux decay.

With the low viscosities for high co-solute concentrations, the smaller axial ΔP resulted in a smaller and more uniform τ_w, as well as a more uniform TMP. An advantage of the hollow fiber geometry is the uniform flow path, unlike the serpentine channels with 90° bends found in flat sheet cassettes that can generate high local ΔP and shear stresses. The more uniform τ_w and TMP are expected to be beneficial for minimizing the rate of reversible flux decline. Furthermore, the concentrated protein solutions with either concentrated histidine or imidazole as co-solutes had less than 1% soluble aggregates by SEC and a high monomer recovery of ~90%,

in contrast with the low recoveries of 60 – 80% for the low co-solute solutions. The high monomer recovery corresponded with slower reversible flux decline. Under extended storage at -40°C, 4°C and 37°C, the soluble aggregate content remained below 1% after 4 weeks at all three storage temperatures for the trehalose-histidine-citric acid system. The high histidine concentration also solubilized the mAb and prevented precipitation of the 250 mg/mL solution at 4°C, whereas the onset of gelation and precipitation was almost immediate for the concentrated low co-solute solutions.

5.6 ACKNOWLEDGEMENTS

The authors would like to acknowledge Muhammad W. Lubis and Anuj K. Kudva for their assistance with some of the mAb concentration measurements. The mAb used in this study was provided by AbbVie Inc. The University of Texas at Austin received research funds from AbbVie Inc. to conduct the study. AbbVie provided financial support and the antibody used in this study. Additional support was provided by the Welch Foundation F-1319 and F-1696 and NSF (CBET-1247945).

5.7 SUPPORTING INFORMATION

5.7.1 Diafiltration and ultrafiltration to 250 mg/mL by centrifugation filtration to form low co-solute controls

Buffers were sterile filtered with the Celltreat bottle top PES filters and then degassed under vacuum for 30 minutes. Centrifugal filters were washed before use by permeating 2 mL DI water through the membrane at 4500 rcf using a Centrifuge 5810R (Eppendorf, Hamburg, Germany). The frozen mAb stock (130 mg/mL) was thawed in a 4°C water bath, and 1.3 mL of the thawed stock was diluted to 13.5 mg/mL with 10.7 mL of the filtered and degassed buffer. The diluted mAb solution was then buffer exchanged by discontinuous diafiltration until the

original buffer constituted less than 1% by volume of the total solution volume. Briefly, the mAb solution was filtered at 4500 rcf for 15 minutes using a Millipore Amicon centrifugal filter with a capacity of 12 mL and a regenerated cellulose membrane with a molecular weight cutoff of 30 kDa. The mAb solution was concentrated to a volume of ~2 mL and a concentration of 80 mg/mL. Additional buffer was added to dilute the retained mAb solution to a volume of 12 mL and a concentration of 13 mg/mL, reducing the volume fraction of the initial buffer to 1.8% (10.8% of 2 mL out of 12 mL). The mAb solution was then concentrated again by centrifugal filtration to a volume of ~2 mL, and the process was repeated 2 -3 more times until the permeate volume was approximately 40 mL, corresponding to less than 1% by volume of the initial buffer in the final solution, assuming ideal mixing. The mAb solution was then concentrated to 80 mg/mL (~2 mL) and transferred to a new Amicon centrifugal filter (with the same capacity and MWCO) for concentration to 250 mg/mL.

The tare weights of the individual filter assembly components (filter, permeate tube and retentate tube) of the second set of Amicon centrifugal filters were recorded before the start of concentration to 250 mg/mL mAb. The mass of mAb loaded into the second set of centrifugal filters was determined from the mass and exact concentration of the buffer-exchanged mAb solution (~80 mg/mL). The desired retentate volume at 250 mg/mL and corresponding mass of the solution plus filter assembly was determined assuming a recovery of 80% of the mAb by mass. The filter assembly was then centrifuged at 4500 rcf in 10 – 15 minutes increments for 60 – 70 minutes. The mass of the retentate/filter assembly was monitored between increments, and filtration was stopped when the combined retentate/filter assembly mass reached the desired mass as calculated earlier. The concentrated mAb solution was then transferred to 0.1 mL conical V-vial (catalog no. 03-341-15; Wheaton, Millville, NJ) for further characterization.

5.7.2 Turbidity measurements by UV-Vis spectroscopy

The turbidity was measured as the absorbance of the mAb solution at 350 nm, where the chromophores in the mAb do not absorb. The absorbance was normalized for the path length, yielding a dimensional turbidity in cm^{-1}. Dilute mAb solutions (≤ 65 mg/mL) were loaded into a 1 cm path length QS quartz cuvette (Hellma GmbH and Co, Mullheim, Germany), while the concentrated (>150 mg/mL) solutions were loaded into a 0.2 cm path length cuvette (Beckman Coulter, Indianapolis, IN). Turbidity measurements were made on both the unfiltered solutions as well as solutions sterile filtered with 0.22 μm PES bottle top (20 mg/mL stock) and 13-mm syringe filters (>150 mg/mL solution). Before sterile filtration, the syringe filters were washed by passing 100 μL DI water through the filter membrane to remove residual impurities in the membrane. Due to the ~100 μL hold-up volume of the syringe filter, around 100 μL of DI was entrained in the filter, causing some dilution of the 250 mg/mL mAb solution during sterile filtration by syringe filters.

5.7.3 Dynamic light scattering of concentrated mAb solutions

An effective average diffusion coefficient of the species in the mAb solution was measured by dynamic light scattering (DLS) on a Brookhaven BI-9000AT (Brookhaven Instruments, Holtsville, NY) at detector angles of 150° and 173° using a 632.8 nm laser. Additional samples were analyzed by DLS on a Brookhaven ZetaPALS at an angle of 90° using a 660 nm laser. The effective diffusion coefficient Dv was determined from the decay time of the DLS autocorrelation function (ACF), which was fit using the CONTIN algorithm. All reported values of D_v are the average of three replicate DLS measurements of 2 minutes each. Samples were not filtered prior to loading into the DLS cuvette due to high losses from filtering viscous material (path length = 0.2 cm; Beckman Coulter, Indianapolis, IN).

The diffusion coefficient of the mAb in the high co-solute solutions will now be shown to be lower than the expected value for the monomer in the same buffer, indicating a change in the

mAb interaction length scale. The autocorrelation function (ACF) from the DLS measurements was fit to a single average effective D_v using the CONTIN algorithm, where the decay time for the first exponential decay was converted to D_v, assuming Stokes-Einstein diffusion of the mAb through buffer. The viscosity η was set equal to η_0 in the Stokes-Einstein equation for the first decay, assuming that the first decay corresponds to a short enough time scale that diffusing protein molecules do not encounter neighboring protein molecules (76). In light of the possible polydispersity of the mAb solution, as well as the complexities involved in fitting the ACF (97), the fitted D_v only represents an effective average diffusivity. The theoretical diffusion coefficient of the monomer $D_{v,0}$ in the given buffer was calculated from the Stokes-Einstein equation (Eqn. 5.8) using η_0 for η and an assumed hydrodynamic radius R_h of 5.5 nm, typical for an IgG mAb.

$$D_v = \frac{k_B T}{6\pi\eta R_H} \tag{5.8}$$

As can be seen in Table 5.15, the ratio of the measured D_v to the theoretical $D_{v,0}$ ($D_v/D_{v,0}$) was 0.24 – 0.36 for the high-co-solute solutions at 250 mg/mL mAb. In contrast, the values for the low co-solute solutions were 0.7 – 0.8 at 250 mg/mL, closer to the value of 1.0 for a purely monomeric dilute solution. Smaller $D_v/D_{v,0}$ values of 0.42 – 0.64 were obtained for the low co-solute solutions made by centrifugation filtration (0.23 for the 150 mM NaCl dispersion), as seen in Table 5.16. However, the resolution of DLS is too low to be able to distinguish diffusion coefficient differences under a factor of 3-4 (98) and thus to discriminate between protein monomer and aggregates up to about 40 nm. The values of $D_v/D_{v,0}$ less than unity for the high co-solute solutions may suggest restricted molecular motion relative to monomer diffusing through the solvent due to crowding(62) or stronger attractive interactions with co-solute (99) or other protein molecules, resulting in the diffusing species encountering a medium viscosity greater than the solvent viscosity. With the exception of the DI water mAb solution, the $D_v/D_{v,0}$ ratio also slowly decreased with increasing mAb concentration between 50 and ~150 mg/mL

before reaching a plateau, as shown in Fig. 5.17. The corresponding DLS ACF's used to obtain the D_v values reported are shown in Fig. 5.16 and Fig. 5.18 – 5.20. The gradual decrease in $D_v/D_{v,0}$ with mAb concentration could indicate the continuous growth of protein entities larger than monomer or an increase in attractive interparticle interactions leading to restricted motion at higher levels of depletion attraction (crowding) (62, 99). However, it is unclear how to choose a medium viscosity for converting the diffusion coefficient to a hydrodynamic diameter, given the diffusing species may contact multiple protein molecules during the long diffusion times of 100 μs. In contrast, self-diffusion of protein through solvent may be measured by neutron spin echo where the correlation time is only 50 ns (32).

5.7.4 Viscosity calibration

5.7.4.1 Liquid volume correlation

The volume of liquid in the conical vial used for viscosity measurements was determined from the height of the liquid meniscus. 200 μL of DI water was pipetted into six different vials in 5 or 25 μL increments using an Eppendorf Research Plus adjustable volume pipette (Eppendorf AG, Hamburg, Germany). The meniscus height was measured for each incremental volume addition by ImageJ analysis of a photo of the liquid column inside the vial, measured from the vial bottom to the bottom of the meniscus. The correlation between the meniscus height and liquid volume was determined from quadratic regression of the average of the volume-height measurements for all six vials, as shown in Fig. 5.21.

5.7.4.2 Determining pressure drop across needle capillary

The axial pressure drop ΔP across the needle capillary of the syringe viscometer was determined using the viscosity standards S60, N44, N35 and N10 (Cannon Instrument Company, State College, PA) as well as DI water. At room temperature (25°C), these solutions have viscosities of 102.4, 70.92, 55.75, 15.39, and 0.986 cP, respectively. The volumetric flow rate of

100 µL of each solution was measured in triplicate in five different vials for an assumed fixed ΔP across the needle capillary, totaling 15 measurements per sample. The ΔP was assumed to be fixed since the needle tip is exposed to atmospheric pressure, while the end of the needle attached to the syringe is assumed to be at a constant lower pressure (established by pulling the syringe plunger up to the 1 mL mark quickly to establish a lower internal pressure), which is unaffected by liquid flow inside the needle during measurement since the liquid does not enter the syringe in the time frame of the measurement. The flow rate was averaged over the 15 runs and plotted against the known viscosity of the liquids. ΔP was then determined from fitting the Hagen-Poiseuille equation to the viscosity data, giving a ΔP of 7942 Pa across the needle, as shown in Fig. 5.22. The viscosity of the actual samples were then determined from the measured volumetric flow rate and the fitted ΔP using the Hagen-Poiseuille equation.

5.7.5 Relevant shear rate regime for capillary syringe viscometer measurements

The wall shear rate, γ_w, applied to the mAb solution during viscosity measurements can be estimated from the fitted ΔP/L and measured viscosity with Eqn. 5.9, assuming Newtonian flow:

$$\gamma_w = \frac{r\Delta P}{2\eta L}\left(\frac{3n+1}{4n}\right) \tag{5.9}$$

where r is the needle radius, L is the needle length and n is equal to 1 for a Newtonian liquid. As indicated by the dashed black lines in Fig. 5.23, the minimum and maximum viscosities measured at high concentration in this study correspond to a shear rate range of 25 – 500 s^{-1}.

5.7.6 Fits of the mAb viscosity profiles for the crowding-shape factor k/ν (Ross-Minton equation)

The fitted k/ν was comparable between the freezing buffer (10 mM His with ~40 mg/mL mannitol) and the two histidine high co-solute solutions with a value of ~0.04 – 0.06, whereas the DI water solution had a much smaller k/ν of 0.026 and the two imidazole solutions had a

higher k/ν of 0.09 and 0.13. The combined parameter k/ν accounts for the effect of both self-crowding ($k = 1/\Phi_{max}$ (26), where Φ_{max} is the maximum packing fraction) as well as the particle shape (where a sphere corresponds to $\nu = 2.5$ and elongated shapes have $\nu > 2.5$) on viscosity (26, 64). Since k/ν is fit as a single parameter, the two effects cannot be easily deconvoluted from a single value for k/ν, making quantitative interpretation difficult (4). However, the crowding factor k is not expected to change significantly between the low and high co-solute solutions at the same mAb concentration/volume fraction. The modestly higher fitted values of k/ν for the high co-solute solutions therefore suggest a small decrease in ν approaching a more spherical mAb molecule. A decrease in ν suggests the adoption of a more compact and folded conformation which would be beneficial for stability and lower viscosities. A smaller value of $D_v/D_{v,0}$ below unity was also observed for the high co-solute solutions as well as the low co-solute solutions with the extremely high protein concentrations, as discussed in the Supporting Information. Although the mechanism of protein diffusion at high concentrations is highly complex, these results may indicate an influence of depletion attraction on the configuration of reversible protein aggregates or clusters (47, 48, 62, 72, 75, 76, 100).

5.7.7 Decline in wall shear stress for low co-solute mAb solutions

The unexpected decrease in τ_w for the low co-solute solutions (Fig. 5.4a; Fig. 5.5a) arose from the decrease in the axial ΔP as seen in Fig. 5.4a, Fig. 5.5a, and Eqn. 5.6. The ΔP is expected to increase with η and the feed cross-flow rate, as described by the Hagen-Poiseuille equation for flow through a cylindrical geometry. Since η increases with the mAb concentration, the reduced ΔP and τ_w likely arose from a decrease in the cross-flow rate. The settings on the TFF pump were unchanged throughout the ultrafiltration experiment, so the theoretical cross-flow rate remained constant. Instead, it is likely that the actual cross-flow rate decreased when the ultraviscous low co-solute solutions exceeded the capacity of the TFF pump to accurately regulate the feed flow-rate. Alternatively, the large ΔP arising from the high viscosity may have caused a negative local

TMP near the back end of the filter module, leading to back-filtration and an increase in P_o and subsequent decrease in ΔP.

5.7.8 Selection of TMP for TFF ultrafiltration

To minimize pressure-driven membrane fouling while maximizing membrane flux during ultrafiltration, the TMP should be maintained at the transition point, known as the knee point (6), between the pressure-dependent and pressure-independent flux regimes. The knee point TMP was identified for our TFF system in a representative high co-solute buffer (40:50:17 mg/mL Tre:His:CitrA) at a cross-flow flux of 750 LMH from flux-TMP profiles generated at 40, 120 and 190 mg/mL (Fig. 5.24). At the lower concentrations of 40 and 120 mg/mL, the knee point TMP appeared to remain between 0.5 and 0.6 bar. The knee point shifted upward to 0.8 bar with the increase in mAb concentration to 190 mg/mL. Above 0.8 bar, a slight decrease in the flux was observed. Due to large axial pressure drops arising from high viscosities at high mAb concentration, the increase in global TMP above 0.8 bar corresponds to a large increase in the inlet pressure, which may have increased the local TMP at the inlet to excessively high values and lead to increased gelation and membrane fouling. Since concentration of the mAb from 100 to 250 mg/mL constituted the majority of the ultrafiltration process based on time (Fig. 5.5b; Fig. 5.11b), we chose to maintain the TMP at 0.8 bar (the knee-point TMP at high mAb concentration) throughout the filtration process.

5.7.9 Comparison of shear stress and pressure drop for hollow fibers and flat sheet cassettes

We report lower shear stresses and pressure drops in our work with hollow fiber TFF modules compared to values seen in literature for flat sheet cassettes (6). The use of the 1 mm ID fibers generates smaller pressure drops and wall shear stresses relative to cassettes with smaller characteristic dimensions of 3.2 cm x 0.5 mm, as seen in literature (6). However, for the same bulk velocity v = Q/A (Q = volumetric flow rate) and flow channel cross-sectional area A,

hollow fibers inherently exhibit larger pressure drops and wall shear stresses than open-channel cassettes, as shown below.

For laminar, Newtonian flow of a fluid with viscosity η through a cylindrical channel (such as a hollow fiber) of radius R, the pressure drop and wall shear stress are given by Eqn. 5.6 and 4.10 respectively.

$$\tau_w = \frac{4\eta Q}{\pi R^3} \tag{5.10}$$

For a corresponding flat sheet cassette with an open, rectangular flow channel of width H and height 2H, the pressure drop and wall shear stress are given by Eqn. 5.11 and 5.12 respectively.

$$\frac{\Delta P}{L} = \frac{3\eta Q}{2H^4} \tag{5.11}$$

$$\tau_w = \frac{3\eta Q}{2H^3} \tag{5.12}$$

Combining Eqn.'s 5.6 and 5.10 – 5.12 and assuming a fixed v ($v=Q/(\pi R^2)=Q/(2H^2)$) reveals that

$$\frac{\left(\frac{\Delta P}{L}\right)_{fiber}}{\left(\frac{\Delta P}{L}\right)_{sheet}} = \frac{8}{3}\left(\frac{H}{R}\right)^2 \tag{5.13}$$

and that

$$\frac{\tau_{w,fiber}}{\tau_{w,sheet}} = \frac{4}{3}\left(\frac{H}{R}\right) \tag{5.14}$$

To compare between hollow fiber and open-channel flat sheet cassettes with both the same bulk velocity v and the same channel cross section A, the ratio H/R must be fixed at $\sqrt{(\pi/2)}=1.253$. Substitution of this value for H/R into Eqn. 5.13 and 5.14 results in ΔP and τ_w ratios of 4.19 and 1.67, respectively, for the hollow fiber relative to the open-channel flat sheet cassette.

For screened cassette devices, an additional correction factor, a, must be introduced for the pressure drop and shear stress to account for parasitic pressure losses from the presence of the screen and sharp bends in the serpentine flow path (12, 60):

$$\frac{\Delta P}{L} = \frac{3a\eta Q}{2H^4} \tag{5.15}$$

$$\tau_w = \frac{3a\eta Q}{2H^3} \tag{5.16}$$

Consequently, for the same bulk velocity and channel cross-sectional area, the ΔP and τ_w ratios are 4.19/a and 1.67/a, respectively, for the hollow fiber relative to the screened cassette, where a has been found from simulation to vary between ~1.5 and 5 for a range of flow channel geometries and flow rates (60).

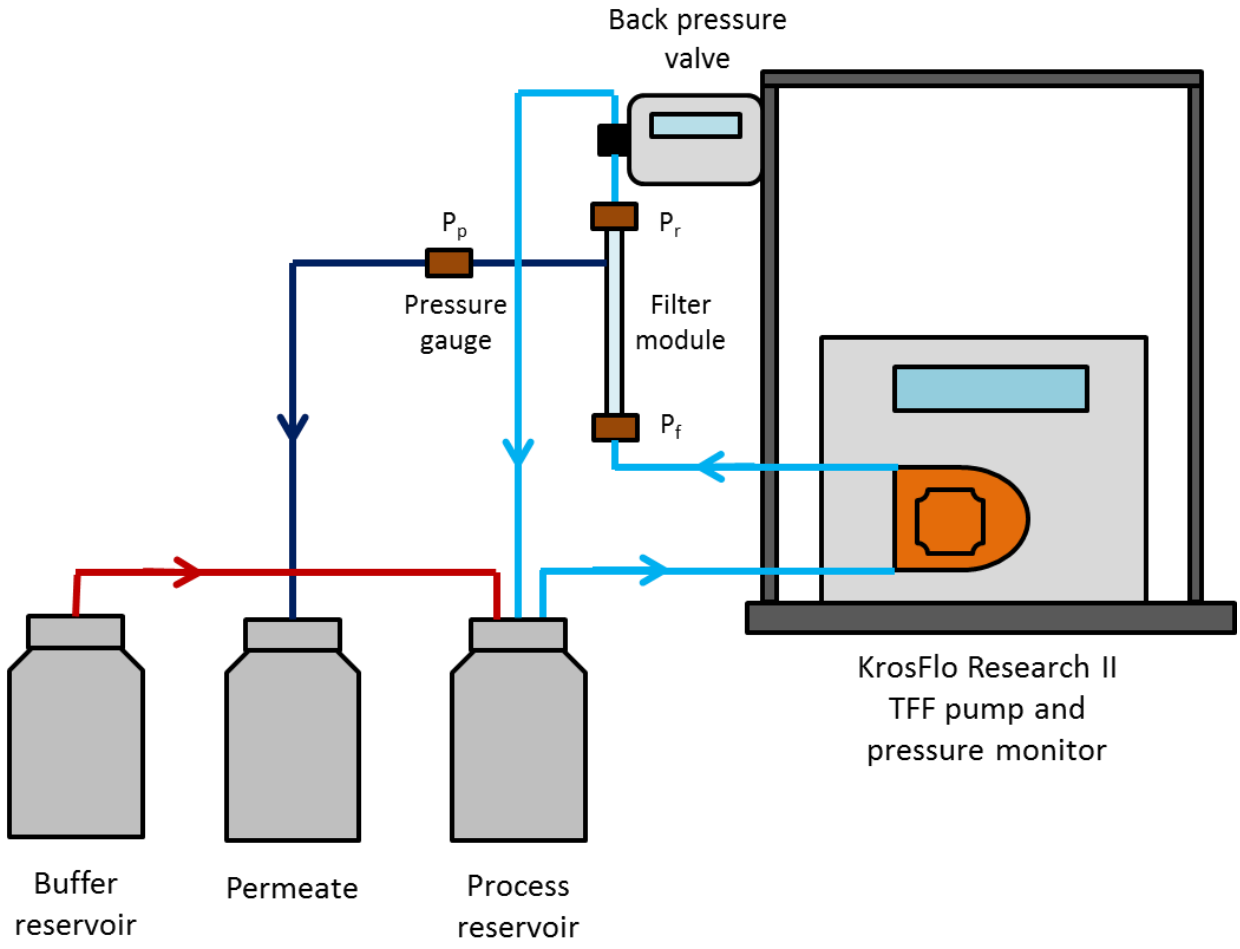

Figure 5.6. Flow path schematic of the Spectrum KrosFlo Research II TFF system.

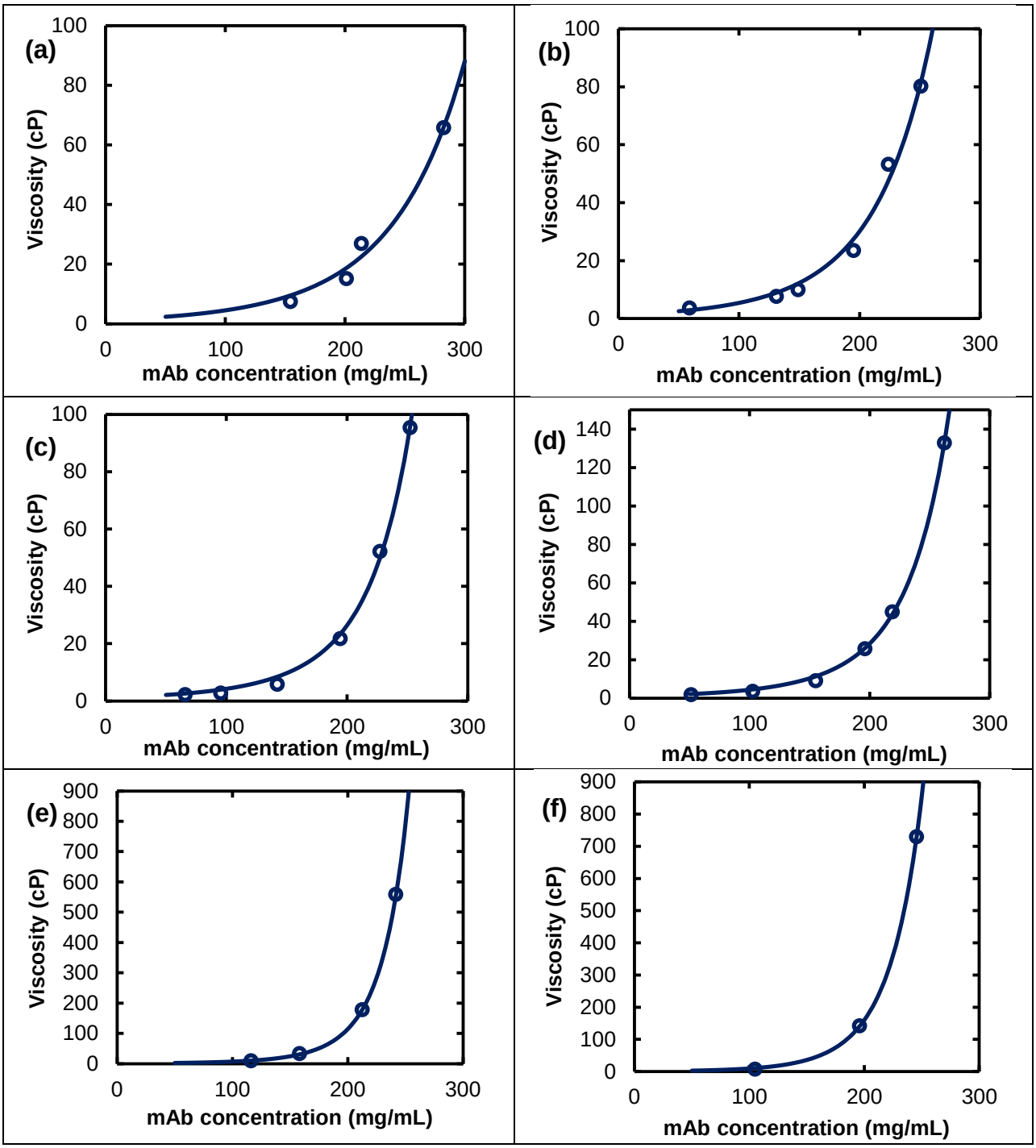

Figure 5.7. Two-parameter fits (−) of the mAb solution viscosity (○) to the Ross-Minton equation during ultrafiltration to 250 mg/mL mAb by TFF for: (a) 40:50:17 mg/mL Tre:His:CitrA, pH 6.0 (Replicate 4); (b) 50:50:12 mg/mL Tre:His:PhosA, pH 6.0; (c) 50:17:10 mg/mL Tre:Im:CitrA, pH 7; (d) 50:17:7 mg/mL Tre:Im:HCl, pH 6.3; (e) freezing buffer; (f) DI water.

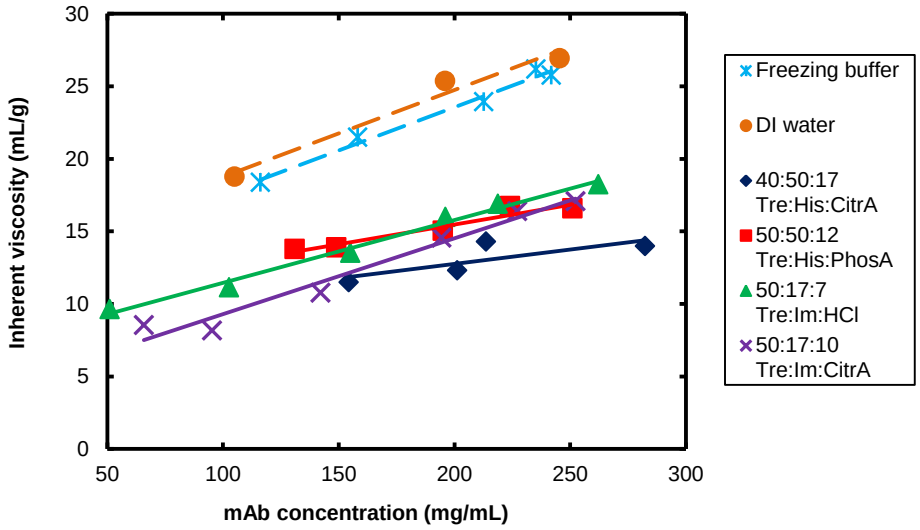

Figure 5.8. Inherent viscosity of mAb solutions during ultrafiltration to 250 mg/mL by TFF. The numbers in the formulation names represent concentration of each excipient in mg/mL. The colored lines serve as guides to the eye and correspond to the data series of the same color.

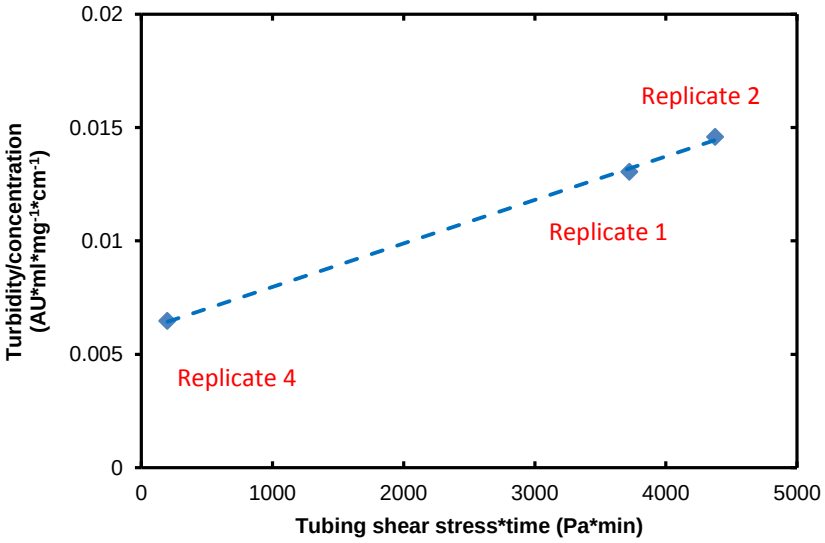

Figure 5.9. Concentration-normalized post-diafiltration turbidity as a function of shear stress*time for the 40:50:17 mg/mL Tre:His:CitrA solution replicates in Table 5.4. The wall shear stress was calculated for flow inside the silicon tubing (Masterflex), rather than the hollow fibers.

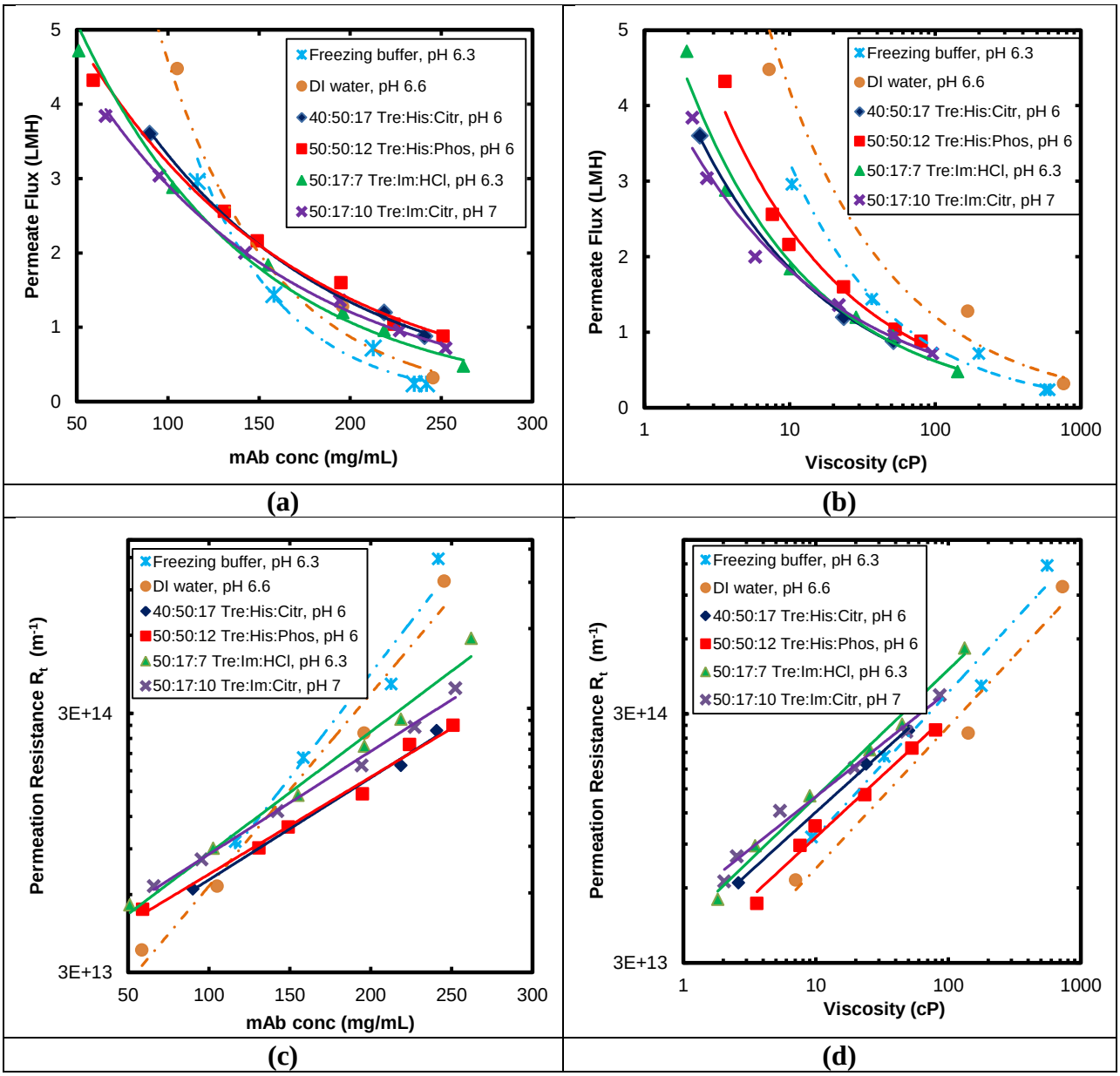

Figure 5.10. TFF membrane flux (in L/m^{2}h) as a function of (a) mAb concentration and (b) solution viscosity; and permeation flux resistance R_t (in m^{-1}) as a function of (c) mAb concentration and (d) solution viscosity during ultrafiltration to 250 mg/mL mAb for low co-solute (- - -) and high co-solute (—) solutions. The numbers in the formulation names represent concentration of each excipient in mg/mL. The flux and resistance curves for the 40:50:17 mg/mL Tre:His:Citr solution corresponds to Replicate 1. The colored lines are a guide to the eye, and correspond to the data series of the same color.

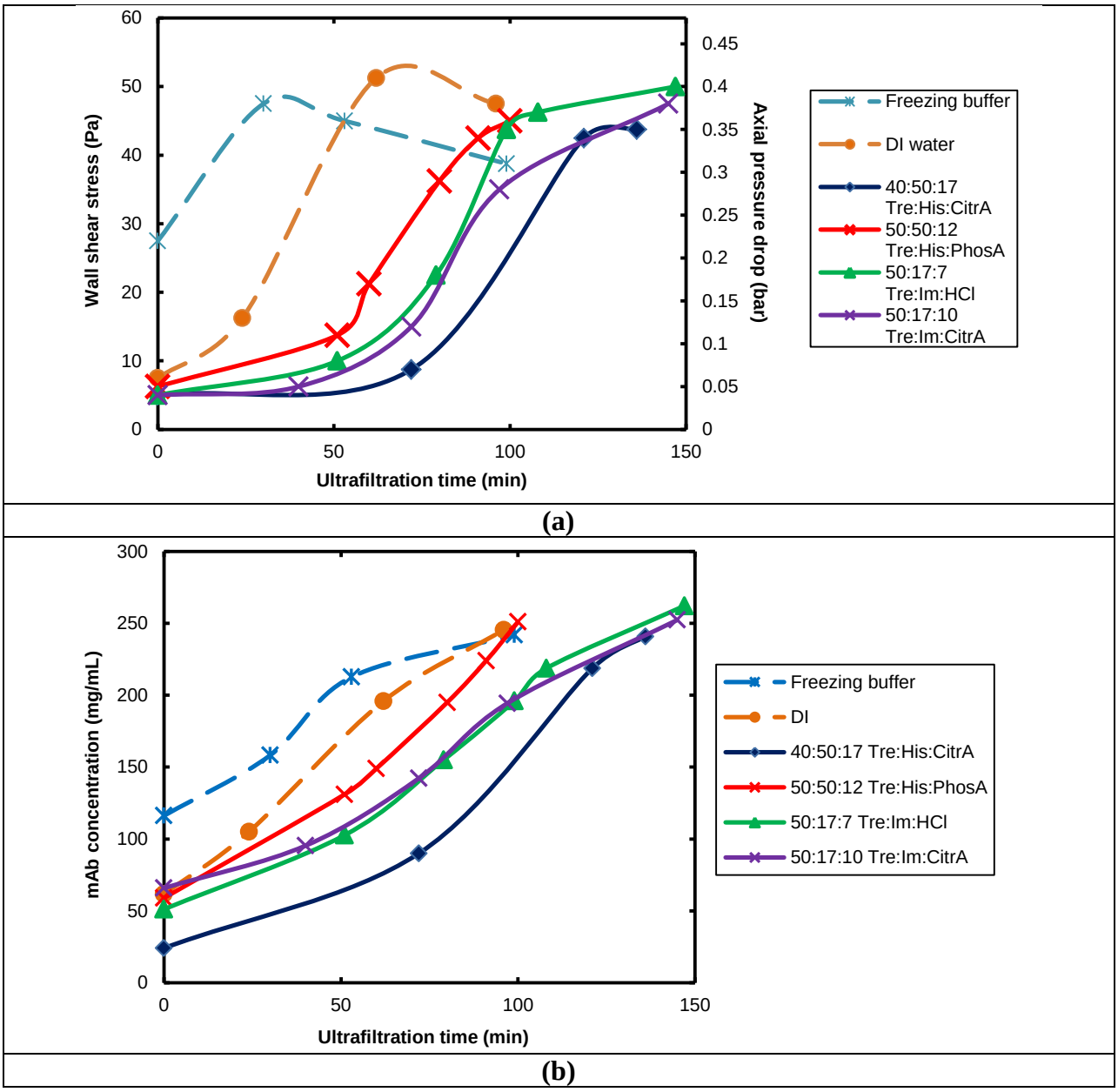

Figure 5.11. Time evolution of (a) pressure drop and wall shear stress and (b) mAb concentration during TFF ultrafiltration for low co-solute (---) and high co-solute solutions (—). The numbers in the formulation names represent concentration of each excipient in mg/mL.The concentration and pressure/shear stress curves for the 40:50:17 mg/mL Tre:His:Citr solution corresponds to Replicate 1.

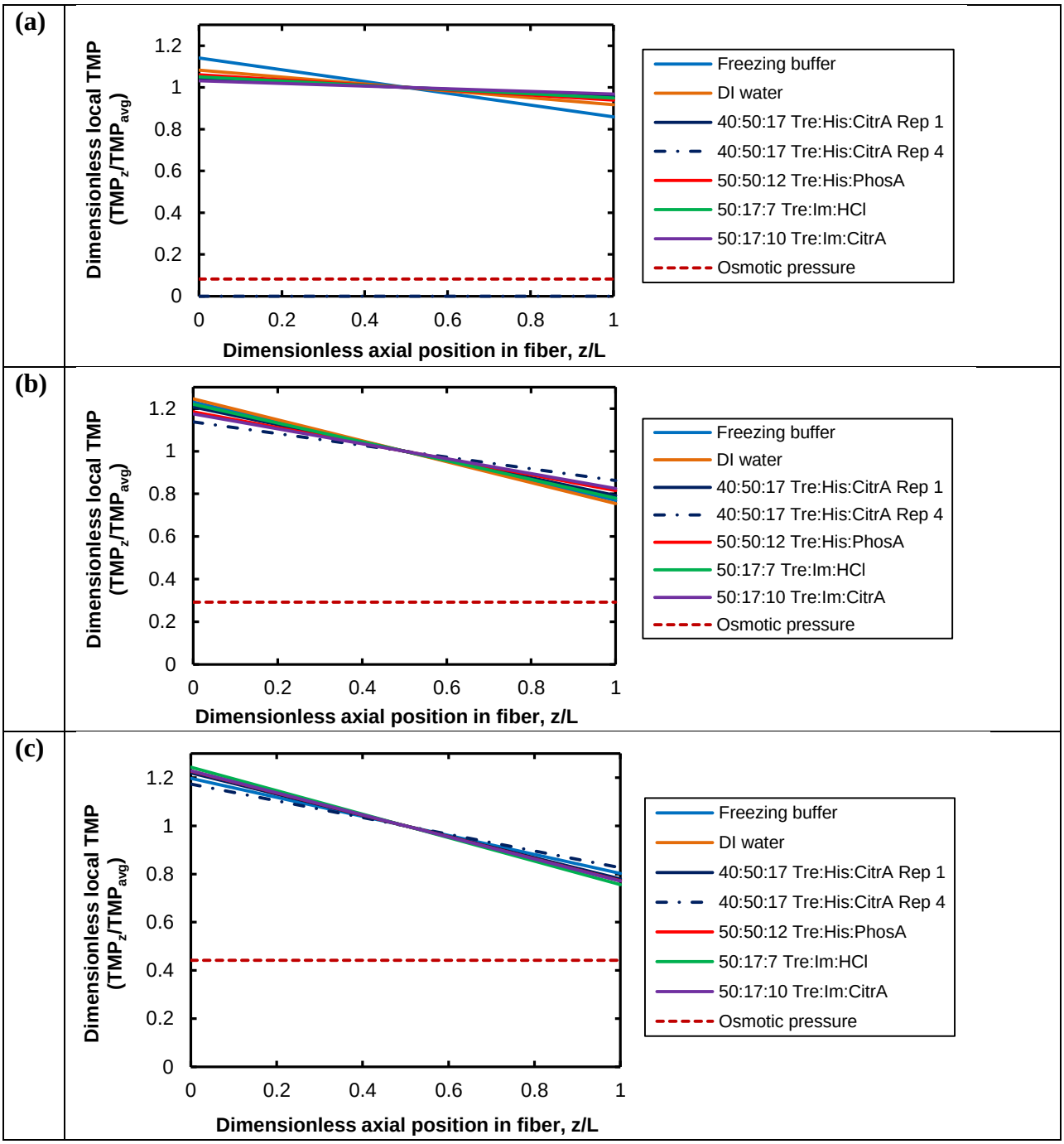

Figure 5.12. Calculated axial dimensionless TMP profiles at (a) 100 mg/mL, (b) 200 mg/mL and (c) 250 mg/mL mAb during ultrafiltration, assuming constant pressure gradient $\Delta P/L$ throughout filter module. $\Delta P/L$ was calculated from the measured ΔP at the corresponding mAb concentration during ultrafiltration.

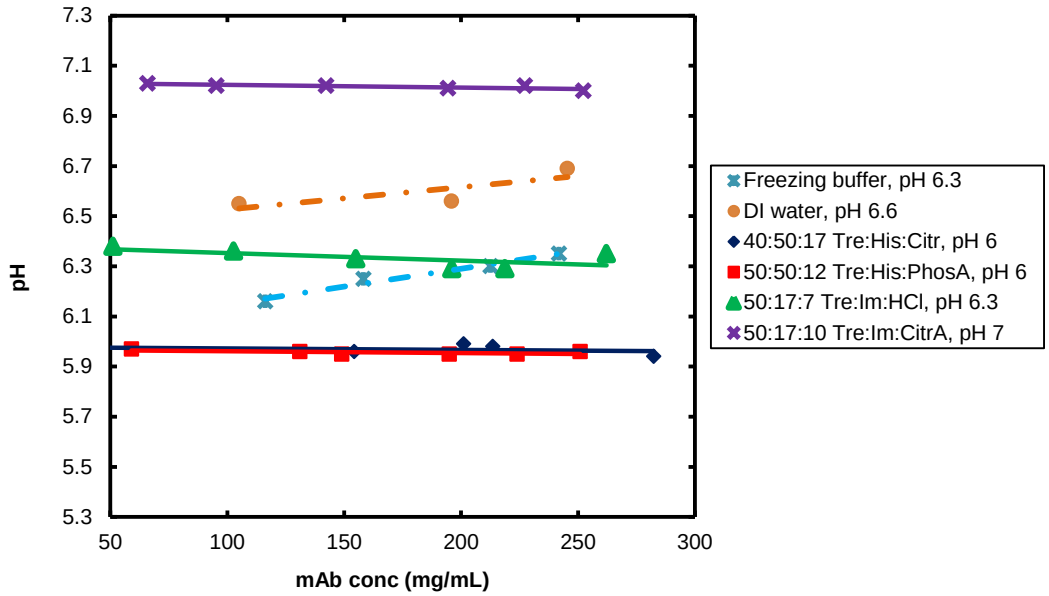

Figure 5.13. pH shift of mAb solutions during ultrafiltration by TFF. The numbers in the formulation names represent concentration of each excipient in mg/mL. The pH of the low co-solute (---) and high co-solute (—) mAb solutions were measured with a Mettler Toledo InLab Micro pH probe (Mettler Toledo, Columbus, OH). The pH shift for the 40:50:17 mg/mL Tre:His:Citr solution corresponds to Replicate 4.

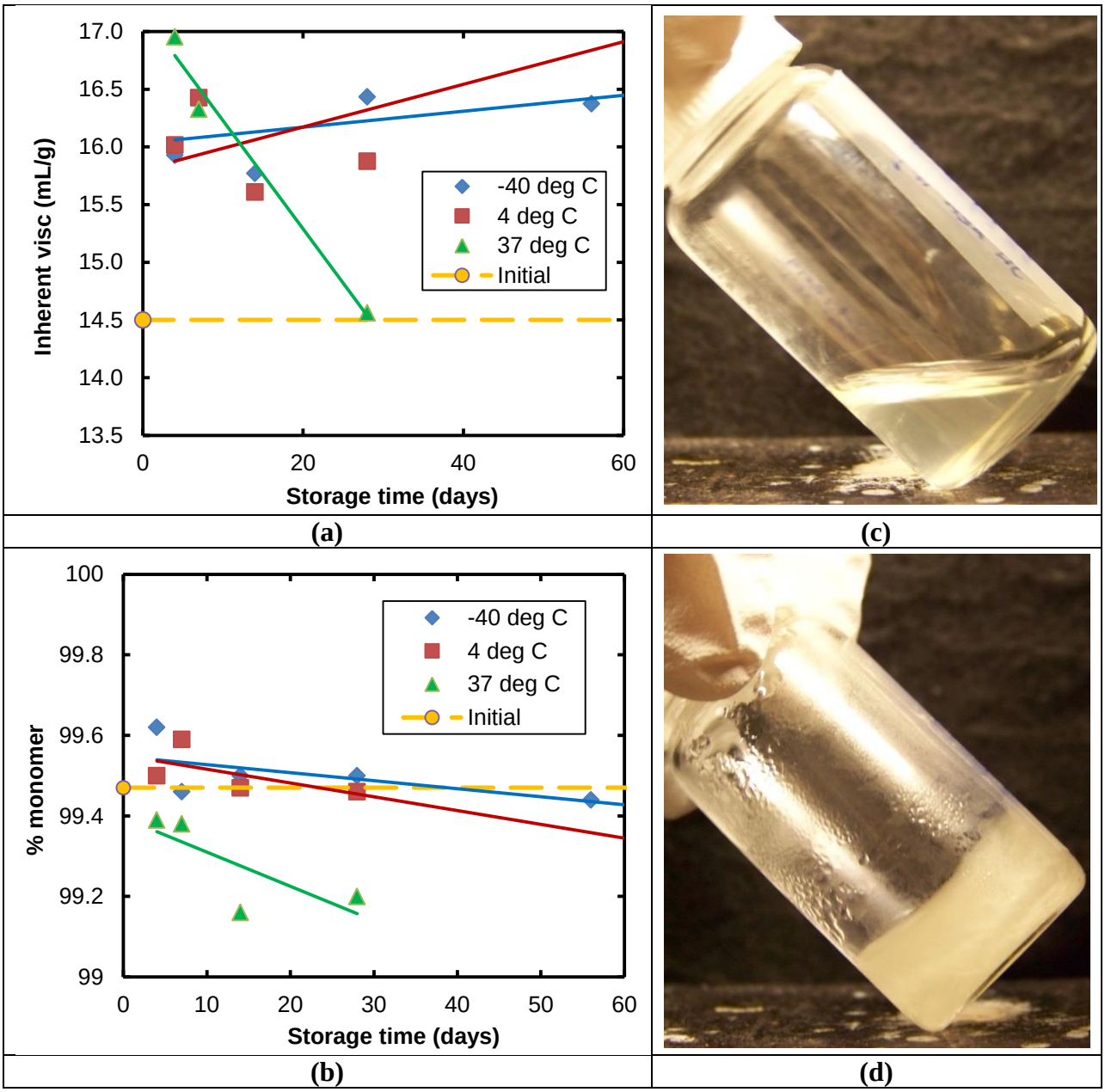

Figure 5.14. Storage stability of Replicate 4 of the 40:50:17 mg/mL Tre:His:Citr solution (Figure 4.2) as characterized by the (a) inherent viscosity and (b) percent monomer by SEC upon dilution to 2 mg/mL mAb. (c) The Replicate 4 solution remained as a clear liquid during prolonged storage at 4°C, whereas (d) a low co-solute solution (235 mg/mL mAb in DI water, Table 5.2) gelled and phase separated within 20 minutes of 4°C storage. Although not pictured, the 240 mg/mL mAb solution in freezing buffer (low co-solute; Table 5.2) also resembled the gelled solution in (d) within minutes of storage at 4°C.

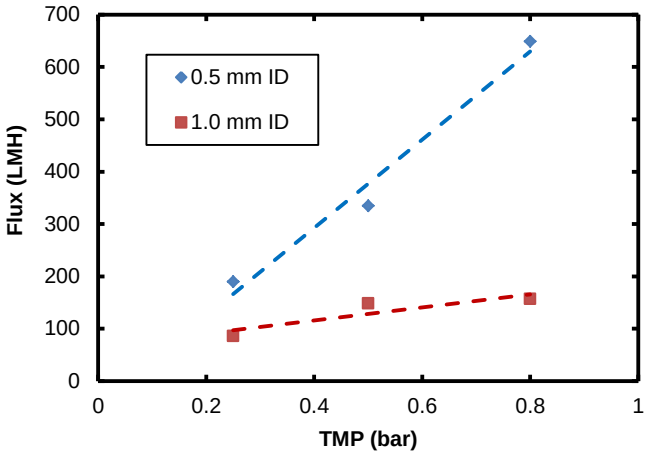

Figure 5.15. New membrane water permeability of the hollow fiber modules used in the TFF experiments. The 0.5 mm ID hollow fiber module had a surface area of 115 cm^2 and a MWCO of 50 kDa. The water permeability test was conducted at a cross-flow flux of 1150 LMH. The 1.0 mm ID hollow fiber module had a surface area of 75 cm^2 and a MWCO of 50 kDa. The water permeability test was conducted at a cross-flow flux of 800 LMH.

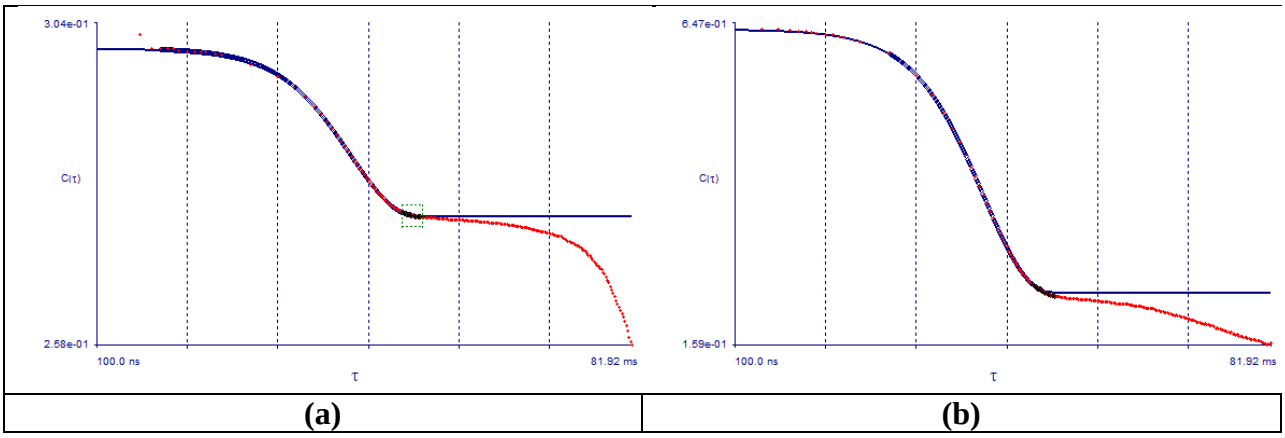

Figure 5.16. Raw (red discrete points) and fitted (blue curve) DLS ACFs of Replicate 4 of the 40:50:17 mg/mL Tre:His:CitrA solution formulation in Fig. 5.2 (a) before and (b) after sterile filtration. The unfiltered solution was stored at 4°C over 3 months after manufacture by TFF. DLS measurements were made at a scattering angle of 170°, and the corresponding detection count rates were 4200 and 1100 kcps respectively. The fitted diffusion coefficients were used to calculate the $D_v/D_{v,o}$ values reported in Table 5.11.

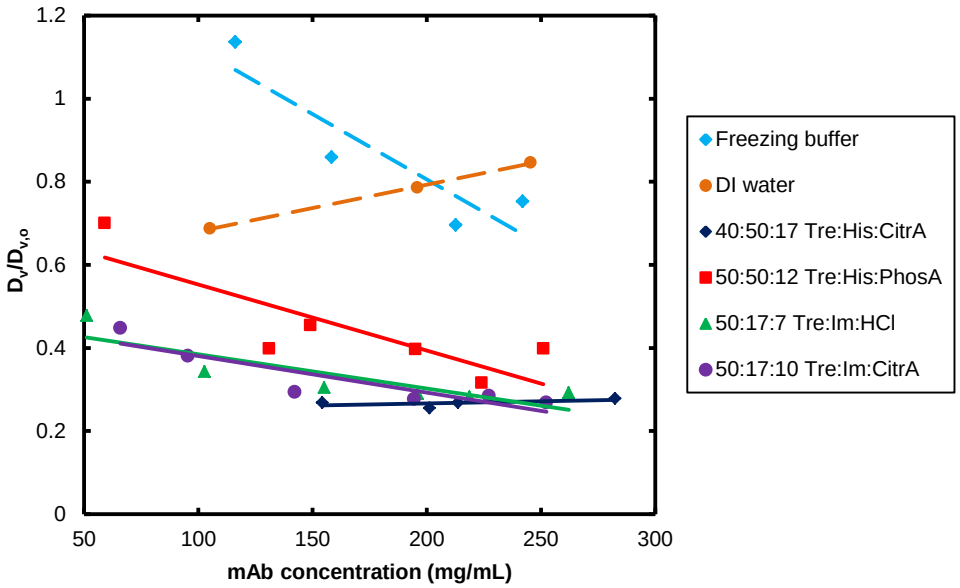

Figure 5.17. Effective diffusion coefficient of mAb solutions during ultrafiltration to 250 mg/mL by TFF. The numbers in the formulation names represent concentration of each excipient in mg/mL. The effective diffusion coefficient D_v was obtained from fitting the DLS autocorrelation function (measured at 150° scattering angle) with the CONTIN algorithm. The theoretical diffusion coefficient of monomer in the same buffer ($D_{v,0}$) was calculated from Stokes-Einstein at 25°C assuming a R_H of 5.5 nm and the solvent viscosity of the buffer. The $D_v/D_{v,o}$ for the 40:50:17 mg/mL Tre:His:Citr solution corresponds to Replicate 4. The colored lines serve as guides to the eye and correspond to the data series of the same color.

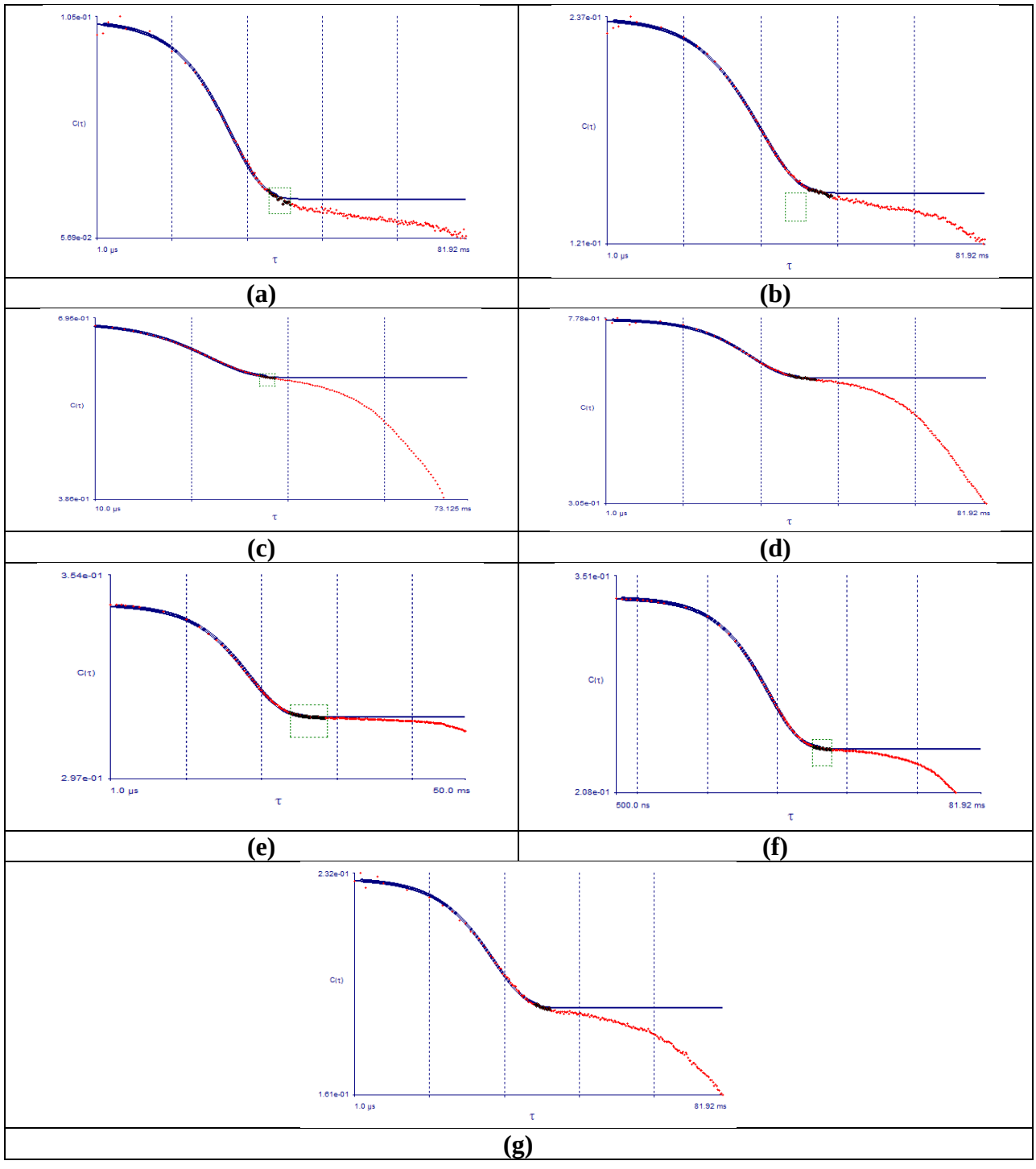

Figure 5.18. Raw (discrete red points) and fitted (blue curve) DLS ACFs of the unfiltered final ~250 mg/mL mAb solutions listed in rows (a) 1, (b) 2, (c) 3, (d) 4, (e) 5, (f) 6, (g) 7 of Table 5.15. The corresponding scattering angle and count rates for each measurement are indicated in Table 5.17.

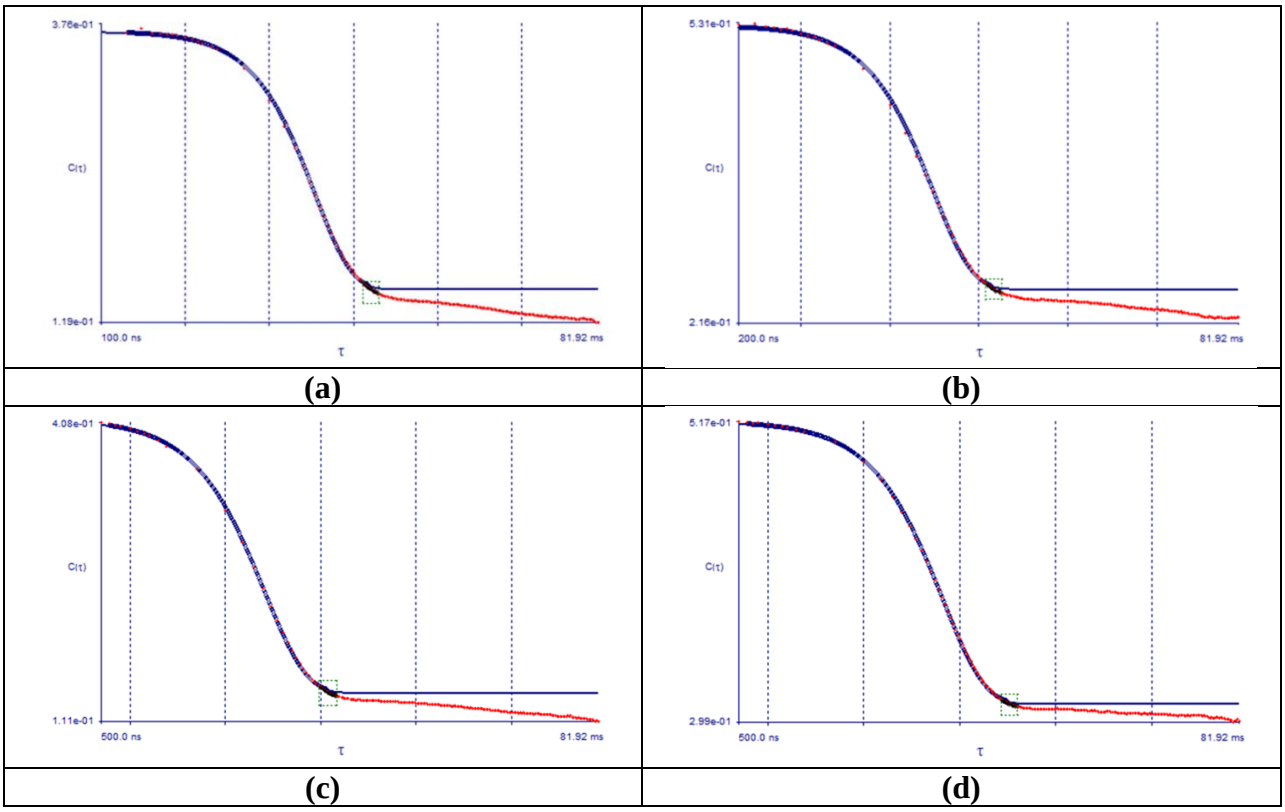

Figure 5.19. Raw (discrete red points) and fitted (blue curve) DLS ACFs of the unfiltered low co-solute mAb solutions listed in rows (a) 1, (b) 2, (c) 3, and (d) 4 of Table 5.16. DLS measurements were made at a scattering angle of 170°, and count rates varied between 600 and 1800 kcps.

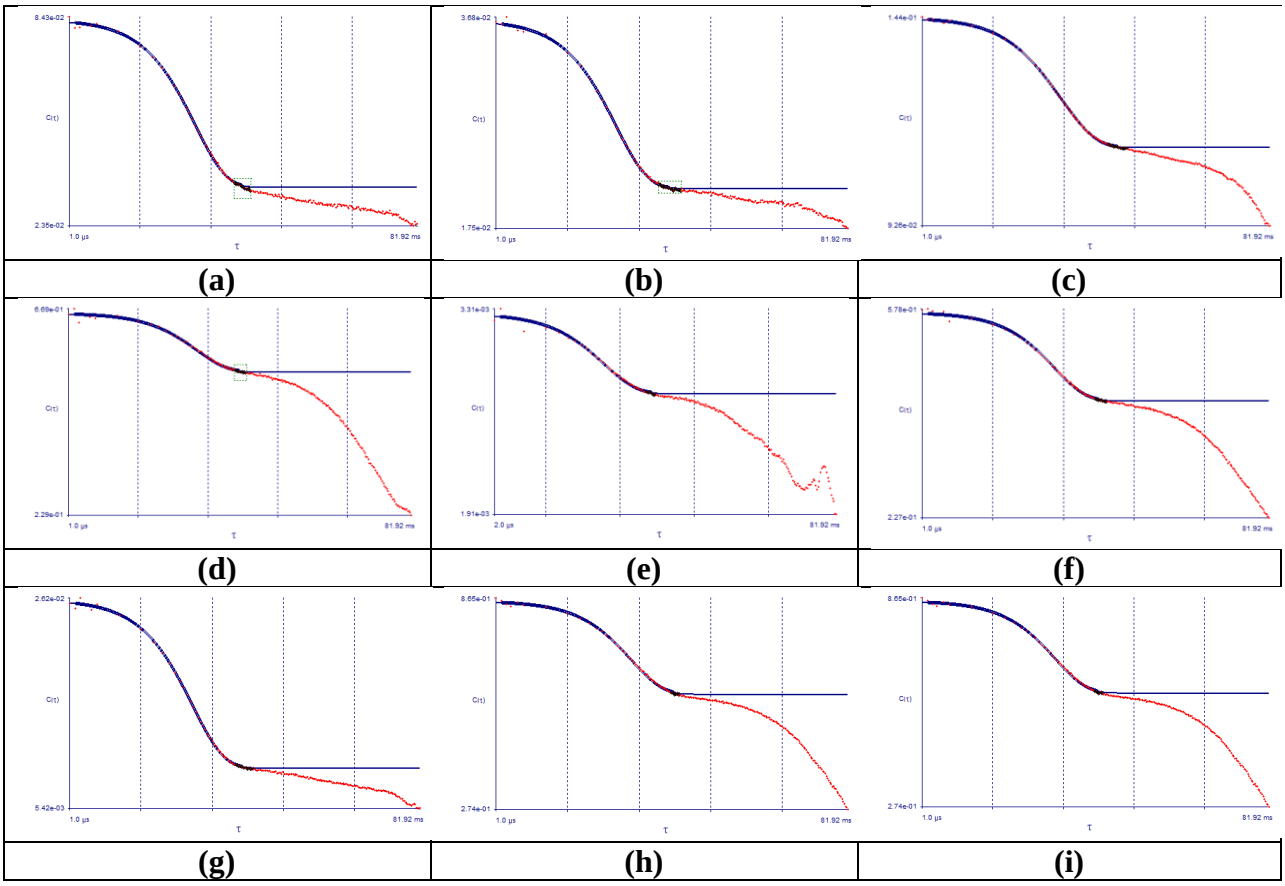

Figure 5.20. Raw (red discrete points) and fitted (blue curve) DLS ACFs of selected unfiltered intermediate mAb solutions at concentrations between 50 and 220 mg/mL. DLS measurements were made at a scattering angle of 150°. The fitted diffusion coefficients were used to calculate the $D_v/D_{v,o}$ values reported in Fig. 5.17. The corresponding sample information (formulation, mAb concentration, count rates) is indicated in Table 5.18.

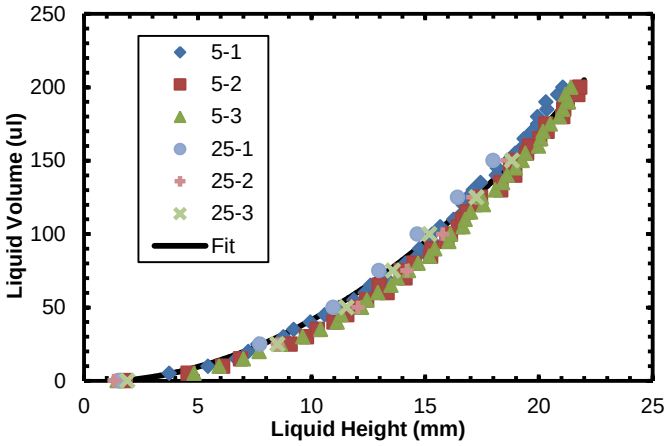

Figure 5.21. Liquid volume as a function of meniscus height for six different conical vials used in viscosity measurements. The first number in the legend is the incremental volume added (in µL) per addition, and the second number is the replicate number for each incremental volume addition. The quadratic fit of the data is $V = 0.426*h^2 - 1.135$, where V is the liquid volume in µL and h is the meniscus height in mm.

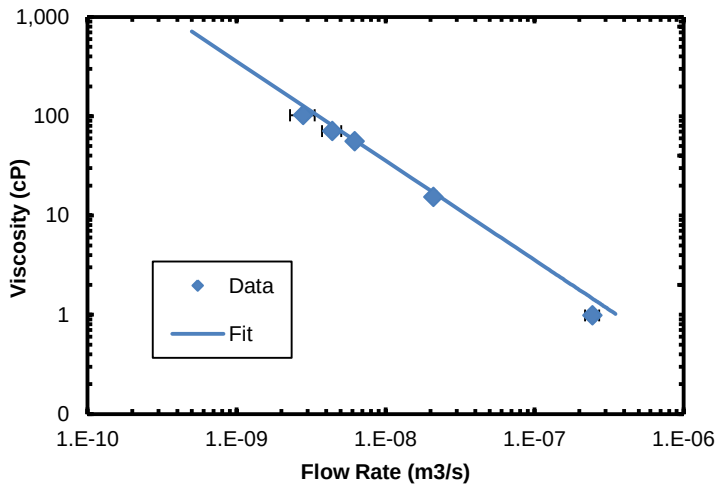

Figure 5.22. Viscosity of known standards (S60, N44, N35, N10 and DI water) versus measured volumetric flow rate. The solid line (—) shows the fit of the data to the Hagen-Poiseuille equation, where ΔP was fit to be 7942 Pa. Error bars shown are the measurement standard deviation for each viscosity standard; some error bars are too small to be seen.

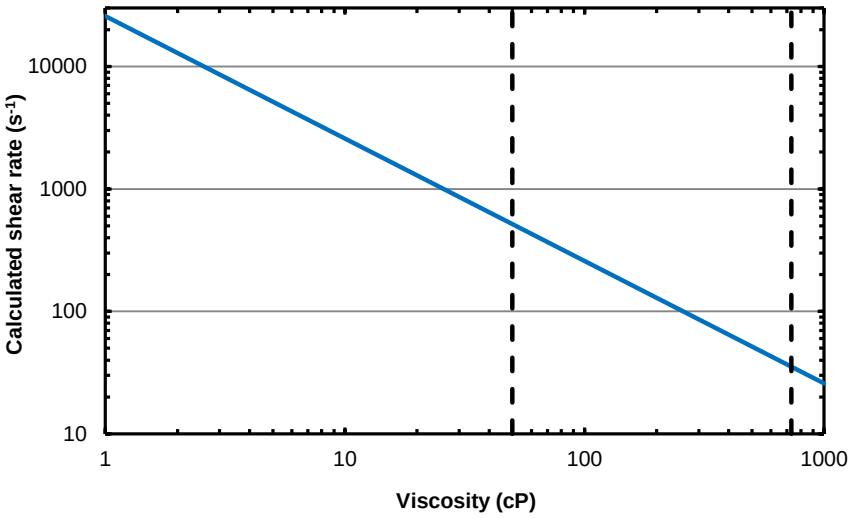

Figure 5.23. Predicted applied wall shear rate during capillary syringe viscometry as a function of solution viscosity

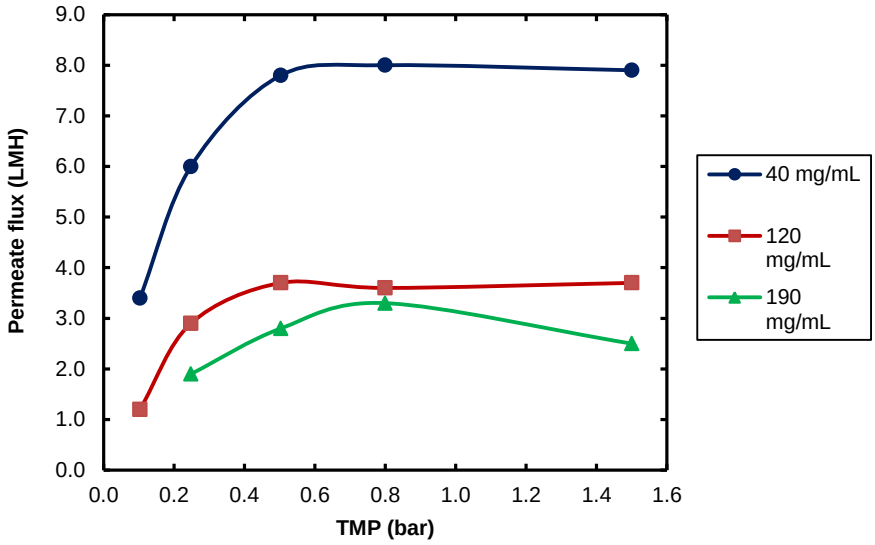

Figure 5.24. TMP-flux profiles at 40, 120 and 190 mg/mL mAb in 40:50:17 mg/ml Tre:His:CitrA for a cross-flow flux of 750 LMH.

mAb conc (mg/mL)	pH	η (cP)	η_{inh} (mL/g)	Effective CONTIN $D_v/D_{v,0}$ (cm^2/s)
284 ± 1.84	6.01	76 ± 6.2	14.9	0.25
256 ± 3.39	6.03	39 ± 1.7	13.9	0.24
237 ± 1.77	6.02	31 ± 1.0	14.0	0.25
183 ± 0.02	6.01	15 ± 1.1	14.2	0.24

Table 5.10. Reversibility of mAb solution viscosity *(η)* and inherent viscosity *(η_{inh})* upon dilution of Replicate 4 of the 40:50:17 mg/mL Tre:His:CitrA (pH 6) formulation in the same buffer. The pH of the pure buffer was 6.00. The normalized effective CONTIN diffusion coefficient $D_v/D_{v,0}$ of the unfiltered solution was measured by DLS at a scattering angle of 90°.

Sample ID	mAb conc (mg/mL)	$D_v/D_{v,o}$
Before filtration	300	0.26
After filtration	223	0.31

Table 5.11. Normalized effective D_v for Replicate 4 (Fig. 5.2a) before and after syringe sterile filtration. D_v was determined from fitting the DLS ACF measured at 170° with the CONTIN algorithm and normalized by the theoretical D_v of mAb monomer diffusing through pure buffer ($D_{v,0;}$ calculated assuming Stokes-Einstein diffusion and solvent viscosity η_0 = 1.27 cP).

mAb conc (mg/mL)	Retentate pH	Permeate pH
66	7.03	---
95	7.02	---
142	7.02	7.04
194	7.01	7.03
227	7.02	7.03
252	7.00	7.03

Table 5.12. Retentate and permeate pH of 50:17:10 mg/mL Tre:Im:CitrA mAb solution during ultrafiltration to 250 mg/mL mAb by TFF. The retentate and permeate pH were measured using a Mettler Toledo InLab Micro pH probe. The measured permeate pH is an average value for the cumulative permeate collected. The measured retentate pH is an instantaneous value as a small amount of retentate was periodically withdrawn and characterized at intermediate mAb concentrations during ultrafiltration. The permeate volume at the first two intermediate concentrations (66, 95 mg/mL) was insufficient for measuring the pH.

Sample	Initial buffer pH	Solution pH post-diafiltration
40:50:17 Tre:His:CitrA	6.01	6.01
50:50:12 Tre:His:PhosA	6.00	5.97
50:17:7 Tre:Im:HCl	6.47	6.38
50:17:10 Tre:Im:CitrA	7.09	7.03

Table 5.13. Change in buffer pH after diafiltration. The pH of the initial protein-free buffer was measured before the start of diafiltration. The pH of the protein solution (~60 mg/mL mAb) was also measured after diafiltration into six diavolumes of the buffer.

Time (days)	Storage temp (°C)	mAb conc (mg/mL)	Viscosity (cP)	Effective $D_v/D_{v,o}$ (cm^2/s)
4	-40	278 ± 5.3	92 ± 3.7	0.26
4	4	274 ± 6.6	88 ± 5.5	0.25
4	37	330 ± 2.7	297 ± 3.9	---[a]
7	-40	263 ± 2.7	82 ± 3.7	0.24
7	4	266 ± 10.0	88 ± 2.3	0.25
7	37	260 ± 10.9	77 ± 0.6	0.24
14	-40	287 ± 5.1	101 ± 0.9	0.24
14	4	288 ± 3.4	98 ± 5.7	0.24
14	37	454 ± 34.8	---	---[b]
28	-40	291 ± 3.5	132 ± 0.8	0.25
28	4	302 ± 6.4	133 ± 1.9	0.25
28	37	299 ± 4.2	86 ± 2.4	0.25
56	-40	279 ± 1.4	106 ± 2.6	0.24
56	4	272 ± 0.5	114 ± 6.1	0.24

a. Remaining sample volume after viscometry and concentration measurements was insufficient for DLS measurements.

b. Sample became too concentrated and viscous to characterize by viscosity and DLS.

Table 5.14. Viscosity and effective normalized D_v of Replicate 4 of the 40:50:17 mg/mL Tre:His:CitrA solution after up to 4-weeks storage at -40°C, 4°C and 37°C. D_v was determined by fitting the DLS ACF measured at 90° with the CONTIN algorithm and normalized by the theoretical D_v of mAb monomer diffusing through pure buffer ($D_{v,0}$; calculated assuming Stokes-Einstein diffusion with the solvent viscosity η_0).

mAb conc ± stdev (mg/mL)	Tre conc		Base	Base conc		Acid	Acid conc		η_0 (cP)	Effective $D_v/D_{v,0}$
	mg/mL	mM		mg/mL	mM		mg/mL	mM		
242±2.5	Freezing buffer								0.98	0.67
245±3.6	DI water								0.93	0.80
282±3.7[a]	40	105	His	50	320	CitrA	17	80	1.11	0.24
241±0.3	40	105	His	50	320	CitrA	17	80	1.11	0.30
251±18.5[b]	50	130	His	50	320	Phos A	12	120	1.12	0.36
252±0.5[b]	50	130	Im	17	250	CitrA	10	50	1.07	0.25
262±4.5	50	130	Im	17	250	HCl	7	190	0.99	0.26

a. The DLS ACF was measured at 90°

b. The DLS ACF was measured at 173°

Table 5.15. Normalized effective D_v for low and high co-solute solutions made by TFF. D_v was determined from fitting the DLS ACF measured at 150° (unless indicated otherwise) with the CONTIN algorithm and normalized by the theoretical D_v of mAb monomer diffusing through pure buffer ($D_{v,0}$; calculated assuming Stokes-Einstein diffusion with the solvent viscosity η_0).

mAb conc (mg/mL)	Exc 1	Exc 1 conc (mM)	Exc 2	Exc 2 conc (mM)	Exc 3	Exc 3 conc (mM)	η_0 (cP)	$D_v/D_{v,0}$
281 ± 8.7	Freezing buffer (replicate 1)						0.98	0.42
271 ± 0.5	Freezing buffer (replicate 2)						0.98	0.47
238 ± 3.3	His	30	HCl	19	---	---	0.98	0.64
230 ± 2.8	His	30	HCl	19	NaCl	150	0.98	0.23

Table 5.16. Normalized effective D_v for low co-solute control solutions made by centrifugation filtration. D_v was determined from fitting the DLS ACF measured at 170° with the CONTIN algorithm and normalized by the theoretical D_v of mAb monomer diffusing through pure buffer ($D_{v,0}$; calculated assuming Stokes-Einstein diffusion with the solvent viscosity η_0).

Figure number	Scattering angle (°)	Count rate (kcps)
4.S13a	150	254.9
4.S13b	150	111.4
4.S13c	90	371.1
4.S13d	150	52.4
4.S13e	173	5000
4.S13f	173	3633.3
4.S13g	150	178.3

Table 5.17. Scattering angle and count rates for DLS ACF's shown in Fig. 5.18.

Figure number	**Sample**	**mAb conc (mg/mL)**	**Count rate (kcps)**
4.S15a	Freezing buffer	158	294
4.S15b		116	617.5
4.S15c	DI water	196	582.1
4.S15d	40:50:17 mg/mL Tre:His:Citr	219	47.1
4.S15e	50:50:12 mg/mL Tre:His:Phos	195	4500
4.S15f	50:17:7 mg/mL Tre:Im:HCl	196	77.1
4.S15g		51	909.5
4.S15h	50:17:10 mg/mL Tre:Im:Citr	227	50.5
4.S15i		194	104.8

Table 5.18. Corresponding formulation, mAb concentration and count rates for DLS ACF's shown in Fig. 5.20.

5.8 REFERENCES

1. Sinko PJ, Martin A. Martin's Physical Pharmacy and Pharmaceutical Sciences. 5 ed. Philadelphia: Lippincott Williams & Wilkins; 2006.
2. Scherer TM, Liu J, Shire SJ. Intermolecular Interactions of IgG1 Monoclonal Antibodies at High Concentrations Characterized by Light Scattering. J Phys Chem. 2010;114:12948-57.
3. Shire SJ, Shahrokh Z, Liu J. Challenges in the Development of High Protein Concentration Formulations. J Pharm Sci. 2004;93(6):1390-402.

4. Liu J, Nguyen MDH, Andya JD, Shire SJ. Reversible Self-Association Increases the Viscosity of a Concentrated Monoclonal Antibody in Aqueous Solution. J Pharm Sci. 2005;94(9):1928-40.

5. Srinivasan C, Weight AK, Bussemer T, Klibanov AM. Non-Aqueous Suspensions of Antibodies are Much Less Viscous Than Equally Concentrated Aqueous Solutions. Pharm Res. 2013.

6. Rosenberg E, Hepbildikler S, Kuhne W, Winter G. Ultrafiltration concentration of monoclonal antibody solutions: Development of an optimized method minimizing aggregation. J Membr Sci. 2009;342(1-2):50-9.

7. Cromwell MEM, Hilario E, Jacobson F. Protein aggregation and bioprocessing. AAPS J. 2006;8(3):E572-E9.

8. Ahrer K, Buchacher A, Iberer G, Jungbauer A. Effects of ultra-/diafiltration conditions on present aggregates in human immunoglobulin G preparations. J Membr Sci. 2006;274(1-2):108-15.

9. Bolton GR, Boesch AW, Basha J, LaCasse DP, Kelley BD, Acharya H. Effect of protein and solution properties on the donnan effect during the ultrafiltration of proteins. Biotechnol Prog. 2011;27(1):140-52.

10. Teeters M, Bezila D, Benner T, Alfonso P, Alred P. Predicting diafiltration solution compositions for final ultrafiltration/diafiltration steps of monoclonal antibodies. Biotechnol Bioeng. 2011;108(6):1338-46.

11. Kanai S, Liu J, Patapoff TW, Shire SJ. Reversible Self-Association of a Concentrated Monoclonal Antibody Solution Mediated by Fab-Fab Interaction That Impacts Solution Viscosity. J Pharm Sci. 2008;97(10):4219-27.

12. Binabaji E, Ma J, Rao S, Zydney AL. Theoretical analysis of the ultrafiltration behavior of highly concentrated protein solutions. J Membr Sci. 2015:JMS151044.

13. Casey C, Gallos T, Alekseev Y, Ayturk E, Pearl S. Protein concentration with single-pass tangential flow filtration (SPTFF). J Membr Sci. 2011;384(1-2):82-8.

14. van Reis R, Zydney A. Bioprocess membrane technology. J Membr Sci. 2007;297(1–2):16-50.

15. Marcos B, Moresoli C, Skorepova J, Vaughan B. CFD modeling of a transient hollow fiber ultrafiltration system for protein concentration. J Membr Sci. 2009;337(1-2):136-44.

16. Bellara SR, Cui ZF. A Maxwell-Stefan approach to modelling the cross-flow ultrafiltration of protein solutions in tubular membranes. Chemical Engineering Science. 1998;53(12):2153-66.

17. Kanani DM, Ghosh R. A constant flux based mathematical model for predicting permeate flux decline in constant pressure protein ultrafiltration. J Membr Sci. 2007;290(1–2):207-15.

18. Belfort G, Davis RH, Zydney AL. The behavior of suspensions and macromolecular solutions in crossflow microfiltration. J Membr Sci. 1994;96(1):1-58.

19. Jaspe J, Hagen SJ. Do Protein Molecules Unfold in a Simple Shear Flow? Biophys J. 2006;91(9):3415-24.

20. Callahan DJ, Stanley B, Li YL. Control of Protein Particle Formation During Ultrafiltration/Diafiltration Through Interfacial Protection. J Pharm Sci. 2014;103(3):862-9.

21. Bee JS, Stevenson JL, Mehta B, Svitel J, Pollastrini J, Platz R, et al. Response of a concentrated monoclonal antibody formulation to high shear. Biotechnol Bioeng. 2009;103(5):936-43.

22. Dizon-Maspat J, Bourret J, D'Agostini A, Li F. Single pass tangential flow filtration to debottleneck downstream processing for therapeutic antibody production. Biotechnol Bioeng. 2012;109(4):962-70.

23. Eppler A, Weigandt M, Schulze S, Hanefeld A, Bunjes H. Comparison of different protein concentration techniques within preformulation development. International Journal of Pharmaceutics. 2011;421(1):120-9.

24. SpectrumLabs. Modified PES Fiber Modules 2014 [Available from: http://www.spectrumlabs.com/filtration/mPES.html.

25. Ross PD, Minton AP. HARD QUASI-SPHERICAL MODEL FOR VISCOSITY OF HEMOGLOBIN SOLUTIONS. Biochem Biophys Res Commun. 1977;76(4):971-6.

26. Burckbuchler V, Mekhloufi G, Giteau AP, Grossiord JL, Huille S, Agnely F. Rheological and syringeability properties of highly concentrated human polyclonal immunoglobulin solutions. Eur J Pharm Biopharm. 2010;76(3):351-6.

27. Yadav S, Liu J, Shire SJ, Kalonia DS. Specific Interactions in High Concentration Antibody Solutions Resulting in High Viscosity. J Pharm Sci. 2010;99(3):1152-68.

28. Connolly Brian D, Petry C, Yadav S, Demeule B, Ciaccio N, Moore Jamie MR, et al. Weak Interactions Govern the Viscosity of Concentrated Antibody Solutions: High-Throughput Analysis Using the Diffusion Interaction Parameter. Biophys J. 2012;103(1):69-78.

29. Yadav S, Shire SJ, Kalonia DS. Factors Affecting the Viscosity in High Concentration Solutions of Different Monoclonal Antibodies. J Pharm Sci. 2010;99(12):4812-29.

30. Yadav S, Laue TM, Kalonia DS, Singh SN, Shire SJ. The Influence of Charge Distribution on Self-Association and Viscosity Behavior of Monoclonal Antibody Solutions. Mol Pharmaceutics. 2012;9(4):791-802.

31. Roberts CJ, Blanco MA. Role of Anisotropic Interactions for Proteins and Patchy Nano-particles. The Journal of Physical Chemistry B. 2014.

32. Yearley Eric J, Godfrin Paul D, Perevozchikova T, Zhang H, Falus P, Porcar L, et al. Observation of Small Cluster Formation in Concentrated Monoclonal Antibody Solutions and Its Implications to Solution Viscosity. Biophys J. 2014;106(8):1763-70.

33. Chari R, Jerath K, Badkar AV, Kalonia DS. Long- and Short-Range Electrostatic Interactions Affect the Rheology of Highly Concentrated Antibody Solutions. Pharm Res. 2009;26(12):2607-18.

34. Moody TP, Kingsbury JS, Durant JA, Wilson TJ, Chase SF, Laue TM. Valence and anion binding of bovine ribonuclease A between pH 6 and 8. Analytical biochemistry. 2005;336(2):243-52.

35. Salis A, Bostrom M, Medda L, Cugia F, Barse B, Parsons DF, et al. Measurements and theoretical interpretation of points of zero charge/potential of BSA protein. Langmuir 2011;27(18):11597-604.

36. Du W, Klibanov AM. Hydrophobic salts markedly diminish viscosity of concentrated protein solutions. Biotechnol Bioeng. 2011;108(3):632-6.

37. Guo Z, Chen A, Nassar R, Helk B, Mueller C, Tang Y, et al. Structure-Activity Relationship for Hydrophobic Salts as Viscosity-Lowering Excipients for Concentrated Solutions of Monoclonal Antibodies. Pharm Res. 2012;29(11):3102-9.

38. Kheddo P, Tracka M, Armer J, Dearman RJ, Uddin S, van der Walle CF, et al. The effect of arginine glutamate on the stability of monoclonal antibodies in solution. International journal of pharmaceutics. 2014;473(1–2):126-33.

39. Fukuda M, Kameoka D, Torizawa T, Saitoh S, Yasutake M, Imaeda Y, et al. Thermodynamic and Fluorescence Analyses to Determine Mechanisms of IgG1 Stabilization and Destabilization by Arginine. Pharm Res. 2014;31(4):992-1001.

40. Fukuda M, Moriyama C, Yamazaki T, Imaeda Y, Koga A. Quantitative Correlation between Viscosity of Concentrated MAb Solutions and Particle Size Parameters Obtained from Small-Angle X-ray Scattering. Pharmaceutical research. 2015:1-10.

41. Inoue N, Takai E, Arakawa T, Shiraki K. Specific Decrease in Solution Viscosity of Antibodies by Arginine for Therapeutic Formulations. Mol Pharmaceutics. 2014;11(6):1889-96.

42. Inoue N, Takai E, Arakawa T, Shiraki K. Arginine and lysine reduce the high viscosity of serum albumin solutions for pharmaceutical injection. J Biosci Bioeng. 2014;117(5):539-43.

43. Binabaji E, Ma J, Zydney A. Intermolecular Interactions and the Viscosity of Highly Concentrated Monoclonal Antibody Solutions. Pharm Res. 2015;32(9):3102-9.

44. Chen B, Bautista R, Yu K, Zapata GA, Mulkerrin MG, Chamow SM. Influence of histidine on the stability and physical properties of a fully human antibody in aqueous and solid forms. Pharm Res. 2003;20(12):1952-60.

45. Scherer TM. The Role of Cosolute-Protein Interactions in the Dissociation of Monoclonal Antibody Clusters. The Journal of Physical Chemistry B. 2015.

46. Heyda J, Mason PE, Jungwirth P. Attractive Interactions between Side Chains of Histidine-Histidine and Histidine-Arginine-Based Cationic Dipeptides in Water. J Phys Chem B. 2010;114(26):8744-9.

47. Johnston KP, Maynard JA, Truskett TM, Borwankar AU, Miller MA, Wilson BK, et al. Concentrated Dispersions of Equilibrium Protein Nanoclusters that Reversibly Dissociate into Active Monomers. ACS Nano. 2012;6(2):1357-69.

48. Borwankar AU, Dinin AK, Laber JR, Twu A, Wilson BK, Maynard JA, et al. Tunable equilibrium nanocluster dispersions at high protein concentrations. Soft Matter. 2013;9(6):1766.

49. Lekkerkerker HNW, Tuinier R. Colloids and the Depletion Interaction. 2011 ed. Dordrecht: Springer; 2011 May 12, 2011. 268 p.

50. Asakura S, Oosawa F. Interaction between particles suspended in solutions of macromolecules. Journal of Polymer Science. 1958;33(126):183-92.

51. Shen VK, Cheung JK, Errington JR, Truskett TM. Coarse-Grained Strategy for Modeling Protein Stability in Concentrated Solutions II: Phase Behavior. Biophys J. 2006;90:1949-60.

52. Shen VK, Cheung JK, Errington JR, Truskett TM. Insights into crowding effects on protein stability from a coarse-grained model. J Biomech Eng. 2009;131(7):071002.

53. Schneider CA, Rasband WS, Eliceiri KW. NIH Image to ImageJ: 25 years of image analysis. Nat Meth. 2012;9(7):671-5.

54. Jezek J, Rides M, Derham B, Moore J, Cerasoli E, Simler R, et al. Viscosity of concentrated therapeutic protein compositions. Adv Drug Deliv Rev. 2011;63(13):1107-17.

55. Heimenz PC, Rajagopalan R. Principles of Colloid and Surface Chemistry. 3rd ed. New York: Marcel Dekker, Inc.; 1997.

56. Monkos K, Turczynski B. A comparative study on viscosity of human, bovine and pig IgG immunoglobulins in aqueous solutions. International Journal of Biological Macromolecules. 1999;26(2–3):155-9.

57. Sablani SS, Goosen MFA, Al-Belushi R, Wilf M. Concentration polarization in ultrafiltration and reverse osmosis: a critical review. Desalination. 2001;141(3):269-89.

58. Cooper AR, editor. Ultrafiltration membranes and applications. New York: Plenum Press; 1979.

59. McCabe W, Smith J, Harriot P. Unit Operations of Chemical Engineering. 7th ed. Columbus: McGraw-Hill Education; 2004.

60. Subramani A, Kim S, Hoek EMV. Pressure, flow, and concentration profiles in open and spacer-filled membrane channels. J Membr Sci. 2006;277(1–2):7-17.

61. Palacio L, Ho C-C, Zydney AL. Application of a pore-blockage—Cake-filtration model to protein fouling during microfiltration. Biotechnol Bioeng. 2002;79(3):260-70.

62. Grimaldo M, Roosen-Runge F, Zhang F, Seydel T, Schreiber F. Diffusion and Dynamics of γ-Globulin in Crowded Aqueous Solutions. J Phys Chem B. 2014;118(25):7203-9.

63. Pathak Jai A, Sologuren Rumi R, Narwal R. Do Clustering Monoclonal Antibody Solutions Really Have a Concentration Dependence of Viscosity? Biophys J. 2013;104(4):913-23.

64. Lilyestrom WG, Yadav S, Shire SJ, Scherer TM. Monoclonal Antibody Self-Association, Cluster Formation, and Rheology at High Concentrations. J Phys Chem B. 2013;117(21):6373-84.

65. Yearley EJ, Zarraga IE, Shire SJ, Scherer TM, Gokarn Y, Wagner NJ, et al. Small-Angle Neutron Scattering Characterization of Monoclonal Antibody Conformations and Interactions at High Concentrations. Biophys J. 2013;105(3):720-31.

66. Yadav S, Sreedhara A, Kanai S, Liu J, Lien S, Lowman H, et al. Establishing a Link Between Amino Acid Sequences and Self-Associating and Viscoelastic Behavior of Two Closely Related Monoclonal Antibodies. Pharm Res. 2011;28(7):1750-64.

67. Karow AR, Bahrenburg S, Garidel P. Buffer capacity of biologics--from buffer salts to buffering by antibodies. Biotechnol Prog. 2013;29(2):480-92.

68. Miao F, Velayudhan A, DiBella E, Shervin J, Felo M, Teeters M, et al. Theoretical analysis of excipient concentrations during the final ultrafiltration/diafiltration step of therapeutic antibody. Biotechnol Prog. 2009;25(4):964-72.

69. Salinas BA, Sathish HA, Bishop SM, Harn N, Carpenter JF, Randolph TW. Understanding and Modulating Opalescence and Viscosity in a Monoclonal Antibody Formulation. J Pharm Sci. 2010;99(1):82-92.

70. Péter F, Lionel P, Emiliano F, Wei-Ren C, Antonio F, Kunlun H, et al. Distinguishing the monomer to cluster phase transition in concentrated lysozyme solutions by

studying the temperature dependence of the short-time dynamics. Journal of Physics: Condensed Matter. 2012;24(6):064114.

71. Porcar L, Falus P, Chen W-R, Faraone A, Fratini E, Hong K, et al. Formation of the Dynamic Clusters in Concentrated Lysozyme Protein Solutions. J Phys Chem Lett. 2009;1(1):126-9.

72. Liu Y, Porcar L, Chen J, Chen W-R, Falus P, Faraone A, et al. Lysozyme Protein Solution with an Intermediate Range Order Structure. J Phys Chem B. 2010;115(22):7238-47.

73. Lonetti B, Fratini E, Chen SH, Baglioni P. Viscoelastic and small angle neutron scattering studies of concentrated protein solutions. Physical Chemistry Chemical Physics. 2004;6(7):1388-95.

74. Soraruf D, Roosen-Runge F, Grimaldo M, Zanini F, Schweins R, Seydel T, et al. Protein cluster formation in aqueous solution in the presence of multivalent metal ions - a light scattering study. Soft Matter. 2014;10(6):894-902.

75. Pan WC, Vekilov PG, Lubchenko V. Origin of Anomalous Mesoscopic Phases in Protein Solutions. J Phys Chem B. 2010;114(22):7620-30.

76. Li Y, Lubchenko V, Vekilov PG. The use of dynamic light scattering and Brownian microscopy to characterize protein aggregation. Review of Scientific Instruments. 2011;82(5):-.

77. Chaudhri A, Zarraga IE, Kamerzell TJ, Brandt JP, Patapoff TW, Shire SJ, et al. Coarse-Grained Modeling of the Self-Association of Therapeutic Monoclonal Antibodies. J Phys Chem B. 2012;116(28):8045-57.

78. Godfrin PD, Castañeda-Priego R, Liu Y, Wagner NJ. Intermediate range order and structure in colloidal dispersions with competing interactions. The Journal of Chemical Physics. 2013;139(15):-.

79. Godfrin PD, Valadez-Perez NE, Castaneda-Priego R, Wagner NJ, Liu Y. Generalized phase behavior of cluster formation in colloidal dispersions with competing interactions. Soft Matter. 2014.

80. Chaudhri A, Zarraga IE, Yadav S, Patapoff TW, Shire SJ, Voth GA. The Role of Amino Acid Sequence in the Self-Association of Therapeutic Monoclonal Antibodies: Insights from Coarse-Grained Modeling. J Phys Chem B. 2013;117(5):1269-79.

81. Castellanos MM, Pathak JA, Colby RH. Both protein adsorption and aggregation contribute to shear yielding and viscosity increase in protein solutions. Soft Matter. 2014;10(1):122-31.

82. Zarraga IE, Taing R, Zarzar J, Luoma J, Hsiung J, Patel A, et al. High shear rheology and anisotropy in concentrated solutions of monoclonal antibodies. J Pharm Sci. 2013;102(8):2538-49.

83. Allmendinger A, Fischer S, Huwyler J, Mahler H-C, Schwarb E, Zarraga IE, et al. Rheological characterization and injection forces of concentrated protein formulations: An alternative predictive model for non-Newtonian solutions. Eur J Pharm Biopharm. 2014;87(2):318-28.

84. Yadav S, Shire SJ, Kalonia DS. Viscosity behavior of high-concentration monoclonal antibody solutions: Correlation with interaction parameter and electroviscous effects. J Pharm Sci. 2012;101(3):998-1011.

85. Schmit JD, He F, Mishra S, Ketchem RR, Woods CE, Kerwin BA. Entanglement Model of Antibody Viscosity. J Phys Chem B. 2014;118(19):5044-9.

86. Štulík K, Pacáková V, Tichá M. Some potentialities and drawbacks of contemporary size-exclusion chromatography. Journal of Biochemical and Biophysical Methods. 2003;56(1–3):1-13.

87. Shukla D, Trout BL. Interaction of Arginine with Proteins and the Mechanism by Which It Inhibits Aggregation. J Phys Chem B. 2010;114(42):13426-38.

88. Fukuda M, Moriyama C, Yamazaki T, Imaeda Y, Koga A. Quantitative Correlation between Viscosity of Concentrated MAb Solutions and Particle Size Parameters Obtained from Small-Angle X-ray Scattering. Pharm Res. 2015;32(12):3803-12.

89. Shukla D, Trout BL. Preferential Interaction Coefficients of Proteins in Aqueous Arginine Solutions and Their Molecular Origins. J Phys Chem B. 2011;115(5):1243-53.

90. Arakawa T, Ejima D, Tsumoto K, Obeyama N, Tanaka Y, Kita Y, et al. Suppression of protein interactions by arginine: A proposed mechanism of the arginine effects. Biophys Chem. 2007;127(1–2):1-8.

91. Hopp TP, Woods KR. Prediction of protein antigenic determinants from amino acid sequences. Proc Natl Acad Sci U S A. 1981;78(6):3824-8.

92. Du Q-S, Meng J-Z, Liao S-M, Huang R-B. Energies and physicochemical properties of cation–π interactions in biological structures. J Mol Graphics Modell. 2012;34:38-45.

93. Liao SM, Du QS, Meng JZ, Pang ZW, Huang RB. The multiple roles of histidine in protein interactions. Chem Cent J. 2013;7.

94. Jiang SY, Cao ZQ. Ultralow-Fouling, Functionalizable, and Hydrolyzable Zwitterionic Materials and Their Derivatives for Biological Applications. Adv Mater. 2010;22(9):920-32.

95. Xie G, Timasheff SN. The thermodynamic mechanism of protein stabilization by trehalose. Biophys Chem. 1997;64(1–3):25-43.

96. Arakawa T, Timasheff SN. Stabilization of protein structure by sugars. Biochemistry. 1982;21(25):6536-44.

97. Hassan PA, Rana S, Verma G. Making Sense of Brownian Motion: Colloid Characterization by Dynamic Light Scattering. Langmuir. 2014.

98. Filipe V, Hawe A, Jiskoot W. Critical Evaluation of Nanoparticle Tracking Analysis (NTA) by NanoSight for the Measurement of Nanoparticles and Protein Aggregates. Pharm Res. 2010;27(5):796-810.

99. Grimaldo M, Roosen-Runge F, Hennig M, Zanini F, Zhang FJ, Zamponi M, et al. Salt-Induced Universal Slowing Down of the Short-Time Self-Diffusion of a Globular Protein in Aqueous Solution. J Phys Chem Lett. 2015;6(13):2577-82.

100. Roosen-Runge F, Hennig M, Seydel T, Zhang F, Skoda MWA, Zorn S, et al. Protein diffusion in crowded electrolyte solutions. Biochim Biophys Acta, Proteins Proteomics. 2010;1804(1):68-75.

Chapter 6: Conclusions and Recommendations

6.1 CONCLUSIONS

6.1.1 Co-solute effects on protein-protein interactions and self-association probed by static structure

Static light scattering was used to quantify the effects of six ionic co-solutes on the attractive PPI strength and extent of self-association for two mAbs (mAb2 and mAb3) from low to high concentration (up to 230 mg/mL). For both mAbs, the PPI strength (quantified by the structure factor $S(0)/S(0)_{HS}$, $G_{22}/G_{22,HS}$, and Yukawa attraction strength K) and oligomer formation (oligomer mass ratio $m_{oligomer}/m_{monomer+dimer}$ and average cluster size $\langle N_c \rangle$) fit from the SLS scattering profiles were consistent with the mAb viscosity across all co-solute systems, with arginine and imidazole causing the largest reductions in both viscosity and attractive PPI strength. However, η_{rel} was more sensitive to nearly all of these experimental and model fit descriptors for mAb3 than mAb2, reflecting potential differences in the mAb packing (fractal dimension), possible formation of reversible oligomers, or dynamic factors (3, 5, 6) that were not considered. The influence of self-association on viscosity could be seen from the more universal correlation between both $<N_c>$ and the oligomer mass ratio with the viscosity across both mAbs. The mass ratio of oligomers to monomer and dimer emphasizes the larger oligomers much more than does $\langle N_c \rangle$, and also emphasizes the relative polydispersity, both of which will influence the mAb packing efficiency and relative viscosity in solution. The large effect of oligomerization on η_{rel} may be anticipated from theoretical self-association models for both Fab-Fab and/or Fab-Fc interactions (6-8).

6.1.2 Co-solute effects on PPI and self-association probed by length-scale dependent dynamic structure

Reproducible measurements of mAb2's diffusion at high concentration (up to 250 mg/mL) and high viscosities (up to ~200 cP) in a range of co-solute formulations (50 – 250 mM

Arg or NaCl, 1 M Im) were successfully achieved by FCS after optimization of experimental methods (via choice of slide passivation strategies, microscope focal depth and labeling strategy) to overcome the challenges associated with these conditions. The generalized Stokes-Einstein (GSE) relation was seen to break down for mAb2 with respect to the macroscopic viscosity, with the least viscous co-solute systems (1 M Imid and 250 mM Arg) showing the greatest negative deviation from the GSE relation. The breakdown was attributed to the use of the labeled mAb as a nanoprobe, resulting in measurement of the local microviscosity (11, 12). The greater deviation of the microviscosity from the macroscopic viscosity for the lowest viscosity systems was attributed to a combination of weaker PPI (seen from the smaller interaction parameter b from fits of D_0/D_s to the length-scale dependent viscosity (LDV) model) and reduced self-association (based on previous SLS measurements of oligomer mass ratios and average cluster sizes for the same mAb and co-solute formulations) (9) leading to smaller $r_p/R_{h,avg}$ probe size ratios. The more GSE-like scaling between D_0/D_s and the macroscopic viscosity for the viscous formulations (50 – 250 mM NaCl) was consistent with the LDV model, given the larger probe size as a consequence of the greater degree of self-association seen previously by SLS and SAXS (9, 10) for those systems.

6.1.3 Contrasting the influence of proline on the viscosity and stability of a highly concentrated mAb with other neutral osmolytes

In contrast to the ionic co-solutes investigated in chapters 2 and 3, the neutral osmolyte proline was found to reduce the viscosity and increase the stability (against aggregation) of a concentrated mAb in a pH-dependent manner, but with a lower molar efficacy than the ionic co-solutes. The reductions in viscosity and aggregation were not simply due to osmotic depletion, as two other neutral osmolytes, glycine and trehalose, raised both properties. The large dipole moment of proline's zwitterionic functionality, in combination with its pyrrolidine ring (which has been shown in simulations to preferentially interact with aromatic residues) may explain its

greater efficacy for reducing protein viscosity and aggregation relative to glycine and trehalose, These properties may allow proline to mitigate attractive electrostatic and hydrophobic interactions, similar to arginine and imidazole, which were shown in the previous chapter to reduce the solution viscosity and self-association by weakening the attractive PPI.

6.1.4 Improved TFF process performance from integration of low-viscosity formulation development

The 10x reduction in viscosity of a concentrated (250 mg/mL) mAb solution by the addition of histidine or imidazole translated to direct gains in the process performance for tangential flow ultrafiltration. The low viscosity histidine/imidazole formulation generated 2x – 3x higher membrane fluxes at high concentration relative to more conventional buffer formulations as well as maintained high protein stability during ultrafiltration despite the prolonged exposure of the mAb to high mechanical stress (high shear flow). The respective gains in process throughput and yield were determined to result from a significant increase in the protein gel concentration c_g and more uniform axial transmembrane pressure (TMP) and shear stress τ_w profiles, as a direct consequence of the weaker PPI and lower viscosities. The large increase in c_g of ~100 mg/mL enhanced the concentration-polarization back-diffusion at the membrane wall, leading to higher membrane fluxes and greater process capability (higher maximum achievable protein concentration). The smaller viscosities led to a reduction in the axial pressure drop ΔP leading to smaller and more uniform τ_w and TMP profiles, both which reduce the extent of protein aggregation and membrane fouling.

6.2 RECOMMENDATIONS AND FUTURE RESEARCH

6.2.1 Relating protein microstructure to viscosity to explain mAb-dependent PPI-viscosity correlations

The divergent viscosities seen for mAb2 and mAb3 as a function of PPI strength (chapter 1) indicates the confounding influence of additional factors beyond PPI strength on mAb

solution viscosity, and may explain the poor correlations between PPI indicators (such as B_{22} and k_D) and viscosity across different mAbs, as is commonly seen in the literature (14). The improved universality of the correlation between the apparent average oligomer size and oligomer mass ratio (determined from fits of the SLS data to the interacting hard sphere self-association model) suggests that self-association, which is influenced by the PPI attraction strength, also plays a significant role in determining the solution viscosity. It would therefore be of interest to extend the investigation of the mAb's biophysical behavior at high concentration (chapter 2, 3) to additional mAbs, and to attempt to derive a physical property that universally explains/predicts the solution viscosity across a variety of mAbs with different PPI profiles and self-association behavior. One factor that has not been investigated in much depth is the microstructure of the protein oligomer. Based on colloidal viscosity models, the viscosity is a strong function of the volume occupied by the solute. For the same mass concentration and oligomer aggregation numbers, the solution volume occupied by the protein may depend strongly on the oligomer microstructure. Future work may therefore investigate the combined influence of the microstructure, quantified by parameters such as the cluster fractal dimension, and the PPI strength and self-association on viscosity, to potentially arrive at a more universal correlation across all mAbs.

6.2.2 Decoupling the influence of hydrodynamic and thermodynamic interactions (PPI) on protein diffusion and viscosity

The structural and dynamic information obtained from SLS and FCS respectively can be used to better understand the collective dynamics of mAbs at high concentration, such as the collective diffusion coefficient D_c routinely measured by DLS. Furthermore, the viscosity, static structure and diffusion behavior of mAbs may be interpreted in the context of the generalized Stokes relation to attempt to decouple the effects of thermodynamic interactions (PPI) on the mAb's biophysical behavior at high concentration from those of the hydrodynamic interactions.

Both types of interactions may enhance or retard the mobility of the mAb, and will consequently influence both the solution viscosity and the mAb diffusive behavior. It would be of interest to compare the relative contributions of the two types of interactions to the mAb viscosity and diffusion at high concentration across different mAbs and co-solutes, to attempt to develop a more fundamental, general understanding of how each factor influences the macroscopic solution behavior of highly concentrated mAbs, and how they are in turn modified by the choice of formulations (co-solute, co-solute concentration, etc.).

6.2.3 Decoupling length-scale effects from PPI influence on mAb self-diffusion and microviscosity

While the length-scale dependent viscosity (LDV) model analysis of the retardation of the mAb self-diffusion (chapter 3) provides some insight into the effects of the PPI and surrounding protein microstructure on the local dynamics and microviscosities experienced by a diffusing mAb, the analysis is complicated by the reversible self-association of the mAb probe. As the microviscosity (defined by the diffusion retardation factor) is a function of both the PPI and length-scale dependent solution structure, uncertainty in the probe size (due to possible self-association) complicates the interpretation of the PPI strength from the LDV model. It would be of interest to attempt to further decouple the effects of PPI from (changing) probe sizes by using other non-associating probes with known size, such as eGFP (enhanced green fluorescent protein). The use of non-associating probes may also provide more insight into the polydispersity of the mAb solution, as the diffusion of these probes would not be complicated by the equilibrium exchange of the probe between monomer and various oligomer states during the duration of the diffusion measurements.

6.3 REFERENCES

1. Yearley EJ, Zarraga IE, Shire SJ, Scherer TM, Gokarn Y, Wagner NJ, et al. Small-Angle Neutron Scattering Characterization of Monoclonal Antibody Conformations and Interactions at High Concentrations. Biophys J. 2013;105(3):720-31.

2. Scherer TM, Liu J, Shire SJ, Minton AI. Intermolecular Interactions of IgG1 Monoclonal Antibodies at High Concentrations Characterized by Light Scattering. J Phys Chem B. 2010;114(40):12948-57.

3. Godfrin PD, Zarraga IE, Zarzar J, Porcar L, Falus P, Wagner NJ, et al. Effect of Hierarchical Cluster Formation on the Viscosity of Concentrated Monoclonal Antibody Formulations Studied by Neutron Scattering. J Phys Chem B. 2016;120(2):278-91.

4. Yearley Eric J, Godfrin Paul D, Perevozchikova T, Zhang H, Falus P, Porcar L, et al. Observation of Small Cluster Formation in Concentrated Monoclonal Antibody Solutions and Its Implications to Solution Viscosity. Biophys J. 2014;106(8):1763-70.

5. Wang W, Lilyestrom WG, Hu ZY, Scherer TM. Cluster Size and Quinary Structure Determine the Rheological Effects of Antibody Self-Association at High Concentrations. J Phys Chem B. 2018;122(7):2138-54.

6. Lilyestrom WG, Yadav S, Shire SJ, Scherer TM. Monoclonal Antibody Self-Association, Cluster Formation, and Rheology at High Concentrations. J Phys Chem B. 2013;117(21):6373-84.

7. Schmit JD, He F, Mishra S, Ketchem RR, Woods CE, Kerwin BA. Entanglement Model of Antibody Viscosity. J Phys Chem B. 2014;118(19):5044-9.

8. Kastelic M, Dill KA, Kalyuzhnyi YV, Vlachy V. Controlling the viscosities of antibody solutions through control of their binding sites. Journal of Molecular Liquids. 2017.

9. Hung JJ, Dear BJ, Karouta CA, Godfrin PD, Bollinger JA, Nieto MP, et al. Protein-Protein Interactions of Highly Concentrated Monoclonal Antibody Solutions via Static Light Scattering and Influence on the Viscosity. J Phys Chem B. (under review).

10. Dear BJ, Bollinger JA, Chowdhury A, Hung JJ, Wilks LR, Karouta CA, et al. X-Ray Scattering and Coarse-Grained Simulations for Protein-Protein Interactions of Monoclonal Antibodies. J Phys Chem B. (under preparation).

11. Nicoud L, Lattuada M, Lazzari S, Morbidelli M. Viscosity scaling in concentrated dispersions and its impact on colloidal aggregation. Physical Chemistry Chemical Physics. 2015;17(37):24392-402.

12. Kalwarczyk T, Sozanski K, Jakiela S, Wisniewska A, Kalwarczyk E, Kryszczuk K, et al. Length-scale dependent transport properties of colloidal and protein solutions for prediction of crystal nucleation rates. Nanoscale. 2014;6(17):10340-6.

13. Woldeyes MA, Calero-Rubio C, Furst EM, Roberts CJ. Predicting Protein Interactions of Concentrated Globular Protein Solutions Using Colloidal Models. J Phys Chem B. 2017;121(18):4756-67.

14. Connolly, Brian D.; Petry, C.; Yadav, S.; Demeule, B.; Ciaccio, N.; Moore, Jamie M. R.; Shire, Steven J.; Gokarn, Yatin R., Weak Interactions Govern the Viscosity of Concentrated Antibody Solutions: High-Throughput Analysis Using the Diffusion Interaction Parameter. Biophys. J. 2012, 103 (1), 69-78.

Bibliography

Ahrer K, Buchacher A, Iberer G, Jungbauer A. Effects of ultra-/diafiltration conditions on present aggregates in human immunoglobulin G preparations. J Membr Sci. 2006;274(1-2):108-15.

Allmendinger A, Fischer S, Huwyler J, Mahler H-C, Schwarb E, Zarraga IE, et al. Rheological characterization and injection forces of concentrated protein formulations: An alternative predictive model for non-Newtonian solutions. Eur J Pharm Biopharm. 2014;87(2):318-28.

Amend JP, Helgeson HC. Solubilities of the common L-α-amino acids as a function of temperature and solution pH. Pure Appl Chem. 1997;69(5):935-42.

Amin S, Barnett GV, Pathak JA, Roberts CJ, Sarangapani PS. Protein aggregation, particle formation, characterization & rheology. Current Opinion in Colloid & Interface Science. 2014;19(5):438-49.

Arakawa T, Ejima D, Tsumoto K, Obeyama N, Tanaka Y, Kita Y, et al. Suppression of protein interactions by arginine: A proposed mechanism of the arginine effects. Biophys Chem. 2007;127(1–2):1-8.

Arakawa T, Timasheff SN. Stabilization of protein structure by sugars. Biochemistry. 1982;21(25):6536-44.

Arakawa T, Timasheff SN. The stabilization of proteins by osmolytes. Biophys J. 1985;47(3):411-4.

Arora J, Hu Y, Esfandiary R, Sathish HA, Bishop SM, Joshi SB, et al. Charge-mediated Fab-Fc interactions in an IgG1 antibody induce reversible self-association, cluster formation, and elevated viscosity. mAbs. 2016;8(8):1561-74.

Asakura S, Oosawa F. Interaction between particles suspended in solutions of macromolecules. Journal of Polymer Science. 1958;33(126):183-92.

ASTRA 6 User's Guide. Santa Barbara, CA: Wyatt Technology Corporation; 2015.

Auton M, Bolen DW, Rosgen J. Structural thermodynamics of protein preferential solvation: Osmolyte solvation of proteins, aminoacids, and peptides. Proteins: Struct, Funct, Bioinf. 2008;73(4):802-13.

Auton M, Rösgen J, Sinev M, Holthauzen LMF, Bolen DW. Osmolyte effects on protein stability and solubility: A balancing act between backbone and side-chains. Biophys Chem. 2011;159(1):90-9.

Baek Y, Singh N, Arunkumar A, Borys M, Li ZJ, Zydney AL. Ultrafiltration behavior of monoclonal antibodies and Fc-fusion proteins: Effects of physical properties. Biotechnol Bioeng. 2017;114(9):2057-65.

Baek Y, Singh N, Arunkumar A, Borys M, Li ZJ, Zydney AL. Ultrafiltration behavior of monoclonal antibodies and Fc-fusion proteins: Effects of physical properties. Biotechnol Bioeng. 2017;114(9):2057-65.

Balbo J, Mereghetti P, Herten D-P, Wade Rebecca C. The Shape of Protein Crowders is a Major Determinant of Protein Diffusion. Biophys J. 2013;104(7):1576-84.

Banachowicz E, Patkowski A, Meier G, Klamecka K, Gapiński J. Successful FCS Experiment in Nonstandard Conditions. Langmuir. 2014;30(29):8945-55.

Banchio AJ, Nägele G. Short-time transport properties in dense suspensions: From neutral to charge-stabilized colloidal spheres. The Journal of Chemical Physics. 2008;128(10):104903.

Banks DS, Fradin C. Anomalous Diffusion of Proteins Due to Molecular Crowding. Biophys J. 2005;89(5):2960-71.

Bauer KC, Suhm S, Wöll AK, Hubbuch J. Impact of additives on the formation of protein aggregates and viscosity in concentrated protein solutions. International Journal of Pharmaceutics. 2017;516(1):82-90.

Baumann P, Schermeyer M-T, Burghardt H, Dürr C, Gärtner J, Hubbuch J. Prediction and characterization of the stability enhancing effect of the Cherry-Tag™ in highly concentrated protein solutions by complex rheological measurements and MD simulations. International Journal of Pharmaceutics. 2017;531(1):360-71.

Bee JS, Stevenson JL, Mehta B, Svitel J, Pollastrini J, Platz R, et al. Response of a concentrated monoclonal antibody formulation to high shear. Biotechnol Bioeng. 2009;103(5):936-43.

Belfort G, Davis RH, Zydney AL. The behavior of suspensions and macromolecular solutions in crossflow microfiltration. J Membr Sci. 1994;96(1):1-58.

Bellara SR, Cui ZF. A Maxwell-Stefan approach to modelling the cross-flow ultrafiltration of protein solutions in tubular membranes. Chemical Engineering Science. 1998;53(12):2153-66.

Binabaji E, Ma J, Rao S, Zydney AL. Theoretical analysis of the ultrafiltration behavior of highly concentrated protein solutions. J Membr Sci. 2015:JMS151044.

Binabaji E, Ma J, Zydney A. Intermolecular Interactions and the Viscosity of Highly Concentrated Monoclonal Antibody Solutions. Pharm Res. 2015;32(9):3102-9.

Blanco MA, Perevozchikova T, Martorana V, Manno M, Roberts CJ. Protein–Protein Interactions in Dilute to Concentrated Solutions: α-Chymotrypsinogen in Acidic Conditions. J Phys Chem B. 2014;118(22):5817-31.

Blanco MA, Sahin E, Li Y, Roberts CJ. Reexamining protein–protein and protein–solvent interactions from Kirkwood-Buff analysis of light scattering in multi-component solutions. The Journal of Chemical Physics. 2011;134(22):225103.

Blanco MA, Sahin E, Robinson AS, Roberts CJ. Coarse-Grained Model for Colloidal Protein Interactions, B-22, and Protein Cluster Formation. J Phys Chem B. 2013;117(50):16013-28.

Blümmel J, Perschmann N, Aydin D, Drinjakovic J, Surrey T, Lopez-Garcia M, et al. Protein repellent properties of covalently attached PEG coatings on nanostructured SiO2-based interfaces. Biomaterials. 2007;28(32):4739-47.

Bolton GR, Boesch AW, Basha J, LaCasse DP, Kelley BD, Acharya H. Effect of protein and solution properties on the donnan effect during the ultrafiltration of proteins. Biotechnol Prog. 2011;27(1):140-52.

Borwankar AU, Dear BJ, Twu A, Hung JJ, Dinin AK, Wilson BK, et al. Viscosity Reduction of a Concentrated Monoclonal Antibody with Arginine·HCl and Arginine·Glutamate. Ind Eng Chem Res. 2016;55(43):11225-34.

Borwankar AU, Dinin AK, Laber JR, Twu A, Wilson BK, Maynard JA, et al. Tunable equilibrium nanocluster dispersions at high protein concentrations. Soft Matter. 2013;9(6):1766.

Braun MK, Grimaldo M, Roosen-Runge F, Hoffmann I, Czakkel O, Sztucki M, et al. Crowding-Controlled Cluster Size in Concentrated Aqueous Protein Solutions: Structure, Self- and Collective Diffusion. J Phys Chem Lett. 2017;8(12):2590-6.

Bucciarelli S, Casal-Dujat L, De Michele C, Sciortino F, Dhont J, Bergenholtz J, et al. Unusual Dynamics of Concentration Fluctuations in Solutions of Weakly Attractive Globular Proteins. J Phys Chem Lett. 2015;6(22):4470-4.

Bucciarelli S, Myung JS, Farago B, Das S, Vliegenthart GA, Holderer O, et al. Dramatic influence of patchy attractions on short-time protein diffusion under crowded conditions. Science Advances. 2016;2(12).

Buck PM, Chaudhri A, Kumar S, Singh SK. Highly Viscous Antibody Solutions Are a Consequence of Network Formation Caused by Domain-Domain Electrostatic Complementarities: Insights from Coarse-Grained Simulations. Mol Pharmaceutics. 2015;12(1):127-39.

Burckbuchler V, Mekhloufi G, Giteau AP, Grossiord JL, Huille S, Agnely F. Rheological and syringeability properties of highly concentrated human polyclonal immunoglobulin solutions. Eur J Pharm Biopharm. 2010;76(3):351-6.

Busch DJ, Houser JR, Hayden CC, Sherman MB, Lafer EM, Stachowiak JC. Intrinsically disordered proteins drive membrane curvature. Nature Communications. 2015;6:7875.

Busch S, Lorenz CD, Taylor J, Pardo LC, McLain SE. Short-Range Interactions of Concentrated Proline in Aqueous Solution. J Phys Chem B. 2014;118(49):14267-77.

Calero-Rubio C, Ghosh R, Saluja A, Roberts CJ. Predicting protein-protein interactions of concentrated antibody solutions using dilute solution data and coarse-grained molecular models. J Pharm Sci. 2017.

Calero-Rubio C, Saluja A, Roberts CJ. Coarse-Grained Antibody Models for "Weak" Protein-Protein Interactions from Low to High Concentrations. J Phys Chem B. 2016;120(27):6592-605.

Callahan DJ, Stanley B, Li YL. Control of Protein Particle Formation During Ultrafiltration/Diafiltration Through Interfacial Protection. J Pharm Sci. 2014;103(3):862-9.

Cardinaux F, Zaccarelli E, Stradner A, Bucciarelli S, Farago B, Egelhaaf SU, et al. Cluster-Driven Dynamical Arrest in Concentrated Lysozyme Solutions. J Phys Chem B. 2011;115(22):7227-37.

Casey C, Gallos T, Alekseev Y, Ayturk E, Pearl S. Protein concentration with single-pass tangential flow filtration (SPTFF). J Membr Sci. 2011;384(1-2):82-8.

Castellanos MM, Clark NJ, Watson MC, Krueger S, McAuley A, Curtis JE. Role of Molecular Flexibility and Colloidal Descriptions of Proteins in Crowded Environments from Small-Angle Scattering. J Phys Chem B. 2016;120(49):12511-8.

Castellanos MM, Pathak JA, Colby RH. Both protein adsorption and aggregation contribute to shear yielding and viscosity increase in protein solutions. Soft Matter. 2014;10(1):122-31.

Chandradoss SD, Haagsma AC, Lee YK, Hwang J-H, Nam J-M, Joo C. Surface Passivation for Single-molecule Protein Studies. Journal of Visualized Experiments : JoVE. 2014(86):50549.

Chang BS, inventor; Integritybio Inc., assignee. Protein formulations containing amino acids patent WO2013063510 A1. 2013.

Chari R, Jerath K, Badkar AV, Kalonia DS. Long- and Short-Range Electrostatic Interactions Affect the Rheology of Highly Concentrated Antibody Solutions. Pharm Res. 2009;26(12):2607-18.

Chaudhri A, Zarraga IE, Kamerzell TJ, Brandt JP, Patapoff TW, Shire SJ, et al. Coarse-Grained Modeling of the Self-Association of Therapeutic Monoclonal Antibodies. J Phys Chem B. 2012;116(28):8045-57.

Chaudhri A, Zarraga IE, Yadav S, Patapoff TW, Shire SJ, Voth GA. The Role of Amino Acid Sequence in the Self-Association of Therapeutic Monoclonal Antibodies: Insights from Coarse-Grained Modeling. J Phys Chem B. 2013;117(5):1269-79.

Chaudhuri R, Cheng Y, Middaugh CR, Volkin D. High-Throughput Biophysical Analysis of Protein Therapeutics to Examine Interrelationships Between Aggregate Formation and Conformational Stability. AAPS J. 2014;16(1):48-64.

Chen B, Bautista R, Yu K, Zapata GA, Mulkerrin MG, Chamow SM. Influence of histidine on the stability and physical properties of a fully human antibody in aqueous and solid forms. Pharm Res. 2003;20(12):1952-60.

Chow C-K, Allan BW, Chai Q, Atwell S, Lu J. Therapeutic Antibody Engineering To Improve Viscosity and Phase Separation Guided by Crystal Structure. Mol Pharmaceutics. 2016;13(3):915-23.

Chowdhury PK. Fluorescence Correlation Spectroscopy: A Brief Review of Techniques and Applications to Biomolecules and Biosystems. Journal of Proteins & Proteomics. 2011;2(2):145-69.

Cichocki B, Felderhof BU. Sedimentation and self-diffusion in suspensions of spherical particles. Physica A: Statistical Mechanics and its Applications. 1989;154(2):213-32.

Connolly Brian D, Petry C, Yadav S, Demeule B, Ciaccio N, Moore Jamie MR, et al. Weak Interactions Govern the Viscosity of Concentrated Antibody Solutions: High-Throughput Analysis Using the Diffusion Interaction Parameter. Biophys J. 2012;103(1):69-78.

Cooper AR, editor. Ultrafiltration membranes and applications. New York: Plenum Press; 1979.

Corbett D, Hebditch M, Keeling R, Ke P, Ekizoglou S, Sarangapani P, et al. Coarse-Grained Modeling of Antibodies from Small-Angle Scattering Profiles. J Phys Chem B. 2017;121(35):8276-90.

Cromwell MEM, Hilario E, Jacobson F. Protein aggregation and bioprocessing. AAPS J. 2006;8(3):E572-E9.

Dear BJ, Bollinger JA, Chowdhury A, Hung JJ, Wilks LR, Karouta CA, et al. X-Ray Scattering and Coarse-Grained Simulations for Protein-Protein Interactions of Monoclonal Antibodies. J Phys Chem B. (under preparation).

Dear BJ, Hung JJ, Truskett TM, Johnston KP. Contrasting the Influence of Cationic Amino Acids on the Viscosity and Stability of a Highly Concentrated Monoclonal Antibody. Pharm Res. 2017;34(1):193-207.

Dharmaraj VL, Godfrin PD, Liu Y, Hudson SD. Rheology of clustering protein solutions. Biomicrofluidics. 2016;10(4):043509.

Dizon-Maspat J, Bourret J, D'Agostini A, Li F. Single pass tangential flow filtration to debottleneck downstream processing for therapeutic antibody production. Biotechnol Bioeng. 2012;109(4):962-70.

Du Q-S, Meng J-Z, Liao S-M, Huang R-B. Energies and physicochemical properties of cation–π interactions in biological structures. J Mol Graphics Modell. 2012;34:38-45.

Du W, Klibanov AM. Hydrophobic salts markedly diminish viscosity of concentrated protein solutions. Biotechnol Bioeng. 2011;108(3):632-6.

Engelke H, Dorn I, Radler JO. Diffusion and molecular binding in crowded vesicle solutions measured by fluorescence correlation spectroscopy. Soft Matter. 2009;5(21):4283-9.

Eppler A, Weigandt M, Schulze S, Hanefeld A, Bunjes H. Comparison of different protein concentration techniques within preformulation development. International Journal of Pharmaceutics. 2011;421(1):120-9.

Esfandiary R, Hayes DB, Parupudi A, Casas-finet J, Bai S, Samra HS, et al. A Systematic Multitechnique Approach for Detection and Characterization of Reversible Self-Association during Formulation Development of Therapeutic Antibodies. J Pharm Sci. 2013;102(1):62-72.

Esfandiary R, Parupudi A, Casas-Finet J, Gadre D, Sathish H. Mechanism of Reversible Self-Association of a Monoclonal Antibody: Role of Electrostatic and Hydrophobic Interactions. J Pharm Sci. 2015;104(2):577-86.

Falus P, Porcar L, Fratini E, Chen W-R, Faraone A, Hong K, et al. Distinguishing the monomer to cluster phase transition in concentrated lysozyme solutions by studying the temperature dependence of the short-time dynamics. Journal of Physics: Condensed Matter. 2012;24(6):064114.

Fernandez C, Minton AP. Automated measurement of the static light scattering of macromolecular solutions over a broad range of concentrations. Analytical biochemistry. 2008;381(2):254-7.

Fesinmeyer RM, Hogan S, Saluja A, Brych S, Kras E, Narhi L, et al. Effect of Ions on Agitation- and Temperature-Induced Aggregation Reactions of Antibodies. Pharm Res. 2009;26(4):903-13.

Filipe V, Hawe A, Jiskoot W. Critical Evaluation of Nanoparticle Tracking Analysis (NTA) by NanoSight for the Measurement of Nanoparticles and Protein Aggregates. Pharm Res. 2010;27(5):796-810.

Fine BM, Lomakin A, Ogun OO, Benedek GB. Static structure factor and collective diffusion of globular proteins in concentrated aqueous solution. The Journal of Chemical Physics. 1996;104(1):326-35.

Fukuda M, Kameoka D, Torizawa T, Saitoh S, Yasutake M, Imaeda Y, et al. Thermodynamic and Fluorescence Analyses to Determine Mechanisms of IgG1 Stabilization and Destabilization by Arginine. Pharm Res. 2014;31(4):992-1001.

Fukuda M, Moriyama C, Yamazaki T, Imaeda Y, Koga A. Quantitative Correlation between Viscosity of Concentrated MAb Solutions and Particle Size Parameters Obtained from Small-Angle X-ray Scattering. Pharm Res. 2015;32(12):3803-12.

Fukuda M, Watanabe A, Hayasaka A, Muraoka M, Hori Y, Yamazaki T, et al. Small-scale screening method for low-viscosity antibody solutions using small-angle X-ray scattering. Eur J Pharm Biopharm. 2017;112:132-7.

Geoghegan JC, Fleming R, Damschroder M, Bishop SM, Sathish HA, Esfandiary R. Mitigation of reversible self-association and viscosity in a human IgG1 monoclonal antibody by rational, structure-guided Fv engineering. mAbs. 2016;8(5):941-50.

Ghosh R, Calero-Rubio C, Saluja A, Roberts CJ. Relating protein-protein interactions and aggregation rates from low to high concentrations. J Pharm Sci. 2016;105(3):1086-96.

Godfrin PD, Castañeda-Priego R, Liu Y, Wagner NJ. Intermediate range order and structure in colloidal dispersions with competing interactions. The Journal of Chemical Physics. 2013;139(15):-.

Godfrin PD, Hudson SD, Hong K, Porcar L, Falus P, Wagner NJ, et al. Short-Time Glassy Dynamics in Viscous Protein Solutions with Competing Interactions. Phys Rev Lett. 2015;115(22):228302.

Godfrin PD, Valadez-Perez NE, Castaneda-Priego R, Wagner NJ, Liu Y. Generalized phase behavior of cluster formation in colloidal dispersions with competing interactions. Soft Matter. 2014.

Godfrin PD, Zarraga IE, Zarzar J, Porcar L, Falus P, Wagner NJ, et al. Effect of Hierarchical Cluster Formation on the Viscosity of Concentrated Monoclonal Antibody Formulations Studied by Neutron Scattering. J Phys Chem B. 2016;120(2):278-91.

Grimaldo M, Roosen-Runge F, Hennig M, Zanini F, Zhang FJ, Zamponi M, et al. Salt-Induced Universal Slowing Down of the Short-Time Self-Diffusion of a Globular Protein in Aqueous Solution. J Phys Chem Lett. 2015;6(13):2577-82.

Grimaldo M, Roosen-Runge F, Zhang F, Seydel T, Schreiber F. Diffusion and Dynamics of γ-Globulin in Crowded Aqueous Solutions. J Phys Chem B. 2014;118(25):7203-9.

Grünberger A, Lai P-K, Blanco MA, Roberts CJ. Coarse-Grained Modeling of Protein Second Osmotic Virial Coefficients: Sterics and Short-Ranged Attractions. J Phys Chem B. 2013;117(3):763-70.

Guo Z, Chen A, Nassar R, Helk B, Mueller C, Tang Y, et al. Structure-Activity Relationship for Hydrophobic Salts as Viscosity-Lowering Excipients for Concentrated Solutions of Monoclonal Antibodies. Pharm Res. 2012;29(11):3102-9.

Haque I, Singh R, Moosavi-Movahedi AA, Ahmad F. Effect of polyol osmolytes on ΔGD, the Gibbs energy of stabilisation of proteins at different pH values. Biophys Chem. 2005;117(1):1-12.

Hassan PA, Rana S, Verma G. Making Sense of Brownian Motion: Colloid Characterization by Dynamic Light Scattering. Langmuir. 2014.

He F, Woods C, Litowski J, Roschen L, Gadgil H, Razinkov V, et al. Effect of Sugar Molecules on the Viscosity of High Concentration Monoclonal Antibody Solutions. Pharm Res. 2011;28(7):1552-60.

Heimenz PC, Rajagopalan R. Principles of Colloid and Surface Chemistry. 3rd ed. New York: Marcel Dekker, Inc.; 1997.

Heinen M, Zanini F, Roosen-Runge F, Fedunova D, Zhang F, Hennig M, et al. Viscosity and diffusion: crowding and salt effects in protein solutions. Soft Matter. 2012;8(5):1404-19.

Heyda J, Mason PE, Jungwirth P. Attractive Interactions between Side Chains of Histidine-Histidine and Histidine-Arginine-Based Cationic Dipeptides in Water. J Phys Chem B. 2010;114(26):8744-9.

Holyst R, Bielejewska A, Szymanski J, Wilk A, Patkowski A, Gapinski J, et al. Scaling form of viscosity at all length-scales in poly(ethylene glycol) solutions studied by fluorescence correlation spectroscopy and capillary electrophoresis. Physical Chemistry Chemical Physics. 2009;11(40):9025-32.

Hopp TP, Woods KR. Prediction of protein antigenic determinants from amino acid sequences. Proc Natl Acad Sci U S A. 1981;78(6):3824-8.

Hoppe T, Minton AP. Incorporation of hard and soft protein-protein interactions into models for crowding effects in binary and ternary protein mixtures: Comparison of approximate analytical solutions with numerical simulation. J Phys Chem B. 2016;120(46):11866-72.

Horn FM, Richtering W, Bergenholtz J, Willenbacher N, Wagner NJ. Hydrodynamic and Colloidal Interactions in Concentrated Charge-Stabilized Polymer Dispersions. Journal of Colloid and Interface Science. 2000;225(1):166-78.

Houser JR, Busch DJ, Bell DR, Li B, Ren P, Stachowiak JC. The impact of physiological crowding on the diffusivity of membrane bound proteins. Soft Matter. 2016;12(7):2127-34.

Hung JJ, Borwankar AU, Dear BJ, Truskett TM, Johnston KP. High concentration tangential flow ultrafiltration of stable monoclonal antibody solutions with low viscosities. J Membr Sci. 2016;508:113-26.

Hung JJ, Dear BJ, Karouta CA, Godfrin PD, Bollinger JA, Nieto MP, et al. Protein-Protein Interactions of Highly Concentrated Monoclonal Antibody Solutions via Static Light Scattering and Influence on the Viscosity. J Phys Chem B. (under review).

Ignatova Z, Gierasch LM. Inhibition of protein aggregation in vitro and in vivo by a natural osmoprotectant. Proc Natl Acad Sci U S A. 2006;103(36):13357-61.

Inoue N, Takai E, Arakawa T, Shiraki K. Arginine and lysine reduce the high viscosity of serum albumin solutions for pharmaceutical injection. J Biosci Bioeng. 2014;117(5):539-43.

Inoue N, Takai E, Arakawa T, Shiraki K. Specific Decrease in Solution Viscosity of Antibodies by Arginine for Therapeutic Formulations. Mol Pharmaceutics. 2014;11(6):1889-96.

Inouye H, Houde D, Temel DB, Makowski L. Utility of Solution X-ray Scattering for the Development of Antibody Biopharmaceuticals. J Pharm Sci. 2016.

Ito L, Shiraki K, Matsuura T, Okumura M, Hasegawa K, Baba S, et al. High-resolution X-ray analysis reveals binding of arginine to aromatic residues of lysozyme surface: implication of suppression of protein aggregation by arginine. Protein Engineering Design and Selection. 2011;24(3):269-74.

Jaspe J, Hagen SJ. Do Protein Molecules Unfold in a Simple Shear Flow? Biophys J. 2006;91(9):3415-24.

Jezek J, Rides M, Derham B, Moore J, Cerasoli E, Simler R, et al. Viscosity of concentrated therapeutic protein compositions. Adv Drug Deliv Rev. 2011;63(13):1107-17.

Jezek J, Rides M, Derham B, Moore J, Cerasoli E, Simler R, et al. Viscosity of concentrated therapeutic protein compositions. Adv Drug Deliv Rev. 2011;63(13):1107-17.

Jiang SY, Cao ZQ. Ultralow-Fouling, Functionalizable, and Hydrolyzable Zwitterionic Materials and Their Derivatives for Biological Applications. Adv Mater. 2010;22(9):920-32.

Johnston KP, Maynard JA, Truskett TM, Borwankar AU, Miller MA, Wilson BK, et al. Concentrated Dispersions of Equilibrium Protein Nanoclusters that Reversibly Dissociate into Active Monomers. ACS Nano. 2012;6(2):1357-69.

Josephson LL, Furst EM, Galush WJ. Particle tracking microrheology of protein solutions. Journal of Rheology. 2016;60(4):531-40.

Kalwarczyk T, Kwapiszewska K, Szczepanski K, Sozanski K, Szymanski J, Michalska B, et al. Apparent Anomalous Diffusion in the Cytoplasm of Human Cells: The Effect of Probes' Polydispersity. J Phys Chem B. 2017;121(42):9831-7.

Kalwarczyk T, Sozanski K, Jakiela S, Wisniewska A, Kalwarczyk E, Kryszczuk K, et al. Length-scale dependent transport properties of colloidal and protein solutions for prediction of crystal nucleation rates. Nanoscale. 2014;6(17):10340-6.

Kalwarczyk T, Sozanski K, Ochab-Marcinek A, Szymanski J, Tabaka M, Hou S, et al. Motion of nanoprobes in complex liquids within the framework of the length-scale dependent viscosity model. Advances in Colloid and Interface Science. 2015;223:55-63.

Kalwarczyk T, Ziębacz N, Bielejewska A, Zaboklicka E, Koynov K, Szymański J, et al. Comparative Analysis of Viscosity of Complex Liquids and Cytoplasm of Mammalian Cells at the Nanoscale. Nano Letters. 2011;11(5):2157-63.

Kanai S, Liu J, Patapoff TW, Shire SJ. Reversible Self-Association of a Concentrated Monoclonal Antibody Solution Mediated by Fab-Fab Interaction That Impacts Solution Viscosity. J Pharm Sci. 2008;97(10):4219-27.

Kanani DM, Ghosh R. A constant flux based mathematical model for predicting permeate flux decline in constant pressure protein ultrafiltration. J Membr Sci. 2007;290(1–2):207-15.

Karow AR, Bahrenburg S, Garidel P. Buffer capacity of biologics--from buffer salts to buffering by antibodies. Biotechnol Prog. 2013;29(2):480-92.

Kastelic M, Dill KA, Kalyuzhnyi YV, Vlachy V. Controlling the viscosities of antibody solutions through control of their binding sites. Journal of Molecular Liquids. 2017.

Kern W. The Evolution of Silicon Wafer Cleaning Technology. Journal of The Electrochemical Society. 1990;137(6):1887-92.

Khan MF, Singh MK, Sen S. Measuring Size, Size Distribution, and Polydispersity of Water-in-Oil Microemulsion Droplets using Fluorescence Correlation Spectroscopy: Comparison to Dynamic Light Scattering. J Phys Chem B. 2016;120(5):1008-20.

Kheddo P, Cliff MJ, Uddin S, van der Walle CF, Golovanov AP. Characterizing monoclonal antibody formulations in arginine glutamate solutions using 1H NMR spectroscopy. mAbs. 2016;8(7):1245-58.

Kheddo P, Tracka M, Armer J, Dearman RJ, Uddin S, van der Walle CF, et al. The effect of arginine glutamate on the stability of monoclonal antibodies in solution. International journal of pharmaceutics. 2014;473(1–2):126-33.

Kuhn AB, Kube S, Karow-Zwick AR, Seeliger D, Garidel P, Blech M, et al. Improved Solution-State Properties of Monoclonal Antibodies by Targeted Mutations. J Phys Chem B. 2017;121(48):10818-27.

Kuhn LA, Swanson CA, Pique ME, Tainer JA, Getzoff ED. Atomic and residue hydrophilicity in the context of folded protein structures. Proteins: Struct, Funct, Bioinf. 1995;23(4):536-47.

Kumar V, Dixit N, Zhou L, Fraunhofer W. Impact of short range hydrophobic interactions and long range electrostatic forces on the aggregation kinetics of a monoclonal antibody and a dual-variable domain immunoglobulin at low and high concentrations. International journal of pharmaceutics. 2011;421(1):82-93.

Kumat TKS, Samuel D, Jayaraman G, Srimathi T, Yu C. The role of proline in the prevention of aggregation during protein folding in vitro. IUBMB Life. 1998;46(3):509-17.

Larson AM, Weight AK, Love K, Bonificio A, Wescott CR, Klibanov AM. Bulky Polar Additives That Greatly Reduce the Viscosity of Concentrated Solutions of Therapeutic Monoclonal Antibodies. J Pharm Sci. 2017;106(5):1211-7.

Le Bon C, Nicolai T, Kuil ME, Hollander JG. Self-Diffusion and Cooperative Diffusion of Globular Proteins in Solution. J Phys Chem B. 1999;103(46):10294-9.

Lehmann S, Seiffert S, Richtering W. Refractive Index Mismatch Can Misindicate Anomalous Diffusion in Single-Focus Fluorescence Correlation Spectroscopy. Macromolecular Chemistry and Physics. 2015;216(2):156-63.

Lekkerkerker HNW, Tuinier R. Colloids and the Depletion Interaction. 2011 ed. Dordrecht: Springer; 2011 May 12, 2011. 268 p.

Li L, Kumar S, Buck P, Burns C, Lavoie J, Singh S, et al. Concentration Dependent Viscosity of Monoclonal Antibody Solutions: Explaining Experimental Behavior in Terms of Molecular Properties. Pharm Res. 2014;31(11):3161-78.

Li Y, Lubchenko V, Vekilov PG. The use of dynamic light scattering and Brownian microscopy to characterize protein aggregation. Review of Scientific Instruments. 2011;82(5):-.

Liao SM, Du QS, Meng JZ, Pang ZW, Huang RB. The multiple roles of histidine in protein interactions. Chem Cent J. 2013;7.

Lilyestrom WG, Shire SJ, Scherer TM. Influence of the Cosolute Environment on IgG Solution Structure Analyzed by Small-Angle X-ray Scattering. J Phys Chem B. 2012;116(32):9611-8.

Lilyestrom WG, Yadav S, Shire SJ, Scherer TM. Monoclonal Antibody Self-Association, Cluster Formation, and Rheology at High Concentrations. J Phys Chem B. 2013;117(21):6373-84.

Liu J, Nguyen MDH, Andya JD, Shire SJ. Reversible Self-Association Increases the Viscosity of a Concentrated Monoclonal Antibody in Aqueous Solution. J Pharm Sci. 2005;94(9):1928-40.

Liu Y, Porcar L, Chen J, Chen W-R, Falus P, Faraone A, et al. Lysozyme Protein Solution with an Intermediate Range Order Structure. J Phys Chem B. 2010;115(22):7238-47.

Lonetti B, Fratini E, Chen SH, Baglioni P. Viscoelastic and small angle neutron scattering studies of concentrated protein solutions. Physical Chemistry Chemical Physics. 2004;6(7):1388-95.

Maeder W, Lieby P, Sebald A, Spycher M, Bolli R. Stability over 24 Months and Tolerability of a New 20% Proline-stabilized Polyclonal Immunoglobulin for Subcutaneous Administration (SCIG). J Allergy Clin Immunol. 2010;125(2, Supplement 1):AB142.

Malchus N, Weiss M. Elucidating Anomalous Protein Diffusion in Living Cells with Fluorescence Correlation Spectroscopy—Facts and Pitfalls. Journal of Fluorescence. 2010;20(1):19-26.

Marcos B, Moresoli C, Skorepova J, Vaughan B. CFD modeling of a transient hollow fiber ultrafiltration system for protein concentration. J Membr Sci. 2009;337(1-2):136-44.

Matheus S, Friess W, Schwartz D, Mahler H-C. Liquid high concentration IgG1 antibody formulations by precipitation. J Pharm Sci. 2009;98(9):3043-57.

McCabe W, Smith J, Harriot P. Unit Operations of Chemical Engineering. 7th ed. Columbus: McGraw-Hill Education; 2004.

McQuarrie D. Statistical Mechanics: University Science Books; 2000.

Miao F, Velayudhan A, DiBella E, Shervin J, Felo M, Teeters M, et al. Theoretical analysis of excipient concentrations during the final ultrafiltration/diafiltration step of therapeutic antibody. Biotechnol Prog. 2009;25(4):964-72.

Minton AP. Recent applications of light scattering measurement in the biological and biopharmaceutical sciences. Analytical biochemistry. 2016;501:4-22.

Minton AP. Static Light Scattering from Concentrated Protein Solutions, I: General Theory for Protein Mixtures and Application to Self-Associating Proteins. Biophys J. 2007;93(4):1321-8.

Monkos K, Turczynski B. A comparative study on viscosity of human, bovine and pig IgG immunoglobulins in aqueous solutions. International Journal of Biological Macromolecules. 1999;26(2–3):155-9.

Moody TP, Kingsbury JS, Durant JA, Wilson TJ, Chase SF, Laue TM. Valence and anion binding of bovine ribonuclease A between pH 6 and 8. Analytical biochemistry. 2005;336(2):243-52.

Mosbaek CR, Konarev PV, Svergun DI, Rischel C, Vestergaard B. High Concentration Formulation Studies of an IgG2 Antibody Using Small Angle X-ray Scattering. Pharm Res. 2012;29(8):2225-35.

Müller CB, Loman A, Richtering W, Enderlein J. Dual-Focus Fluorescence Correlation Spectroscopy of Colloidal Solutions: Influence of Particle Size. J Phys Chem B. 2008;112(28):8236-40.

Myers HP. Introductory solid state physics. 2 ed. Boca Raton, FL: CRC Press; 1997.

Neergaard MS, Kalonia DS, Parshad H, Nielsen AD, Møller EH, van de Weert M. Viscosity of high concentration protein formulations of monoclonal antibodies of the IgG1 and IgG4 subclass – Prediction of viscosity through protein–protein interaction measurements. European Journal of Pharmaceutical Sciences. 2013;49(3):400-10.

Nichols P, Li L, Kumar S, Buck PM, Singh SK, Goswami S, et al. Rational design of viscosity reducing mutants of a monoclonal antibody: Hydrophobic versus electrostatic inter-molecular interactions. mAbs. 2015;7(1):212-30.

Nicoud L, Jagielski J, Pfister D, Lazzari S, Massant J, Lattuada M, et al. Kinetics of Monoclonal Antibody Aggregation from Dilute toward Concentrated Conditions. J Phys Chem B. 2016.

Nicoud L, Lattuada M, Lazzari S, Morbidelli M. Viscosity scaling in concentrated dispersions and its impact on colloidal aggregation. Physical Chemistry Chemical Physics. 2015;17(37):24392-402.

Nicoud L, Lattuada M, Yates A, Morbidelli M. Impact of aggregate formation on the viscosity of protein solutions. Soft Matter. 2015.

Odijk T. Depletion Theory of Protein Transport in Semi-Dilute Polymer Solutions. Biophys J. 2000;79(5):2314-21.

Pal N, Verma SD, Singh MK, Sen S. Fluorescence Correlation Spectroscopy: An Efficient Tool for Measuring Size, Size-Distribution and Polydispersity of Microemulsion Droplets in Solution. Analytical Chemistry. 2011;83(20):7736-44.

Palacio L, Ho C-C, Zydney AL. Application of a pore-blockage—Cake-filtration model to protein fouling during microfiltration. Biotechnol Bioeng. 2002;79(3):260-70.

Pan WC, Vekilov PG, Lubchenko V. Origin of Anomalous Mesoscopic Phases in Protein Solutions. J Phys Chem B. 2010;114(22):7620-30.

Pathak Jai A, Sologuren Rumi R, Narwal R. Do Clustering Monoclonal Antibody Solutions Really Have a Concentration Dependence of Viscosity? Biophys J. 2013;104(4):913-23.

Pecora R. Dynamic Light Scattering: Applications of Photon Correlation Spectroscopy. New York: Springer 1985.

Pemberton TA, Still BR, Christensen EM, Singh H, Srivastava D, Tanner JJ. Proline: Mother Nature's cryoprotectant applied to protein crystallography. Acta Crystallogr, Sect D: Biol Crystallogr. 2012;68(Pt 8):1010-8.

Péter F, Lionel P, Emiliano F, Wei-Ren C, Antonio F, Kunlun H, et al. Distinguishing the monomer to cluster phase transition in concentrated lysozyme solutions by studying the temperature dependence of the short-time dynamics. Journal of Physics: Condensed Matter. 2012;24(6):064114.

Piazza R, Iacopini S. Transient clustering in a protein solution. The European Physical Journal E. 2002;7(1):45-8.

Porcar L, Falus P, Chen W-R, Faraone A, Fratini E, Hong K, et al. Formation of the Dynamic Clusters in Concentrated Lysozyme Protein Solutions. J Phys Chem Lett. 2009;1(1):126-9.

Quang LJ, Sandler SI, Lenhoff AM. Anisotropic Contributions to Protein–Protein Interactions. J Chem Theory Comput. 2014;10(2):835-45.

Reitan NK, Juthajan A, Lindmo T, de Lange Davies C. Macromolecular diffusion in the extracellular matrix measured by fluorescence correlation spectroscopy. BIOMEDO. 2008;13(5):054040--9.

Richter S, Boyko V, Schröter K. Gelation Studies on a Radical Chain Cross-Linking Copolymerization Process: Comparison of the Critical Exponents Obtained by Dynamic Light Scattering and Rheology. Macromolecular Rapid Communications. 2004;25(4):542-6.

Roberts CJ, Blanco MA. Role of Anisotropic Interactions for Proteins and Patchy Nanoparticles. J Phys Chem B. 2014;118(44):12599-611.

Roberts CJ. Protein aggregation and its impact on product quality. Current Opinion in Biotechnology. 2014;30:211-7.

Roberts CJ. Therapeutic protein aggregation: mechanisms, design, and control. Trends in Biotechnology. 2014;32(7):372-80.

Roos M, Ott M, Hofmann M, Link S, Rössler E, Balbach J, et al. Coupling and Decoupling of Rotational and Translational Diffusion of Proteins under Crowding Conditions. Journal of the American Chemical Society. 2016;138(32):10365-72.

Roosen-Runge F, Hennig M, Seydel T, Zhang F, Skoda MWA, Zorn S, et al. Protein diffusion in crowded electrolyte solutions. Biochim Biophys Acta, Proteins Proteomics. 2010;1804(1):68-75.

Roosen-Runge F, Hennig M, Zhang F, Jacobs RMJ, Sztucki M, Schober H, et al. Protein self-diffusion in crowded solutions. Proc Natl Acad Sci U S A. 2011;108(29):11815.

Rosenberg E, Hepbildikler S, Kuhne W, Winter G. Ultrafiltration concentration of monoclonal antibody solutions: Development of an optimized method minimizing aggregation. J Membr Sci. 2009;342(1-2):50-9.

Ross PD, Minton AP. HARD QUASI-SPHERICAL MODEL FOR VISCOSITY OF HEMOGLOBIN SOLUTIONS. Biochem Biophys Res Commun. 1977;76(4):971-6.

Sablani SS, Goosen MFA, Al-Belushi R, Wilf M. Concentration polarization in ultrafiltration and reverse osmosis: a critical review. Desalination. 2001;141(3):269-89.

Saha D, Joshi YM, Bandyopadhyay R. Characteristics of the secondary relaxation process in soft colloidal suspensions. Epl. 2015;112(4).

Salinas BA, Sathish HA, Bishop SM, Harn N, Carpenter JF, Randolph TW. Understanding and Modulating Opalescence and Viscosity in a Monoclonal Antibody Formulation. J Pharm Sci. 2010;99(1):82-92.

Salis A, Bostrom M, Medda L, Cugia F, Barse B, Parsons DF, et al. Measurements and theoretical interpretation of points of zero charge/potential of BSA protein. Langmuir 2011;27(18):11597-604.

Salvi G, De Los Rios P, Vendruscolo M. Effective interactions between chaotropic agents and proteins. Proteins: Struct, Funct, Bioinf. 2005;61(3):492-9.

Samuel D, Kumar TK, Ganesh G, Jayaraman G, Yang PW, Chang MM, et al. Proline inhibits aggregation during protein refolding. Protein Sci. 2000;9(2):344-52.

Samuel D, Kumar TKS, Jayaraman G, Yang PW, Yu C. Proline is a protein solubilizing solute. Biochem Mol Biol Int. 1997;41(2):235-42.

Scherer TM, Liu J, Shire SJ, Minton AI. Intermolecular Interactions of IgG1 Monoclonal Antibodies at High Concentrations Characterized by Light Scattering. J Phys Chem B. 2010;114(40):12948-57.

Scherer TM. Cosolute Effects on the Chemical Potential and Interactions of an IgG1 Monoclonal Antibody at High Concentrations. J Phys Chem B. 2013;117(8):2254-66.

Scherer TM. Role of Cosolute–Protein Interactions in the Dissociation of Monoclonal Antibody Clusters. J Phys Chem B. 2015;119(41):13027-38.

Schmit JD, He F, Mishra S, Ketchem RR, Woods CE, Kerwin BA. Entanglement Model of Antibody Viscosity. J Phys Chem B. 2014;118(19):5044-9.

Schneider CA, Rasband WS, Eliceiri KW. NIH Image to ImageJ: 25 years of image analysis. Nat Meth. 2012;9(7):671-5.

Schneider CA, Rasband WS, Eliceiri KW. NIH Image to ImageJ: 25 years of image analysis. Nat Meth. 2012;9(7):671-5.

Schwille P, Haustein E. Fluorescence Correlation Spectroscopy - An Introduction to its Concepts and Applications2001.

Shen VK, Cheung JK, Errington JR, Truskett TM. Coarse-Grained Strategy for Modeling Protein Stability in Concentrated Solutions II: Phase Behavior. Biophys J. 2006;90:1949-60.

Shen VK, Cheung JK, Errington JR, Truskett TM. Insights into crowding effects on protein stability from a coarse-grained model. J Biomech Eng. 2009;131(7):071002.

Shire SJ, Shahrokh Z, Liu J. Challenges in the Development of High Protein Concentration Formulations. J Pharm Sci. 2004;93(6):1390-402.

Shukla A, Mylonas E, Di Cola E, Finet S, Timmins P, Narayanan T, et al. Absence of equilibrium cluster phase in concentrated lysozyme solutions. Proc Natl Acad Sci U S A. 2008;105(13):5075.

Shukla D, Schneider CP, Trout BL. Molecular level insight into intra-solvent interaction effects on protein stability and aggregation. Adv Drug Deliv Rev. 2011;63(13):1074-85.

Shukla D, Trout BL. Interaction of Arginine with Proteins and the Mechanism by Which It Inhibits Aggregation. J Phys Chem B. 2010;114(42):13426-38.

Shukla D, Trout BL. Preferential Interaction Coefficients of Proteins in Aqueous Arginine Solutions and Their Molecular Origins. J Phys Chem B. 2011;115(5):1243-53.

Sinko PJ, Martin A. Martin's Physical Pharmacy and Pharmaceutical Sciences. 5 ed. Philadelphia: Lippincott Williams & Wilkins; 2006.

Snead WT, Hayden CC, Gadok AK, Zhao C, Lafer EM, Rangamani P, et al. Membrane fission by protein crowding. Proc Natl Acad Sci U S A. 2017;114(16):E3258.

Some D, Pollastrini J, Cao S. Characterizing Reversible Protein Association at Moderately High Concentration Via Composition-Gradient Static Light Scattering. J Pharm Sci. 2016;105(8):2310-8.

Soraruf D, Roosen-Runge F, Grimaldo M, Zanini F, Schweins R, Seydel T, et al. Protein cluster formation in aqueous solution in the presence of multivalent metal ions - a light scattering study. Soft Matter. 2014;10(6):894-902.

Sorret Lea L, DeWinter Madison A, Schwartz Daniel K, Randolph Theodore W. Challenges in Predicting Protein-Protein Interactions from Measurements of Molecular Diffusivity. Biophys J. 2016;111(9):1831-42.

Sozański K, Wiśniewska A, Kalwarczyk T, Hołyst R. Activation Energy for Mobility of Dyes and Proteins in Polymer Solutions: From Diffusion of Single Particles to Macroscale Flow. Phys Rev Lett. 2013;111(22):228301.

SpectrumLabs. Modified PES Fiber Modules 2014 [Available from: http://www.spectrumlabs.com/filtration/mPES.html.

Srinivasan C, Weight AK, Bussemer T, Klibanov AM. Non-Aqueous Suspensions of Antibodies are Much Less Viscous Than Equally Concentrated Aqueous Solutions. Pharm Res. 2013.

Stachowiak JC, Hayden CC, Sasaki DY. Steric confinement of proteins on lipid membranes can drive curvature and tubulation. Proc Natl Acad Sci U S A. 2010;107(17):7781.

Starr TE, Thompson NL. Local Diffusion and Concentration of IgG near Planar Membranes: Measurement by Total Internal Reflection with Fluorescence Correlation Spectroscopy. J Phys Chem B. 2002;106(9):2365-71.

Štulík K, Pacáková V, Tichá M. Some potentialities and drawbacks of contemporary size-exclusion chromatography. Journal of Biochemical and Biophysical Methods. 2003;56(1–3):1-13.

Subramani A, Kim S, Hoek EMV. Pressure, flow, and concentration profiles in open and spacer-filled membrane channels. J Membr Sci. 2006;277(1–2):7-17.

Sun Y, Li X, Düzgüneşv N, Takaoka Y, Ohi S, Hirota S. The Shape Parameter of Liposomes and DNA-Lipid Complexes Determined by Viscometry Utilizing Small Sample Volumes. Biophys J. 2003;85(2):1223-32.

Svergun DI, Koch MH, Timmins PA, May RP. Small angle X-ray and neutron scattering from solutions of biological macromolecules. New York: Oxford University Press; 2013. 368 p.

Szymański J, Patkowski A, Wilk A, Garstecki P, Holyst R. Diffusion and Viscosity in a Crowded Environment: from Nano- to Macroscale. J Phys Chem B. 2006;110(51):25593-7.

Tanford C. The physical chemistry of macromolecules. New York: John Wiley & Sons; 1961.

Teeters M, Bezila D, Benner T, Alfonso P, Alred P. Predicting diafiltration solution compositions for final ultrafiltration/diafiltration steps of monoclonal antibodies. Biotechnol Bioeng. 2011;108(6):1338-46.

Tokuyama M, Oppenheim I. Dynamics of hard-sphere suspensions. Phys Rev E. 1994;50(1):R16-R9.

Torquato S, Truskett TM, Debenedetti PG. Is Random Close Packing of Spheres Well Defined? Phys Rev Lett. 2000;84(10):2064-7.

Tuteja A, Mackay ME, Narayanan S, Asokan S, Wong MS. Breakdown of the Continuum Stokes−Einstein Relation for Nanoparticle Diffusion. Nano Letters. 2007;7(5):1276-81.

van Blaaderen A, Peetermans J, Maret G, Dhont JKG. Long-time self-diffusion of spherical colloidal particles measured with fluorescence recovery after photobleaching. The Journal of Chemical Physics. 1992;96(6):4591-603.

van Reis R, Zydney A. Bioprocess membrane technology. J Membr Sci. 2007;297(1–2):16-50.

Vondrášek J, Mason PE, Heyda J, Collins KD, Jungwirth P. The Molecular Origin of Like-Charge Arginine−Arginine Pairing in Water. J Phys Chem B. 2009;113(27):9041-5.

Wang F, Shi Y, Luo S, Chen Y, Zhao J. Conformational Transition of Poly(N-isopropylacrylamide) Single Chains in Its Cononsolvency Process: A Study by Fluorescence Correlation Spectroscopy and Scaling Analysis. Macromolecules. 2012;45(22):9196-204.

Wang G, Varga Z, Hofmann J, Zarraga IE, Swan JW. Structure and Relaxation in Solutions of Monoclonal Antibodies. J Phys Chem B. 2018;122(11):2867-80.

Wang S, Zhang N, Hu T, Dai WG, Feng X, Zhang X, et al. Viscosity-Lowering Effect of Amino Acids and Salts on Highly Concentrated Solutions of two IgG1 Monoclonal Antibodies. Mol Pharmaceutics. 2015.

Wang W, Lilyestrom WG, Hu ZY, Scherer TM. Cluster Size and Quinary Structure Determine the Rheological Effects of Antibody Self-Association at High Concentrations. J Phys Chem B. 2018;122(7):2138-54.

Wang W, Singh SK, Li N, Toler MR, King KR, Nema S. Immunogenicity of protein aggregates-Concerns and realities. International journal of pharmaceutics. 2012;431(1-2):1-11.

Wang Y, Li C, Pielak GJ. Effects of Proteins on Protein Diffusion. Journal of the American Chemical Society. 2010;132(27):9392-7.

Weiss M, Hashimoto H, Nilsson T. Anomalous Protein Diffusion in Living Cells as Seen by Fluorescence Correlation Spectroscopy. Biophys J. 2003;84(6):4043-52.

Whitaker N, Xiong J, Pace SE, Kumar V, Middaugh CR, Joshi SB, et al. A Formulation Development Approach to Identify and Select Stable Ultra–High-Concentration Monoclonal Antibody Formulations With Reduced Viscosities. J Pharm Sci. 2017;106(11):3230-41.

Widengren J, Mets U, Rigler R. Fluorescence correlation spectroscopy of triplet states in solution: a theoretical and experimental study. The Journal of Physical Chemistry. 1995;99(36):13368-79.

Woldeyes MA, Calero-Rubio C, Furst EM, Roberts CJ. Predicting Protein Interactions of Concentrated Globular Protein Solutions Using Colloidal Models. J Phys Chem B. 2017;121(18):4756-67.

Woll D. Fluorescence correlation spectroscopy in polymer science. RSC Advances. 2014;4(5):2447-65.

Xie G, Timasheff SN. The thermodynamic mechanism of protein stabilization by trehalose. Biophys Chem. 1997;64(1–3):25-43.

Yadav S, Laue TM, Kalonia DS, Singh SN, Shire SJ. The Influence of Charge Distribution on Self-Association and Viscosity Behavior of Monoclonal Antibody Solutions. Mol Pharmaceutics. 2012;9(4):791-802.

Yadav S, Liu J, Shire SJ, Kalonia DS. Specific Interactions in High Concentration Antibody Solutions Resulting in High Viscosity. J Pharm Sci. 2010;99(3):1152-68.

Yadav S, Scherer TM, Shire SJ, Kalonia DS. Use of dynamic light scattering to determine second virial coefficient in a semidilute concentration regime. Analytical biochemistry. 2011;411(2):292-6.

Yadav S, Shire SJ, Kalonia DS. Factors Affecting the Viscosity in High Concentration Solutions of Different Monoclonal Antibodies. J Pharm Sci. 2010;99(12):4812-29.

Yadav S, Shire SJ, Kalonia DS. Viscosity behavior of high-concentration monoclonal antibody solutions: Correlation with interaction parameter and electroviscous effects. J Pharm Sci. 2012;101(3):998-1011.

Yadav S, Sreedhara A, Kanai S, Liu J, Lien S, Lowman H, et al. Establishing a Link Between Amino Acid Sequences and Self-Associating and Viscoelastic Behavior of Two Closely Related Monoclonal Antibodies. Pharm Res. 2011;28(7):1750-64.

Yajima H, Yamamoto H, Nagaoka M, Nakazato K, Ishii T, Niimura N. Small-angle neutron scattering and dynamic light scattering studies of N- and C-terminal fragments of ovotransferrin. Biochim Biophys Acta, Gen Subj. 1998;1381(1):68-76.

Yang Z, Galloway JA, Yu H. Protein Interactions with Poly(ethylene glycol) Self-Assembled Monolayers on Glass Substrates: Diffusion and Adsorption. Langmuir. 1999;15(24):8405-11.

Yearley EJ, Zarraga IE, Shire SJ, Scherer TM, Gokarn Y, Wagner NJ, et al. Small-Angle Neutron Scattering Characterization of Monoclonal Antibody Conformations and Interactions at High Concentrations. Biophys J. 2013;105(3):720-31.

Yearley Eric J, Godfrin Paul D, Perevozchikova T, Zhang H, Falus P, Porcar L, et al. Observation of Small Cluster Formation in Concentrated Monoclonal Antibody Solutions and Its Implications to Solution Viscosity. Biophys J. 2014;106(8):1763-70.

Zarraga IE, Taing R, Zarzar J, Luoma J, Hsiung J, Patel A, et al. High shear rheology and anisotropy in concentrated solutions of monoclonal antibodies. J Pharm Sci. 2013;102(8):2538-49.

Zettl U, Hoffmann ST, Koberling F, Krausch G, Enderlein J, Harnau L, et al. Self-Diffusion and Cooperative Diffusion in Semidilute Polymer Solutions As Measured by Fluorescence Correlation Spectroscopy. Macromolecules. 2009;42(24):9537-47.

Zhao H, Brown Patrick H, Schuck P. On the Distribution of Protein Refractive Index Increments. Biophys J. 2011;100(9):2309-17.

Zondlo NJ. Aromatic-Proline Interactions: Electronically Tunable CH/pi Interactions. Acc Chem Res. 2013;46(4):1039-49.